Module-Level Modelling Approach for Li-Ion Batteries: a Cloud-based Digital Twin Simulation Platform

Ph.D. Thesis Dissertation

Doctoral Program in Applied Engineering

Mondragon Goi Eskola Politeknikoa

Electronics and Computing Department

Presented by

Olatz Lizaso Eguileta

Supervised by:

Dr. Unai Iraola Iriondo (MU)

Dr. Eduardo Miguel Garcia de Cortazar (Ikerlan)

Hernani, Jul 2023

This Ph.D. Thesis received funding from the BIKAINTEK 2019 program (grant number 20-AF-W2-2019-00005), and it was carried out in a collaboration framework between IKERLAN Technology Research Centre and Cegasa Energía.

Abstract

Title: Development and Validation of a Digital Twin Simulation Platform for Li-ion Batteries.

The adoption of large-scale Lithium-ion Batteries (LIBs) has been growing steadily and evolving. These installations involve the interconnection of multiple batteries to form larger and more powerful systems capable of providing megawatt-hours (MWh) of stored energy. LIBs have emerged as a promising solution for electrical energy storage due to their decreasing prices and improved manufacturing efficiency. This combination has made LIBs more accessible, and their demand has rapidly increased in key applications such as electric vehicles and stationary applications.

In the context of LIBs, specifically in the case of modules, individual heterogeneities and imbalances among the different cells that compose the module pose a significant technological challenge. In fact, these disparities can compromise the energy efficiency and overall lifespan of the battery module. While numerous studies have been conducted on individual cells, there is a significant gap in understanding and adequately considering the effects and complexities at the module level.

In this thesis, an innovative methodology is proposed to develop module-level battery models that include thermal and electrical components, as well as a State of Charge (SoC) estimator. These module-level models are based on equivalent circuits extrapolated from widely-used cell-level models. A detailed thermal model is proposed to capture the interactions between each cell within the battery system, and an electrical model is developed to simulate the behavior of individual cells through co-simulation or parallel execution. Additionally, an approach to implement these models in a cloud-based simulation platform is presented, enabling estimations of each cell's performance, identification of potential issues, and providing sufficient computational capacity.

The proposed methodology has been validated at laboratory level by means of a prototype specifically built for this purpose. The correct operation of the thermal and electrical model and the SoC estimator at the cell level has been demonstrated by means of a series of laboratory tests. These models have then been adapted at module level, taking into

account the electrical and geometrical characteristics of the module. By means of a series of laboratory tests carried out on the module prototype, the correct extrapolation of the cell models to the module level has been demonstrated. In addition, and with the aim of evaluating the heterogeneity and imbalance detection capacity of the developed models, two case studies have been conducted. In them, certain anomalies have been introduced in the laboratory prototype, and it has been proved that the models exhibit these functionalities. In particular, two types of anomalies have been introduced: a) the first one consists of a voltage unbalance between the cells of the module and b) the second one consists of a thermal unbalance in the module by means of a thermal blanket. In both case studies, the ability to detect irregularities in the module has been demonstrated.

The proposed methodology has been validated at the laboratory level using a specifically designed prototype. The correct operation of the thermal and electrical models, as well as the SoC estimator at the cell level, has been demonstrated through a series of laboratory tests. Subsequently, these models have been adapted to the module level, taking into account the corresponding electrical and geometric characteristics. Through a series of laboratory tests conducted on the module prototype, the proper extrapolation of cell-level models to the module level has been demonstrated. Furthermore, two case studies have been conducted to evaluate the capability of the developed models to detect heterogeneities and imbalances. These case studies involved the introduction of anomalies in the laboratory prototype, such as voltage imbalances between module cells and thermal imbalances using a thermal blanket. In both cases, the models showed the ability to detect irregularities in the module.

In general, the methodology proposed in this thesis allows to have a holistic model of a LIB at module level, which represents the electrical and thermal behaviour of each of the cells that compose the module, thus contributes to a better understanding allowing an adequate monitoring of the system.

Key words: Digital Twin, Cloud computing, Battery models, State of Charge

Laburpena

Titulua: Litio-ioi Baterietarako Modulu-mailako Modelatze Ikuspegia: Hodeian Oinarritutako Digital Twin Simulazio Plataforma

Eskala handiko Litio-Ioizko Bateriek (LIBek) etengabeko hazkunde eta bilakaera daramate. MWh-rarteko energia biltegiratzeko gai diren instalazio handi eta sendo hauek eratzeko bateria askoren arteko konexioa beharrezkoa da. Energia elektrikoaren biltegiratze-sistemen artean, LIBak etorkizun handiko irtenbide gisa nabarmentzen dira hauen prezioa jaitsi eta fabrikazioaren eraginkortasuna hobetu den neurrian. Honela, LIBen instalazioa bideragarriagoa da eta hauen eskaria azkar handitu da energiaren funtsezko aplikazioetan, hala nola ibilgailu elektrikoetan eta aplikazio geldikorretan.

LIBen testuinguruan, eta bereziki LIBen moduluetan, hauek osatzen dituzten zelulen arteko heterogeneotasun eta desoreka indibidualak erronka teknologiko esanguratsua dira. Izan ere, ezberdintasun horiek modulu osoaren eraginkortasun energetikoa eta bizitza erabilgarria arriskuan jar ditzakete. Banakako zelda horien esparruan ikerketa ugari egin diren arren, barne-efektu guztien kontsiderazio eta konplexutasunen modulu-mailako ulermenean gabezia nabarmena dago.

Testuinguru honetan, tesi honek bateriaren ereduak modulu-mailan garatzeko metodologia berritzailea aurkeztu du. Eredu horiek efektu termiko eta elektrikoak algoritmoen bidez deskribatzen dituzte. Horrez gain, bateriaren karga-egoera (SoC, ingelesezko siglen arabera) estimatzen duen algoritmoa proposatu da. Modulu-mailako ereduak zelda-mailan erabili ohi diren zirkuitu baliokideen estrapolazioan oinarritzen dira. Modu honetan, zelda guztiak eta hauen elkarrekintzak kontuan hartzen dituen modulu-mailako eredu termikoa eta zelda bakoitza paraleloan simulatuko duen eredu elektrikoa ere proposatu dira. Jarraian, eredu horiek hodeian oinarritutako simulazio-plataforma batean inplementatzeko estrategia aurkeztu da. Oro har, metodologia honek moduluko zelda bakoitzaren egoera estimatzeko eta arazo potentzialak identifikatzeko beharrezko konputazio-ahalmena duen ingurunea eskaintzen du.

Abstract

Metodologia honen balioztatzean prototipo bat eraiki eta entseatu da zelda-mailako eredu termiko, elektriko eta SoC estimatzaileak zuzen funtzionatzen dutela frogatzeko. Ondoren, eredu horiek modulu-mailara egokitu dira, moduluaren ezaugarri elektriko eta geometrikoak kontuan hartuta. Moduluaren prototipoa laborategian entseatuz zelda-mailako ereduak modulu-mailara behar bezala estrapolatu direla frogatu da. Gainera, garatutako ereduen heterogeneotasunak eta desorekak detektatzeko gaitasuna ebaluatzeko, bi azterketa-kasu gauzatu dira laborategiko moduluaren prototipoan hainbat anomalia ezarriz: a) lehenak, moduluko zelden arteko tentsio-desoreka du, eta b) bigarrenak, berriz, manta termiko baten bidez eragindako desoreka termikoa. Moduluan irregulartasunak detektatzeko gaitasuna bi azterketa-kasuetan frogatu da.

Oro har, tesi honetan proposatutako metodologiak LIBen modulu-mailako eredu holistikoa garatzeko aukera ematen du. Eredu huek modulua osatzen duten zelda bakoitzaren portaera elektriko eta termikoak irudikatzen dituzte eta, hala, sistema modu egokian monitorizatu daiteke.

Hitz gakoak: Digital Twin, Cloud computing, Bateria-ereduak, Karga-egoera

Resumen

Título: Enfoque de Modelado a Nivel de Módulo para Baterías de Ión-Litio: una Plataforma de Simulación de Gemelo Digital Basada en la Nube

La adopción de Baterías de Litio-ion (LIBs) a gran escala ha experimentado un crecimiento constante y continuo. Estas instalaciones implican la interconexión de múltiples baterías para formar sistemas más grandes y potentes, capaces de proporcionar megavatios-hora (MWh) de energía almacenada. Las LIBs han surgido como una solución prometedora para el almacenamiento de energía eléctrica debido a su disminución de precios y mejora en la eficiencia de fabricación. Esta combinación ha hecho que las LIBs sean más accesibles y su demanda haya aumentado rápidamente en aplicaciones clave, como vehículos eléctricos y aplicaciones estacionarias.

En el contexto de las LIBs, y específicamente en el caso de los módulos, las heterogeneidades y desequilibrios individuales entre las diferentes celdas que conforman el módulo representan un desafío tecnológico significativo. De hecho, estas disparidades pueden comprometer la eficiencia energética y la vida útil del módulo de la batería en su conjunto. Aunque se han realizado numerosos estudios en el ámbito de las celdas individuales, existe una brecha significativa en la comprensión y la consideración adecuada de los efectos y la complejidad a nivel de módulo.

En esta tesis, se propone una metodología innovadora para desarrollar modelos de batería a nivel de módulo que incluyen componentes térmicos, eléctricos y un estimador de SoC. Estos modelos a nivel de módulo se basan en circuitos equivalentes extrapolados de modelos ampliamente utilizados a nivel de celda. Se propone un modelo térmico que detalla todas las celda y su interacción en un sistema de baterías, así como un modelo eléctrico que ejecuta individualmente cada celda mediante co-simulación o ejecución simultánea en procesos paralelos. Además, se presenta un enfoque para implementar estos modelos en una plataforma de simulación basada en la nube, lo que permite obtener estimaciones de cada celda del módulo, identificar problemas potenciales y proporcionar un entorno con suficiente capacidad computacional.

Abstract

La metodología propuesta se ha validado a nivel de laboratorio utilizando un prototipo específicamente diseñado para este propósito. Se ha demostrado el correcto funcionamiento del modelo térmico, eléctrico y del estimador de SoC a nivel de celda a través de una serie de ensayos de laboratorio. Luego, estos modelos se han adaptado a nivel de módulo teniendo en cuenta las características eléctricas y geométricas correspondientes. Mediante una serie de ensayos de laboratorio realizados en el prototipo del módulo, se ha demostrado la correcta extrapolación de los modelos de celda a nivel de módulo. Además, se han ejecutado dos casos de estudio para evaluar la capacidad de detección de heterogeneidades y desequilibrios de los modelos desarrollados. Estos casos de estudio involucraron la introducción de anomalías en el prototipo de laboratorio, como desequilibrios de tensión entre las celdas del módulo y desequilibrios térmicos mediante el uso de una manta térmica. En ambos casos, se demostró la capacidad de detección de irregularidades en el módulo.

En general, la metodología propuesta en esta tesis proporciona un modelo holístico de una LIB a nivel de módulo, que representa los comportamientos eléctricos y térmicos de cada una de las celdas que lo componen. Esto permite una monitorización adecuada del sistema y contribuye a un mejor entendimiento y monitorización de las LIBs a gran escala.

Palabras clave: Gemelo Digital, Cloud computing, Modelos de Batería, Estado de Carga

Contents

List of Figures

List of Tables

Acronyms

AFE	Analogue Front-Ends
AI	Artificial Intelligence
ANFIS	Adaptive Neuro-Fuzzy Inference Systems
ANN	Artificial Neural Networks
API	Application Programming Interface
AWS	Amazon Web Services
BD	Big Data
BMS	Battery Management System
CAD	Computer-Aided Design
CFD	Computational Fluid Dynamics
Cp	Specific Heat Capacity
CPS	Cyber Physical System
CPU	Central Processing Unit
DFN	Doyle Fuller Newman

DNN	Deep Neural Networks
DoD	Depth of Discharge
DT	Digital Twin
DTSP	Digital Twin Simulation Platform
EC2	Elastic Compute Cloud
ECM	Equivalent Circuit Model
EHC	Entropic Heat Coefficient
EIS	Electrochemical Impedance Spectroscopy
EKF	Extended Kalman Filter
EMS	Energy Management System
EV	Electric Vehicle
EVM	Equivalent Module Voltage
FL	Fuzzy Logic
GCP	Google Cloud Platform
HPPT	Hybrid Pulse Power Test
HTTP	Hypertext Transfer Protocol
IaaS	Infrastructure as a Service
IoT	Internet of Things
IT	Information Technology
KF	Kalman Filter

LFP	Lithium Iron Phosphate
LIB	Lithium-ion Battery
LTM	Lumped Thermal Model
LW	LithiumWerks
MA	Microsoft Azure
MQTT	Message Queuing Telemetry Transport
MWh	Megawatt-Hour
NMC	Nickel Manganese Cobalt
NN	Neural Network
NR	Newton-Raphson
NTC	Negative Temperature Coefficient
OCP	Open Circuit Potentiometry
OCV	Open Circuit Voltage
P2D	Pseudo-2D Model
PaaS	Platform as a Service
PC	Personal Computer
PCM	Phase Change Material
PF	Particle Filter
PNGV	Partnership for a New Generation of Vehicles
PV	Photovoltaic

RAM	Random Access Memory
RC	Resistor-Capacitor
RDS	Relational Database Service
ROM	Read-Only Memory
RPi	Raspberry Pi
S3	Simple Storage Service
SaaS	Software as a Service
SOA	Safe Operating Area
SoA	State of the Art
SoC	State of Charge
SoF	State of Function
SoH	State of Health
SoP	State of Power
SoX	X-key States
SP	Sigma Point
SPI	Serial Peripheral Interface
SPKF	Sigma Point Kalman Filter
SPM	Simple Particle Model
SQL	Structure Query Language
SVM	Support Vector Machines

TMS	Thermal Management System
UI	User Interface
UKF	Unscented Kalman Filter
USB	Universal Serial Bus
VF	View-Factor
VPC	Virtual Private Cloud

List of Symbols

Symbol	Description	Unit
A	Area of the cell perpendicular to stationary heat flow rate	[m^2]
C_i	Capacitor parameters in the RC phases from the ECM	[K]
C_{th}	Thermal capacitance of the cell	[J/K]
Cp	Thermal inertia of the cell	[$J/(m^2 \cdot K \cdot s^{1/2})$]
$J_f(z_0)$	Jacobian matrix representing the partial derivatives of the cell heat transfer equations with respect to cell temperatures	[W/K]
MAE	Mean Average Error of battery estimation	[%]
$MaxE$	Maximum Error of battery estimation	[%]
$MinE$	Minimum Error of battery estimation	[%]
Q	Capacity of the cell	[Ah]
R_i	Resistor parameters in the RC phases from the ECM	[K]
R_{CHG}	Internal resistance of the battery during charging	[Ω]
R_{DCH}	Internal resistance of the battery during discharging	[Ω]
R_{int}	Internal resistance of the battery	[Ω]
R_{th}	Thermal conductivity of the cell	[$W/(m \cdot K)$]
T_0	Internal temperature of the cell	[K]
T_{amb}	Ambient temperature	[K]
T_e	Temperature of a surface surrounding the cell	[K]
T_s	Temperature of the cell surface	[K]
T	Temperature of the cell	[K]

Symbol	Description	Unit
U^{avg}	Average OCV of the cell	[V]
ΔT	Cell temperature change during modelling time interval	[K]
Δt	Time interval of battery modelling	[s]
$\dot{Q}_{accu}$	Heat accumulated within the cell	[W]
$\dot{Q}_{cd,i}$	Conduction heat transfer from the center of the cell to all of its surfaces	[W]
$\dot{Q}_{cv,i}$	Convection heat transfer from the cell surface to the surrounding air	[W]
$\dot{Q}_{gen}$	Heat generation of the cell	[W]
$\dot{Q}_{rd,i}$	Radiation heat exchange of a cell with its neighboring cells	[W]
ϵ	Thermal emissivity of the cell surface	[]
η	Efficiency of the cell	[%]
$\frac{\Delta T}{\Delta x}$	Cell temperature gradient along the x axis	[K/m]
$\frac{\Delta T}{\Delta y}$	Cell temperature gradient along the y axis	[K/m]
$\frac{\Delta T}{\Delta z}$	Cell temperature gradient along the z axis	[K/m]
$\frac{dU^{avg}}{dT}$	Entropic Heat Coefficient of the cell	[V/K]
$\frac{\partial T}{\partial t}$	Cell temperature change with respect to time	[K/s]
$\frac{\partial^2 T}{\partial x^2}$	Cell temperature gradient change along the x axis	[K/m^2]
$\frac{\partial^2 T}{\partial y^2}$	Cell temperature gradient change along the y axis	[K/m^2]
$\frac{\partial^2 T}{\partial z^2}$	Cell temperature gradient change along the z axis	[K/m^2]
ρ	Cell density	[kg/m^3]
σ	Stefan-Boltzmann constant	[5 67 $\cdot 10^{-8}$W/(m^2·K^4)]
c_p	Specific heat of the cell	[J/(kg $\cdot$ K)]
f_z	Function matrix of the cell heat transfer equations that compose the Jacobian matrix	[W]
h_t	Voltage hysteresis during the change of input current direction	[V]
h_{conv}	Convection heat transfer coefficient	[W/(m^2·K)]
$i_{diff,t}$	Diffusion currents during the change of input current direction	[A]

Symbol	Description	Unit
i	Current through the cell	[A]
k	Thermal conductivity of the cell	[W/(m · K)]
m	Mass of the cell	[kg]
n	Time step of battery modelling	[]
q_{conv}	Volumetric heat diffusion rate to the surroundings	[W/m^3]
q_{gen}	Volumetric heat generation rate of the cell	[W/m^3]
q_{rad}	Volumetric heat diffusion rate from the surroundings	[W/m^3]
v	Terminal voltage of the cell	[V]
z_0	The root matrix of the cell temperature variables being differentiated in the Jacobian matrix	[K]
z_n	Estimated SoC of the cell	[]

Introduction

The use of Lithium-ion Batteries (LIBs) has experienced significant growth in recent years due to their versatility and energy storage capabilities [1, 2] as can be seen in Figure 1. Energy storage has become a key technology with the potential to transform the way energy is produced and consumed in society today. LIBs play a key role in this revolution, allowing electrical energy to be stored efficiently and used when and where it is needed. Manufacturing efficiency improvements, market competition and increased demand for batteries for various applications, such as Electric Vehicles (EVs) and energy storage, have led to a decrease in LIB prices as depicted in Figure 2, making them more affordable and accessible to a wide range of applications and the general public [3].

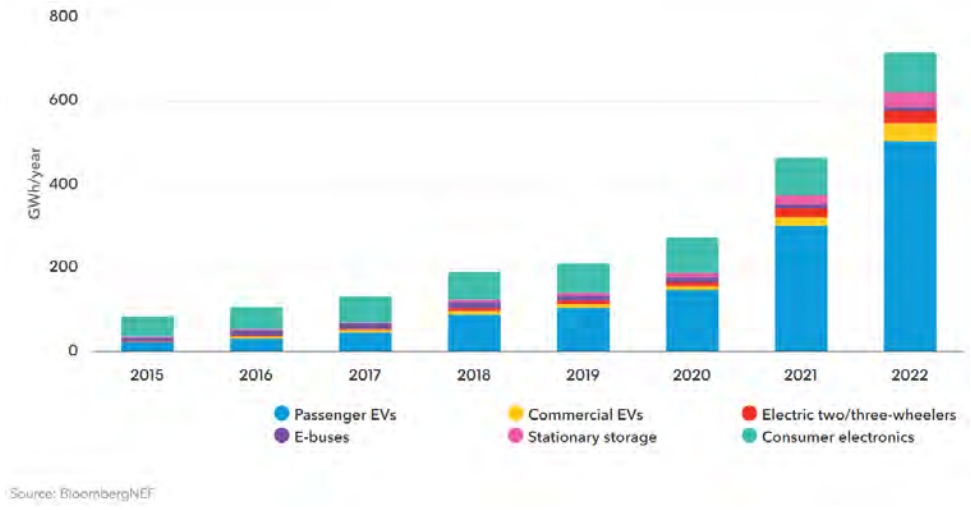

Figure 1: Annual LIB demand by application. *Adapted from:*[2].

LIBs offer an adaptable and efficient solution to meet the energy demands of different applications, such as EVs and off-grid power supply [1]. With a wide variety of sizes and chemistry types, these batteries are ideal for various needs, whether that includes higher power, endurance, range, or even large-scale applications in the Megawatt-Hour (MWh) range [4–6]. The analysis and optimisation of these installations, which involve a large number of cells connected in modules and multiple modules forming packs, present significant technical and scientific challenges. By researching key aspects such as battery

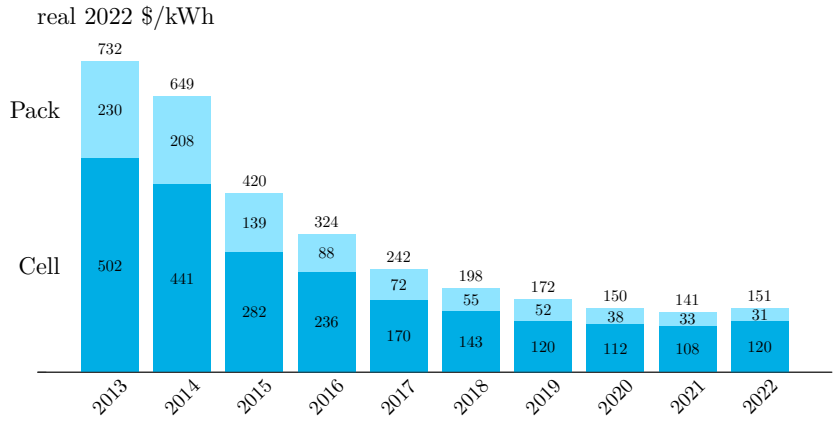

Figure 2: Falling Prices for Lithium-Ion Batteries, 2013-2022. *Adapted from:*[3].

performance, efficiency, thermal management, lifetime and safety of these systems, a deep understanding of battery technology is being acquired and innovative solutions being developed for industry. These challenges and possibilities make this field a promising area of research.

Current deployed battery installations are growing in size and capacity, with an increase in the MWh scale. In large-scale battery systems, thousands of cells or modules connected in series-parallel configurations are typically used to suit the needs of each application. In addition, due to digitalisation and technological advances, these batteries are increasingly connected to each other. The demand for large-scale energy storage systems has increased significantly in various sectors, such as renewable energy generation and electric transportation. To achieve higher capacity and more efficient operation, multiple batteries are interconnected to form larger and more powerful systems. In addition, advances in communication technology and digitisation have enabled greater integration and control of battery systems. Interconnection of batteries facilitates real-time monitoring, centralised control and intelligent energy management. This results in better coordination and optimisation of battery performance, maximising battery life and improving the reliability of the entire system.

These technologies enable the collection of real-time operational data from deployed batteries. This abundance of data presents opportunities for various applications, including data analysis techniques such as machine learning, pattern detection, and anomaly identification. The interconnection of batteries and the analysis of the collected data offer multiple opportunities in various aspects. This includes analysis of battery efficiency, development of more sophisticated management algorithms, research into new battery technologies or customisation of batteries for different applications.

This data can be used to create digital replicas of batteries, known as Digital Twin (DT) [7]. In the case of batteries, a DT is a virtual copy that interacts closely with the physical entity and uses all the data generated over its lifetime to provide additional services and optimise its performance [8]. DTs can be a very powerful tool to help implement the benefits of the aforementioned data.

In this context of a large amount of data available, DT algorithms become more capable and effective, since they can take benefit from data obtained from different cells or battery packs, overcoming the limitation of using data collected solely in a single Battery Management System (BMS). The data generated by the different batteries could be stored in a single database. Thus, the database could store data from new operating conditions and then recognise degradation patterns of the individual batteries by having more knowledge to compare. Moreover, remote control is possible due to the incipient connectivity, which offers the possibility of create new and more advanced strategies and to offer additional services, such as anomaly detection in operation or predictive maintenance.

Detecting abnormal temperatures in lithium battery modules is crucial to ensure safety and optimal performance. Temperature sensors are employed to monitor variations and transmit data to a management system, enabling corrective measures to be taken when dangerous temperatures are detected. However, due to the cost of these sensors, temperature measurements are typically limited to two or three strategic points within the module, resulting in a lack of temperature information from the rest of the module. In large-scale LIBs, it is common to find lithium cells with different SoC and State of Health (SoH). This variability presents imbalances and heterogeneities in the module as shown in Figure 3, which can affect its performance and energy efficiency.

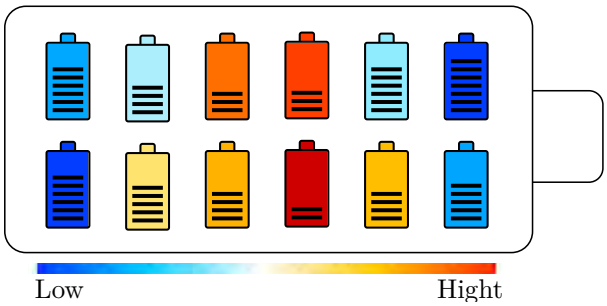

Figure 3: Illustration depicting the disparities and heterogeneities among states within the module.

Optimisation of module performance is achieved by obtaining accurate estimates at the module level, which improves the performance of the entire module, not just its individual cells. These accurate estimates also enable early identification of potential problems within the module, which facilitates predictive maintenance and prevents major failures before they happen. In addition, by analysing the operating conditions that cause faster degradation of the module, corrective action can be taken in a timely way to prolong its lifetime and maximise its efficiency.

Consideration of the cells in the LIB module is therefore crucial to understand and address these imbalances, heterogeneities and variations in cell states. In the context of this thesis, the cell will be considered as the smallest unit, and these cells will be grouped into battery modules through series and parallel connections. These modules will be combined to form a complete battery pack or system.

Individual cells have their own SoC or temperature and are subject to non-linear and coupled phenomena, which have a direct impact on the performance of the module. Such imbalances can manifest themselves in terms of voltage, SoC, temperature and even SoH [9–11]. These disparities compromise the simple sum of the cells that compose the module and can significantly influence the safety of the system. When cells exhibit imbalances in terms of voltage, SoC or temperature, these imbalances compromise the simple sum of the cells and can lead to sub-optimal operation or even dangerous situations.

Imbalances in voltage and SoC, for example, can result in uneven load distribution between cells, which leads to unequal use of cell capacity and can lead to overcharging or over-discharging of some cells. This can negatively affect the stability and lifetime of the system as a whole. In addition, temperature imbalances can result in uneven heating of the cells, which in turn can accelerate degradation and increase the risk of failure or even fire. Therefore, proper monitoring of the cells that form the module is required. Accurate, reliable and real-time models need to be developed to obtain up-to-date information on the state of the LIBs [12–15]. This is essential to optimise energy performance, improve efficiency and ensure the safety of the system as a whole.

The algorithms used in LIBs play a key role in estimating their X-key States (SoX) and analysing their behaviour. While some states, such as voltage and temperature, can be directly measured by sensors, other critical states such as SoC and SoH are difficult or even unfeasible in practice to measure accurately and non-invasively during normal battery operation. To address this challenge, battery models have been developed based on voltage, current and temperature measurements, which are data that can be directly measured and collected. In the literature, there are several scientific articles proposing different types of battery models and estimations [16–18]. However, most of these works focus on the cell-level and do not adequately consider the effects and complexity at the module-level.

Module-level studies are less common and, in many cases, the information to develop them is limited or proprietary, belonging to companies in the industry. Information on technical specifications of the individual cells used, temperature and voltage data, thermal management information or detailed data on module structure and connections. Lack of access to this information may limit comprehensive studies at module level. In the limited cases where module-level work is conducted, the module is generally considered as the smallest unit to be estimated, which oversimplifies the reality and underestimates the real effects such as [19]. This effect can be complex interactions between cells within the module, such as thermal, voltage or SoC imbalances, for example.

Within the framework of this thesis, a methodology for the development and deployment of a Digital Twin Simulation Platform (DTSP) is proposed, using simulation tools known as DT and cloud-based technologies. This platform will focus on module-level models that consider the characteristics and behaviour of individual cells within the module. The development of a module-level thermal model to estimate the thermal gradient inside the module is proposed, as well as a cell-by-cell electric model together with a SoC estimation algorithm. These models and estimator, by considering all the cells in the module, are computationally intensive and require more processing power. Therefore, a new issue may arise related to running these heavier algorithms in commercial BMS. These systems may lack the computational power needed to efficiently run these algorithms or may not be specifically designed for this type of task. This problem is addressed by taking advantage of the incipient connectivity, that allows the deploying these models in the Cloud. Additionally, since the DT of LIBs are a medium for broader purposes such as plant or fleet management strategies, where cloud connectivity is needed, this approach enables the application of key communication and networking technologies such as virtualisation, service-oriented architecture, real-time monitoring and opens up the potential of longer and safer LIBs lifetime.

In the previous paragraphs, the main challenges related to the monitoring of LIBs at the module-level, considering the states of each cell, have been mentioned. In summary, the importance of developing module-level models and state estimators to carry out a deeper and real-time monitoring of the module has been highlighted, as well as the lack of works addressing this issue in the scientific literature. Therefore, the hypotheses formulated for this study are as follows:

- **H1**: Models of modules that consider individual cells provide relevant additional information to that obtained by module sensors.

- **H2**: Cloud Computing technologies may offer the computational power and memory required to the deployment of module-level models, which allows additional services to be offered compared to local environments.

- **H3**: The implementation of the advanced algorithms in the Cloud could allow to detect anomalies and battery failures more efficiently and faster, which will lead to the mitigation of the computational load of the onboard BMS and improve system performance.

To evaluate these hypotheses, the following objectives are formulated. These objectives will be pursued to verify the validity of the hypotheses after reviewing the State of the Art (SoA). The main objective of this PhD thesis is to address the identified challenges and accomplish the following:

Develop, Validate, and Deploy Module Level Models within a Cloud-based Digital Twin Simulation Platform for Lithium-Ion Battery that incorporate the SoX variations of individual cells

Besides the main objective, other secondary objectives are defined for the successful development of this Ph.D. Thesis:

- *O1:* **Develop and validate cell-level models** to understand the behaviour and interactions of basic system characteristics, in order to use them as a basis for extrapolation to more advanced module-level models.

- *O2:* **Develop and validate module-level models** to understand and predict the behaviour of the overall system and the interactions of multiple cells in the module, using the models developed in the previous objective as a basis.

- *O3:* **Develop a secure and scalable cloud architecture** that enables efficient deployment and execution of models, ensuring proper integration with all the services and resources comprising the system.

- *O4:* **Select the most appropriate compute and memory resources** on the cloud platform to improve system performance and efficiency, ensuring optimal resource utilisation.

- *O5:* **Develop an alarm system for early detection and notification of potential problems** in the BMS, anticipating system failures, improving system efficiency and security, minimizing interruptions or issues during operation, and empowering users to take corrective action.

- *O6:* **Develop and assemble a functional prototype**, establish and optimize necessary connections and communication channels, and configure the Cloud platform to enable seamless transmission and reception of real-time data from the prototype.

To achieve this purpose, the thesis document has been organised in six main Chapters summarised in Figure 4.

Chapter 1 aims to identify the appropriate modelling framework for the development of the target simulation platform. To achieve this, firstly, DT-based technologies are discussed, as well as the basic and more advanced functionalities of current BMSs, which include monitorisation of physical parameters, estimation of battery states, electrical and thermal management, communications and fault detection. Following, the main methods of electrical and thermal modelling of LIB cells are reviewed. Furthermore, a review of the literature related to extrapolation strategies of these models to module-level is carried out. Finally, the cloud services offered in the market are analysed, to determine the most suitable one. Within this comprehensive review, the main shortcomings and possible areas of improvement in the current SoA will be highlighted. These findings will provide a solid basis for the definition of the contributions proposed in this Doctoral Thesis.

Chapter 2 introduces the overall methodology designed to guide the research activities undertaken in this thesis. Four key stages are defined and comprehensively detailed: i) Parameter estimation of the target cells (Stage 0), ii) Development and validation of the electrical and thermal models at the cell-level (Stage 1), iii) Module prototype assembly and data connectivity to the cloud (Stage 2), iv) Extrapolate cell models to the module level, integrate them effectively, and validate their accuracy (Stage 3), and v) Implementation of the module-level models in the DTSP (Stage 4). Each stage is discussed in depth, presenting the anticipated contribution and relating the different hypotheses with each stage.

Chapter 3 focuses on the development of the electrical and thermal models at the cell level. First, the sellected cell is presented. Then, the electric and thermal models are explained in detail. Afterwards, laboratory tests carried out to estimate the parameters describing the electrical and thermal characteristics of the target cells are described. Finally, the results obtained after implementing these models are presented. Each model is validated against slow dynamic profiles and faster, more realistic profiles. In addition, an exhaustive discussion of these results is carried out.

Chapter 4 focuses on the assembly of the prototype module developed within the scope of this thesis, as well as on the extrapolation and validation of the models at module level. The primary objective of this prototype is to validate the entire simulation platform (DTSP) and conduct validation tests to gather data for comparative analysis against estimations made. The chapter begins by providing a comprehensive description of the module's characteristics, including its nominal specifications after assembly, as well as the necessary hardware for cloud connectivity. Next, the additional required tests for parameter estimation at the module level are detailed. The chapter then outlines the extrapolation of the thermal and electrical models from the cell level to the module level, incorporating new geometries for the thermal model and detailing the parallel execution of individual electric cell-level models, as each cell is assigned a dedicated model for simultaneous processing. The results obtained with each of the models are then presented, evaluating them with both low dynamic profiles and faster dynamic profiles. Finally, the approach adopted for the integration of these two models at module level is presented.

Chapter 5 focuses on the description and validation of the DTSP developed in the cloud. The initial Section provides a comprehensive overview of the diverse Cloud services employed in the design and establishment of the simulation platform. Two case studies are then studied: i) anomalies in the operation of the module and ii) the simulation of the disconnection of the DT from the module. The results obtained in each case are presented and their relevance and applicability are discussed. Finally, a critical discussion on the use of DT tools in the battery context is made.

Chapter 6 draws the key conclusions from the various activities carried out in the framework of this research. It lists the substantial contributions made and outlines the limitations inherent in the developed models , highlighting prospects for future research. A rigorous evaluation is made of the hypotheses put forward, and future research lines are proposed.

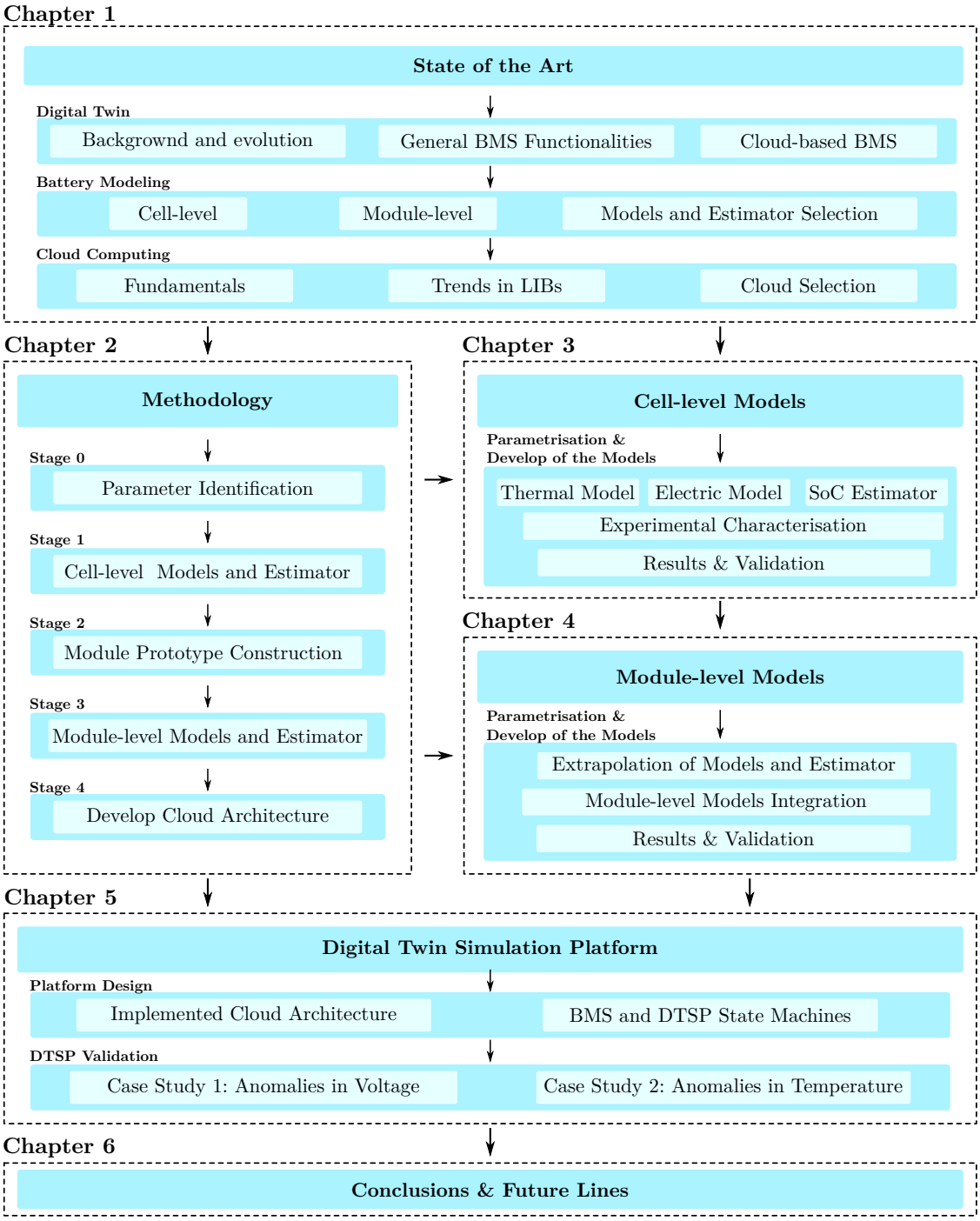

Figure 4: Document structure.

1

State of the Art

Summary

In this first chapter, a comprehensive review of the current state of the art in technologies relevant to the modelling of battery modules at the module level is presented. This includes an exploration of the techniques and technologies associated with Industry 4.0 that hold potential for this application. The analysis covers DT technologies in the context of lithium-ion batteries, models and state estimators at both the cell and module level (in particular, those based on equivalent circuits), and the use of Cloud technologies for the deployment of such models. The main gaps identified in the existing literature are highlighted and form the basis for defining key contributions of this PhD thesis and the research activities.

1.1 Introduction

In this chapter, the current SoA in LIB modeling at the cell and module levels will be reviewed. The first section will focus on the advancements and applications of DT technologies specifically in the context of batteries (Section 1.2). This will provide guidance on the technologies that will be utilized throughout the thesis and help define the adopted functionalities. The subsequent sections will delve into the existing literature on cell-level models (Section 1.3), module-level models (Section 1.4), and the utilization of Cloud computing (1.5) in battery modeling. By examining these four key aspects, a comprehensive understanding of the current state of the art in LIB modeling will be achieved.

1.2 Digital Twin in the Lithium-Ion Battery Framework

Digitalisation and the incorporation of technologies are transforming industry and daily life, requiring businesses to adapt to survive [20]. From the Industrial Revolution to the present day, significant changes have been driven by innovations in energy, communication and digitalisation [21–23]. Today, we are in the era of the Fourth Industrial Revolution or Industry 4.0, where hyperdigitisation and cyber-physical concepts are fundamental [24]. This new approach promotes the creation of smart factories and more sophisticated products, supported by technologies such as collaborative robotics, additive manufacturing, the Internet of Things (IoT), Big Data (BD) and Cloud Computing [25].

In the context of Industry 4.0, batteries play a key role in the evolving energy framework [26]. Over time, advances have been made in the modelling and simulation of electrical storage systems, especially driven by the telecommunications industry [27, 28]. These approaches have evolved into more sophisticated models that accurately represent the performance of the system and its interaction with the environment. The cutting-edge models are able to self-manage and understand the state of the system and the environment in which they operate, known as "Digital Twins" [29].

These virtual copies are intelligent systems that rely on realistic and accurate models to achieve a deep understanding of the process and environment involved. However, the concept of LIB modelling has changed over time. The concept of DT is often diffused with similar terms such as Digital Model or Digital Shadow. In each of these concepts, however, the level of interaction between the physical object and its virtual counterpart differs [30]. This is represent in Figure 1.1. The Digital Model lacks data exchange, while the Digital Shadow receives data from the physical object. The DT surpasses both by enabling bidirectional data exchange, allowing for mutual control and impact between the physical and virtual entities.

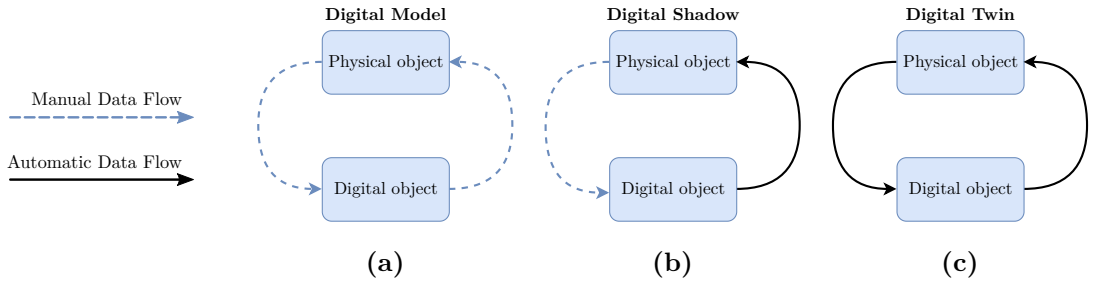

Figure 1.1: Data Flow in a) Digital Model; b) Digital Shadow; c) Digital Twin.

1.2.1 Background and evolution of the term

The concept of the "Digital Twin" was introduced in early 2003 and became popular in 2014 with a Whitepaper published by Grieves [31]. He proposed a general and standard 3D dimension architecture for DT. So, DT was defined as a three-dimensional architecture that combines the physical and virtual product through data connections represented in Figure 1.2. NASA defined DT in 2010 as "*an integrated multiphysics, multi-scale, probabilistic simulation of an as-built vehicle or system that uses the best available physical models, sensor updates, fleet history, etc., to mirror the life of its corresponding flying twin*" [32]. In the aerospace industry, the concept has been successfully implemented [33].

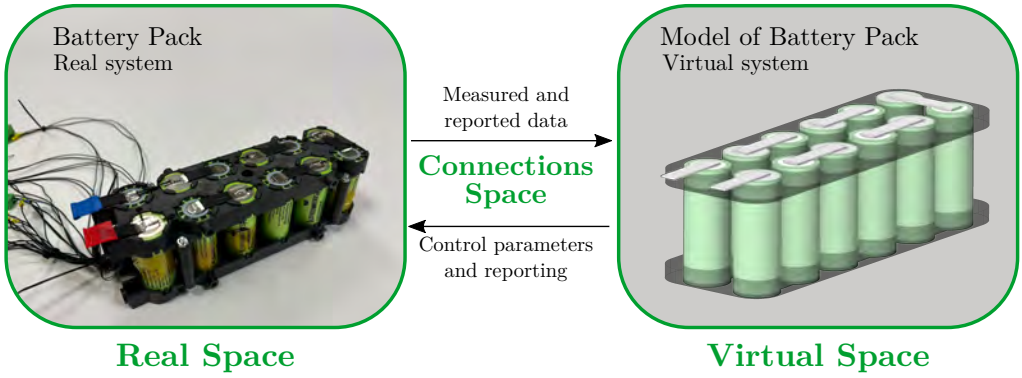

Figure 1.2: 3D Digital Twin System.

Subsequently, the definition of DT has undergone several evolution in each area in terms of concept, core elements and specific applications [34–36]. However, all agree on the importance of establishing a synchronous connection between the physical product and its virtual replica. In 2012, both NASA and the US Air Force identified DT as a key technology [37]. In 2014, when Grieve published the Whitepaper [31], the idea of DT was widely disseminated, leading to its introduction in various application domains.

Since 2017, Gartner has listed DT as one of the 10 most promising technology trends for the coming decades [38–41]. In between, in 2018, a significant change has been made to the original DT architecture, adding two additional dimensions: DT Services and DT Data [42, 43]. From 2020 on, the application of DT has been observed in various areas, including

the field of energy and LIBs. Various studies and reviews have shown exponential growth in the application of DT, especially from 2019 onwards [44–48]. In the field of batteries, the use of DT started to appear mainly in 2017 and 2018, and has now experienced a significant increase [49–52]. The whole evolution of the DT concept is summarised in Figure 1.3.

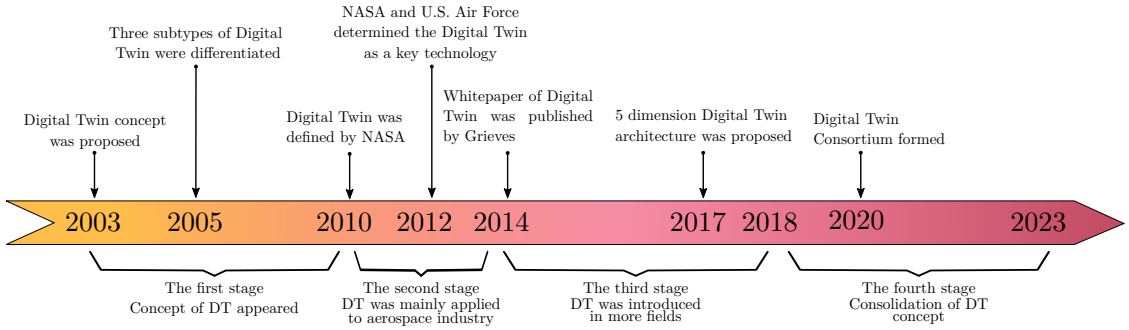

Figure 1.3: Digital Twin Concept Timeline from 2003 to Today.

Implementing the DT concept in the battery framework, a 5D simulation tool is developed as is represented in Figure 1.4 [42]. This innovative approach encompasses five key dimensions: the physical space, the virtual space, the services, the DT data and the connection linking them [31, 42, 43]. In the *Physical Space*, there is the actual battery and its sensors that collect information such as voltages, currents and temperatures [53]. Meanwhile in the *Virtual Space*, a precise digital replica of the battery is created in terms of geometry, properties and behaviour [54–56]. Through this digital replica, services such as simulation, monitoring, optimisation, fault detection or efficient predictive maintenance are provided allowing for in-depth analysis and informed decision making to improve battery performance and efficiency [53, 57]. This improvement of the *Services Space* benefits both users and manufacturers by extending the range of control and efficiency in battery usage, which is especially relevant in key economic sectors such as electromobility, industry and stationary applications [43, 58].

Digital Twin Data is collected from a variety of sources throughout the life of the battery and represents a complete picture of the object [59]. This data, along with simulations and modelling, is used to analyse battery operating conditions and fine-tune battery performance. Managing large volumes of data in real-time involves significant computational cost. However, through the creation of a DT specific to a battery model, it is possible to optimise its use in multiple applications. Finally, the *Connection Space* is crucial to ensure the active and synchronous interconnection of the other four dimensions mentioned above. This space ensures real-time data flow and allows the physical, virtual, service and data dimensions of the DT to interact effectively.

The DT concept has undergone significant developments in various applications in recent years [59]. In the field of electric batteries, the *Digital Battery* or *Battery Twin* concept has been developed, looking for maximisation of their performance and opera-

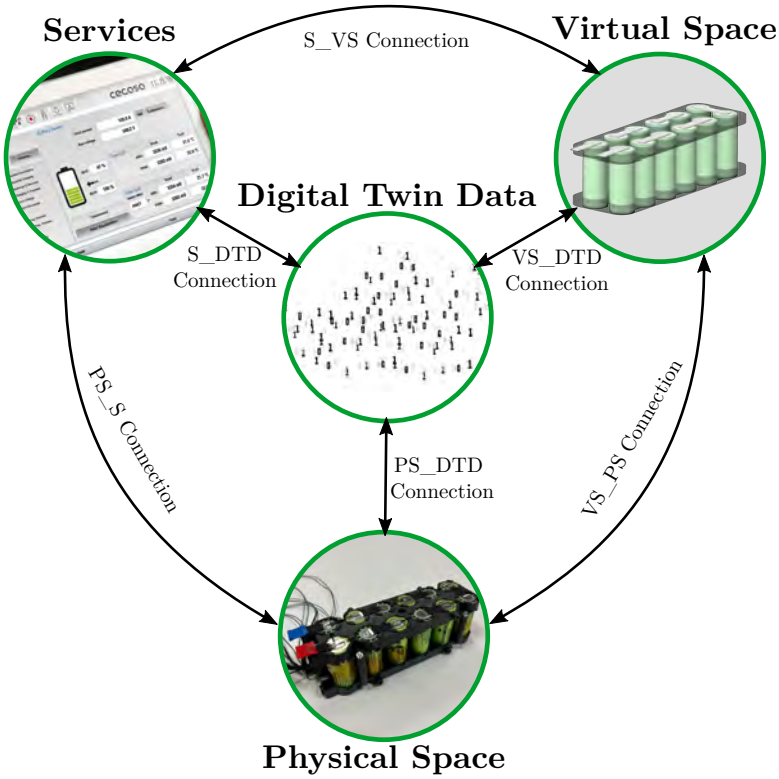

Figure 1.4: 5D Digital Twin System. *Adapted from* [42].

tional efficiency. These batteries are found in a wide range of electronic devices, including EVs and stationary applications [60, 61]. The DT allows for complete battery monitoring, providing an in-depth view of the state of the battery and ensuring its correct operation [62]. However, the biggest problem that modern batteries still have today is an intrinsic inability to measure their internal state, which is addressed by estimation algorithms implemented in BMSs. The adoption of a Cloud-based DT would offer greater computational capabilities and increased data storage capacity, thus improving the monitoring and optimisation of battery performance.

1.2.2 General Functionalities of Actual BMSs

In recent years, there has been an increased adoption of tools such as DT models to add an additional layer of capabilities to existing BMSs. DTs have been presented as a solution that enables the development of real-time virtual models of physical systems. This trend is also reflected in the field of LIBs. In a DT battery, there is a close interaction between the physical entity, its virtual counterpart and field data collection throughout its lifetime. Furthermore, it offers a new concept of networked battery management and service [63].

A BMS is a electronic entity that primarily aims to guarantee safety and achieve efficient performance in the battery context [64–66]. In order to ensure safety, it is imperative that the battery operates within its Safe Operating Area (SOA), without exceeding predetermined voltage, temperature and current limits. In parallel, performance optimisation involves the execution of electrical and thermal management functions, with the purpose of meeting the demands of the application while maximising LIB life. The main functions of the BMS are listed below and represented in the schematic diagram of Figure 1.5.

- Conversion of physical magnitudes into electric signals by means of sensors and integrated circuits. This continuous collection of physical parameters from the battery pack is essential for the LIB to operate within the SOA [67]. The data collected mainly by BMS units are current, voltage, and cell temperature. In addition, they can also monitor time, location, and ambient temperature, among others.
- Estimation of battery SoX to optimise performance and lifetime such as SoC, SoH, State of Power (SoP), etc.
- Electrical power management encompasses a number of crucial operations, including switching the application on and off, as well as controlling the charging and discharging processes. Cell balancing is also performed to ensure uniform charging and discharging in all cells of the battery pack [68].
- Thermal management: fan control, refrigerant fluid pumping, etc. [69].
- Communication with internal elements of the BMS itself as well as with peripheral elements controlling the LIB such as the power converter or higher level management systems.
- Detection and analysis of faults in the battery and BMS circuits, and activation of the corresponding alerts and alarms.

The hardware topology of a BMS for large multi-cell LIBs is generally based on two types of units [70, 71]: i) slave BMSs that include an Analogue Front-Ends (AFE) responsible for monitoring the physical quantities of the LIBs; and ii) a master BMS responsible for commanding the slaves, processing the data and performing more advanced management, safety and diagnostic functions that require programmable electronic devices with more processing power such as microcontrollers.

The slave units monitor the battery cells in the pack using sensors at different sampling rates. Accurate measurement of LIB cell voltage is crucial to avoid overcharging and over-discharging. The protective functions of the BMS do not need a very strict accuracy requirement for current measurement, but it is necessary to minimise errors in the estimation of battery states. It is also important to measure the temperature of the cells to keep them within an optimal range. This way, their lifespan is prolonged and their thermal and chemical stability ensured/guaranteed.

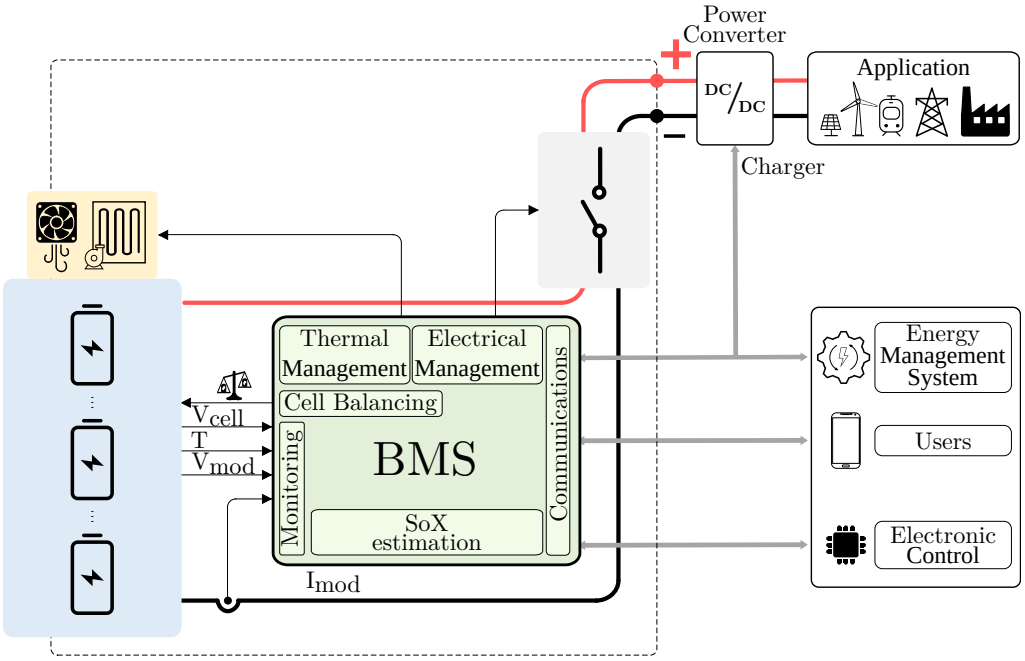

Figure 1.5: Block diagram of the main functionalities of a generic BMS.

The BMS master unit, on the other hand, performs critical safety functions to ensure a rapid response in the event that action is required. It can monitor the total current and voltage of the whole battery module/system/pack, allowing it to communicate with the charger and perform thermal and electrical functions. It protects the battery from overcharging and deep discharge, overheating or short circuits through monitoring and fault detection strategies.

Implementing more advanced functionalities often requires specialised algorithms and hardware systems technology. Commercial BMSs are generally not designed to run these functionalities natively, so additional servers and technologies are often required. These servers can provide more advanced data storage, processing and analysis capabilities, allowing more complex and sophisticated tasks to be performed in the context of the BMS. An increasingly used option in recent research is the use of Cloud-based technologies, more detailed in Section 1.5.3. This allows extending the functionalities of the BMS towards more complex and advanced tasks and facilitates the transfer of data between the BMS and other external devices or platforms.

1.2.3 Cloud-based BMS functionalities

In this study, it is proposed to use Cloud-based technologies to implement more robust and reliable LIB algorithms that perform real-time diagnostics of performance anomalies. Implementing these models in the Cloud releases resources and capabilities of the embedded BMS so that it can focus on its core LIB functionalities of monitoring and safety. Furthermore, it should be noted that at no point is it intended to replace the BMS hardware.

Besides, most of the above-mentioned basic functions of the BMS are not excessively complex and resource-intensive due to the limited/constrained processing capabilities inherent in embedded electronic systems. These functions can be referred to as low-level tasks since they are related to the monitoring and protection of the LIB. However, one of the challenges is that the current design of the BMS often limits accessibility for the user or operator, making it challenging to update implemented algorithms and corresponding firmware. With an internet connection, new additional functionalities called high-level tasks are enabled, such as more advanced battery estimation algorithms based on Artificial Intelligence (AI) with higher computational costs, or optimisation tools for the operation of several battery systems. They are more related to the power and energy flow management of the whole system. In other words, tasks that are more related to the end application. Therefore, smart BMSs with aggregated Cloud-based technologies require, in addition to those functions mentioned above, monitoring of all cells, more advanced fault estimation, fault prediction, remote control capability or data visualisation, among other things. All this is summarised in Figure 1.6.

Advances in technology and the digitisation of batteries enable the connection of deployed and mostly isolated LIBs to date. This is possible by equipping the new BMSs with additional components needed to establish a connection to the Cloud by incorporating an IoT device. This will allow for a Cloud infrastructure, an Application Programming Interface (API) and a User Interface (UI) [49, 63].

The main goal of the IoT is to connect devices to the Internet and enable them to communicate and interact with other IoT-equipped devices in order to monitor and control them remotely. Software is developed to convert the physical magnitudes obtained by the integrated circuits of the slaves into appropriate variables or data values.

Among the different processing units, the Raspberry Pi (RPi) is one of the most popular devices due to its ability to provide good computational, sensing, connectivity capabilities and the large online community that provides support and documentation [72]. Considering the strength of RPi as a compact and inexpensive computer, it has been one of the most chosen ones for the collection of battery information and establish communication with the Cloud platform and other related systems. Li et al. [49] used a RPi to send and receive data from a LIB system to a Cloud DT. They used the RPi as a gateway to send the measured data from the Nickel Manganese Cobalt (NMC) chemistry

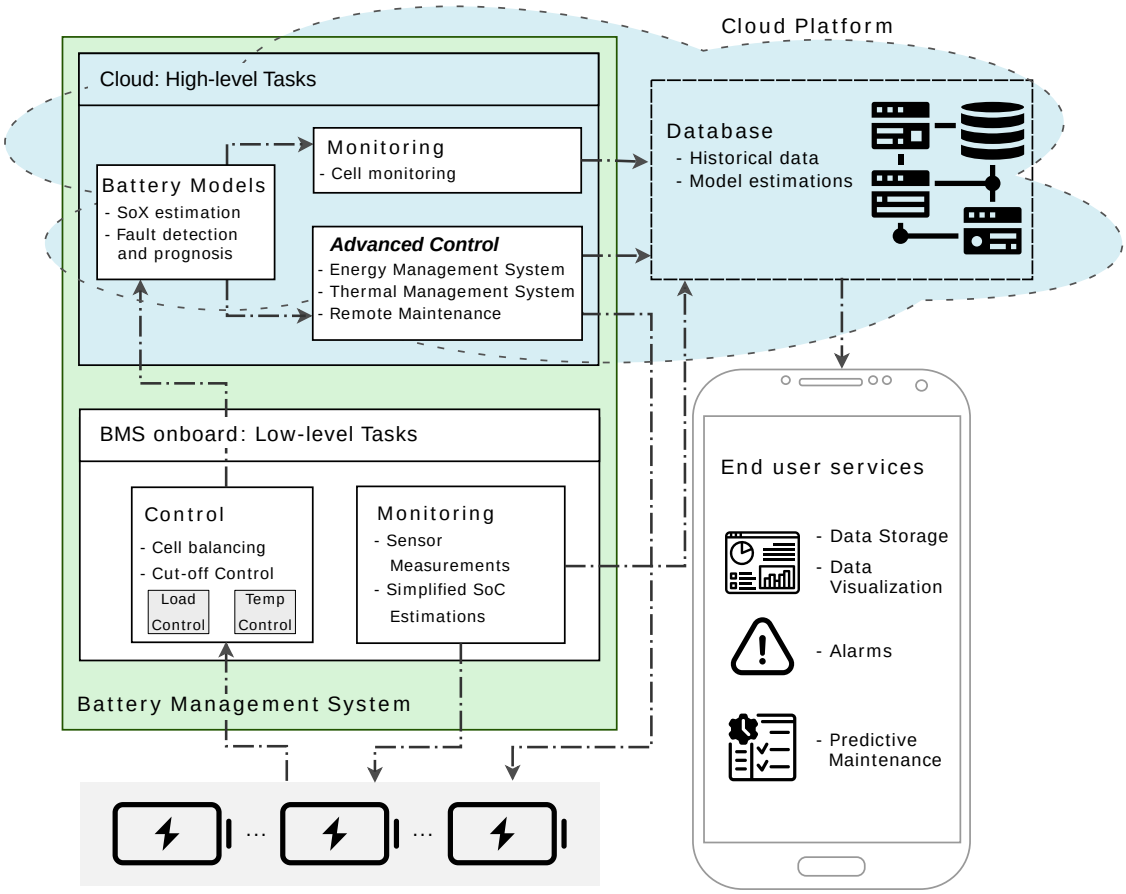

Figure 1.6: Block diagram of Cloud-based BMS Main Functionalities.

LIB to the Cloud where they calculate the SoX with the acquired data. In another area of research, Gimeno-Sales et al. [73] used a RPi in the data gateway phase as a low-cost server for wireless communication collecting data from all connected slave BMS units of a Photovoltaic (PV) plant.

The data measured by the slaves is sent via Message Queuing Telemetry Transport (MQTT) protocols to the Cloud to ensure security and privacy [72]. The BMS protocols can communicate and send all data, measured at each point in time or in batches of data. For this, various APIs are developed to be able to interact with technologies such as Python, Structure Query Language (SQL), MQTT to integrate their custom functionalities [63]. Therefore, a stable and robust internet connection is required to be able to perform these functions in real time.

Compared to conventional physical BMS, the use of DT tools provides new opportunities for enhanced visualisation, alarm services and the implementation of critical networking and communication technologies. DT enable real-time analysis and adaptation of control strategies, which helps to optimise LIB performance and extend their lifetime,

as well as to improve reliability and safety. The development of application-based or web-based UIs allows real-time visualisation of the LIB state, including the internal state of each cell. In addition, access to historical operating data is provided. By monitoring cell and battery state in real time, DTs facilitate early detection of faults and enable predictive maintenance scheduling, reducing downtime and associated costs. DTs can help identify and correct inefficiencies in energy use, resulting in better resource use.

On the other hand, Cloud Computing-based solutions allow reducing the need for components such as measurement sensors and local Computing elements, resulting in a more compact embedded/physical BMS with the extended computational capabilities in the Cloud. In addition, the unlimited data storage provided by the Cloud facilitates the handling and analysis of large volumes of information.

However, this Cloud BMS architecture has some limitations to consider. The constant Internet connection required can be a challenge in environments or applications with connectivity limitations. Disconnection from the network would imply the interruption of the added services and how this would affect the performance of the LIBs and the integrity of the collected data in the long term has not yet been fully investigated. In addition, there are costs involved in developing and building Cloud infrastructure, including the storage of large amounts of data, which could be a limiting factor for some organisations or projects. All these aspects are summarized in Table 1.1, where the pros and cons of the Digital Twin approach are presented.

Table 1.1: Main benefits and drawbacks of the use of DTs in LIBs.

Benefits	**Drawbacks**
- Optimising performance and service life	- Dependence on internet connectivity
- Facilitates fault detection and predictive maintenance	- Implementation and maintenance costs
- Improves energy efficiency	- Data security and privacy

1.3 Cell-level Battery Modeling

In electrical applications where the battery is essential, it is necessary to know the internal state of the battery in the cases that the battery is the main object of the system or the performance of the application depends in its Electrical Storage System. This is reflected in applications like electromobility, in which the capacity of the battery defines its autonomy, or in micro grids in which a good control of the capacity becomes crucial to avoid leaving a whole community without energy supply. In addition, battery internal state monitoring helps to avoid the premature degradation of the components.

Current batteries present difficulties in measuring the actual internal state of the cells, requiring estimation of values such as SoC and SoH. Models and state stimators are used in the BMS to monitor and protect the LIBs. Over time, batteries experience degradation

that affects their performance, so SoH estimators and degradation models are used to determine the remaining life of the LIB. Although there are a large number of studies on these aspects [15, 74–78], this thesis does not focus specifically on them.

The performance of the estimators depends on the accuracy of the models. However, having battery models that represent the behaviour with high fidelity and detail infers in heavy models with high computational cost. The computational power that batteries have locally (edge computation capability) depends on the processing units integrated in the BMS. The speed of simulation is also affected as the cost of Computing increases. For this reason, it has been necessary to find a balance between the accuracy of the models and their Computing power, usually leading to reduced order models of debatable accuracy. For this reason, thermal models will be discussed in more detail in Section 1.3.1, the electrical models in Section 1.3.2, and Section 1.3.3 will examine in detail the SoC estimators that have been proposed in the scientific literature.

1.3.1 Thermal models

This Subsection focuses on the description of thermal models at the cell level that have been investigated in academia. First, the effect of temperature on LIB cells is examined. Then, the two main types of thermal models that have been commonly used to estimate the temperature gradient in the cell and the heat generation in the cell are summarised. Finally, a detailed analysis is carried out and a specific thermal model is selected for use in the context of this thesis.

1.3.1.1 Thermal effects in the Lithium-ion Battery

Battery temperature plays a critical role in the safety, performance, and longevity of LIBs. To address this, researchers and manufacturers have focused on developing Thermal Management Systems (TMSs) to monitor, control, and mitigate the impact of temperature on LIBs. The acceptable operational temperature range for LIBs is generally between -20°C~60°C [79], with optimal performance observed between 15°C~35°C [80]. Maintaining proper battery temperature is crucial for ensuring efficient and safe operation of LIBs as is ilustrated in Figure 1.7.

Lithium-ion batteries have an optimal temperature range that varies according to the approach to functional safety, performance and ageing [81]. Maintaining ambient temperature (around 20°C~25°C) is ideal for normal battery operation [82], while fast charging can be optimised by pre-heating or pre-cooling the battery [83]. At low temperatures, battery capacity is reduced and various negative effects appear [84], such as increased internal resistance [85], limited diffusion of lithium ions at the electrodes [86, 87] and the formation of lithium plates on the anode [88]. To improve performance at low temperatures, new materials and electrolytes with high ionic conductivity and low freezing point are being investigated [69].

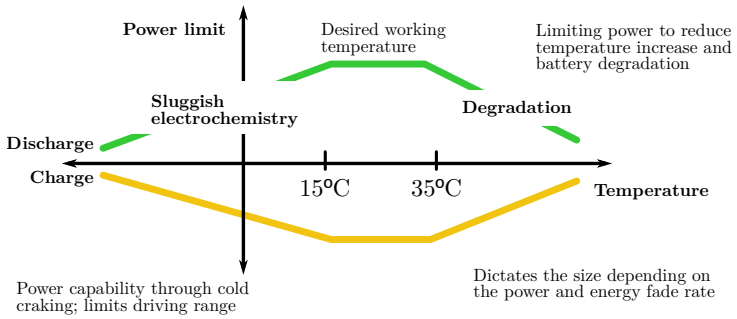

Figure 1.7: Optimal operating temperature range in a Lithium-ion battery. *Adapted from* [80].

The heat generated in lithium-ion batteries has a significant impact on their performance and must be properly controlled to ensure optimal operation. Temperature distribution within the cells is a key factor and is influenced by heat generation and heat transfer. During charging and discharging, heat is produced due to electrochemical reactions and phase changes. The temperature distribution inside the cells depends on the amount and transfer of heat generated. So, it is essential to manage the heat in lithium-ion batteries to ensure their optimal performance. Authors like Bandhauer et al. [89] or Bernardi et al. [90] discussed different main sources of heat inside the modules that are summarized in the Figure 1.8.

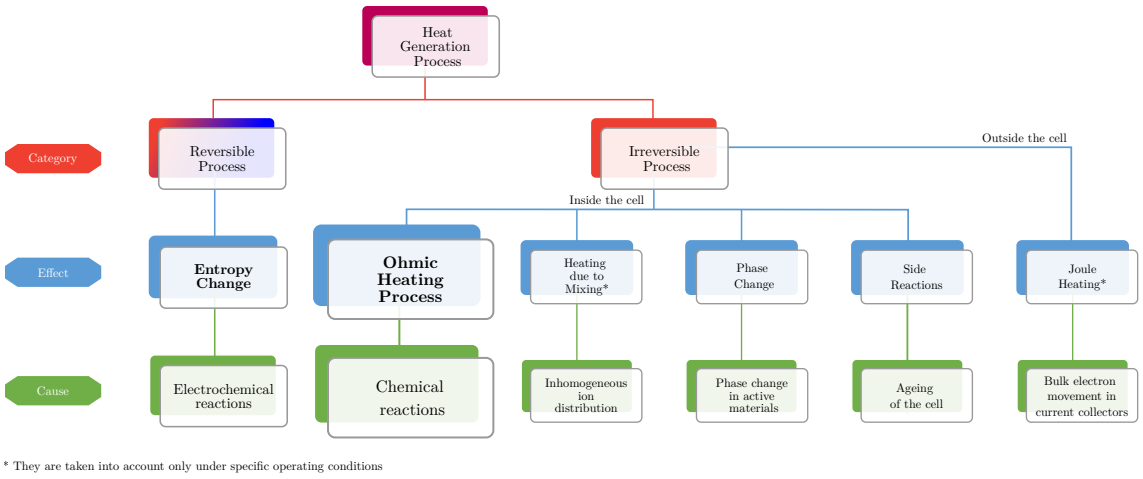

Figure 1.8: Categories and process of the heat generation within lithium-ion batteries. *Adapted from* [79].

The thermal behavior of LIBs is influenced by various heat sources. The reversible entropic heat reflects the change in lithium ions on the electrodes and can be endothermic or exothermic depending on the SoC during the charging or discharging process. The Joule effect, which generates heat due to internal resistance, dominates the thermal performance of the battery and contributes to irreversible heat generation [91, 92]. Other factors such as mixture enthalpy, phase change, secondary reactions, and electron movement in current collectors also generate heat and can impact battery aging and capacity loss [93–95].

1.3.1.2 Thermal Models of Lithium-ion Battery Cells

In the following Sections two main approaches to modelling the transfer of the heat generated on each cell to the outside will be analysed: i) Numerical Distributed Models and ii) LTM. These modelling approaches vary both in accuracy and in the computational cost of the thermal model.

Numerical Distributed Models.

Numerical models, such as Computational Fluid Dynamics (CFD), are used to accurately monitor battery cell temperature. These models employ simulations based on the finite element method and CFD techniques to calculate temperature profiles in two or three dimensions. By considering physical parameters and heat transfer mechanisms, CFD models provide precise estimations of temperature distribution and heat fluxes within the system. These models require additional computational resources, but they offer a comprehensive understanding of battery thermal behavior. Figure 1.9 demonstrates an example of a CFD model. Using partial differential equations, the CFD-based model discretises them by applying the conservation principles in each of the infinitesimal control volumes of the geometry. The equations perform a systematic count of changes in mass, momentum, and energy due to the flow of fluid around the analysed geometry. For that end, the corresponding equations are taken into account.

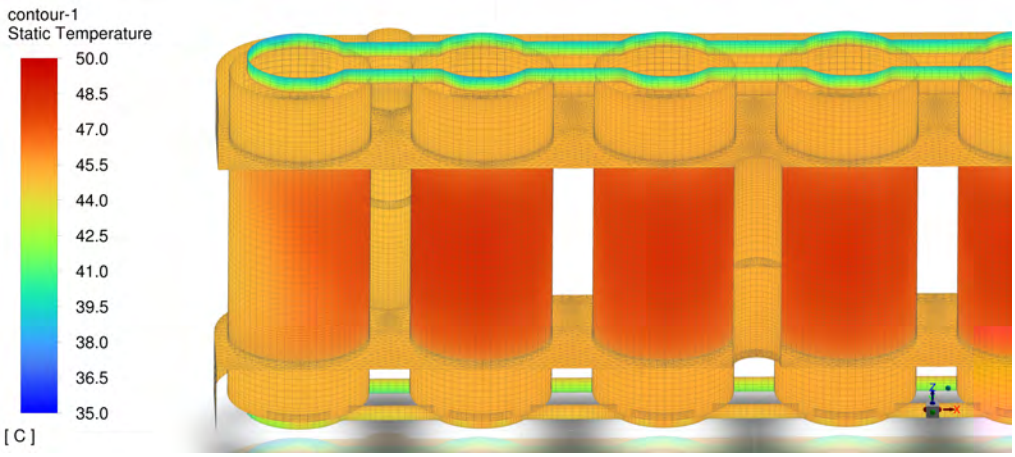

Figure 1.9: Temperature distribution of the battery with 3D numerical model.

$$k\left(\frac{\partial^2 T}{\partial x^2}+\frac{\partial^2 T}{\partial y^2}+\frac{\partial^2 T}{\partial z^2}\right)+q_{\text{gen}}=\rho c_p\frac{\partial T}{\partial t} \tag{1.1}$$

where, k is thermal conductivity, $\left(\frac{\partial^2 T}{\partial x^2}+\frac{\partial^2 T}{\partial y^2}+\frac{\partial^2 T}{\partial z^2}\right)$ discretises the temperature of the cell along its three-axis geometry, q_{gen} is the heat generation of the cell, $\rho c_p\frac{\partial T}{\partial t}$ term represents the heat storage of the cell where ρ is the cell density, c_p is the specific heat and $\frac{\partial T}{\partial t}$ is the temperature change during time.

CFD models are utilised in battery system studies for design and analysis purposes [96–98]. These models simulate fluid flow and heat transfer, providing insights into temperature distribution, cooling system efficiency, and hot spot identification. They enable analysis of thermal performance, evaluation of different cooling configurations, optimisation of designs, and validation against real data. The advantages include accurate temperature profiles, detailed thermal behavior, and geometrical analysis of batteries. However, drawbacks include high computational demands, long computation times, additional costs, and the need for extensive parameter identification. As a result, simplified models are more commonly employed in BMS and TMS applications.

Lumped Thermal Models (LTM).

Lumped models solve the energy balance to calculate the temperature distribution across the Lithium-Ion cell based on equivalent electrical circuits. These circuits represent heat transfer phenomena and heat sources using capacitors, resistors, and current sources. The model assumes uniform temperatures inside and on the cell surface, with a constant ambient temperature. The temperature difference is represented by voltage. This simplified approach allows for 1D heat transfer analysis, which can be extended to three axes. An illustrative example of an equivalent LTM is shown in Figure 1.10.

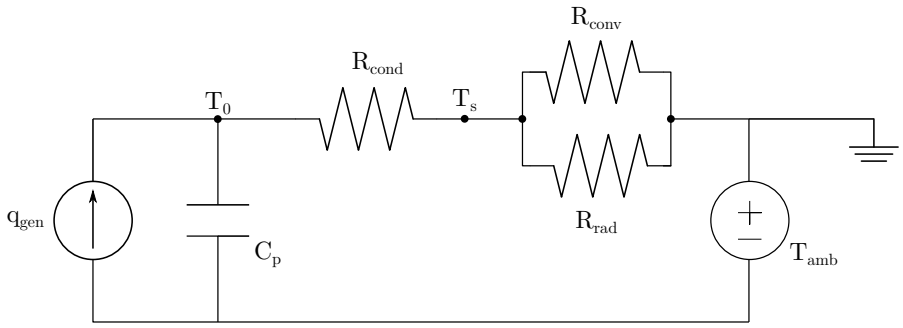

Figure 1.10: 1D Analytical Lumped Model for a LIB single cell.

In Figure 1.10, C_{th} and R_{th} represent the thermal capacitance and thermal conductivity of the cell, respectively. T_0 denotes the internal temperature of the cell, while T_s corresponds to the temperature on the cell surface. Additionally, q_{gen} is utilised to characterise the internal volumetric heat generation within the cell. Furthermore, the parallel resistances q_{conv} and q_{rad} describe the heat diffusion to and from the surroundings. Lastly, T_{amb} refers to the ambient temperature.

The LTM is commonly used to estimate the temperature of LIB cells. It provides accurate temperature profiles and allows for the analysis of heat generation and transfer. The LTM is an efficient and computationally less demanding alternative to CFD based models for thermal analysis of LIBs. It has been applied in various studies to assess thermal behavior, optimise design, and validate results [99–103]. However, LTM models have limitations, such as their dependency on specific cell parameters and the need for

application-specific characterisation. Despite these limitations, the LTM remains a valuable tool for estimating LIB temperature and providing insights for system design and thermal management. Additionally, its lower complexity need less computational power making it suitable for real-time applications.

1.3.1.3 Thermal Model selection for a Digital Twin environment

In the previous section, the two most common approaches to constructing a thermal model in the field have been reviewed. These include Distributed Numerical Models and the so-called Lumped Thermal Models. The two types share a common baseline by considering the heat generated and stored in the LIB cell, as well as the heat transferred by conduction, convection and radiation. However, their main difference lies in the method used to calculate the internal heat of the cell.

CFD based models offer detailed analysis of heat and mass transport phenomena in LIBs, capturing internal processes and providing high accuracy. However, these models require significant computational power, time, and technical expertise to implement. Detailed input data is necessary, making data acquisition challenging and costly. Results can be sensitive to boundary conditions, and while CFD based models are effective for small-scale phenomena like battery cells, they may struggle to fully represent larger battery packs or modules. These models are often used to design battery components, but their specialised software and limitations meant they were not suitable for use as a thermal model for the DT battery in this thesis.

LTMs simplify heat distribution using equivalent circuits, treating the battery as a single entity without particle-level details. Each electrical component represents a thermal phenomenon, and voltage differences indicate temperature variations within the cell. These models are known for their simplicity, assuming uniform temperature throughout the cell volume. They require fewer computational resources and offer faster solutions compared to CFD based models.

However, LTMs may lack accuracy in extreme operating conditions as they oversimplify the computational problem. While they provide a general understanding of temperature distribution, they are dependent on the cell or battery module's geometry. Developing a new LTM is relatively straightforward by obtaining cell parameters, making them more versatile than CFD models and applicable to various scenarios.

LTMs offer simplicity, easy interpretation of results than those of CFD based models, and compatibility with other systems and models. They are suitable for real-time operation, providing accurate average temperature estimation for cells. LTMs have low computational cost and integrate well with BMS and TMS. They are the preferred choice for the simulation platform in this thesis, offering robustness and the ability to calculate temperature distribution for different current profiles.

For all these factors, it has been decided to use an LTM of the cell applied in three dimensions for temperature estimation. By employing these simplified approach, it is possible to obtain suitable results for the thermal analysis of the battery DT without the need for complex and expensive software. In addition, the model will consider the SoC of the battery to correctly choose the parameters to be applied in its mathematical formulation. The model will also take into consideration the irreversible heat generated (Joule losses) and the irreversible heat (entropic heat). A detailed description of this model will be provided in Section 3.3.

1.3.2 Electric Models

The electrical battery models describe their voltage response to certain operating conditions, strongly depending on cell temperature, SoC and current. An important function of the BMS is to compute the estimation of factors such as SoC, SoH, power or energy available. Battery electrical models provide a theoretical description of the electrical behaviour of the battery, while battery state estimators use real-time measurements to estimate the current state of the battery. By combining both approaches, more accurate monitoring and effective battery control can be achieved in a variety of applications. A high fidelity and simultaneously low-cost computational method is required as mathematical equations or models that represent the input/output (current/voltage) dynamics of the battery [104].

When selecting a battery model for a specific application, important considerations include accuracy requirements, model complexity, computational cost, data availability, and ease of implementation. After reviewing various literature sources [105–107], the electric models have been classified into three main groups: Electrochemical Models, Equivalent Circuit Models (ECMs), and Data-Driven Models.

Electrochemical models, such as the Simple Particle Model (SPM) [108–110], the Pseudo-2D Model (P2D) [111–113] and the Doyle Fuller Newman (DFN) model [114–116], are based on the physics and chemistry of batteries. While these models offer high accuracy, they require extensive parameter identification and are not suitable for simulating behaviors at larger scales. Additionally, the complexity of electrochemical processes [117] and the limitations of current measurement techniques [118] make them impractical for this research.

Data-driven approaches have gained popularity due to their flexibility and ability to avoid explicit models [119]. Methods like Artificial Neural Networks (ANN) [120], Deep Neural Networks (DNN) [121], Adaptive Neuro-Fuzzy Inference Systems (ANFIS) [122], and Support Vector Machines (SVM) [123] have been used to describe battery behavior. However, these models heavily rely on the availability of large amounts of experimental data, which may be limited in this thesis. Moreover, it is important to note that data-driven algorithms often require significant computational resources and can be associated with lengthy training times. Considering these factors, both electrochemical models and

data-driven models have been excluded from the selection of the electrical model for this research.

When selecting an electrical model for a LIB, several factors must be taken into account, such as required accuracy, model complexity, computational cost and ease of implementation. In this context, electrical models based on ECM will be considered. This choice is based on the search for a balance between accuracy and simplicity of the model. The ECM provides an adequate representation of the battery dynamics, while maintaining the simplicity and ease of implementation needed for this work. In the subsequent Subsection 1.3.2.1, an analysis will be conducted on the various types of equivalent circuits documented in the literature, aiming to identify the most appropriate circuit for the simulation platform addressed in this thesis.

1.3.2.1 Equivalent Circuit Models of Lithium-ion Battery Cells

ECMs of LIBs are models that describe the internal processes of the battery using electrical approximations. They use electrical circuits with passive elements such as voltage sources, resistors and capacitors to represent the physical phenomena occurring inside the cell [124]. These models require a correct definition of the parameter values, which vary according to the SoC, temperature and SoH of the battery [125]. After defining the parameters, the models are validated by dynamic profiling, typically at the cell level [126]. However, they can lose accuracy when different input profiles are applied or when performance needs to be extrapolated to the battery module level. There are different models with different characteristics and complexities, from basic models based on Thevenin's theorem to models with multiple Resistor-Capacitor (RC) stages. This Section presents a broad classification of the discussed ECMs, as illustrated in Figure 1.11, providing an overview of the classification undertaken in this PhD.

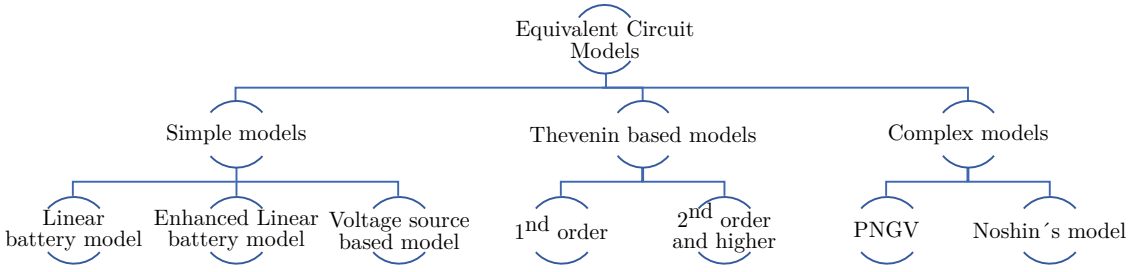

Figure 1.11: Electric Model classification.

The *Linear Battery Model*, depicted in Figure 1.12a, consists of an ideal voltage source (Open Circuit Voltage (OCV)) and an internal resistance (R_{int}) that represents energy losses [126]. It is suitable for stationary applications but lacks accuracy in capturing dynamic transient phenomena. The model can be enhanced by incorporating specific resistors for charging (R_{CHA}) and discharging (R_{DCH}) [106], as shown in Figure 1.12b. The *Enhanced Linear Battery Model* considers the variation of internal resistance with

SoC but lacks dynamism and neglects temperature influence [127]. The *Voltage Source-based Battery Model* uses multiple voltage sources to represent battery phenomena but is not dynamic and doesn't consider transient effects or temperature influence [128]. This model is commonly used in traction applications for lead-acid and lithium-ion batteries [129]. While these models are computationally efficient, they do not accurately capture high dynamic transient phenomena, especially when applied to battery packs. This simple models are illustrated in Figure 1.12.

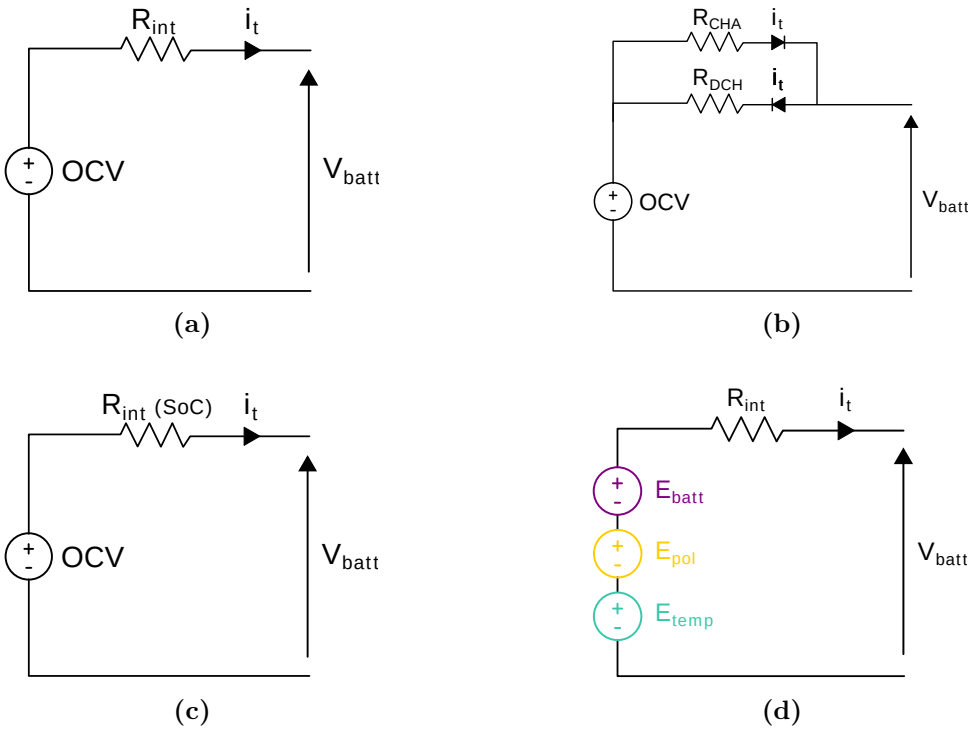

Figure 1.12: Simple Equivalent Circuit Models. a) Linear Battery Model, b) Linear Battery Model with diodes for charging and discharging, c) Enhanced Linear Battery Model, and d) Voltage Source-based Battery Model

The *Thevenin First Order Model* is a circuit consisting of an OCV voltage source in series with a resistor representing the internal resistance of the LIB, and an RC circuit in parallel described in Figure 1.13a. This model accounts for transient phenomena, such as polarisation, by introducing a slow voltage response after the application or disappearance of current. This model is widely used in applications such as EV and stationary applications [82]. In the literature, it has been used to estimate the OCV of LIB packs for EV and to model the charge/discharge characteristics of LIBs [130].

The *Second or Higher Order Thevenin Model* incorporates more RC phase pairs in the ECM, representing the ohmic polarisation and concentration polarisation associated with electrochemical reactions by ion diffusion in the electrolyte described in Figure 1.13b. The first RC phase captures the short-term transient effects, while the other RC phases represent the long-term transient effects. Although more RC phases can be added to

increase the accuracy, this also increases the computational cost and speed of execution. In addition, the ECM can be combined with other models to create multidisciplinary approaches that consider electrical, thermal and battery degradation aspects [131, 132].

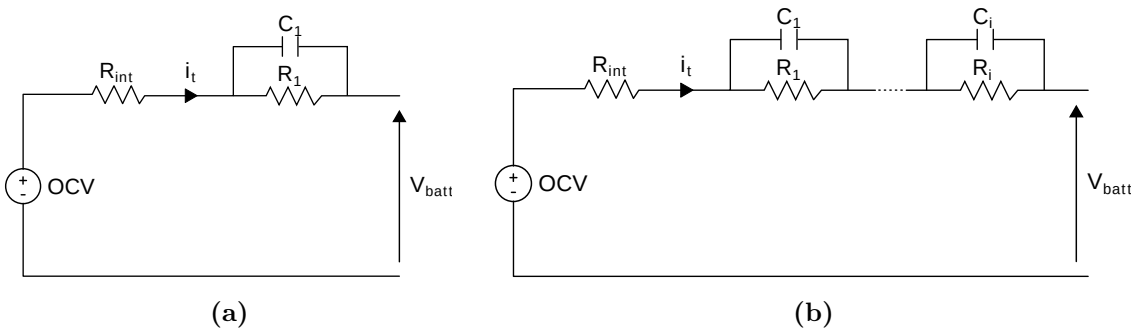

Figure 1.13: Thevenin based Equivalent Circuit Models. a) First Order, and b) Second and Higher Order

The *Partnership for a New Generation of Vehicles (PNGV)* or *Freedom Car* model [133] is a model developed by the US and major automotive companies (Daimler AG, Ford and General Motors) for battery simulation in EVs described in Figure 1.14a. This model extends the Thevenin Model by adding a series capacity. It allows for changes in OCV during dynamic cycling and scales the battery capacity. It also takes into account the effects of LIB polarisation and activation [134]. Compared to other models, the PNGV model has demonstrated good performance in dynamic simulation and SoC estimation, especially in the long term. However, it has not surpassed the results achieved by the second-order Thevenin model, which has shown the best performance in simulating LIB behavior [135].

The *Noshin model*, described in Figure 1.14b, is a variant of the Thevenin model that takes into account hysteresis and non-linearity of the internal parameters of a battery [136]. This model uses different resistors for charge and discharge, as well as resistors that account for polarization effects in the battery model. It also includes four RC phases to represent polarisation effects and a resistor for self-discharge. It was proposed to analyse the performance of LIBs in plug-in hybrid vehicles. However, the authors later had to modify the complex model to a simpler one for battery SoC estimation [137].

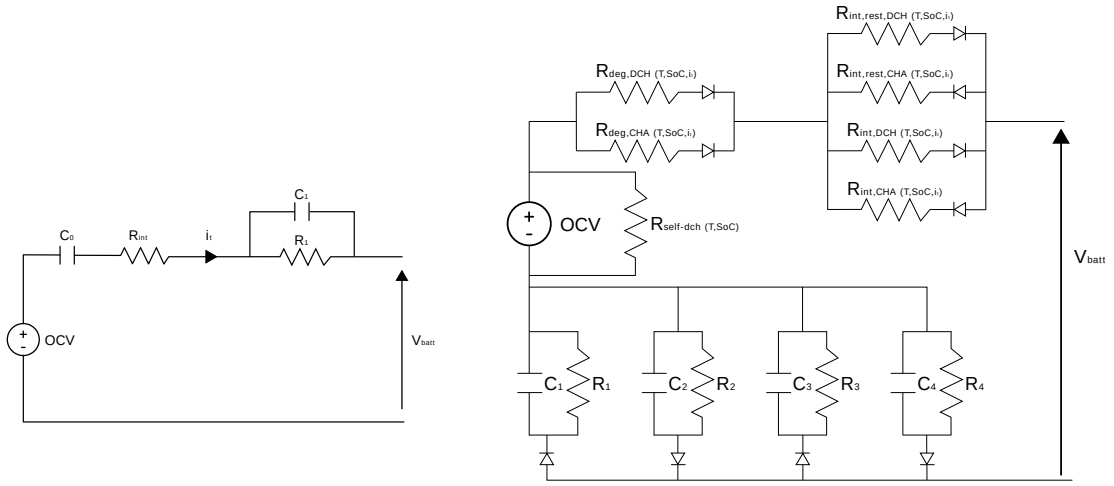

(a) **(b)**

Figure 1.14: Complex Models. a) PNGV, and b) Noshin´s Model

1.3.2.2 Electric Model selection for a Digital Twin environment

Electric battery models are crucial for BMSs to monitor battery condition accurately and then, estimate the SoC of the LIB. These models should be simple, computationally efficient, and accurate simulating battery behavior. However, data-driven models have limitations, such as the need for large amounts of high-quality data, lack of interpretability, sensitivity to operating conditions and the difficulty in capturing the underlying physics of the battery. On the other hand, implementing Electrochemical Models is challenging due to complex process of parameter obtaining and manufacturing variations. In contrast, ECMs are simpler, widely used, and suitable for various applications. ECMs use measurable variables like voltage, current, and temperature to estimate battery behavior, including thermal effects. The complexity of ECMs varies based on circuit design and the inclusion of additional elements to capture dynamic processes, such as the non-linear hysteresis.

An analysis of different types of equivalent circuits has been carried out. The simplest models, such as the Linear *Battery Model*, the *Enhanced Linear Battery Model* and the *Voltage Source Based Model*, do not consider all the internal dynamic phenomena of a battery, which affects their performance and accuracy. Therefore, these models have been excluded in the development of the DT in this thesis.

In contrast, more complex models such as the one proposed by the *PNGV* and the *Noshin´s Model* significantly increase the complexity and computational burden without providing significant improvements in model performance. The PNGV model, developed by several automotive companies, is designed specifically for EV applications. On the other hand, the Noshin´s model was created to account for more internal phenomena, but this results in overly complex models that require simplification.

Therefore, it has been decided to use an intermediate model that balances accuracy and complexity. *Thevenin-based Battery Models* are a good choice for this purpose. The complexity of these models is based on the number of RC phases included in the ECM. Typically, these circuits contain one or two RC phases. In this case, a Thevenin-based ECM with three RC phases is selected for simulation, taking into account the hysteresis phenomenon to capture the electrical behavior of the battery. This model fulfills the requirements of being lightweight, fast, and accurate, making it suitable for implementation in a DT of an EV.

The model response describes the voltage measured at the cell terminals. It also enables the determination of the diffusion currents ($i_{diff,t}$), the hysteresis voltages (h_t) and their instantaneous response in cases where the input current changes the direction, and also in the estimation of the SoC. The detailed description of this model will be presented in Section 3.4.

This LIB model will be complemented by a SoC estimator. These models and estimators often work together to obtain more accurate state estimates. The analysis of the different SoC estimators will be carried out in the corresponding Section 1.3.3.

During this analysis, several methods and algorithms used to accurately estimate the SoC of the LIB will be examined and compared in next Section. These estimators are critical to obtain reliable information about the amount of energy stored in the battery at any given time. The selection of the right estimator is crucial for accurate monitoring and effective battery management. The objective of this analysis is to provide a comprehensive evaluation of the available SoC estimators in order to identify the best option in terms of accuracy and reliability for the system under consideration.

1.3.3 SoC Estimators

An efficient BMS ensures the safety and reliability of LIBs by monitoring battery states such as SoC, SoH, and SoP. It operates within safe limits, activates cut-off mechanisms if necessary, and maximizes battery capacity utilization.

LIBs are non-linear electrochemical systems and their behaviour is totally unconscious, highly complex, variable over time and dependent on various internal and external conditions. Their performance depends on different factors such as charge current, operating temperature or their SoH. Therefore, the precise estimation of the SoC of the LIB is a difficult task since it cannot be directly evaluated using any physical sensor, so an estimate has to be made.

1.3.3.1 SoC Estimators of Lithium-ion Battery Cells

The SoC is determined using different models/algorithms that are usually stored in the battery micro controller. These systems use the Read-Only Memory (ROM) to store basic data such as the amount of discharge or charge/discharge efficiency and the Random Access Memory (RAM) to store historical data such as the number of charge/discharge cycles. However, the complexity of some algorithms such as SoC estimation can exceed the capacity of these micro controllers, so they are executed on a computer or even in the Cloud in the case of the largest algorithms, as they are required to work in real time.

In this overview of different SoC estimation methods, different reviews in the literature have been analysed [138–142]. Based on them, some of the most commonly used methods that follow the classification of Figure 1.15 will be analysed, according to their nature.

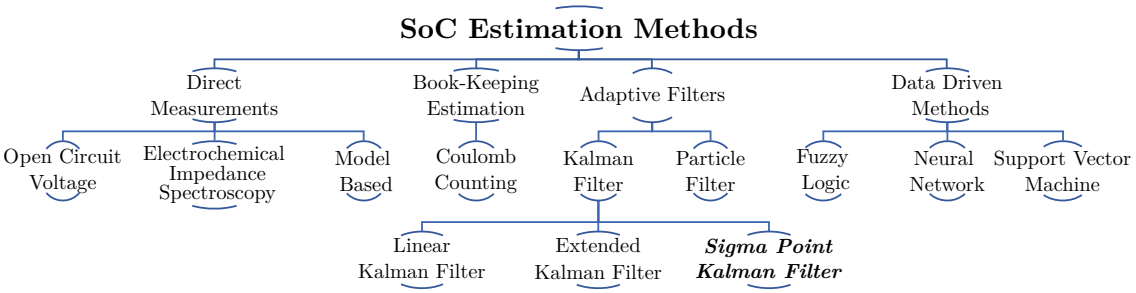

Figure 1.15: SoC estimation classification.

The direct OCV measurement technique is based on the ratio of OCV to the SoC of a battery, but is not suitable for accurate real-time estimates. It is used as a calibration support technology for other SoC estimation algorithms. The Electrochemical Impedance Spectroscopy (EIS) technique characterises battery impedance by injecting sinusoidal currents [143], but loses accuracy outside the characterised range and requires specific equipment to generate the excitation signals. Model-based estimates use state equations to describe battery behaviour, but often require additional supporting methods.

Book-Keeping based estimation is widely used and relies on the Coulomb Counting technique [144], which consists of integrating the battery current over time to estimate its SoC. However, this technique requires accurate current measurement and relies on prior information of the SoC and battery capacity. Cumulative errors caused by current sensor can affect the accuracy of the estimation. Despite these limitations, it is used in combination with other recalibration techniques to improve SoC estimation accuracy.

Kalman Filter (KF) and Particle Filter (PF) are adaptive filtering techniques used to achieve higher accuracy in SoC estimation. Typically, a subset of relevant particles is selected to approximate the density function in Monte Carlo-based PFs. This selection process enhances the efficiency of the estimation method. However, to further enhance performance, PFs are often combined with other techniques. On the other hand, KFs allow estimating the dynamics and internal state of a battery, but their implementation

is more complex. KFs utilize noisy measurements of battery inputs and outputs to estimate the unobservable internal states and dynamics of a battery. This noise can originate from various sources, including inherent model uncertainties and measurement errors. It is typically assumed to follow a Gaussian distribution, with a mean of zero and independence among different sources of noise. To handle the non-linearity of battery models, techniques derived from Kalman filtering, such as the Extended Kalman Filter (EKF), are commonly employed. The EKF is utilized to approximate the battery model and improve the estimation accuracy of battery states [145–147]. However, this increases the computational cost and there can be linearisation errors in highly nonlinear systems. For systems up to third order, the Unscented Kalman Filter (UKF) can be used to optimise and minimise linearisation errors [148]. However, the UKF is less robust and more complex than the EKF. Another variant is the Sigma Point Kalman Filter (SPKF) [149, 150], which uses a deterministic approach to calculate the covariance and mean, improving the efficiency of SoC estimation with a better approximation of the covariance matrix and better estimation of the internal states.

Finally, there are the Data-Driven Methods. While Data-Driven Methods offer the advantage of pattern extraction and prediction from data, they have limitations such as lack of interpretability, reliance on data quality and quantity, challenges in generalization and robustness, and limited extrapolation capabilities. Consideration of specific application requirements is crucial before relying solely on Data-Driven Methods for estimation tasks. Among these techniques there are Fuzzy Logic (FL), Neural Network (NN) or SVM, for example.

To assess the performance of various SoC estimation methods, it is important to analyze the errors associated with each technique. In this study, the mean average error (MAE), maximum error ($MaxE$), and minimum error ($MinE$) of the methods described in the literature [142] were examined. A summary of these errors is presented in Figure 1.16.

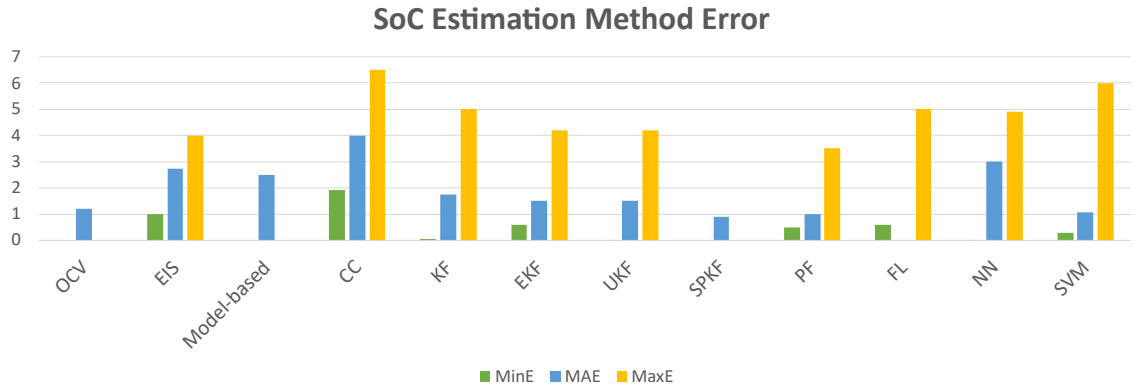

Figure 1.16: Comparison of SoC Estimation Method Errors in [%].

1.3.3.2 SoC Estimator selection for a Digital Twin environment

The type of estimator should be carefully selected according to the requirements of each application. On the one hand, it is necessary to consider the computational capacity available in the BMS, finding a balance between the computational complexity of the estimator and its conceptual complexity. In general, simpler estimators are preferred. In addition, the purpose of the SoC estimator must be taken into account. For example, if the SoC is intended to be used for battery monitoring, adaptive filters offer confidence limits without a significant increase in computational cost, which makes them more robust than other estimators. Finally, the accuracy of SoC estimates in a given implementation depends directly on the accuracy of the used model and, to a large extent, on the type of estimation algorithm employed. Improving the accuracy of the battery model and SoC estimator can be achieved by establishing a strong correlation between the battery's OCV and its SoC. Additionally, taking into account hysteresis effects in electrode materials, such as lithium iron phosphate (Lithium Iron Phosphate (LFP)), can further enhance the accuracy of the estimation process. This involves a trade-off between accuracy and computational complexity that must be selected to meet the requirements of the application.

Direct measurements are a simple and straightforward method for estimating the SoC of a battery, offering accuracy under ideal conditions. However, they have limitations in providing accurate estimates under certain conditions, especially during transients, and are subject to the influence of temperature and battery ageing. On the other hand, book-keeping estimators offer accuracy over a wide range of conditions and flexibility to adapt to different battery types, but require accurate initial SoC information, which can be challenging. In addition, these estimators can have a cumulative error due to the integration of current over time.

Data-driven estimators possess the advantage of effectively handling non-linear and intricate relationships, enabling them to capture patterns that may pose challenges for other estimation methods. With a sufficiently large and high-quality data set, these models have the potential to provide accurate SoC estimates. However, their implementation requires a significant amount and quality of data, and they have the limitation of being difficult to interpret due to a lack of transparency in their internal processes. This makes it difficult to understand how decisions are made within the model.

In this thesis, the previously mentioned estimators have been discarded and adaptive filters have been chosen for the estimation of the battery SoC. This choice is based on the following reasons: adaptive filters provide flexibility in accommodating variations in operating conditions, allowing for accurate SoC estimates across a wide range of conditions.

In contrast to the EKF, the SPKF offers significant advantages that make it a favoured choice in certain cases. The SPKF is able to more effectively handle non-linearities by approximating the probability distribution using Sigma Points (SPs), resulting in more accurate estimates of the system state. In addition, the SPKF exhibits lower sensitivity to

modelling errors and uncertainties in the model parameters, as it propagates uncertainty through the model via the SPs. This makes it more robust in situations where the system model is uncertain. However, the use of SPKF implies a higher computational complexity due to the calculations and operations required to generate and propagate the SPs. Based on the above advantages and features, the SPKF has been selected as the preferred option due to its ability to handle nonlinearities more effectively, its lower sensitivity to modelling errors and its higher robustness.

1.3.4 Integration of models

Different electrical and thermal models for LIBs have been analysed. Specific models and a SoC estimator were selected for design in this thesis. The electrical model is an equivalent circuit with two or more RC phases and considers battery hysteresis. The thermal model is a module-level analytical equivalent circuit (LTM) using temperature measurements and a current profile. Both models require the upstream temperature and SoC as inputs.

The electrical and thermal models can be used in combination to estimate the SoC and temperature of LIBs. These models can interact and feed back to improve the accuracy of estimates and predictions. Feedback between these two models can allow for more accurate estimation of SoC and battery temperature.

This has been reflected in different works that have been published. Looking at the review of the literature, different works can be observed where two or more models have been integrated to monitoring the LIB. In [151] an electrothermal model was used for the optimisation of the fast charge of the LIB. In this work an ECM with two RC phases was integrated with an LTM model, all at the cell level. In [152] the similar principle of integrating both ECMs was used to develop an electrothermal model at the cell level. In the same way, the authors of [153] integrated an electrochemical model and an LTM model into one electrochemical model. Examples have also been observed in which, besides integrating electrical and thermal models, researchers have developed an electrothermal degradation model capable of estimating the SoH of the LIB cell [154].

1.4 Module-level Battery Modeling

This section provides a comprehensive review of the This Section covers a comprehensive review of the SoA in LIB module modelling and estimators. It is closely related and continues from the previous Section, Section 1.3, where the importance and utility of electrical and thermal models of LIB cells, as well as SoC estimators, has been highlighted. in module-level modeling and estimators for lithium-ion battery (LIB) systems. Building upon the previous section's emphasis on the significance of electrical and thermal models for LIB cells, as well as SOC estimators, this section aims to analyze their implementation in LIB modules within the scientific community. The objective is to assess the various approaches employed and identify any potential gaps or limitations in the existing literature. Additionally, alongside the separate analyses of the models in Sections 1.4.1, 1.4.2 and 1.4.3.

Various kinds of algorithms used in previous research have been analysed, evaluating their advantages and disadvantages, with the aim of selecting one of each type to be developed in the context of this thesis. As a result, a LTM capable of estimating the temperature at different points of the cell, taking into account the generation, accumulation and transmission of heat by conduction, convection and radiation, has been chosen. This model is applied in three dimensions.

On the other hand, an ECM has been chosen together with a SoC estimator based on an adaptive SPKF filter. The ECM will incorporate two or more RC phases to estimate the voltage response of the cell, and will also take into account the hysteresis of the cell when modelling it. The voltage estimate obtained will then be used by the SPKF to correct the SoC estimate.

1.4.1 Thermal models

Battery thermal models are essential for the design, management and safe operation of battery modules. These models allow to estimate and thus control the thermal behaviour of LIBs. Module temperature is an important factor in the efficient and safe operation of the module in order to avoid overheating and to keep the temperature within the optimal range of the SOA. It also directly affects the rate of degradation of the LIB.

These tools allow users to predict the temperature distribution within the module, which can help optimise the design to ensure efficient heat dissipation. Battery thermal models are based on the fundamental laws of thermodynamics and heat transfer. These models consider several factors, such as heat generation during charging and discharging, thermal conductivity of battery materials, convection and radiation of heat to the environment, and heat storage within the battery.

There are several types of thermal models, ranging from simplified LTM to more complex CFD based models as discussed in Section 1.3.1.

1.4.1.1 Thermal Models of Lithium-ion Battery Modules

A single cell typically functions effectively on its own. However, when this cell works in coordination with other cells (as modules are made up of more than one cell connected), the battery module can experience severe temperature changes. Therefore, in order to monitor the electrical and thermal characteristics of a module, the thermal behaviour of each individual cell of such module and its thermal interaction with neighbouring cells must be considered. The cooling of the system, if any, must also be considered.

At this stage, we will reanalyze the two types of models discussed in 1.3.1. This is because it is intend to extrapolate the cell-level LTM to the module level, while also employing a CFD-based model to obtain detailed parameters for the entire model. The utilization of these two models will be presented below.

Numerical Distributed Models.

CFD technology has been used in several research works related to battery TMS. In the study [155] for example, CFD is used to analyse the thermal effects of different cooling structures in battery packs. On the other hand, in [156] CFD is used to investigate air cooling strategies and analyse their impact on the thermal characteristics of battery modules. Furthermore, in [157] the use of CFD is proposed to study the performance of an axial cooling system with a bionic surface structure. These works highlight the importance of CFD in the analysis and design of cooling strategies to improve the thermal performance of LIBs.

Regarding the optimization of operating conditions, CFD has been employed to optimize the cooling plate conditions [158], compare different cooling systems such as air and liquid [159], and optimize the battery pack structure and design cooling strategies [160]. In [161], an experimental demonstration of active thermal control of a LIB module is given. In addition, in [162], a three-dimensional thermal overheat propagation model for a large-format LIB module is presented. The model can be used to study the mechanisms of thermal overheating propagation and to design safer battery modules.

In summary, the use of CFD in these research papers highlights its importance in the analysis and design of cooling strategies, as well as in the optimisation of operating conditions to improve the thermal performance of battery systems. CFD is used to simulate and predict fluid flow and heat transfer, allowing the evaluation of different cooling designs and strategies and their impact on the thermal characteristics of batteries.

Lumped Thermal Models.

In recent research on LIBs, there is a trend in the use of simplified thermal models, known as LTMs. These models allow the thermal behaviour of batteries to be analysed efficiently and quickly compared to more complex numerical models. In this way, there have been observed works [102, 163–166] that use the LTM to simulate the battery temperature.

Some of these works use LTM to estimate the temperature distribution of the module together with cooling systems such as heat pipes (helped with conduction elements between battery and heat pipes) [163], cooling flow [164], or a hybrid cooling system (Phase Change Material (PCM) and liquid cooling) [165]. In [166], PCM and nine aluminium tubes for liquid coolant circulation are also used as cooling system.

The works also vary in how the model is validated. For example in [102] a Fluent simulation is used to validate the results. In [165] both CFD model simulation results and thermocouple measurements at different points in the battery are used.

1.4.1.2 Module-level Thermal Model for a Digital Twin environment

According to the analysis of the scientific publications, there is a wide variety of thermal modelling work at the module level. All these developments vary in the type of model used, the purpose for which the model is used and among them the complexity of the model (Complexity is referred to the technical difficulty required to develop them or the level of detail they cover).

Thus, it has been observed that CFD-based models are mostly used for the design phase of the battery module or the design of the LIB TMS. These tools are very powerful and calculate the temperature distribution of the cells or the cooling components in great detail. However, all the studies found have in common that the model is used ofline, meaning that the model is used in an early stage before the module is deployed. No research has been found where the CFD model is used to estimate the temperature in real time.

On the other hand, it has been noted that in recent years there is an increasing usage of LIBs as thermal models for LIB modules. These models provide a simplified representation of the physical phenomena compared to CFD models. LTMs offer a practical and efficient solution for real-time battery temperature estimation. Additionally, as discussed in Section 1.3.1, the parameter estimation and development of LTMs are generally less complex compared to CFD models.

The module level thermal model to be developed in this thesis is based on the LTM model chosen in Section 1.3.1. This type of model is very adaptable to different geometries and to the sum of thermal phenomena as just observed [102, 163–166]. However, few studies have been found where this type of model has been used with LIBs that have

natural convection. Not having a cooling system means that the radiative heat dissipation is higher and the convective heat dissipation is smaller.

When radiation heat transfer is taken into account, a non-linearity is introduced into the model, which makes the energy balance of the model more complex. Furthermore, this radiative heat transfer is directly related to the visible surface area between two objects. This means that the amount of radiant heat transferred depends on the surfaces facing each other and visible to each other. This visible surface is defined by a "view factor" between the two adjacent cells. In addition, the convection coefficient h_{conv} will also depend on the distance and the location of each cell in the module.

Therefore, the research aims to integrate both types of models for the development of the module-level LTM model in this thesis. The development would have two phases. A preliminary phase involves creating a CFD model of the module, which includes tasks such as meshing and conducting simulations to obtain important parameters such as h_{conv} and the "view factor" between the cells. And a second phase where the LTM model is implemented at the module level together with the parameters obtained from the CFD.

1.4.2 Electric models

ECMs are powerful tools used in the battery industry to simulate and predict the behaviour of battery cells. These simplified models use standard circuit elements to represent the electrical properties of the cells. At the module level, ECMs allow the behaviour of cell arrays to be modelled, which is useful for predicting module performance and designing more efficient BMSs.

1.4.2.1 Electric Models of Lithium-ion Battery Modules

The research and development of module-level devices, such as module-level ECMs, remains an active area of research in the field of batteries. These devices have demonstrated their effectiveness and versatility in various battery applications, offering accurate and efficient models to predict battery behavior under different operating conditions. They contribute to optimizing battery design and enhancing energy management. Numerous studies have explored the development and application of module-level ECMs to improve the understanding and performance of battery systems [151, 167–175].

In this context, some of the studies focus on battery management in hybrid and EVs [176, 177], presenting models to analyse the internal resistance, SoC and discharge efficiency of batteries. They also cover aspects related to the variation of resistance as a function of temperature [169] and highlight the importance of having an accurate model to be able to propose improvements in SoC estimation algorithms [177]. All these works have in common that they define the LIB module as the smallest unit to be simulated, that is, they do not take into account the individual cells.

Other works focuses on the modelling of large-scale battery packs [151, 178, 179]. These works use ECMs at the pack level. These works evaluate the reliability of the developed ECMs and analyse the thermal performance of the LIB modules. In the case of these works, they have as well in common the battery pack as the smallest unit to be simulated. This means they do not take into account the differences that may exist between the modules in the system, as well as the states of the individual cells.

A common factor in these works is the use of the ECM as the electrical model of the LIBs. However, they differ in the level at which the ECM is applied for the estimation of the LIB terminal voltage. A common limitation observed in the reviewed studies is the lack of consideration for the state of individual cells within the lithium-ion battery (LIB) system.

1.4.2.2 Module-level Electric Model for a Digital Twin environment

At the module level, the use of module-level ECMs allows for the modeling of a group of cells connected in series or parallel. This approach is valuable in predicting the performance of battery modules under different operating conditions and in designing more effective BMS. However, the existing use of ECMs in previous studies may overlook important details regarding the electrical behavior of the battery pack. In this thesis, the focus is on developing an ECM specifically for the LIB module, with a higher level of detail compared to previous works. By working at the module level, the proposed ECM aims to capture and analyze the behavior of individual cells within the module, offering the potential to identify and diagnose problems that may arise in specific cells. This level of granularity is crucial for ensuring the safety and efficiency of the overall battery system.

When combining ECMs, it is essential to take into account the interaction between cells and the variability in their properties. If the cells within a module display differences in internal resistances or capacities, a module-level ECM that does not consider the individual cells may fail to capture these variations adequately. In such cases, more sophisticated models capable of accounting for the variability between cells may be necessary. By incorporating cell-specific characteristics and considering the interplay between cells, these advanced models can provide a more accurate representation of the module's behavior and enable better performance analysis and optimization.

Module-level ECMs that considering all the cells provide an accurate representation of the battery system as a whole. However, their accuracy may be limited due to the simplicity of the individual models and the complexity of the interactions between the cells. In addition, if the cells exhibit variations in properties or degradation, the ECM may not capture these differences. Development and validation of module-level ECMs can be more challenging, as they require data from all cells and complex solution algorithms, which increases cost and development time.

Based on the aforementioned approaches, several areas for improvement have been identified. Firstly, the complexity associated with developing an electrical model for LIB modules is a significant challenge. Additionally, the reviewed studies predominantly treat the module as a single entity, neglecting the individual cells within it. These simplified models consider module-level characteristics and parameters without accounting for the specific behavior of each cell. Consequently, these models may overlook certain phenomena occurring at the cell level within the module. Enhancements in modeling techniques are necessary to capture the intricacies of individual cells and accurately represent the dynamic behavior of the entire module.

The selection of the ECM at the module level in this thesis is based on the electrical model chosen in Section 1.3.2. The analysis of electric module-level models reveals that many existing works tend to employ simplistic representations when modeling LIBs in EVs or large-scale battery systems, lacking in-depth detail. However, among the objectives of this research is the development of module-level models with more information on the states of each cell. This identified gap in the literature presents an opportunity for further research and development in the field of module-level LIB modeling. Section 4.4 of Chapter 4 will focus on the electrical modelling of the battery module.

1.4.3 SoC estimators

In Section 1.3.3, a SPKF has been chosen as the SoC estimator of the LIBs of each cell. Then, in Section 1.4.2, electrical models have been analysed at the cell level where the objective is the estimation of the battery terminal voltage (either at the cell level or at the module level). In addition, the development of an ECM for each cell has been proposed in order to estimate the SoC of each cell in the module. The main objective of this Section is to perform a SoA analysis of the SoC estimators for LIBs at the module level. As the SPKF has already been chosen as estimator, this analysis will focus on this specific estimator type.

1.4.3.1 SoC Estimators of Lithium-ion Battery Modules

Observing the research works that have been carried out with the SPKF for the estimation of the SoC of LIB modules, few works have been found. Moreover, these works focus on estimating the SoC of the LIB at module terminals. Individual cell SoC is not taken into account.

In certain applications, the SPKF has been employed as a SoC estimator, often in conjunction with Coulomb Counting, as seen in [180] for EV applications. Additionally, a fusion of the Lagrange multiplier method and SPKF was proposed in [181] for both LIB model identification and SoC estimation. These studies highlight the versatility and effectiveness of the SPKF algorithm in SoC estimation for various battery applications.

The authors in [134] utilised a SPKF SoC estimator together with PNGV ECM, also for a EV. A comparative study and validation of state estimation algorithms was carried out in [182] where it was concluded that the SPKF is the most accurate SoC estimator for the battery module.

1.4.3.2 Module-level SoC Estimator for a Digital Twin environment

All of these SoC estimators are integrated with electrical models based on ECMs, as it is intended to be done in this doctoral thesis. Similar to the electrical model at module level (Section 1.4.2), it is proposed to estimate the SoC of each of the cells at each time step. Thus, the voltage estimated by the ECM of each cell together with the measurements performed would be used for a correction of the SoC of each cell.

1.5 Cloud Computing Technologies for Batteries

The growing demand for energy and the need to address environmental challenges have driven the transition to renewable energy sources and EVs. LIBs play a crucial role in this shift, thanks to their high energy density, durability and versatility in various applications. In parallel, Cloud Computing has transformed the way data is managed, processed and analysed, offering efficient and scalable solutions. This SoA aims to investigate the application of Cloud Computing in LIB management and how the combination of these technologies can improve battery performance and sustainability.

1.5.1 Cloud Computing Fundamentals

Cloud Computing is based on the supply of Computing services over the Internet, which allows users to access Computing, storage and data analysis resources in a flexible and scalable way [183]. This technology, created in 2003, was first cited in 1996 by US scientist George Favarolo in the journal Technology Review [184]. The services offered on Cloud platforms are managed by remote data centres, which provide high Computing speed. The only technical requirement to access the Cloud is an Internet connection. As a result, companies using the Cloud services have significantly reduced their hardware infraestructure, which makes them more economically efficient in terms of Computing.

Virtualisation plays a central role in Cloud Computing, as it enables the creation of virtualised Computing environments shared by multiple users. Scalability and elasticity are key features of Cloud Computing, as they allow users to adjust Computing resources according to their needs. In recent years, the use of this technology has experienced exponential growth. However, Cloud Computing would not have been possible without the IoT, BD and Cyber Physical System (CPS) technology introduced by Industry 4.0.

Service models in Cloud Computing encompass Infrastructure as a Service (IaaS), Platform as a Service (PaaS) and Software as a Service (SaaS) [185]. In addition to these, Cloud providers sometimes offer a fourth possibility in which the user must design and develop the Cloud platform from scratch. These models offer different levels of control and responsibility over Computing resources, from management of hardware and operating systems in IaaS to access to specific applications in SaaS.

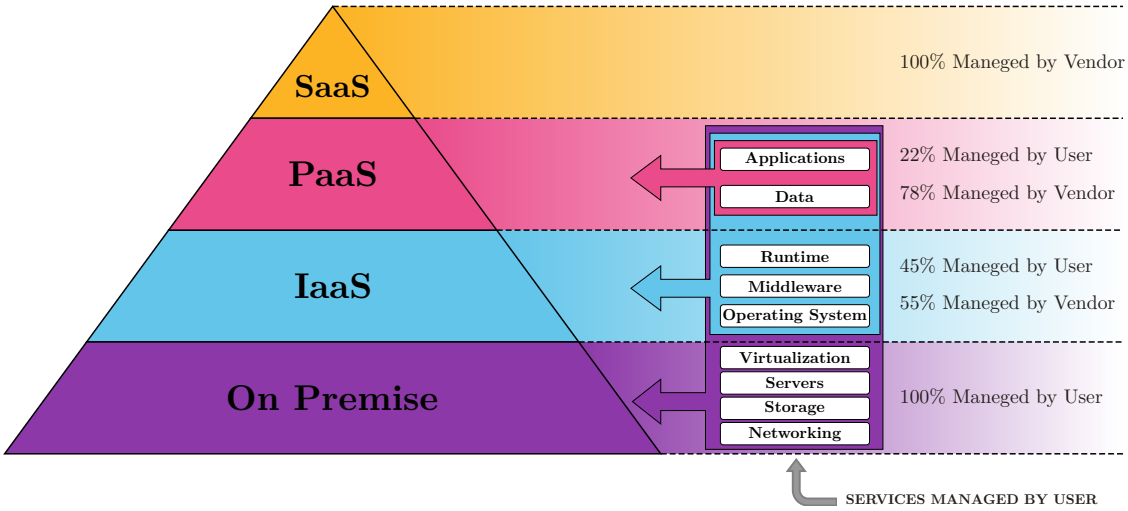

Figure 1.17: Service models in Cloud Computing.

As shown in Figure 1.17, the SaaS implies that Cloud service providers offer ready-to-use applications over the Internet, allowing users to access them through a web browser or a dedicated UI without the necessity to install additional software (e.g. LinkedIn or Office 365). The user only accesses the application without having to manage it. PaaS provides a development platform in the Cloud, making it easier for developers to create and deploy applications without worrying about the underlying infrastructure. The user focuses on application development, while the provider takes care of the underlying infrastructure. IaaS provides virtualised Computing resources, such as servers and storage, which users can configure and manage according to their needs. The user has full control over the configuration and management of the resources. Finally, "On-premise" refers to the deployment and management of an organisation's own on-premise server infrastructure. In this case, the organisation is responsible for everything from hardware to storage.

Deployment models span public, private and hybrid Cloud, which vary in terms of control, security and cost. A thorough analysis of the use, modification or authorised access to information and services by the people or companies involved is necessary. As shown in Figure 1.18, there are three different types of Cloud [186, 187].

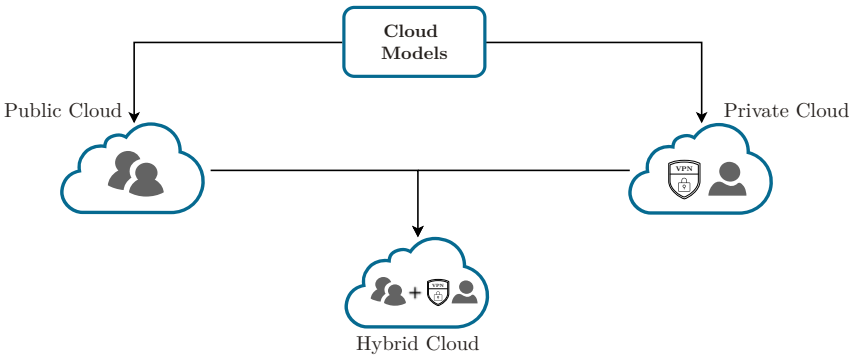

Figure 1.18: Public, Private and Hybrid Cloud Models.

There are various Cloud Computing models that offer different levels of security and characteristics. The public Cloud is open access to any people through the Internet, being inexpensive but presenting greater security risks. On the other hand, the private Cloud is focused on companies and provides greater security, although it is more complex and costly to manage. As for the hybrid Cloud, it combines elements of the public and private Cloud to take advantage of the computational power of both environments. The choice of the appropriate Cloud model must take into account the specific needs and requirements of each organisation or application.

Cloud Computing architecture is divided into two parts: the Front End and the Back End [185, 188]. The Front End, also known as the client platform, is the interface that users can manipulate and connects to the Back End via the Internet. There are various tools to access the Front End, such as web browsers, Cloud applications and computer interfaces. On the other hand, the Back End is the core of the Cloud Computing architecture and is composed of hardware and storage located on remote servers. Cloud service providers are responsible for managing and controlling the Back End, which hosts most of the components of the Cloud infrastructure. The robustness and reliability of the Back End are critical to ensure a robust and reliable Cloud platform. Cloud architecture composed of three main elements is ilustrated in Figue 1.19.

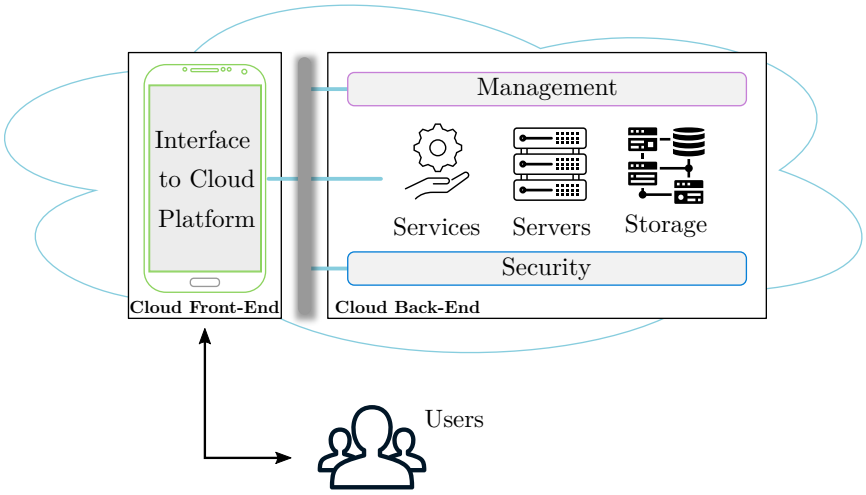

Figure 1.19: The architecture of Cloud Computing composed of three main elements: the Front End, the Back End and the connection between the two via the Internet.

In recent years, Cloud Computing has experienced remarkable growth. According to Harvard Business Review, 56% of companies use at least three Cloud Computing-based applications every day, and it is projected that by 2025, 80% of companies will be using Cloud services databases. This increase in Cloud Computing adoption has led to an increase in the number of available platforms and vendors. According to research conducted in 2021, there are 360 providers and 550 different platforms. The main players in the Cloud services market are Amazon Web Services (AWS), Microsoft Azure (MA) and Google Cloud Platform (GCP), which offer a wide variety of services and tools for deploying and managing Cloud-based applications.

AWS, founded in 2002, has positioned itself as a market leader with more than 200 services and multiple areas of utility in Europe [189, 190]. MA, established in 2008, offers 200 services and products, with a choice of operating systems and programming languages [191, 192]. GCP, also launched in 2008, is the third largest platform, providing 90 services, although its connectivity is slightly lower than other platforms [193, 194]. Each Cloud provider has free offerings, minimum billing times and guarantees of security and reliability. All this information gathered from the main Cloud Computing providers [189, 191, 193] is summarised in Table 1.2.

Table 1.2: Comparison of the three largest Cloud providers. AWS: Amazon Web Services, MA: Microsoft Azure, GCP: Google Cloud Platform.

	AWS	**MA**	**GCP**
Services	200	200	90
Utility areas	80	54	73
Utility areas in Europe	6	7	7
Operating systems	4	2	2
Programming languages	8	7	7
Free trier	12 months	12 months	3 months
Minimum billing time	1 sec	1 min	1 min
Connectivity	99.95%	99.95%	99.5%
Security and reliability	99.9987%	99.9792%	99.9982%

1.5.2 Current Market Trends in Cloud Computing and Lithium-ion Batteries

Cloud Computing is influencing the LIB industry in a variety of ways, from optimising battery management to improving supply chain efficiency. Below are some of the key trends in the LIB Cloud Computing market:

1. Integration of BMS with the Cloud: modern BMSs are being designed to connect to the Cloud, enabling real-time monitoring and analysis of battery data. This makes it easier to identify problems and implement solutions more quickly and efficiently. An example of this is the work of Yang et al. [72], which integrates with the Cloud to provide detailed information on battery performance.

2. DTs and IoT technologies: DTs are virtual models of physical devices or systems that can be used to simulate and optimise their performance. In the case of LIBs, DTs can help predict the degradation and remaining life of batteries, as well as optimise their performance under different operating conditions. A study by Zhang et al. [195] presents a DT-based approach for EV battery management using Cloud Computing.

3. Cloud data analytics and predictive maintenance: Cloud Computing enables the analysis of large volumes of LIB data, which can be used to predict remaining life and schedule predictive maintenance. This can reduce maintenance costs and improve battery reliability [196]. An example of this is the work of Eaty et al. [50], which proposes a Cloud-based approach for predictive maintenance of LIBs in EVs.

4. Real-time collaboration and communication: Cloud Computing facilitates real-time collaboration and communication between the different actors involved in the LIB supply chain, such as manufacturers, suppliers and customers. This can improve efficiency in the supply chain and enable faster response to changes in market demand.

5. AIs and machine learning: Cloud Computing enables the use of AIs and machine learning algorithms to analyse and process data from LIBs. These algorithms can be used to optimise battery performance, predict failures and improve energy efficiency. For example, a study by Zhang et al. [197] presents a deep learning-based approach to predict LIB degradation using Cloud data.

6. Data security and privacy: As the adoption of Cloud Computing in the LIB industry increases, so does the concern for data security and privacy. Companies are investing in Cloud security solutions to protect battery data and ensure user privacy. An example of this is the work of Sheikh et al. [198], which proposes a Cloud-based approach to ensure data security and privacy in EV battery management.

1.5.3 Use of the Cloud in the framework of this thesis

Section 1.5.2 has identified current market trends in the field of Cloud Computing applied to LIBs. It has been observed that the Cloud is mainly used for: i) integration of BMSs with the Cloud, ii) DT and IoT technologies, iii) Cloud data analytics and predictive maintenance, iv) real-time collaboration and communication, v) AI and machine learning, and vi) data security and privacy.

During the research carried out in this thesis, some but not all of these trends will be applied due to scope and time constraints. Firstly, Cloud Computing technology will be employed to integrate the battery BMS with the Cloud. This will allow battery measurements to be sent to a simulation platform developed in the Cloud, where the necessary estimations will be carried out. This integration will enable real-time monitoring and analysis of the system, facilitating early detection of problems or anomalies. It will also enable decision-making to improve battery efficiency or implement Energy Management System (EMS) or TMS strategies.

A second utility offered by the Cloud is the opportunity to enable Internet connectivity between the BMS and the Cloud thanks to IoT technologies. However, this requires programming and preparation of the communication protocols of the systems. In addition, a DT of the battery can be created in the Cloud, where more complex and advanced models that require large amounts of data or more processing power can be deployed. These models could exceed the capabilities of commercial BMSs. The contribution of the Cloud to the DT developed in this thesis is to provide the computational power required to run these models. The Cloud will allow for more sophisticated estimations and additional information beyond the sensor data.

As mentioned above, this will be achieved with the support of IoT technologies, which will enable real-time collaboration and communication. By equipping the BMS with IoT technologies, it is possible to connect to the Cloud both via wired and wireless connection. In this work, this technology will be used to send data and perform real-time computations, as well as to update the BMS with battery SoC estimates. In the event of a Cloud disconnection, the BMS will perform simpler SoC estimates. Once the connection is re-established, the DT will perform the corresponding estimates and correct the SoC of the battery.

Furthermore, the Cloud platform will have a database where both the measurements and the estimates made for each cell and module will be stored. This database will be protected with passwords and keys to guarantee the security and privacy of the data. Initially, it is planned to store all the information obtained for future usage. However, as this data increases, it may be necessary to perform an analysis and store representative historical data from the LIB.

Regarding Cloud data analytics and predictive maintenance, this thesis does not address this trend commonly associated with the use of the Cloud. As mentioned above, this DT will serve for a more detailed monitoring of the LIB module and also for the detection of anomalies on its operation. On the other hand, AI and machine learning will also not be employed, as the models to be implemented are equivalent circuits together with an adaptive filter estimator. This estimator requires information from the previous time step, but does not depend on a large volume of data and does not need to be trained.

1.6 Discussion & Conclusions of the Chapter

The aim of the SoA review has been to outline the previous knowledge related to the modelling of LIBs at the module-level, as well as the technologies required to deploy these heavier models in a simulation platform based on Cloud computing technologies. Therefore, this section aims to identify the challenges present in this field, as well as to highlight the main shortcomings and possible improvements compared to current research work. The conclusions obtained serve as a basis for the contributions proposed in this Doctoral Thesis.

Section 1.2 reviewed the Digital Twin technology and its implementation in the context of LIBs. The origin of the DT concept and its evolution since its emergence in 2003 has been explored. The different types of applications in which it has been used have been analysed, with an emphasis on its usefulness in the field of batteries. For this thesis, DT has been defined as a 5-dimensional tool, following the definition provided in the reference [42]. These dimensions include the physical space (the battery module), the virtual space (where the models and estimators of the LIB are located), the data space (which contains all the measurements and estimations of the LIB throughout its lifetime), the services space (which adds value to the module) and finally, the connections space (which is responsible

for the communication between all the spaces).

In the context of LIBs, these DTs work in combination with the BMS of the batteries, which are responsible for performing the measurements and can have server or Cloud connection functions. The basic functionalities of a current BMS have been reviewed and, in addition, the new functionalities made possible by Cloud Computing based technologies have been analysed. In this review, the benefits obtained by operating the BMS in parallel with the Cloud have been highlighted, including: i) optimisation of performance and lifetime, ii) fault detection and predictive maintenance, and iii) improvement of energy efficiency. As a result, it has been concluded that the adoption of a Cloud-based DT would provide greater computational capabilities and increased data storage capacity, thus improving the monitoring and optimisation of the module performance.

In section 1.3, two types of battery models have been analysed at the cell level, the electric model and the thermal model, as well as the different types of battery SoC estimators. A classification of each type of algorithm has been made in order to select one for implementation in the cell selected in this thesis. A wide variety of studies have been found where thermal and electrical models as well as SoC estimators are applied in LIB cells. On this basis, those models that do not fit the framework of this thesis have been discarded.

First, two types of thermal models have been analysed: Numerical Distributed Models (CFD-based models) and Lumped Thermal Models (LTM). It has been observed that the former estimate the cell temperature gradient in great detail, but are more commonly used in the early stages of cell and battery system design. On the other hand, LTMs simplify the complex calculations of CFD-based models and provide sufficiently accurate estimates of the temperature in the cells, while being simpler to develop and obtain the necessary parameters. Therefore, it has been decided to use an LTM model as the thermal model in this thesis.

Different electrical models of the cells have been analysed, discarding electrochemical and data-driven models due to their complexity and lack of sufficient data. The simplest models, such as those based on voltage sources or linear models, did not consider the influence of SoC or temperature on the model parameters. More complex models were also not selected due to their higher complexity without significant performance improvement. Instead, an ECM model based on a Thevenin model has been chosen, which will consider the non-linear hysteresis of batteries, especially LFP batteries. The choice of the number of RC branches will be discussed in detail in the corresponding section.

Research on SoC estimators for LIB battery cells has been reviewed, discarding simple and data-driven approaches due to their limitations. Instead, a Kalman filter, specifically a SPKF, was chosen, which offers the ability to handle uncertainty, model non-linear behaviour and achieve adequate computational efficiency. This allows for more accurate and reliable estimates of battery condition under various operating conditions.

In Section 1.4, an analysis was conducted on the trends in the literature regarding module-level battery modelling. It was observed that there is a limited number of studies that take into account the individual cell state in module-level modelling. The majority of published studies treat the module as the smallest unit of analysis, leading to a lack of essential information regarding cell interactions. Therefore, the decision was made to address this research gap and utilize the cell-level models as a foundation for extrapolating to the module level.

Finally, in Section 1.5, the application of Cloud computing technologies in the field of batteries was examined. The different types of Cloud services were defined based on the level of contract and privacy, as well as Cloud architectures. Additionally, the three leading providers of this technology (AWS, MA, and GCP) were compared in terms of services, operating systems, programming languages, security, reliability, cost, and free tier. After analyzing these characteristics, it was concluded that AWS is the most suitable platform for DT application in LIBs due to its superior security and reliability.

In order to address the identified challenges and literature gaps, this doctoral research proposes the development, validation, and implementation of cell-level models in a Cloud-based Digital Twin Simulation Platform, incorporating the variations of SoC and temperatures in individual cells. The following chapters provide detailed explanations and validation of the selected cell-level models, along with a proposed methodology for their extrapolation and implementation in the Cloud-based DTSP. Overall, this research highlights the potential benefits of incorporating DTs in battery systems, the importance of selecting appropriate models at the cell and module levels, and the advantages of leveraging Cloud computing resources. The findings contribute to advancing the understanding and development of module-level modeling methodologies for battery systems.

2

Methodology

Summary

The second Chapter of this PhD thesis presents a comprehensive and original design methodology which is the main contribution of the work. This methodology is intended for the development of a DTSP using Cloud Computing technologies. This Chapter presents the formulated hypothesis, and the validation methodology to validate them. To this end, the designed phases are presented, along with the corresponding objectives of each stage. An overview of the validation methodology is described, as well as a more detailed analysis of each stage.

2.1 Methodology overview

The main objective of this PhD is to develop a DTSP based on Cloud Computing technologies which contains deployed battery models at module-level considering cell-to-cell state variations as explained in the introduction. Starting from the well known cell-level electric and thermal models, this thesis proposes a methodology for the extrapolation of both models to the module-level. A methodology has been developed in order to guide the main research activities that were developed in the context of this thesis.

The designed methodology aimed to i) evaluate the different hypotheses raised in the introduction, ii) develop and implement a DT simulation platform to meet the main objectives related to battery modules and iii) address the main gaps identified during the SoA analysis.

The proposed methodology, illustrated in Figure 2.1, is composed by five main stages:

Stage 0: Electric and Thermal Model Parameter Identification.

Stage 1: Cell-level Models Development and Validation.

Stage 2: Built Module Prototype.

Stage 3: Extrapolation of Cell-level Models to Module-level Models.

Stage 4: Design and Development of the Cloud Architecture.

Stage 0 is needed to determine the required parameters to develop the electric and thermal models both at cell and module-level. These models form an integral part of the subsequent stages of the methodology. In Stage 1, models are developed and validated at the cell-level against static tests and then against dynamic and realistic profiles. Stage 2 entails the definition and building of a prototype battery module, which is then used to perform the tests at module-level. Steps 3 and 4 are the core of the proposed design methodology, evaluating the technical feasibility of the project. In these two stages, the module-level models are developed, validated and deployed on the Cloud platform. At the end of this methodology, all the hypotheses presented in the introduction of this thesis are verified or refuted.

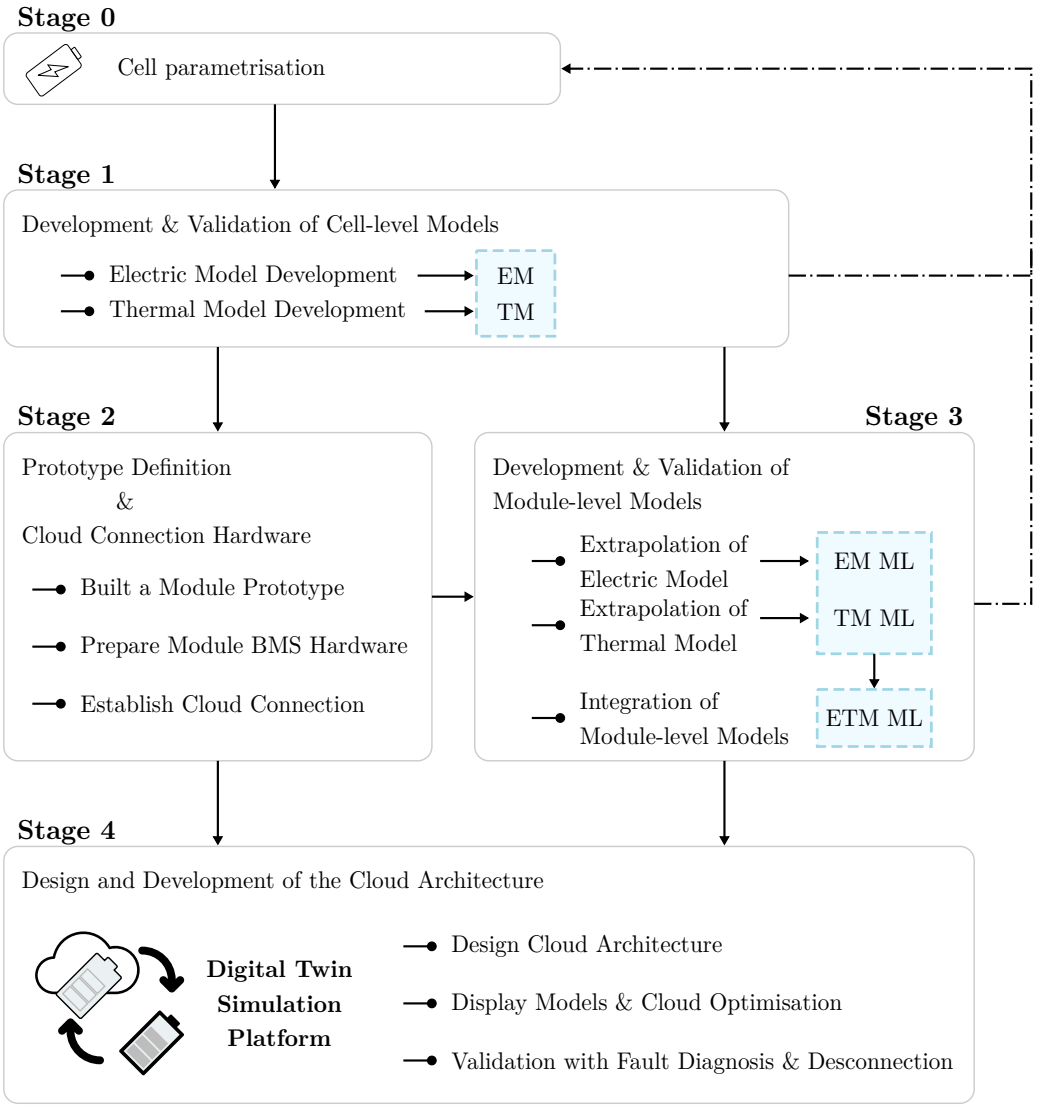

Figure 2.1: Methodology designed for the Development and Validation of a DTSP of LIBs. The solid lines represent the sequential execution process, the dashed lines represent the possibility to need to repeat a part of the process.

2.2 Stage 0: Electric and Thermal Model Parameter Identification

In the context of developing electric and thermal models for LIBs at both cell and module-levels, Stage 0 aims to identify the necessary parameters for creating such algorithms. The identification of those parameters is crucial for the accuracy and reliability of the entire simulation platform in the Cloud.

The parameters in an electric model of a LIB represent key characteristics, such as internal resistance, capacity, and open OCV, which simplify its electrical behavior. On the other hand, in thermal models, the parameters reflect properties related to the thermal response of the battery. The parameters may be identified by performing a characterisation over a wide range of operating conditions of the target cells.

The objective of the stage is to obtain the parameters needed to create the battery models, which involves specific tests under a wide range of operating conditions, such as different temperatures, SoC and discharge rates (C-rates). These parameters are carefully deviased from the tests. The parameters obtained are be introduced then in the selected models as fickle variables that depend on the battery SoX and temperature. Once the parameters are introduced into the models, the data from sensors is observed and checked to determine if the models consistently produce similar outputs. If they do not meet the desired requirements or do not adequately describe the electrical and thermal behaviour of the battery, the parameters adjustment must be repeated until the results are accurate and adequately match the desired characteristics. This is linked to Stage 1, where the cell-level models that utilize these parameters obtained in Stage 0 will be validated.

2.3 Stage 1: Cell-level Models Development and Validation

The stage 1 covers the development of the algorithms at the cell level. These algorithms are composed of an electrical model embeded in a SoC estimator and a thermal model. Cell-level models will be developed and validated to understand and examine the behavior and interactions of essential system characteristics. These models will be the basis for the development of more complex models at the module level. Studying cell-level behaviour, valuable knowledge and understanding will be gained for future application to battery modules.

This first stage in its entirety is focused on achieving the first objective (O1) established in this thesis. A more detailed description of this first stage of the methodology can be found in Figure 2.2.

O1: Develop and validate cell-level models to understand the behaviour and interactions of basic system characteristics, in order to use them as a basis for extrapolation to more advanced module-level models.

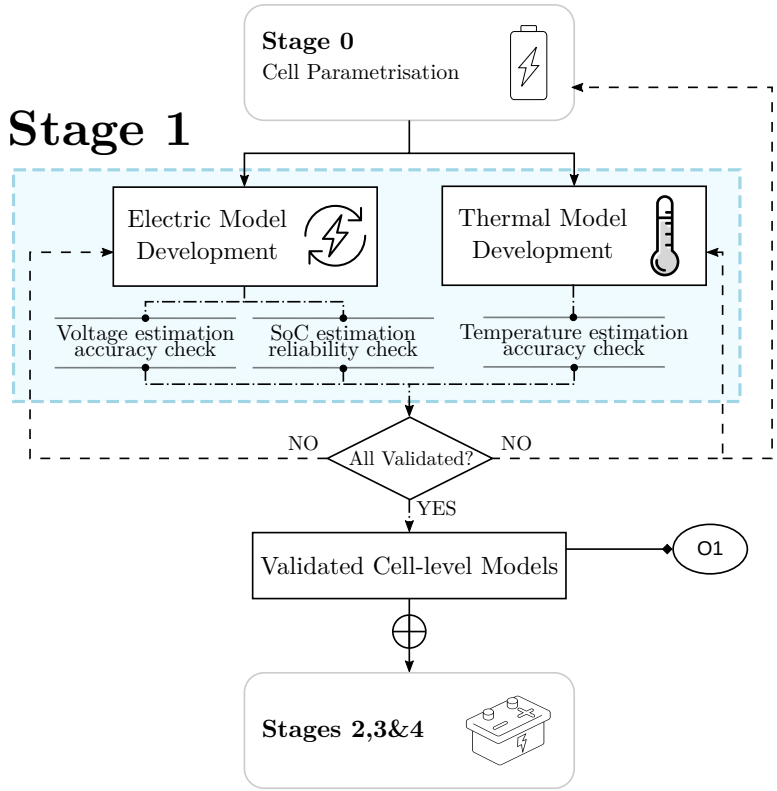

Figure 2.2: Detailed procedure of the Stage 1 of the designed methodology. The solid lines represent the sequential execution process, the dashed lines represent the possibility to need to repeat a part of the process.

More specifically, this stage focuses on the coding of the two aforementioned models and the SoC estimator. For this purpose, an electrical model will be developed to calculate the voltage at the cell terminals. This voltage will be used as input to the SoC estimator of the cell, which is the reason why the greatest accuracy of the model will be required . Once the electrical model is considered accurate, the reliability of the SoC estimator will be tested.

On the other hand, a thermal model of the cell will also be developed in order to estimate the temperature distribution in the cell. When evaluating the effectiveness of this model, the accuracy of the temperature estimation at different points of the cell will be sought.

These algorithms describing the cell must be rigorously selected. To this end, a comprehensive state-of-the-art review of thermal models, electrical models and SoC estimators has been performed in Chapter 1. From this review of the SoA, it has been concluded that the LTM is the type of model that best fits within the framework of this thesis. This model will be further discussed in Chapter 3 in section 3.3.

For the cell electric model, integration of two algorithms is proposed: an ECM to estimate the voltage and a SPKF to correct the SoC of the cell. This model will be deeper analysed in Chapter 3 in Section 3.4 and the estimator in Section 3.5.

These models must be verified against laboratory tests. This step is essential as these models will be the baseline for future phases of the methodology followed in this PhD. At the end of this stage of the methodology, objective 1 (O1) of this thesis will have been met which involves the development and validation of the electrical and thermal models of the selected cell. Furthermore, in this stage the research advances have been published in two conferences, as well as in a journal article in a high impact journal.

2.4 Stage 2: Built Module Hardware

Stage 2 of the proposed methodology addresses the physical implementation of the thesis. This stage, includes the assembly of a physical prototype of a battery module in relation to fulfilling objective 8 of the thesis. On the other hand, the configuration of this module to connect it with the Cloud must also be done in relation to objective 7. The purpose of the prototype module is to have a testing and data collection system, which will be used later to validate the complete system. To this end, a series of steps have been followed in this stage summarised in Figure 2.3.

The prototype assembly begins by defining the fundamental characteristics of a LIB module. These characteristics focus on the configuration and geometry of the module, which will have a direct impact on the design of the module-level models. Also, location points for current, voltage and temperature sensors must be carefully selected. These sensors will play a crucial role in acquiring the data necessary for model development and validation. This aforementioned process is further detailed in Chapter 4 in Section 4.2.

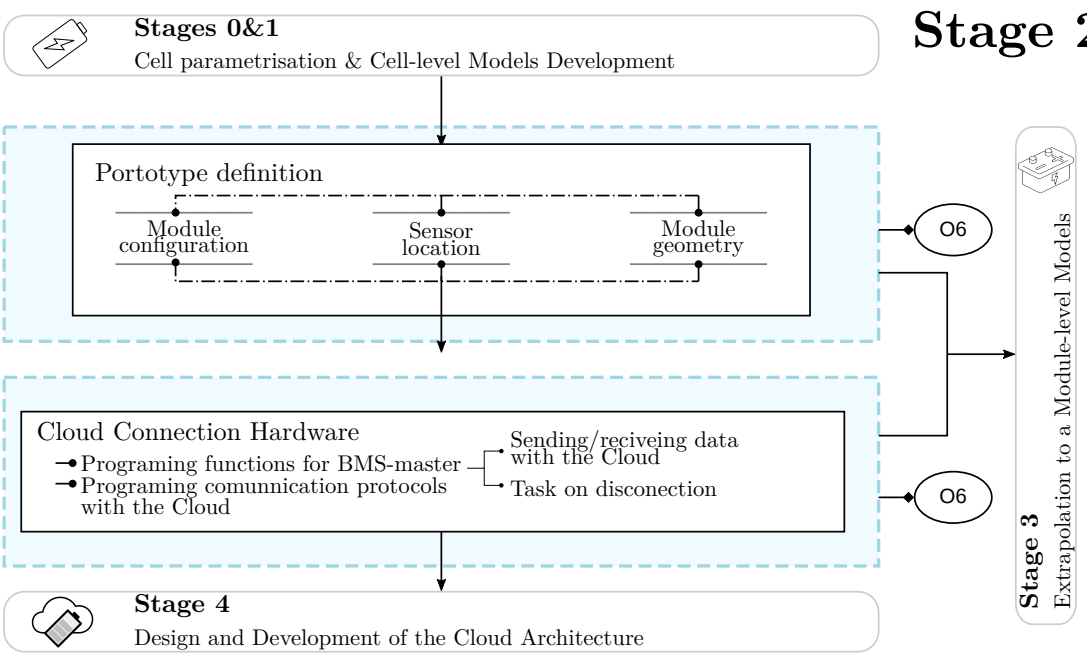

Figure 2.3: Detailed procedure of the Stage 2 of the designed methodology.

Once the prototype has been obtained, it will be idem to establish the connection with the Cloud platform under development. This involves setting the BMS-master tasks, which will be responsible for communicating with the platform via the Internet. These tasks must be programmed following the necessary protocols required by the IoT Gateway, to ensure the correct sending and receiving of data to the Cloud. In addition, extra tasks will be configured for the BMS-master to accomplish in case the connection to the Cloud is lost..

After finishing this stage in the methodology, objective 6 of this thesis will have been accomplished. The former (*O6*) involves building a prototype that will be used for testing in stages 3 and 4 setting up connections between the BMS and the Cloud.

> *O6:* Develop and assemble a functional prototype, establish and optimize necessary connections and communication channels, and configure the Cloud platform to enable seamless transmission and reception of real-time data from the prototype.

2.5 Stage 3: Extrapolation of Cell-level Models to Module-level Models

Stage 3 of the proposed methodology is the core part of this thesis, as it is where the major contribution is made in terms of progress and significant contributions. In this stage, the parameters obtained in Stage 0 and the models developed in stage 1 will be used as a starting point to propose models at module level. The goal is to develop and validate the module level extrapolated models (*O2*), which will play a fundamental role in answering the first hypothesis raised in the thesis (**H1**). Consequently, this step plays a crucial role in the methodology and contributes significantly to obtaining reliable results. A detailed overview of the state 3 procedure is provided in Figure 2.4.

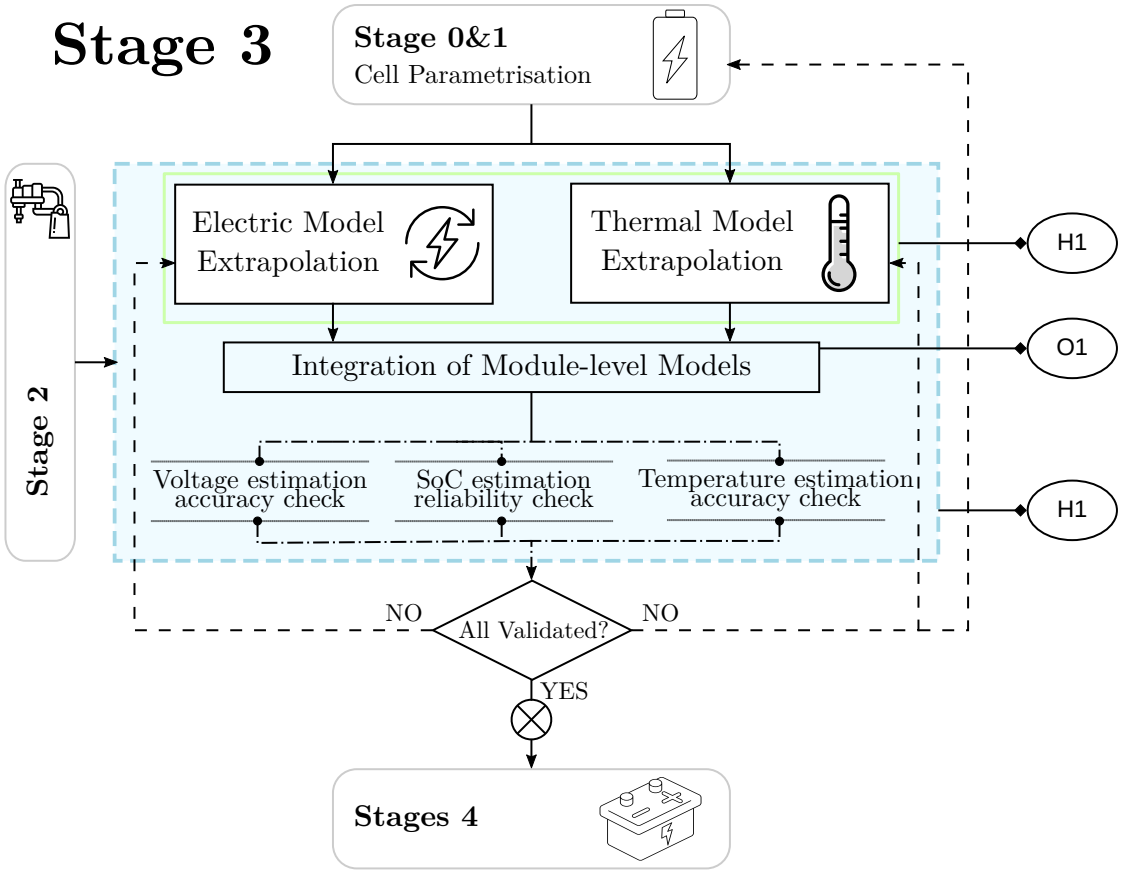

Figure 2.4: Detailed procedure of the Stage 1 of the designed methodology. The solid lines represent the sequential execution process, the dashed lines represent the possibility to need to repeat a part of the process.

The cell-level models developed and validated in Stage 1 serve as the foundation of Stage 3. In this stage, the objective is to extend the individual cell models to a module-level scale. As mentioned earlier, the module-level models will focus on analyzing each cell of the prototype constructed in Stage 2 separately. These models should be capable

of estimating, detecting, and quantifying the interactions between different variables that impact the current state of the cells of the module. Neglecting them may result in less accurate model predictions and potentially lead to incorrect conclusions.

To adapt the cell-to-module models, a separate extrapolation approach is proposed. The electrical cell model developed in Stage 2 will be implemented individually for each cell, taking into account the specific states of each cell to determine the appropriate parameters for each calculation. To improve computational efficiency, the module's electrical model will execute the cell models in parallel using a multiprocess approach, allowing for faster calculations across all cells instead of a sequential process.

Concerning the thermal model, it is necessary to consider the interaction between the cells. Therefore, it is proposed to adapt the cell model to a module model describing each cell individually. In order to achieve this, the thermal model of the cell developed in step 1 will be utilised. One of these models will be placed at the corresponding position for each cell in the prototype created during Stage 2, taking into consideration its specific geometry. Adjacent nodes will be connected to form a single mesh equivalent circuit describing all cells and their interactions in terms of heat transfer. It is important to note that increasing the number of cells in the module will require more computational power, as the number of equations to be solved will also increase.

Stage 3 focuses on the adaptation of the cell models developed in Stage 1 to be applicable at the module level, considering the specific characteristics of the assembled prototype from Stage 2. This adaptation is crucial for accomplishing the second objective (*O2*) of this PhD project, which involves the development of module-level models. These models serve as the foundation for the subsequent implementation of the DTSP in Stage 4, utilizing Cloud technologies.

> *O2:* Develop and validate module-level models to understand and predict the behaviour of the overall system and the interactions of multiple cells in the module, using the models developed in the previous objective as a basis.

At the end of stage 3, a partial evaluation of the **H1** hypothesis related to the models at the module-level of lithium-ion batteries will be performed. This assessment will be completed and corroborated at the end of step 4 of the methodology. In addition, it is planned to disseminate the results obtained through the development of these models at module level through the publication of a scientific article in a high impact journal.

> **H1:** Models of modules that consider individual cells provide relevant additional information to that obtained by module sensors.

2.6 Stage 4: Design and Development of the Cloud Architecture

In the initial stages of this methodology, models were created and evaluated at the cell and module level. In addition, a module prototype was built consisting of interconnected battery cells. This enabled the configuration of the necessary hardware to monitor battery state and establish connections to the Cloud platform. In the fourth and final stage, the required services will be selected and the Cloud architecture will be developed, where all the algorithms developed in the previous stages will be implemented. This stage aims to address the hypothesis **H2** and **H3** , to achieve this, the objectives *O3*, *O4* and *O5* are addressed. The fourth stage of this work is shown in Figure 2.5.

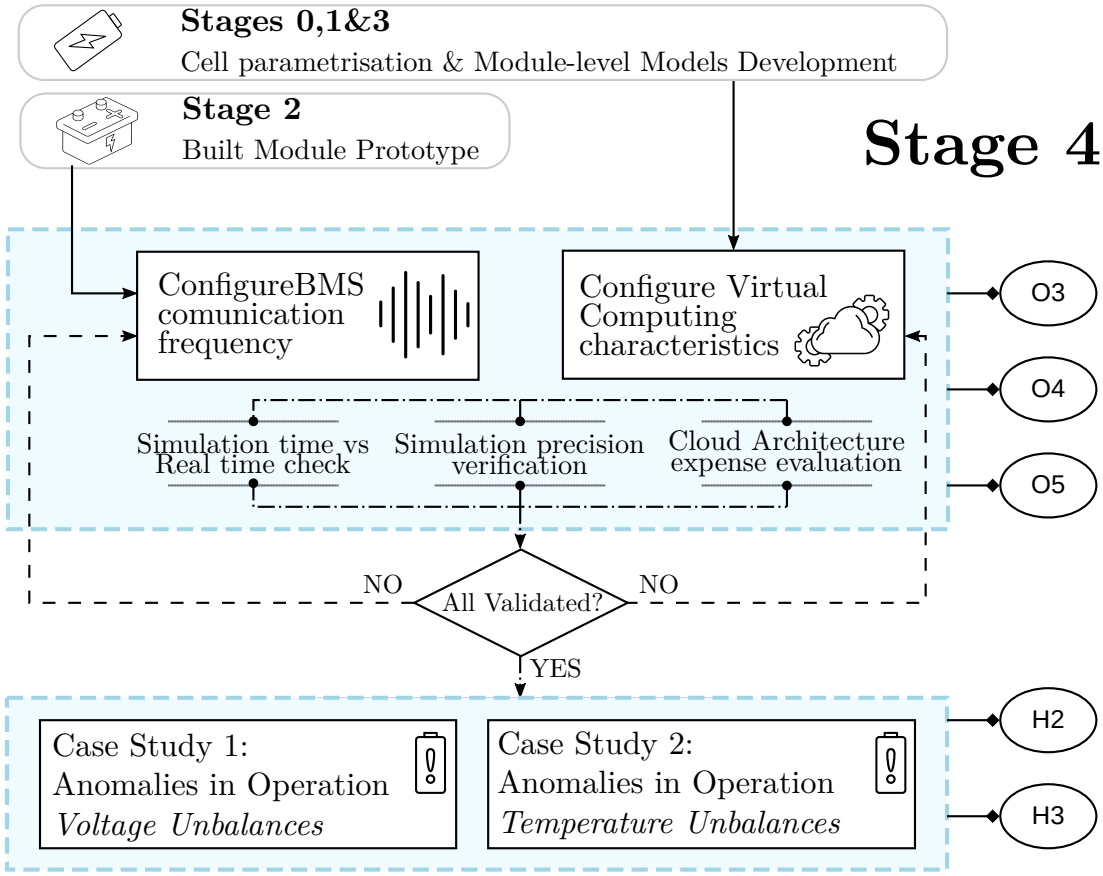

Figure 2.5: Detailed procedure of the Stage 1 of the designed methodology. The solid lines represent the sequential execution process, the dashed lines represent the possibility to need to repeat a part of the process.

At the begining of Stage 4, an analysis and selection of the Cloud services provider will be carried out in order to create a simulation platform and deploy the models at module level. The services offered by the provider will be studied and the necessary services will be chosen. In addition, connections between the services will be configured, if necessary.

In this process, several objectives are pursued. Objective 3 (*O3*) focuses on creating a secure and scalable Cloud architecture that enables the efficient implementation and execution of the algorithms. Objective 4 (*O4*) focuses on properly selecting the resources of the contracted Cloud services. Finally, objective 5 (*O5*) seeks to develop a visualisation platform to present the results obtained.

> *O3:* Develop a secure and scalable Cloud architecture that enables efficient deployment and execution of models, ensuring proper integration with all the services and resources comprising the system.
>
> *O4:* Optimise compute and memory resources in the Cloud platform to improve system performance and efficiency, including appropriate selection of virtual machine instance and type and constant monitoring of performance and analysis of the obtained data.
>
> *O5:* Create an easy-to-use, real-time visualisation tool of module and cell status, using estimated SoX data, that allows users to monitor system performance, identify problems in a timely manner, and view historical operation data for further analysis and optimisation.

Furthermore, step 4 is crucial for the evaluation of hypotheses H2 and H3. In order to evaluate the hypotheses made, two case studies will be carried out. In the first case study, an anomaly in temperature will be introduced in the prototype module, while in the second case, the prototype will be unbalanced. These case studies will allow to analyse the behaviour of the system in anomalous situations and to evaluate the robustness of the simulation platform in different scenarios. Hypothesis H2 aims to verify the potential benefits of deploying these algorithms using Cloud-based technology. It involves assessing whether the proposed architecture is able to support the processing and storage of data generated by the battery module and the estimation algorithms. Furthermore, assess whether it offers adequate scalability and flexibility to adapt to the needs of the system. Hypothesis H3, on the other hand, refers to the ability of the simulation platform and its algorithms to detect faults or anomalies in the behaviour of the battery module, and can be evaluated through the proposed tests of imbalance in the cell states (in terms of temperature and voltage).

> **H2:** Cloud Computing technologies may offer the computational power and memory required to the deployment of module-level models, which allows additional services to be offered compared to local environments.
>
> **H3:** The implementation of the most advanced algorithms in the Cloud could allow to detect anomalies and battery failures more efficiently and faster, which will lead to the mitigation of the computational load of the onboard BMS and improve system performance.

3

Cell-level Models

Summary

This Section presents the various cell-level models developed within the scope of this thesis, specifically focusing on the detailed description of the electrical and thermal models. Firstly, the cell used in this thesis is presented. Then, each of the model is further detailed by presenting the used equations. The electrical model is a ECM, while the thermal model is a LTM. Furthermore, the SPKF method employed for correcting the estimation of SoC estimation of the LIB is presented. In addition, the tests carried out to obtain the parameters that are used to make the models are presented. Finally, both models and the estimator are validated against laboratory tests.

3.1 Introduction

The goal of this Chapter is to develop module-level algorithms to estimate the thermoelectric aspects of the LIB module. To achieve this objective, this Chapter focuses on developing the cell-level baseline models, which will serve as the background for extrapolation in later Chapters at the module level.

This Chapter begins by presenting the selected cell and its relevant characteristics for this work. Then, the mathematical and technical fundamentals of each model selected after the SoA review are described, as well as the SoC estimator used in this thesis. Next, the necessary tests to obtain the electrical and thermal parameters of the models are detailed, following Stage 0 of the proposed methodology. The procedure for each test is described in detail and the parameters obtained are presented. These parameters are introduced in the model and their adequacy is evaluated (Stage 1 of the proposed methodology). In case of unsatisfactory results, the Stage 0 tests are repeated until the desired objectives are reached.

This Chapter is structured as follows: In Section 3.2, the cell selected for the experimental validation is presented. The thermal model is presented in Section 3.3, while the electrical model is discussed in Section 3.4. The use of the SPKF filter to support the electrical model and correct the SoC estimation of the cell is presented in Section 3.5. Laboratory tests conducted to obtain the necessary parameters for the ECM and LTM models are described in Section 3.6. The validation of these models through static and dynamic tests conducted in the laboratory is addressed in Section 3.7. Finally, Section 3.8 provides a summary of the Chapter and highlights the main conclusions derived from this research.

3.2 Cell selection

Along the whole thesis, cylindrical 2.5 Ah LFP cells from the manufacturer LithiumWerks (LW) have been used, specifically the model ANR26650m1B [199]. The main characteristics of the selected cells are presented in Table 3.1, and the cell is shown in Figure 3.1.

Due to their LFP chemistry, similar to the cells used by the company Cegasa Energia, the ANR26650m1B cells from LW were chosen. In addition, their small capacity enables tests to be carried out with contained laboratory resources, which has been a determining factor in their choice.

LithiumWerks ANR26650m1B	
Chemistry	LFP
V_{nom}	3.3 V
Q_{nom}	2.5 Ah
Max. Cha CC Current	10 A (4C)
Max. Dch CC Current	50 A (20C)
Temperature Range	0 to 55 °C
Diameter	26 mm
Length	65 mm
Cell mass	0.076 kg

Table 3.1: Cell main Characteristics.

Figure 3.1: Cell Image.

3.3 Cell-level Thermal Model: Lumped Thermal Model

This Section describes in detail the LTM developed in the framework of this thesis, specifically, the LTM at the cell-level. After a thorough review of the SoA, two types of thermal models have been identified as the most commonly employed in the battery field: CFD-based models and LTM based on equivalent electrical circuits. A LTM has been chosen due to its simplicity and ease of development. The parameters can be obtained easily, and it provides the option to work in real-time.

Thermal models estimate cell temperature by considering various thermal processes during operation and rest. They use input current and temperature to estimate the heat gradient in the battery cell and heat transfer to the cell's surrounding. LTMs employ electrical circuits of different complexity to calculate the temperature distribution in LIB cells. These circuits simulate heat accumulation and transfer using capacitors, resistors, and a current source. The models assume uniform temperatures within the cell and constant ambient temperature during simulation. This allows to make simplifications of CFD based models. The model simplifies heat transfer in 1D model as it is illustrated in Figure 3.2a. Then, it is implemented in the three axes to observe the temperature at different points within the cell, illustrated in Figure 3.2b.

In Figure 3.2b, the capacity Cp describes the thermal inertia of the cell. The voltage source symbolises the heat generation of the cell. The various thermal resistances represent the diffusion of heat in different directions from the cell core to various surfaces, as well as along those surfaces. In this study, two primary directions of heat transfer have been taken into account. The first is the axial direction, which refers to heat transfer along the main axis or length of the cell, both upwards and downwards. The second is the radial direction, which involves heat transfer from the center of the cell towards the periphery, across the cell's radius. Since a cooling system is not utilised in this study, it is important to account for heat diffusion through radiation as well.

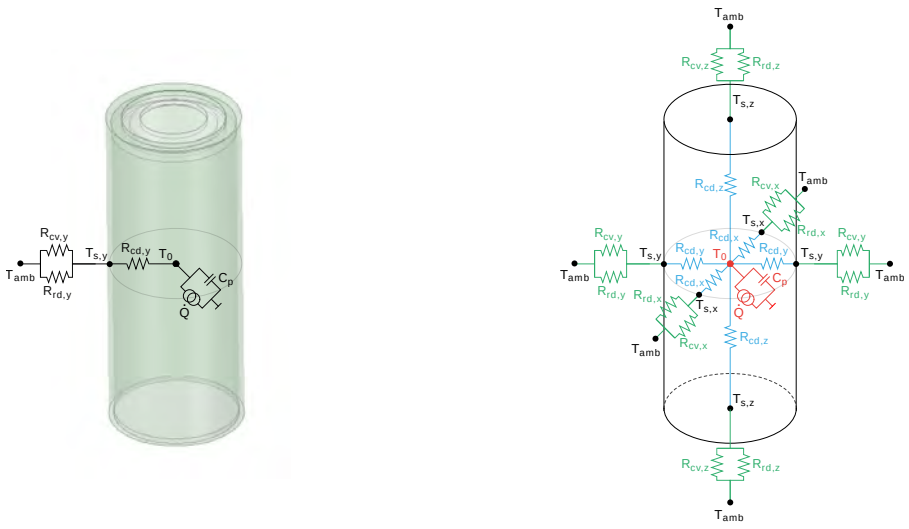

(a) **(b)**

Figure 3.2: LTM a) simplified 1D model and b) complete 3D model.

When calculating the different types of thermal resistances, namely conductive, convective, and radiative, specific parameters are considered. The thermal conductivity (k) is directly related to the material of the cell and represents its resistance to heat flow. The convective coefficient (h) depends on the properties of the fluid surrounding the cell, in this case, the air inside the module, which facilitates natural convection. Lastly, the thermal emissivity (ϵ) is influenced by the characteristics of the two surfaces involved in radiation and is affected by their relative geometric configuration.

The output of the model is based on an energy balance for which temperature optimisation is required. In order to optimise the temperature distribution within the cell during operation, the model solves a set of equations using initial approximations based on the principles of thermodynamics. The equations employed are based on the approach proposed by Bernardi et al. [200]. However, in this study, a simplified version of the equation presented by Bernardi et al. is utilised, focusing specifically on the processes of heat generation, heat storage capacity, heat transfer, and heat dissipation. The optimised equations used in this study are described in detail in the following 3.1 and 3.2 equations.

$$\dot{Q}_{accu} = \dot{Q}_{gen} - \sum \dot{Q}_{cond,i} \tag{3.1}$$

$$\dot{Q}_{cond,i} = \dot{Q}_{conv,i} + \dot{Q}_{rad,i} \tag{3.2}$$

The heat generation of each cell ($\dot{Q}_{gen}$) is calculated, assuming heat generation occurs at the center of the cell. Additionally, the accumulated heat ($\dot{Q}_{accu}$) is computed, taking into account the estimated temperature from the previous step and the thermal dynamics of the cell. Furthermore, the heat transferred through conduction ($\dot{Q}_{cd,i}$) from the center

of the cell to all its surfaces is calculated in all three dimensions. In this study, the analysis considers the main axes of the cell, including the upward, downward, and radial directions. The perimeter of the cell surface is divided into four points for radial heat transfer as depicted in 3.2b. Each transferred heat quantity to the cell surfaces is then dissipated to the surrounding environment. This dissipation occurs through convection ($\dot{Q}_{cv,i}$) and radiation ($\dot{Q}_{rd,i}$) processes. Convection refers to the heat transfer to the air surrounding and within the module. Radiation, on the other hand, involves the heat exchange with neighboring cells. In the upcoming, each of these equations will be examined individually,

Heat Generation

The temperature distribution within the cells depends on the amount of heat generated per unit volume in the module, and how this heat is transferred in and out of it. The heat generation ($\dot{Q}_{gen}$) can be divided into reversible and irreversible heat. The transfer of electric charges creates irreversible thermal energy loses, and the electro-chemical reactions generate reversible heat. The reversible entropic heat reflects the change in lithium ions on the electrodes and can be endothermic or exothermic depending on the SoC during the charging or discharging process, and the rest of heat generation is irreversible. These irreversible processes are usually simplified only into heat generated by Joule losses. It is worth mentioning that within the scope of this thesis the thermal behaviour is assumed uniform throughout the cell in a lumped approach and thermal diffusion or local effects are neglected. A simplified form of the approach proposed by Bernardi et al. [200] has been proposed in [201–203] and it is used in this thesis to describe the heat generation sources.

$$\dot{Q}_{gen} = \dot{Q}_{rev} + \dot{Q}_{irev} \tag{3.3}$$

$$\dot{Q}_{gen} = (v - U^{avg}) + i \cdot T \cdot \frac{dU^{avg}}{dT} = i^2 \cdot R_{int} + i \cdot T \cdot EHC \tag{3.4}$$

where, i is the current through the cell in Amperes; v is the terminal voltage of the cell in Volts; U^{avg} is the average OCV in Volts; T is the temperature of the cell in Kelvin and $\frac{dU^{avg}}{dT}$ is the Entropic Heat Coefficient (EHC) in (V/K). The term that corresponds to R_{int} represents the power dissipated due to the internal resistance of the cell when current flows through the cell. The EHC must be pre-calculated in the laboratory as well as the Internal Resistance (R_{int}) (Section 3.6). Note that the EHC depends on the current SoC-level, whereas R_{int} depends on both SoC and T.

Heat Accumulation

The variable $\dot{Q}_{accu}$ denotes the magnitude of the thermal power contained in the cell at each time interval (accumulated heat). Its sign indicates the variations of the cell temperature, both in increments and decrements. The accumulated heat is calculated by equation 3.5:

$$\dot{Q}_{accu} = m \cdot c_p \cdot \frac{\Delta T}{\Delta t} \tag{3.5}$$

where, m is the mass of the cell in $[kg]$, c_p is the specific heat of the cell in $[\frac{J}{kg \cdot K}]$, and ΔT is the temperature difference in [K] during the Δt time interval in [s] between time step n and the previous time step $(n-1)$.

Heat Transfer by Conduction

Heat generated by the battery and not accumulated flows through the cell materials via conduction. Conduction is the transfer of heat through a material medium by direct contact between particles due to the existence of a temperature gradient. The amount of heat transferred by conduction is given by Fourier's law. The resulting heat flow due to thermal conduction ($\dot{Q}_{cond}$) in the materials is a function of the location in the cell.

$$\dot{Q}_{cond} = k_x A_x \frac{\Delta T}{\Delta x} + k_y A_y \frac{\Delta T}{\Delta y} + k_z A_z \frac{\Delta T}{\Delta z} \tag{3.6}$$

where, $k = k(x, y, z)$ is the coefficient of thermal conduction expressed in $[\frac{W}{m \cdot k}]$, describing a specific property of each material used to characterise the heat transport at stationary rate, A is the area through which heat flows perpendicularly at a stationary rate expressed in $[m^2]$, and $\frac{\Delta T}{\Delta x}$ is the temperature gradient in $[K]$ in x direction. This expression can be simplified if there is a principal heat diffusion pathway, neglecting the heat losses in the other directions. However, in this thesis all directions of the main axes will be considered (x, y, z).

Heat Transfer by Convection

Convection is the resulting process of the thermal energy exchange when a fluid is in contact with a solid surface at a different temperature. The cooling of the LIB is accomplished by the removal of heat through the surrounding fluid. This process of heat removal by convection ($\dot{Q}_{conv}$) can occur naturally or by forced convection. The first is generated by the difference in density inside the fluid. In the second case an external driving force moves a fluid on a surface removing the heat in a more efficient way. In this case, convection with the cell is a natural process. The amount of heat transferred by convection is given by Newton's law of cooling, as expressed in equation 3.7.

$$\dot{Q}_{conv} = h_i A_i \Delta T \tag{3.7}$$

where, h is the heat transfer coefficient of thermal convection expressed in $[\frac{W}{m^2 \cdot K}]$. It describes a specific property of the fluid flow for heat transfer depending on factors such as natural or forced convection, location, geometry, surface roughness, and the medium surrounding the battery. The coefficient is also influenced by properties of the fluid,

including density, viscosity, and speed. A represents the surface area in contact with the fluid and is expressed in $[m^2]$. ΔT refers to the temperature difference between the surface of the solid (battery) and the fluid, expressed in $[K]$.

Heat Transfer by Radiation

Heat transfer by radiation is the transfer of thermal energy in the form of electromagnetic waves. Every solid body transmits energy through the radiation phenomenon from its surface, and this heat depends directly on the average temperature of the whole body and the nature of its surface. The rate of heat transfer by radiation ($\dot{Q}_{rad}$) between two grey bodies is calculated by applying Stefan-Boltzmann's law. In this case, the LIB cells are considered grey bodies.

$$\dot{Q}_{rad} = \varepsilon \sigma A({T_s}^4 - {T_e}^4) \tag{3.8}$$

where, ε is the surface emissivity of the considered specific material, being a dimensionless number (with a value between 0 and 1) and related the ability of a body to radiate thermal heat, σ term is the Stefan-Boltzmann constant equivalent to $5.67 \cdot 10^{-8}$ $[\frac{W}{m^2 \cdot K^4}]$, A is the surface area of the body expressed in $[m^2]$; and T_s and T_e are the surface temperatures of the two contiguous bodies that transfer heat by radiation between them expressed in $[K]$.

The resulting thermal potential of the cell is the sum of all the heat processes occurring in and out of it it (generation, accumulation, and dissipation). The heat balance equation to calculate the evolution of the temperature, considering a uniform temperature of the batteries, can be defined as:

$$m \cdot c_p \cdot \frac{\Delta T}{\Delta t} = i^2 \cdot R_{int} + i \cdot T \cdot EHC - \sum k_i A_i \frac{\Delta T}{\Delta i} \tag{3.9}$$

$$k_i A_i \frac{\Delta T}{\Delta i} = h_i A_i \Delta T + \varepsilon \sigma A({T_s}^4 - {T_e}^4) \tag{3.10}$$

The LTM model provides an initial estimate of the seven temperatures of each cell, with respect to the inlet current of the cell, depending on the soc and the temperature of the cell itself at the previous instant $(n-1)$. These temperatures are then optimised to find the thermodynamic energy balance defined in equations 3.9 and 3.10.

The model optimises the temperature distribution inside the cell by considering the heat transfer factors by means of the Newton-Raphson (NR) method. This iterative process refines the initial temperature approximations until the desired accuracy is achieved. The absence of a cooling system forces the consideration of heat dissipation by natural convection and radiation, resulting in a non-linear system. The NR method iteratively solves the system by updating the temperature approximations at different points in the cell.

The NR follows the following steps:

1. An initial approximation of the roots (z_0) is made, in this case temperatures.

$$z^0 = \begin{bmatrix} T_0, & T_1, & T_2, & T_3, & T_4, & T_5, & T_6 \end{bmatrix}^T \tag{3.11}$$

2. Calculate the values of the function matrix (f_z) with the initial approximations, in this case, equation 3.9 and equation 3.10 are applied on each surface of the cell.

$$f_{z^0} = \begin{bmatrix} f_0, & f_1, & f_2, & f_3, & f_4, & f_5, & f_6 \end{bmatrix}^T \tag{3.12}$$

3. Obtain the Jacobian matrix of the f_z matrix.

$$J_f(z_0) = \begin{bmatrix} \frac{\partial f_0}{\partial z_0} & \frac{\partial f_0}{\partial z_1} & \cdots & \frac{\partial f_0}{\partial z_n} \\ \frac{\partial f_1}{\partial z_0} & \frac{\partial f_1}{\partial z_1} & \cdots & \frac{\partial f_1}{\partial z_n} \\ \vdots & \vdots & \ddots & \vdots \\ \frac{\partial f_m}{\partial z_0} & \frac{\partial f_m}{\partial z_1} & \cdots & \frac{\partial f_m}{\partial z_n} \end{bmatrix} \tag{3.13}$$

4. Apply Gaussian elimination to obtain a new temperatures approximation by (3.11).

$$z^1 = z^0 + \Delta x^0 = J_f(z_0)^{-1} \cdot f_{z^0} \tag{3.14}$$

5. Repeat steps 2-4 until the determined error tolerance is reached.

This model will be validated by applying the obtained parameters described in Section 3.6. The corresponding results are presented in Section 3.7.1.

3.4 Cell-level Electric Model: Equivalent Circuit Model

The electrical model to be implemented in the DTSP is an ECM. Based on the literature review conducted in Chapter 1, it has been established that the use of an ECM is the most suitable option with the requirements of this thesis. The ECM offers several advantages. It accurately represents battery behavior, it can be adapted to various battery types, is computationally efficient, easy to understand as it uses familiar electrical components, and can be easily validated through experiments in the laboratory. This ECM represents the battery by means of an electrical circuit as an analogue to the behaviour of the cell. It uses data from laboratory tests and tuned parameters to estimate the terminal voltage of the cell. Their-level of complexity usually depends on the number of included

RC pairs. In this work, an ECM with three RC phases is chosen, in addition to an element to model the battery hysteresis. Three RC phases have been introduced into the electric ECM cell model to capture the cell's dynamics, as it was required for validation purposes. The model schematic implementation is shown in Figure 3.3.

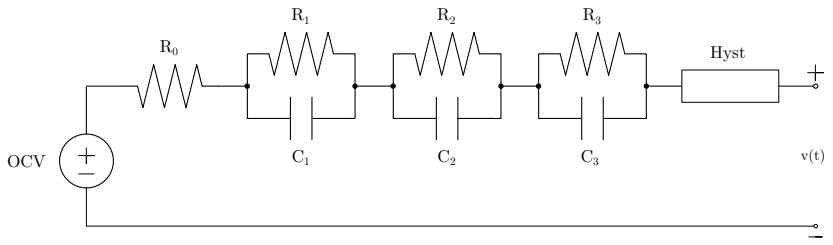

Figure 3.3: ECM at cell-level to be implemented in the DTSP.

In the model, the constants OCV, R_0, R_1, C_1, R_2, C_2, R_3, and C_3, are the parameters obtained from laboratory tests that are chosen by interpolation processes generally according to the SoC and the temperature of the cell (Section 3.6). In addition, the element "hyst" encompasses additional parameters related to hysteresis, which will be further explained in the section covering the acquisition of these parameters. These parameters are chosen at each time step to obtain the cell voltage calculation ($v(t)$) from the ECM model. The equations to calculate the cell voltage based on each ECM element will be detailed in the following.

The ECM electrical model captures the internal states of the cell, such as hysteresis state, which are related to the internal processes of the cell. These internal states influence the electrical behaviour of the cell, such as the voltage and response to current during charging and discharging. To address the influence of these internal states on the modelling and estimation of the SoC, the SPKF is used to correct and adjust these states based on the actual measurements obtained from the system. In this research work, the SPKF developed by [149, 150] will be employed, and its detailed description will be provided in Section 3.5. The model is based on state space equations, as this facilitates the integration with the SPKF. The SPKF, which will be discussed below in Section 3.5, plays a crucial role in the SoC estimation process. In the context of the SPKF, the augmented state vector refers to an extended state vector that includes in addition to the model states (such as diffusion currents or hysteresis), an additional variable state which is the SoC.

The SoC of the battery is defined as 100% when the cell is fully charged and 0% when the cell is fully discharged. It is used for energy and power calculations for example and gives an idea of how much energy is available at the moment. The SoC is a unit-less number and in this thesis is defined by the symbol z_n.

There are several ways to estimate this SoC as discussed in Section 1.3.3. In this thesis, the SoC state is updated by Coulomb Counting method, which estimates the SoC of the battery by the equation 3.15.

$$z(n+1) = z(n) + \frac{\eta(n)\Delta t}{Q} i(n) \tag{3.15}$$

where, Δt is the time interval, Q is the current cell capacity expressed in $[Ah]$, $\eta(n)$ is cell efficiency and $i(n)$ is the current through the cell at time n.

The augmented state vector of the ECM model is crucial to the output equation. The Kalman filter plays a key role in correcting and adjusting the states of the augmented vector using battery voltage measurements. Therefore, the mentioned states that are part of the ECM output equation will be defined. The *output equation* (3.16) is defined as:

$$v(n) = v_{OCV}(n) + v_{h_n}(n) - \sum i_{R_i}(n) - v_{R_0}(n) \tag{3.16}$$

where, $v(n)$ is the cell terminal voltage, v_{OCV} is the OCV in step n, v_{h_n} is the cell hysteresis in time n, $-\sum i_{R_i}$ is the sum of the voltage drops across the three RC phases of the model and v_{R_0} is the voltage drop in the internal resistance of the cell.

Subsequently, the individual components of the output equation in the ECM will be defined and analyzed.

Open Circuit voltage (OCV)

The voltage source of the model is called OCV and describes the voltage of the cell when no load is applied (in a relaxed state). The OCV values of a cell are determined empirically at many SoC points using the OCV vs SoC test. This element is usually a function of the SoC and the cell internal temperature (Section 3.6).

$$v_{OCV}(n) = OCV(n) \tag{3.17}$$

Internal Resistance (R_0)

The series resistance (R_0) represents the resistive voltage drop of the cell. This element is considered to be a function of the SoC and dependent on the temperature of the cell.

$$v_{R_0}(n) = R_0 \cdot i(n) \tag{3.18}$$

where, R_0 is the internal resistance of the cell and $i(n)$ is the current through the cell at time n.

R-C phases (R_i, C_i)

Polarisation refers to any deviation of the cell terminal voltage from the OCV due to the passage of current through the cell [204, 205]. This phenomenon is due to the

diffusion processes that exist in the lithium. This diffusion voltage is approximated by the RC phases in the ECM. The diffusion voltage of the cell is typically influenced by two key factors: the SoC of the cell and its internal temperature (Section 3.6).

The current trough each R_i and C_i are assumed to be equal, and the sum of these is the overall current through cell terminal $i(n)$. The current flow through each R_i is used to calculate the diffusion current of the cell. Then, the diffusion states ($i_{R_i}(n)$) are calculated with the equation 3.19.

$$i_{R_i}(n+1) = \exp\left(\frac{-\Delta t}{R_i C_i}\right) i_{R_i}(n) + \left(1 - \exp\left(\frac{-\Delta t}{R_i C_i}\right)\right) i(n) \tag{3.19}$$

where, Δt is the time interval between the current n and the previous $(n-1)$, R_i and C_i are the resistor and capacitor values in the ECM RC phases, $i_{R_i}(n)$ is the diffusion current through the R_i resistor at time n and $i(n)$ is the current through the cell at time n.

Hysteresis ("hyst")

The element labelled as "*hyst*" represents the hysteresis of the cell. This non-linear effect causes a difference between the relaxed state voltage and the OCV of the cell, which varies based on the direction and magnitude of the previously applied currents. The hysteresis effect is influenced by the recent history of cell use [206], and can lead to errors in estimating the battery state.

The hysteresis in the cell is represented as $v_{h_n}(n)$ which is calculated based on the hysteresis state $h(n)$. This hysteresis voltage includes cell hysteresis state (v_{h_n}) and instantaneous hysteresis ($v_{h_{n0}}$.) The hysteresis state is SoC-dependent and only changes when the cell's SoC changes, unlike the diffusion voltages which vary with time.

$$v_{h_n}(n) = v_{h_n} + v_{h_{n0}} \tag{3.20}$$

Hysteresis does not have the same value when charging or discharging the cell. In this thesis, an average value of hysteresis has been considered and applied for both charging and discharging processes of the cell. It depends on the SoC of the cell, then it depends on the current flow. The hysteresis is positive when the battery is charging and negative when is discharging. This hysteresis is observed in the OCV vs SoC curves that are obtained in the laboratory (Section 3.6). M is the value of the maximum positive and negative value of hysteresis at any given SoC. These hysteresis voltages will be used for calculating the cell terminal voltage, as explained before, by the use of the following equation:

$$h(n+1) = \exp\left(-\left|\frac{\eta(n) i(n) \gamma \Delta t}{Q}\right|\right) h(n) - \left(1 - \exp\left(-\left|\frac{\eta(n) i(n) \gamma \Delta t}{Q}\right|\right)\right) \operatorname{sgn}(i(n)) \tag{3.21}$$

where, $\eta(n)$ is cell efficiency, $i(n)$ is the current through the cell at time n, γ is a positive constant that refines the decay rate, Δt is the time interval between the current n and the previous $(n-1)$, Q is the current cell capacity, $h(n)$ is the hysteresis voltage and $sgn(i(n))$ forces the equation to be stable for both charging and discharging.

Therefore, the cell hysteresis voltage will be defined as $(M \cdot h(n))$. On the other hand, M_0 is the instantaneous hysteresis representing the instantaneous drop of the voltage at each SoC level, when the cell switches from charging to discharging or vice versa. The instantaneous drop of the hysteresis voltage is modelled by 3.22:

$$s(n) = \begin{cases} \text{sgn}(i(n)), & |i(n)| > 0 \\ s(n-1), & \text{otherwise} \end{cases} \tag{3.22}$$

The instantaneous hysteresis component changes immediately when the sign of input current changes. $s(n)$ is equal to ± 1 depending on the battery is charging or discharging. When the cell is in a rest condition, it maintains its previous value. Therefore, the cell instantaneous hysteresis voltage will be defined as $(M_0 \cdot s(n))$. Thus, the overall hysteresis voltage is calculated as follows:

$$v_{h_n}(n) = M \cdot h(n) + M_0 \cdot s(n) \tag{3.23}$$

Output Equation

The output equation of the model gathers all the phenomena described above, and it is defined as:

$$v(n) = OCV(n) + M_0 s(n) + Mh(n) - R_1 i_{R_1}(n) - R_2 i_{R_2}(n) - R_3 i_{R_3}(n) - R_0 i(n) \tag{3.24}$$

The above explanation covers the interpretation and the meaning of the individual states in the output equation of the ECM model. However, to obtain a complete picture of the model, it is important to highlight that these states are combined into a system of state space equations. It consists of a set of equations that represent the relationships between the state variables and the inputs of the system. These state space equations will be discussed in more detail in the next section.

3.5 Cell-level SoC Estimator: Sigma Point Kalman Filter

Battery state estimation is a challenging task that requires the use of a state estimator. In this thesis, the implementation of a SPKF estimator developed by Dr. Gregory L. Plett in [149, 150] is proposed. A SPKF is an algorithm designated to estimate the state of a dynamic system with noisy measurements. SPKFs to capture the non-linearities in the system dynamics and measurement functions [207, 208]. The filter combines information from voltage and current measurements with a mathematical model of the system (using Equation 3.24) to generate more accurate estimates of the SoC, considering both the measurements and their associated uncertainties. In this case, the dynamic state being estimated is the SoC of the battery cell. Additionally, the ECM model requires the estimation of other states for calculating the cell voltage, as discussed in Section 3.4. These states include the polarisation currents (i_{R_1}, i_{R_2}, and i_{R_3}) calculated in Equation 3.19 and the hysteresis state (h_n) calculated in Equation 3.21.

In the previous Section, the states used in the electrical model and the cell's SoC estimation method have been defined (augmented state vector). These will be expressed in a state space. The BMS takes discrete measurements that the SPKF can applied using discrete equations. The general expressions of a linear state space discrete system are shown in equations 3.25 and 3.26.

$$x_{n+1} = A_n x_n + B_n u_n + \mathrm{w}_n \tag{3.25}$$

$$\mathrm{y}_n = C_n x_n + D_n u_n + \mathrm{v}_n \tag{3.26}$$

In those equations, w_k represents disturbances or errors introduced by the sensors used to measure system variables. These errors may include electronic noise, calibration errors or any other factor affecting the accuracy of the measurements made. Meanwhile, v_n represents modelling errors, that is, deviations between the mathematical model used in the state space and the true dynamics of the system.

When dealing with nonlinear systems like LIB cells, the state space representation needs to be linearised to approximate the real system. The SPKF is used for this function. The objective of the SPKF is to improve the SoC estimation provided by the ECM by weighting both the predicted and estimated values. Thus, the linearised state space of the discrete system would be written as the equations 3.27 and 3.28.

$$x_{n+1} = f(x_n, u_n) + \mathrm{w}_n \tag{3.27}$$

$$\mathrm{y}_n = g(x_n, u_n) + \mathrm{v}_n \tag{3.28}$$

Equation 3.27 is used to calculate the estate vector, while equation 3.28 represents the output (models voltage equation 3.24). x_n represents the states of the battery at time n defined in equation 3.29. The dimension of this will depend on the number of states of

the system, in the case of this thesis five states of the cell are observed. u_n is a known input signal from the measurements (in the case of the cell the measured current), w_n is an unknown random noise input signal and v_n is an unknown input signal from the noise of the sensors. y_n is the system output, in the case of a cell the terminal voltage. The state vector, denoted by the symbol x_n, represents various dynamic effects taking place within the cell. It encompasses all above-mentioned states and is defined as:

$$x_n = \begin{bmatrix} z_n & i_{R1_n} & i_{R2_n} & i_{R3_n} & h_n \end{bmatrix}^T \tag{3.29}$$

The dynamics of the cell are considered in discrete time in order to compute it. In the implemented model, each time step defined is defined by the index n, while the used sampling rate (time difference between each step n) will be one second. Therefore, the ECM will update its state and output values with this time interval. At this point, the current state becomes the previous state ($n \rightarrow n-1$). For the application of the SPKF, the following assumption is made:

Sensor noises (w_n) and modelling errors (v_n) are considered as uncorrelated white Gaussian random processes. The value of the covariance matrix will be known ($\sum_w$ and $\sum_v$) and its mean will be zero.

To define the state space of the SPKF, the following definitions will be considered:

- The sub-circuit rate factor, denoted as RC, is defined as $A_{RC_i} = \exp\left(\frac{-\Delta t}{R_i C_i}\right)$.
- The hysteresis will be defined as $A_H = \exp\left(-\left|\frac{\eta(n) i(n) \gamma \Delta t}{Q}\right|\right)$.

So, the *state space* is defined as:

$$\begin{bmatrix} z(n+1) \\ i_{R_1}(n+1) \\ i_{R_2}(n+1) \\ i_{R_3}(n+1) \\ h(n+1) \end{bmatrix} = \begin{bmatrix} 1 & 0 & 0 & 0 & 0 \\ 0 & A_{RC_1} & 0 & 0 & 0 \\ 0 & 0 & A_{RC_2} & 0 & 0 \\ 0 & 0 & 0 & A_{RC_3} & 0 \\ 0 & 0 & 0 & 0 & A_H \end{bmatrix} \cdot \begin{bmatrix} z(n) \\ i_{R_1}(n) \\ i_{R_2}(n) \\ i_{R_3}(n) \\ h(n) \end{bmatrix} + \begin{bmatrix} -\frac{\eta(n)\Delta t}{Q} & 0 \\ -(1 - A_{RC_1}) & 0 \\ -(1 - A_{RC_2}) & 0 \\ -(1 - A_{RC_3}) & 0 \\ 0 & (A_H - 1) \end{bmatrix} \cdot \begin{bmatrix} i(n) \\ \mathrm{sgn}(i(n)) \end{bmatrix} \tag{3.30}$$

The SPKF is implemented in six fundamental steps, three steps for the estimation of the states (Step 1a,b&c) and another six steps for the correction of the output estimate (Step 2a,b&c). In the prediction step, the new state matrix is calculated based on the initial value (previous step, $n-1$). In addition, the uncertainty or covariance matrix is predicted according to the different noises in the system.

The update step refers to the current time step. In this step, the updates with the performed measurements (cell terminal voltage y_n) are taken into account. The Kalman gain is calculated and then it is decided which weights to give to each of the values. Finally, the new state matrix and the new covariance matrix are calculated based on L_n. These last two matrices will be the estimates made by the SPKF.

This estimator will be validated by applying the obtained parameters described in Section 3.6. The corresponding results are presented in Section 3.7.2.

The procedure followed by the SPKF is outlined below. Before presenting the overview of the relevant equations in the SPKF method, Table 3.2 shows all the nomenclature used in [149, 150].

Table 3.2: List of SPKF symbols

Symbol	
" $\widehat{}$ "	Predicted or Estimated Quantity
" $\sim$ "	Difference Between a True and Predicted or Estimated Quantity: $\tilde{x} = x - \hat{x}$
$()^-$	Prior Information: Predicted Quantity based only on Past Measurements
$()^+$	Posterior Information: Estimated Quantity based on both Past and Present Measurements
$()^a$	Augmented Matrix
x_n	Model State Vector
χ_n or Σ_n	Covariance Matrix
w_n	Process Noise
v_n	Sensor Noise
u_n	Input: Measured Cell Input Current
y_n	Output: Measured Cell Terminal Voltage
L_n	Kalman Gain Matrix

Defining:

$$x_n^a = \begin{bmatrix} x_n, & w_n, & v_{n+1} \end{bmatrix}^T \tag{3.31}$$

$$\chi_n^a = \begin{bmatrix} \chi_n^x & 0 & 0 \\ 0 & \chi_n^w & 0 \\ 0 & 0 & \chi_n^v \end{bmatrix} \tag{3.32}$$

$$p = 2 \cdot \dim(x_n^a) \tag{3.33}$$

Initialisation time ($n = 0$):

$$\hat{x}_0^+ = E[x_0] \tag{3.34}$$

$$\Sigma_{\tilde{x},0}^{a,+} = E[(x_0^a - \hat{x}_0^{a,+})(x_0^a - \hat{x}_0^{(a,+)})^T] = \text{diag}(\Sigma_{\tilde{x},0}^+, \Sigma w, \Sigma_v) \tag{3.35}$$

$$\Sigma_{\tilde{x},0}^+ = E[(x_0 - \hat{x}_0^+)(x_0 - \hat{x}_0^+)^T] \tag{3.36}$$

$$\hat{x}_0^{a,+} = E[x_0^a] = \begin{bmatrix} (\hat{x}_0^+)^T, & \bar{w}, & \bar{v} \end{bmatrix}^T \tag{3.37}$$

For $n = 1, 2, 3...$:

Step 1a: State-prediction time update.

$$\chi_{n-1}^{a,+} = \begin{Bmatrix} \hat{x}_{n-1}^{a,+}, & \hat{x}_{n-1}^{a,+} + \gamma\sqrt{\Sigma_{\tilde{x},n-1}^{a,+}}, & \hat{x}_{n-1}^{a,+} - \gamma\sqrt{\Sigma_{\tilde{x},n-1}^{a,+}} \end{Bmatrix} \tag{3.38}$$

$$\chi_{n,i}^{x,+} = f\begin{pmatrix} \chi_{n-1,i}^{x,+}, & u_{n-1}, & \chi_{n-1,i}^{w,+}, & n-1 \end{pmatrix} \tag{3.39}$$

$$\hat{x}_n^- = \Sigma_{i=1}^p \alpha_i^{(m)} \hat{x}_{n,i}^{x,-} \tag{3.40}$$

Step 1b: Error-covariance time update.

$$\Sigma_{\tilde{x},0}^+ = \Sigma_{i=1}^p \alpha_i^{(c)} (\chi_{n-1,i}^{x,-} - \hat{x}_n^+)(\chi_{n-1,i}^{x,-} - \hat{x}_n^+)^T \tag{3.41}$$

Step 1c: Output estimate.

$$Y_{n,i} = f\begin{pmatrix} \chi_{n,i}^{x,-}, & u_{n-1}, & \chi_{n-1,i}^{v,+}, & n \end{pmatrix} \tag{3.42}$$

$$\hat{\text{y}}_n = \Sigma_{i=0}^p \alpha_i^{(m)} Y_{n,i} \tag{3.43}$$

Step 2a: Estimator gain matrix.

$$\Sigma_{\tilde{\text{y}},n} = \Sigma_{i=0}^p \alpha_i^{(m)} (Y_{n,i} - \hat{\text{y}}_k)(Y_{n,i} - \hat{\text{y}}_n)^T \tag{3.44}$$

$$\Sigma^{-}_{\tilde{x}\tilde{y},n} = \Sigma^{p}_{i=0}\alpha^{(c)}_{i}(\chi^{-}_{n,i} - \hat{x}^{-}_{n})(\chi_{n,i} - \hat{y}_{n})^{T} \tag{3.45}$$

$$L_k = \frac{\Sigma^{-}_{\tilde{x}\tilde{y},n}}{\Sigma_{\tilde{y},n}} \tag{3.46}$$

Step 2b: State-estimate measurement update.

$$\hat{x}^{+}_{n} = \hat{x}^{-}_{n} + L_n(y_n - \hat{y}_n) \tag{3.47}$$

Step 2c: Error-covariance measurement update.

$$\Sigma^{+}_{\tilde{x},n} = \Sigma^{-}_{\tilde{x},n} - L_n\Sigma_{\tilde{y},n}L^{T}_{n} \tag{3.48}$$

3.6 Experimental Characterisation for Cell-level Models Parameter Identification

In order to develop a comprehensive DTSP of a LIB, it is essential to understand the characteristics of both the individual cells and the module as a whole. In the following Section, the LW ANR26650m1B cells, which will be used in the implementation of the corresponding models, will be analysed in detail.

All the experimental tests will be carried out in the Energy Storage and Smart Buildings Laboratories that Ikerlan S.COOP has at its headquarters in Galarreta (Hernani). For the characterisation of the battery cells and modules the used equipment is described in Appendix A. In this Section, the results of each of these tests will be described in detail, outlining the procedures involved in measuring and obtaining the requisite parameters. These can be divided into two categories: i) electric characterisation tests (i.e. Capacity Test, OCV vs SoC, Hybrid Pulse Power Test (HPPT), and Hysteresis Test and ii) thermal characterisation tests (i.e. Open Circuit Potentiometry (OCP) Test and Calorimetry Test)

3.6.1 Electrical Characterisation of the ANR26650m1B Cell

The electrical model, ECM, presented in Section 3.4, is a simplified circuit that represents the electrical behavior of the battery. It consists of electrical elements, and its values are derived from conducted laboratory tests . This Subsection describes the results obtained in the electrical characterisation tests carried out on the LW cells.

Note: This Section briefly describes the testing performed and gives the obtained results.

Parameter: Cell Capacity and Efficiency.

The Capacity Test was designed to comprehensively evaluate the Ah capacity of the cell under varying environmental conditions, including temperature and current. Additionally, the calculation of the cell's efficiency parameter η, was derived from the measured Ah discharged and charged during the test at the different temperatures and current rates.

The test were carried out across a temperature range of 10°C to 45°C with three full charge and discharge cycles performed. The charging and discharging processes were executed at rates of 0.2C (200 mA), 0.5C (500 mA) and 1C (2.5 A). Figure 3.4 summarises all the tests performed at different C-rates and different temperatures. A complete charge and discharge cycle has been sampled from each test and plotted on a voltage vs Ah charged or discharged curve. The Figure 3.4a illustrates three full charge and discharge curves at the mentioned C-rates under ambient temperature of 10°C. Similarly, Figure 3.4b represents the cycles at 25°C, and Figure 3.4c shows the cycles at 45°C.

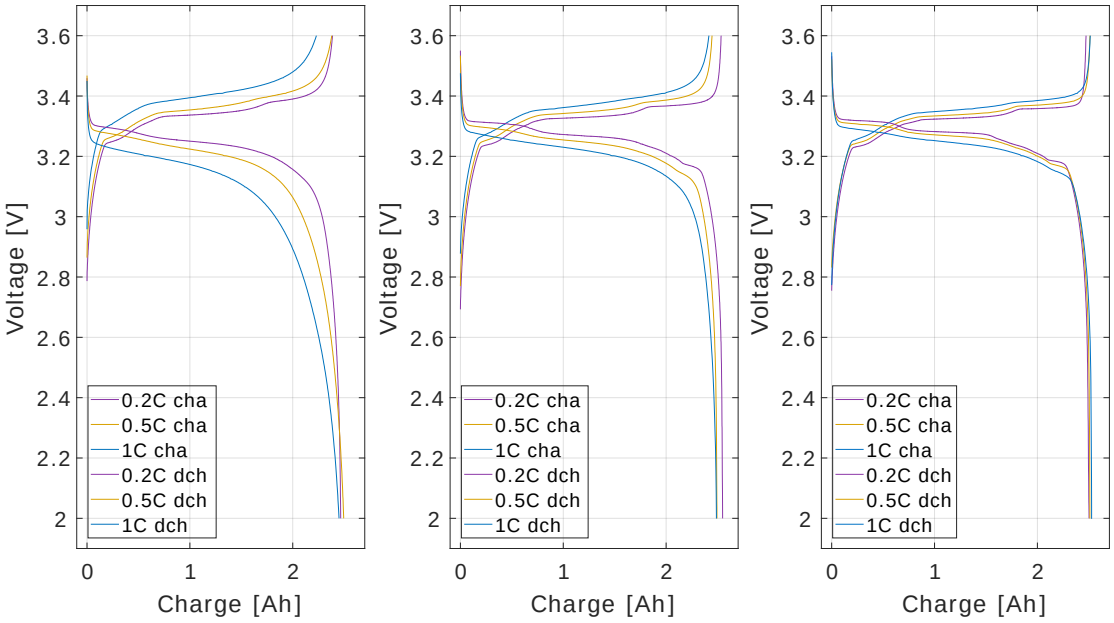

Figure 3.4: Capacity Test Curves of Cell during Charge and Discharge at 0.2C, 0.5C & 1C at a) 10°C chamber ambient temperature, b) 25°C chamber ambient temperature, and c) 45°C chamber ambient temperature.

The values obtained in the 1C test will be the capacity parameters to be introduced in the electrical model of the cell. It has been decided to use this value since the final application will have this c-rate as the nominal load. The Ah values obtained at the end of each charge and discharge have been used to obtain the efficiency of the cell. An evaluation of the cell capacity has been carried out by means of the average Ah discharged during the capacity test. With the values of Ah charged and discharged, the η parameter was determined, which represents the cycling efficiency of the cell. This efficiency represents

the amount of Ah that can be discharged from the cell in relation to the Ah charged. For this reason, this efficiency only applies when the cell is being charged.

$$eta = \frac{\mathrm{Ah}_{dch}}{\mathrm{Ah}_{cha}} \cdot 100 \tag{3.49}$$

Parameter: Open Circuit Voltage.

The objective of the test is to acquire charge and discharge curves that establish a correlation between the SoC and OCV of the battery. The test involves discharging the fully charged battery at 0.2C, in 5% Depth of Discharge (DoD) increments. After each 5% DoD discharge, the battery is kept at rest for 3 hours to attain the equilibrium voltage or OCV. Subsequently, the battery is charged at 5% DoD intervals, allowing 3 hours of rest at each SoC. The OCV vs SoC curves are thus obtained, depicting the relationship between the resting voltage of the cells and the SoC during both charging and discharging.

Figure 3.5 illustrates the results obtained in the OCV test performed at 25°C. In addition, the same tests were performed at 10 and 45 °C, obtaining the OCV vs SoC curves for both charging and discharging. Based on this data, the average OCV was calculated across the entire SoC range for each temperature. This average OCV was then used in the model.

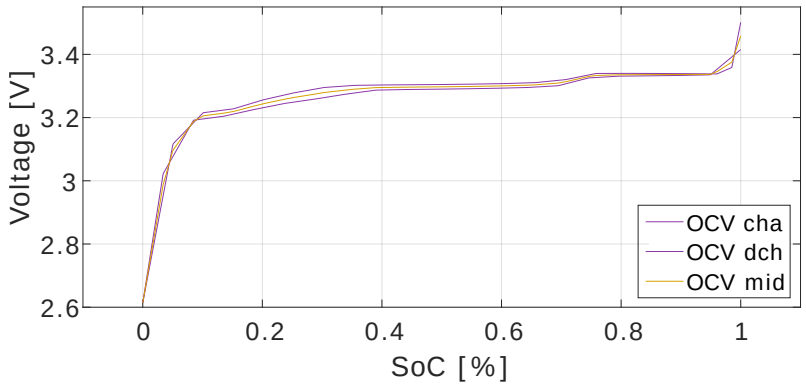

Figure 3.5: OCV vs SoC Curves of Cell during Charge, Discharge and Average and the at 25°C.

Parameter: Hysteresis.

The hysteresis effect is a fundamental element of battery dynamics, which refers to the different equilibrium voltages to which the OCV of the battery converges during charge and discharge cycles. This hysteresis is observed in the OCV vs SoC curves that are obtained in the laboratory. The ECM model, discussed in Section 3.4, takes into account hysteresis using the parameter M, which represents the maximum positive and negative hysteresis values at different SoC levels. Additionally, the instantaneous hysteresis, denoted as M_0, captures the vertical voltage drop specific to each SoC level in the battery.

The hysteresis of the cells depends on the SoC and the temperature in which the cell operates. To obtain the different hysteresis related parameters a quasi-OCV test have been performed. That is, the cell has been charged and discharged to achieve different levels of SoC with a very low current, i.e. C/25 (100 mA). This minimises the effect of the internal resistance of the cell, allowing to isolate the hysteresis effect. The test started with the cell fully charged, and successive charges and discharges were performed with a 5% DoD reduction at each charge. In this way, the cell was charged to 95% SoC, discharged to 5% SoC, charged to 90% SoC, and so on until the cell reached 50% SoC. The performed test is illustrated in Figure 3.6.

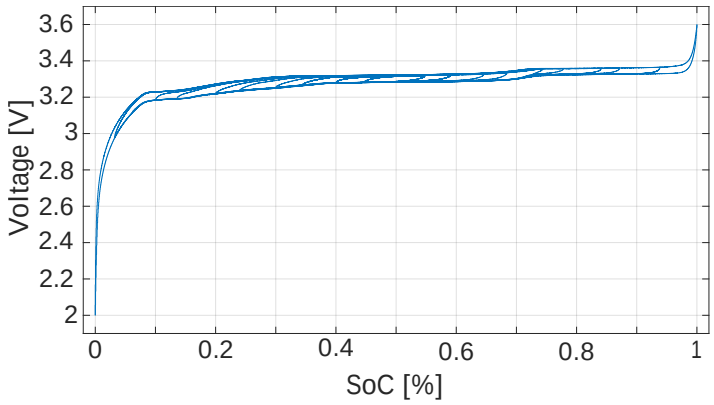

Figure 3.6: Charge and Discharge at C/25 (100 mA) Hysteresis Test to obtain the Hysteresis Parameters at 25°C.

The data obtained from the test was used in the Parameter Estimator tool in Matlab Simulink. A specific ECM model, defined in section 3.4, was employed in Simulink for the optimisation process. Subsequently, the hysteresis values (M, M_0 and G) have been optimised to fit this test. Hysteresis related parameters obtained are temperature and SoC dependent.

Parameter: Internal Resistances.

The internal resistance of batteries is a crucial parameter for their characterisation. In the case of LIBs, the internal resistance varies depending on several factors, including i) SoC, ii) current rate during charging and discharging pulses, iii) operating temperature, and iv) duration of the charge and discharge pulses. This test allows for the determination of the internal resistance values under various operating conditions.

To measure the internal resistance, an HPPT test composed of charge and discharge pulses has been performed for different SoCs and temperatures. Specifically, 0.5C (500 mA) and 1C (2.5 A) pulses have been applied to the battery, covering the range from 0% to 100% SoC at 5% DoD intervals. Each pulse has had a duration of 30 seconds. Figure 3.7 illustrates an HPPT test performed at 10°C, 25°C, and 45°C.

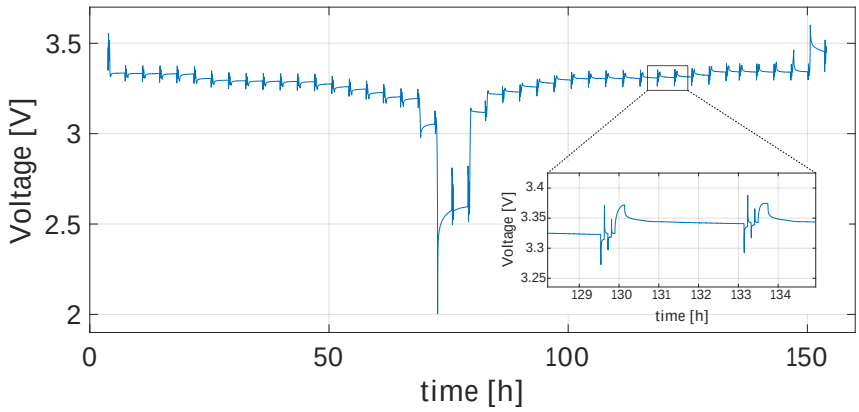

Figure 3.7: HPPT carried out to obtain the internal resistance and the RC of the cell at 25°C.

The electrical ECM, which consists of three RC phases, has been used to obtain the resistance parameters of the cell . Similar to the cell hysteresis, these parameters have been estimated with the Parameter Estimator in Matlab Simulink. In the first step, the cell hysteresis values have been optimised. Once these values were obtained, they were fixed and the internal resistance ($R0$) and the parameters of the three RC circuit elements were adjusted. This involved optimising the values of $R1$, $R2$, $R3$, as well as the time constants τ_1, τ_2, and τ_3. In an ECM, a RC branch models the battery's transient response. The time constants (τ) associated with these branches dictate the charging and discharging rates of the battery. By adjusting resistor and capacitor values, these time constants have been customized to fit the cell´s performance in various conditions. This ensures a more realistic representation of the battery's transient behavior in the circuit model.

3.6.2 Thermal Characterisation of the ANR26650m1B Cell

This Section describes the performed test and obtained results of the thermal characterisation for the LW cells. For the thermal modelling, a LTM has been used. This model represents the thermal behaviour of the cell using an analog electrical circuit, which includes components to describe the generation and accumulation of heat, as well as its dissipation. In addition the specific heat capacity of the cells has been measured. The required parameters for the developed LTM are detailed below.

Note: This Section briefly describes the testing performed and gives the obtained results.

Parameter: Entropic Heat Coefficient.

The EHC parameter is defined as the variation of the OCV of a cell in relation to temperature (equation 3.50). This parameter is directly related to the reversible heat generated by a cell. The measurement of this coefficient is performed by OCP tests. This is an experiment in which the temperature of the climatic chamber is varied while keeping the SoC constant at each step. In other words, the EHC represents the sensitivity of the cell's OCV to temperature variations at a given SoC.

$$EHC(SoC) = \frac{dU^{\text{avg}}}{\mathrm{d}T} \tag{3.50}$$

The test consists of discharging a fully charged battery at 5% DoD intervals at 0.2C. After each 5% DoD discharge, the battery is allowed to rest for 3 hours to reach the equilibrium voltage or OCV. When it reaches this OCV voltage, the thermal cycle shown in Figure 3.8 is applied, and the voltage variation during this profile executuion is measured. This thermal cycling consists of five different temperature stages (25°C, -5°C, 10°C, 40°C, 25°C). Each of the stages lasts 3 hours, assuring a proper thermal stabilization of the cell.

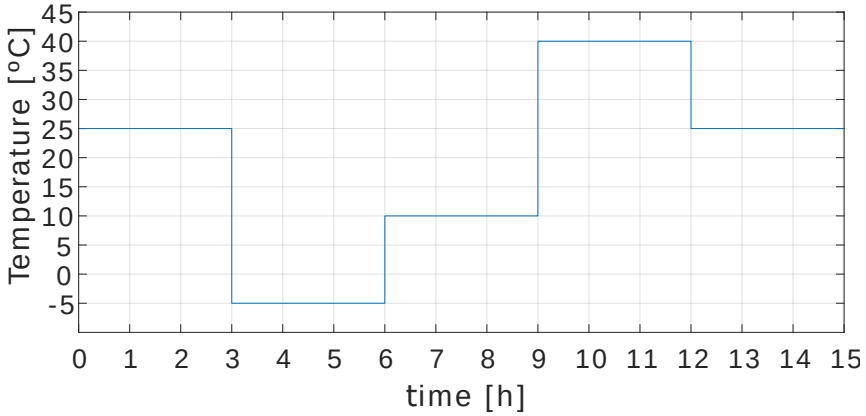

Figure 3.8: Example of thermal cycle applied for EHC calculation

Once the test has been performed, the voltage variations within the different SoCs are analysed, as seen in Figure 3.9a. To determine the temperature coefficient from this data, the voltage was fitted to the function described by equation 3.51, which includes the constants A, B, and C, where the constant B corresponds to the EHC $\mathrm{d}U^{\text{avg}}/\mathrm{d}T$. This fit can be observed in Figure 3.9b.

$$V(t,T) = A + BT + Ct \tag{3.51}$$

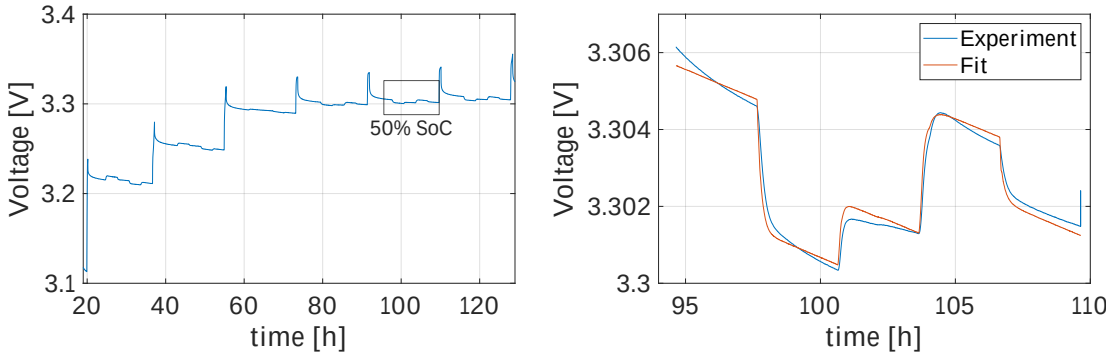

Figure 3.9: EHC measurement procedure with a) OCV voltage variation measurement of the EHC test and b) Obtention of the EHC by adjusting the OCV variation to 50% of the SoC.

Once the EHC is obtained from the fitting equation, the EHC vs SoC curve can be obtained as a function of the SoC-level of the cell. This curve shows the OCV variation per degree Kelvin with respect to the SoC of the cell, which will define the reversible heat behaviour depending on the current applied and the cell temperature. The obtained EHC values are presented in Figure 3.10.

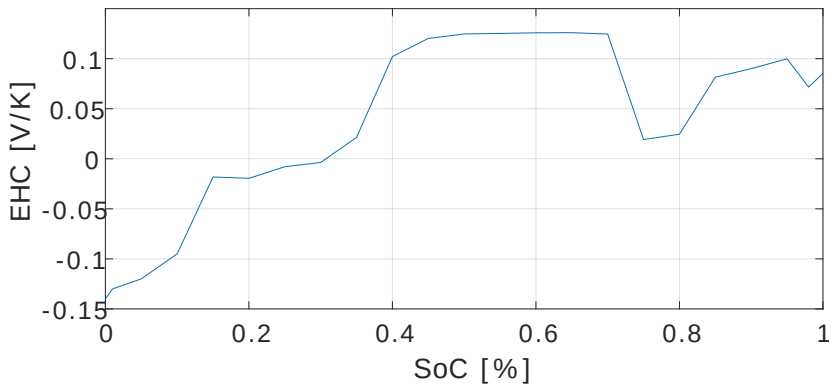

Figure 3.10: Obtained EHC values.

Parameter: Specific Heat Capacity.

The Specific Heat Capacity (Cp) is a necessary parameter for the calculation of the heat storage of the thermal model. This parameter has been obtained by means of an experimental test where the amount of heat released or absorbed by a cell has been measured. For this purpose, a calorimetry test has been carried out in the Accelerating Rate Calorimeter (ARC) (THT, EV Standard Calorimeter) using the setup seen in Figure 3.11. The aim of this procedure is to measure the heat required by the cell to increase its temperature by one degree.

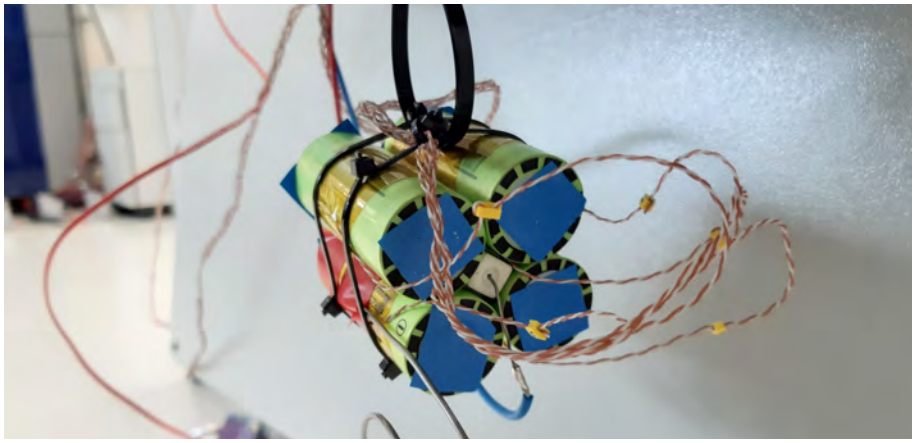

Figure 3.11: Calorimetry test for Cp measurement for LW cylindrical cell.

As explained before, to carry out this text it is necessary to introduce a cell into the calorimeter which is an adiabatic chamber (no heat exchange between the chamber and the outside) and contains a thermocouple to measure the temperature differences. In the calorimeter the cell is heated by means of a thermal resistor applying a known amount of energy. Examples are given in Table 4.2. Then, the temperature change in the cell is measured over time. Knowing the mass of the cell, the amount of heat applied and the temperature variation, the Cp of the cell can be calculated using the formula 3.52.

$$\dot{Q} = m \cdot C_p \cdot \frac{\Delta T}{\Delta t} \tag{3.52}$$

where $\dot{Q}$ is the amount of heat applied, m is the mass of the cell, ΔT is the temperature variation and Δt is the time interval between time n and the previous time step $(n-1)$ in $[s]$.

Table 3.3: Conditioning and Selection of Similar Cells.

	P [W]	**Delta T [ºC]**	**Cp [J/kg*K]**	**Cpavg**
Cell sample	4.9	22.7	1161	**1163**
	18.7	22.2	1165	

The LTM and ECM models, discussed in Sections 3.3 and 3.4 respectively, rely on the selection of appropriate parameters. The subsequent Section presents the validation tests performed on the LW cells in the laboratory. These tests aim to validate the cell-level models by confirming the accuracy of the parameters obtained from the cell characterisation tests described earlier in this Section.

3.7 Results & Discussion of Cell-level Models

This Section aims to validate the cell-level models and estimator, which completes Stage 1 of the methodology proposed in Chapter 2. At the same time, it fulfils the first objective set for this thesis, which is to develop and validate cell-level models to understand the behaviour and interactions of basic system features, in order to use them as a basis for extrapolation to more advanced module models.

3.7.1 Results & Discussion: Cell-level LTM Validation

The validation of the thermal model (LTM) consisted of testing the cell under different operating conditions to ensure correct operation. Two types of tests were carried out and used to characterise the cell, the OCP test and the HPPT test, that were not included in the parameter estimation process (section 3.6).

Figures 3.12a and 3.12b show the test profiles used to represent cell operation. In Figure 3.12a, a current profile at 1C consisting of three complete charge and discharge cycles of the cell is presented. The cell was charged using a constant current-constant voltage (CC-CV) charging method. This profile, with low dynamics, was performed at three different temperatures: 10°C, 25°C and 45°C. The objective was to observe whether the parameters describing the thermal dynamics are adequate.

On the other hand, the current profile shown in Figure 3.12b is dynamic. This was also used to test variable profiles to assess whether the thermal model is able to correctly estimate the cell under demanding temperature conditions. These profiles were also performed at the three temperatures mentioned above.

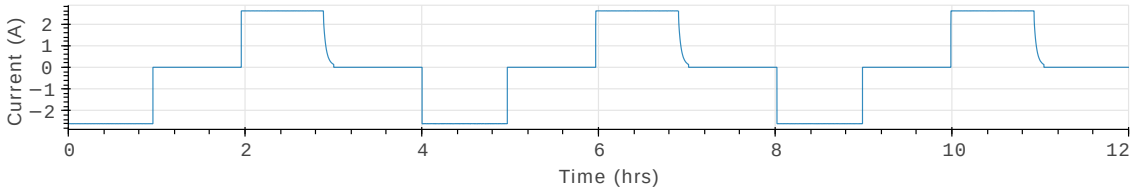

(a)

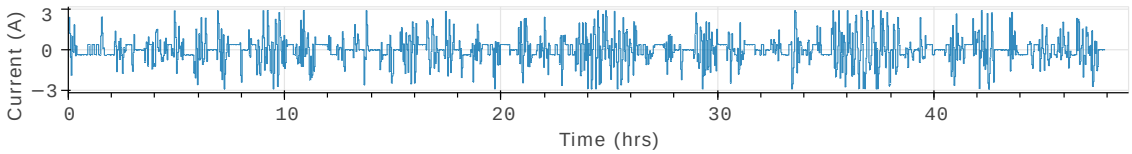

(b)

Figure 3.12: Applied profiles in the cell level thermal model. a) Capacity test, and b) Dynamic profile.

To obtain the cell data during the validation tests, thermocouples were placed at the six points on the cell surface where the model estimates each temperature as shown in Figure 3.13a. Each thermocouple was connected to an Agilent temperature meter. These measurements were then compared with the estimates made by the LTM. Figure 3.13b shows the measurements collected from a complete charge/discharge cycle of the cell.

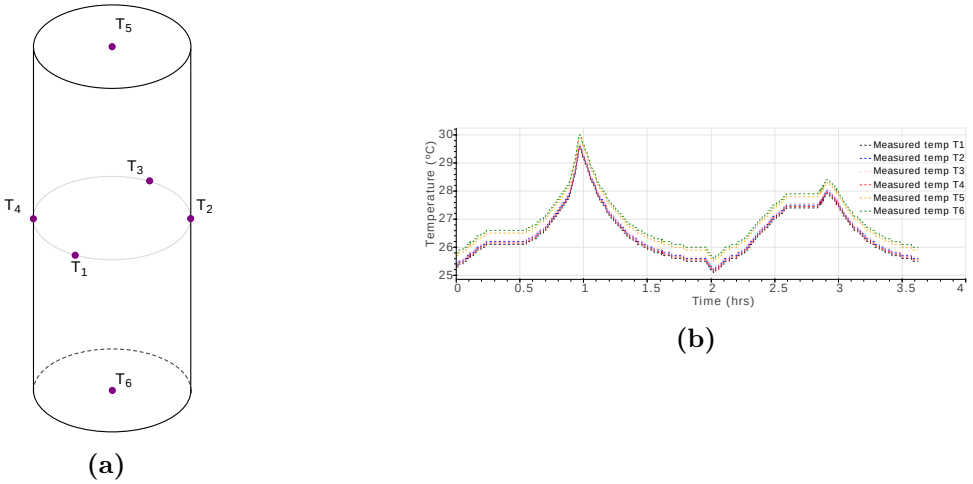

Figure 3.13: Thermocouples in a cell: a) location of thermocouples in the cell and b) measurements obtained from these thermocouples.

Figure 3.13b illustrate the location in which each thermocouple has been located within the cell during the test. On the other hand, Figure 3.13a shows the temperature measurements obtained during the test at the points indicated in the Figure 3.13b.

The temperature measurements shown in Figure 3.13b exemplify the results of the three conducted tests. In Figure 3.14, all the predictions for the points on the cell surface are shown. The colored lines represent the estimated values, while the black dashed line represents the measured values for all the points on the surface. Figures 3.14a, 3.14b, 3.14c and 3.14d present the estimation made by the thermal model in the radial surfaces of the cell. In addition, Figures 3.14e and 3.14f show the estimation and measurement of the temperatures at the top and bottom of the cells, respectively.

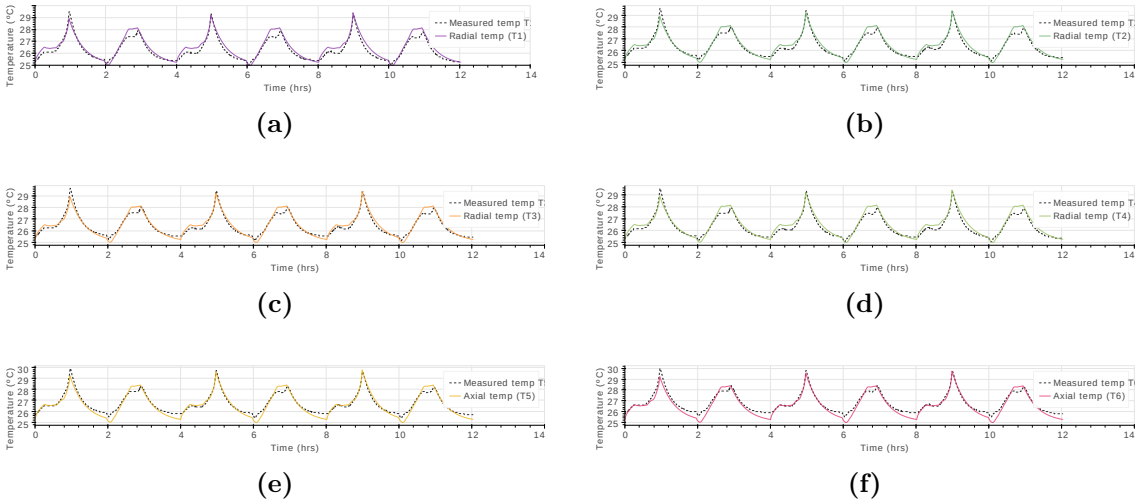

Figure 3.14: Capacity test at 25°C ambient temperature. The graphs show the temperature measured by the NTC vs. the estimated temperature at the location of a) T1, b) T2, c) T3, d) T4, e) T5, f) T6.

Figures 3.14a-3.14f show an adequate trend in the estimation of the temperature change along the cell. In this figure, it can be observed that the temperature gradient within the cell is minimal since it is measured across six points on the cell's surface. This indicates that the temperature dispersion within the same cell is small. Furthermore, the measurement taken at point T1, which corresponds to the radial surface of the cell, will be used as the reference signal for the LTM system. However, all the errors obtained by the LTM at each estimated point will still be presented for a comprehensive analysis.

Figure 3.15 shows the results obtained during the same capacity test performed at an ambient temperature of 25°C in the climatic chamber illustrated in 3.14. Figure 3.15a shows the SoC profile of the cell, in Figure 3.15b, the temperature measured at point T1 of the cell and the temperature estimation provided by the LTM are depicted. Finally, in Figure 3.15c six lines represent the errors obtained when comparing the estimated temperature versus the measured temperature at each specific point on the cell surface.

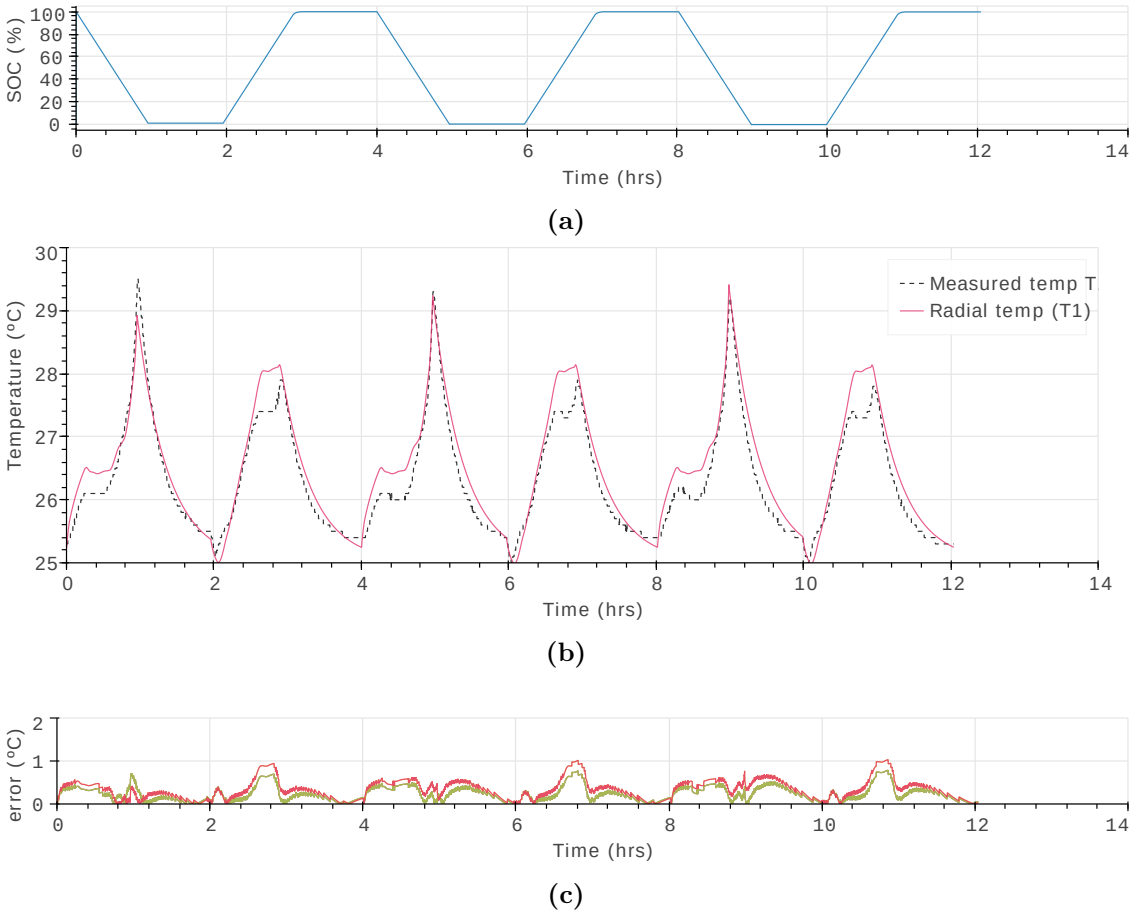

Figure 3.15: Capacity test at 25°C ambient temperature. The plots show a) SoC during the test, b) measured temperature at point T1 on the cell surface versus LTM estimated temperature, and c) LTM error in °C.

For the temperature estimation points on the radial surfaces, the mean errors of the estimates are 0.31°C and the maximum absolute error is 0.78°C. For the estimations on the axial surfaces of the cell (top and bottom surfaces), the mean errors are 0.43°C and the maximum absolute error is 1.03°C. These results show that the model is able to follow the slow dynamics of the cell at an ambient temperature of 25°C.

The same type of test was repeated at two other temperatures: 10°C and 40°C ambient temperature. In these cases, only the results of the temperature estimations and the corresponding measurement of T1 will be shown to verify that the LTM can also follow the thermal dynamics at these two temperatures.

Figure 3.16 shows the estimations made by the LTM in the the capacity test performed at 10°C ambient temperature in the climatic chamber. Following the same procedure as in the 25°C test, Figure 3.16 show the temperatures estimated by the LTM (coloured curve) versus the measurements (black discontinuous curve). Figure 3.16c shows all the errors

obtained.

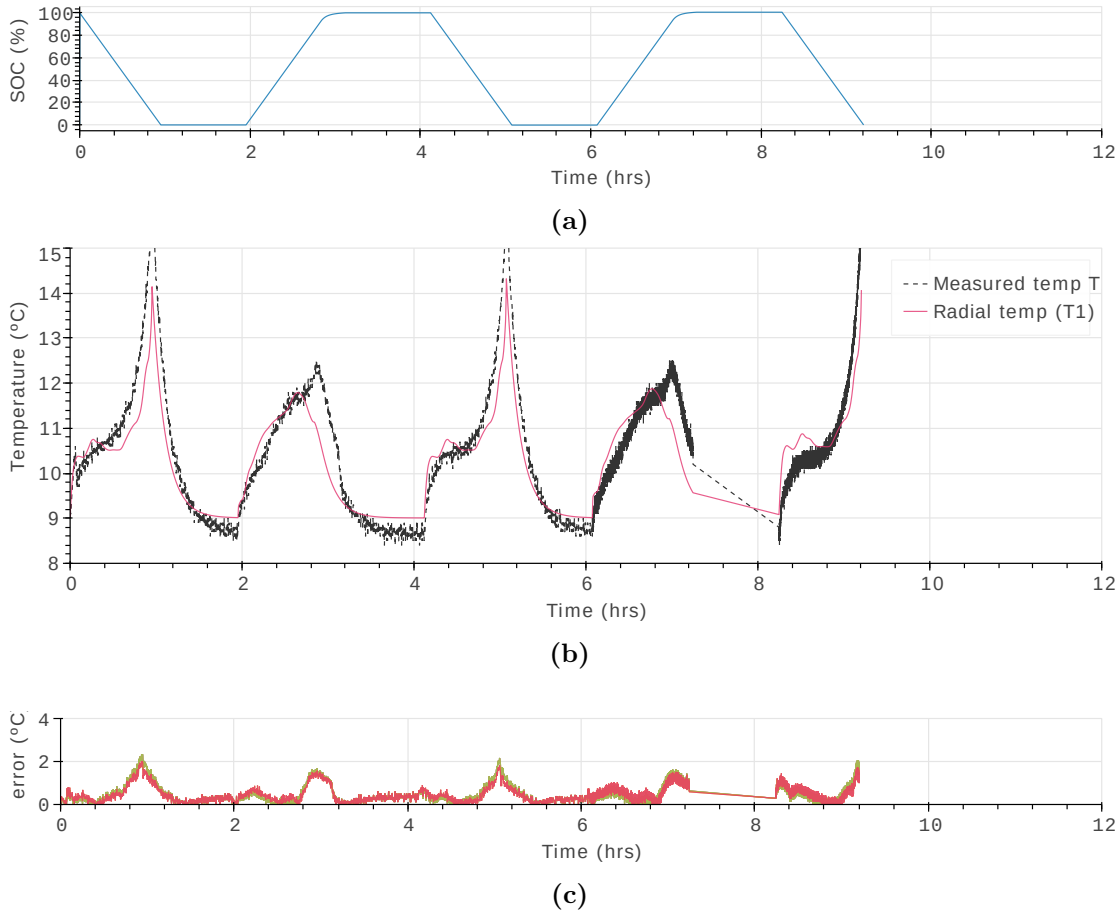

Figure 3.16: Capacity test at 10°C ambient temperature. The plots show a) SoC during the test, b) measured T1 temperature versus LTM estimated temperatures, and c) LTM error in °C.

When estimating the capacity test at an ambient temperature of 10°C, the LTM demonstrates a strong ability to capture and track the temperature trends within the cell, as evidenced by Figure 3.16. The mean errors in the radial surface measurements, specifically at point T1, are 0.523°C. Similarly, for the axial surface measurements, the mean error at point T5 is 0.55°C.

The latest capacity test was conducted at an ambient temperature of 45°C. In Figure 3.17, the estimated temperature is presented, following the same logic as the previous capacity tests. Additionally, Figure 3.17c displays the errors obtained in the temperature estimates, allowing for a comprehensive analysis of the model's performance.

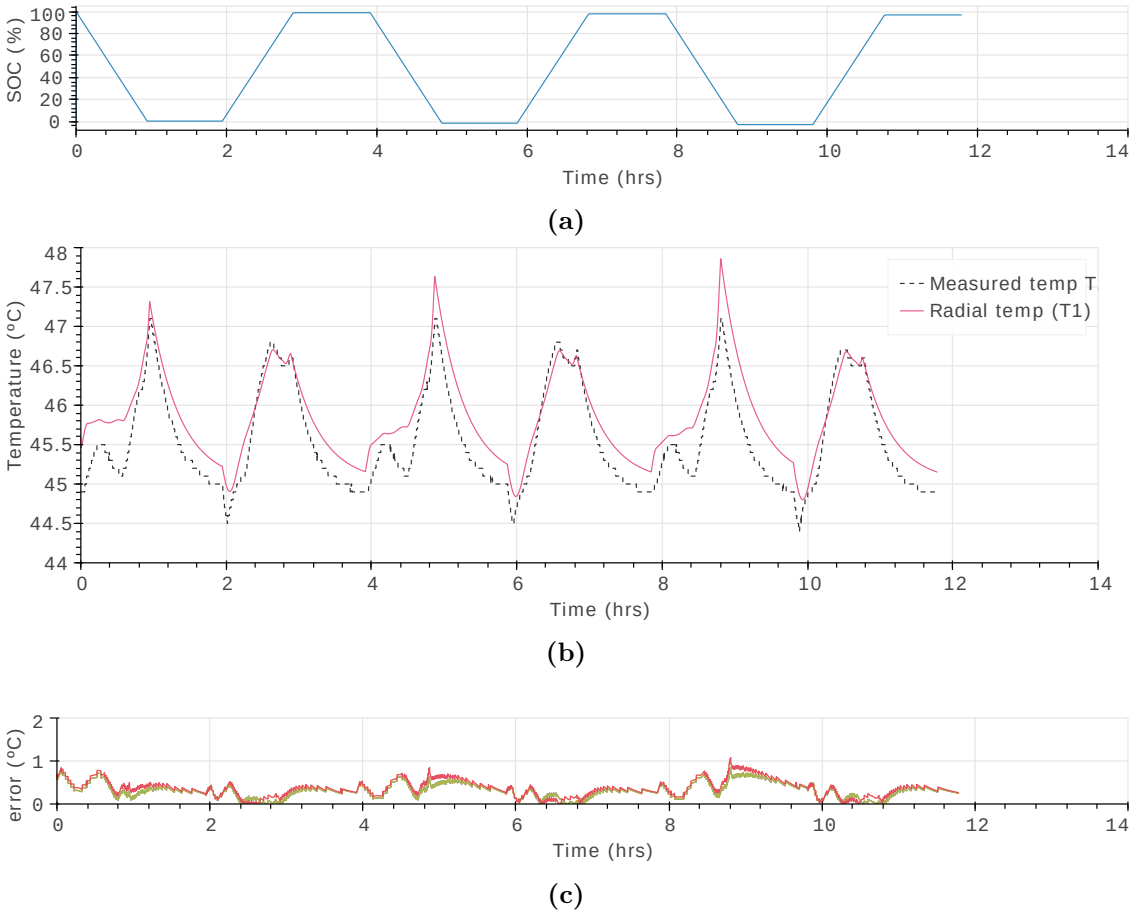

Figure 3.17: Capacity test at 45°C ambient temperature. The plots show a) SoC during the test, b) measured T1 temperature versus LTM estimated temperatures, and c) LTM error in °C.

When estimating the capacity test at 45°C ambient temperature, the average errors in the measurements of the radial surfaces are 0.33°C, while the maximum absolute error is 0.86°C. As for the estimations on the axial surfaces, the mean error obtained is 0.28°C and the maximum absolute error is 0.75°C. These results indicate that the LTM correctly follows the temperature trends during full charges and discharges at 45°C ambient temperature.

In addition to the capacity tests, more dynamic profiles were also tested, as shown in Figure 3.12b. These tests aim to verify whether the developed LTM is able to estimate the cell temperature when the it operates at faster dynamics, applying current with varying C-rates. In this test, the cell was fully charged using a CC-CV charging cycle and then discharged to 50% SoC. When the cell reached 50% SoC, the dynamic profile from Figure 3.12b was applied that reaches a C-rate of up to 1.5C. Figure 3.18 shows the dynamic profile test with the measured data, performed at 25°C ambient temperature.

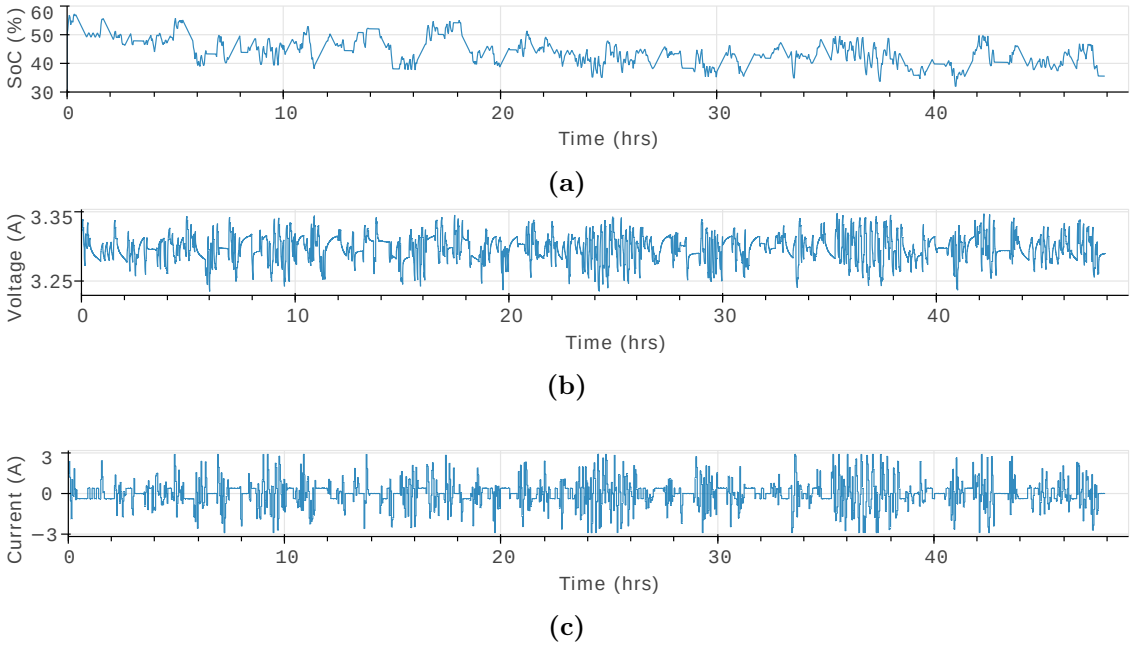

Figure 3.18: Dynamic test. The plots show a) SoC during the test, b) voltage measured during the test, and c) applied current profile.

Figure 3.19a shows the temperature estimation at the T1 surface together with the measurements made by the cycler. The three tests have been plotted on a single graph. The curves represented in pink correspond to the dynamic test at 45°C ambient temperature, the green curve represents the test at 25°C and the blue curve represents the test at 10°C. The same colours are applied to the graph representing the dynamic test at 45°C ambient temperature. These colours are also applied to the graph showing the errors obtained in these estimations shown in Figure 3.19b.

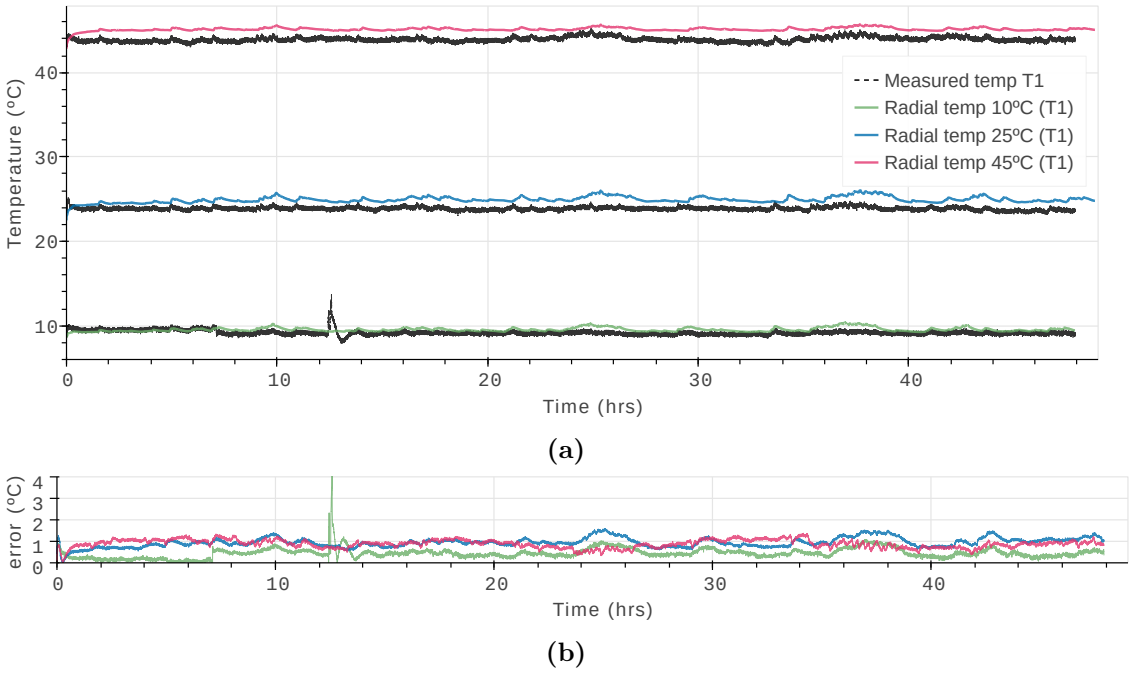

(a)

(b)

Figure 3.19: Capacity test at 10°C, 25°C and 45°C ambient temperature. The plots show a) measured T1 temperature versus LTM estimated temperatures in each ambient temperature, and c) LTM error in °C.

As shown in Figure 3.19, the mean error of the LTM model at the cell level at 10ºC is 0.45°C. At 25°C this mean error is 0.94°C and at 45°C the error is 0.88°C. The maximum errors at the three temperatures are 4.18°C, 1.61°C and 1.39°C. The test conducted at 10 degrees Celsius exhibits a peak temperature rise, which is attributed to external factors. These errors are within the acceptable range, considering that the error of the thermocouples is ± 1.5°C. Therefore, the LTM model is considered validated, as well as the parameters obtained in Section 3.6. This model then, will be the basis for the extrapolation of the model at module level in Chapter 4.

3.7.2 Results & Discussion: Cell-level ECM and SPKF Validation

The electrical ECM has been validated together with the SPKF SoC estimator. First, the parameters obtained in Section 3.6 were used to make estimates using only the electrical model. This allowed verifying whether the defined parameters correctly represent the voltage response of the cell in the tests used to characterise them. Once the electrical model was validated, simulations were carried out with the dynamic profile and capacity test using the SPKF estimator. The results obtained at each step to further validate the ECM together with SPKF are detailed below.

As mentioned above, estimations were performed with the tests used to obtain the electrical parameters. The first test used to obtain parameters was the quasi-OCV test depicted in Figure 3.20b in which the parameters related to hysteresis were optimised. Figure 3.20a shows the SoC profile when applying the quasi-OCV current profile. Figure 3.20c shows the voltage estimated by the ECM compared to the voltage measured by the battery cycler. Finally, Figure 3.20d shows the error obtained in the voltage.

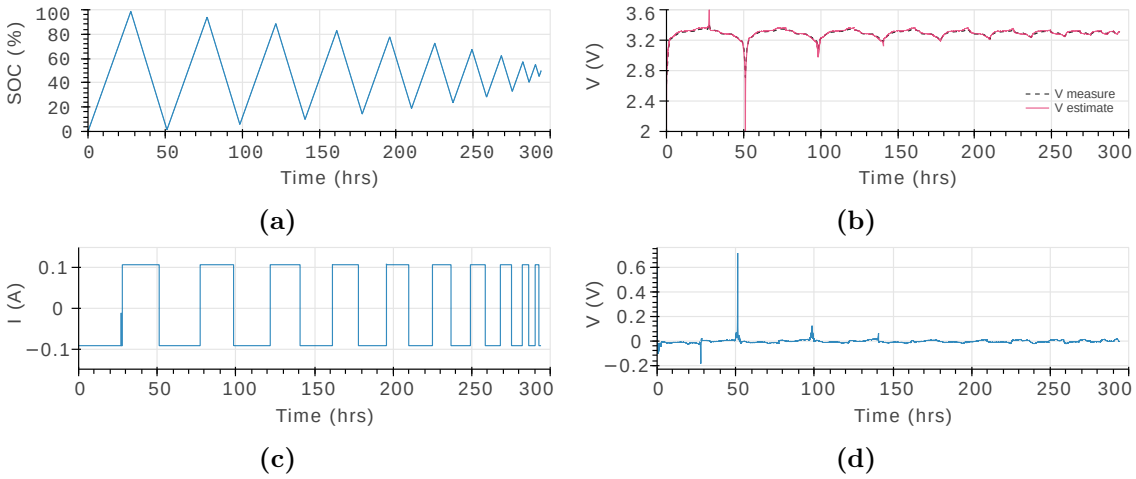

Figure 3.20: Hysteresis test at 25°C ambient temperature. The plots show a) SoC during the test, b) measured voltage versus ECM estimated voltage, c) applied current profile, and d) ECM error in voltage.

Figure 3.20 demonstrates how the hysteresis parameters fit well to be able to estimate the dynamics in this quasi-OCV test with errors of 0.003 V and max error of 0.65V. Then, the parameters representing the RC branches were obtained and the R_0 was redefined, as explained in section 3.6. This second parameter optimisation was performed with the HPPT test. In this case, additional RC phases were incrementally added to the model until the optimal number of RC phases was determined to accurately capture the behavior of the cell. After optimization, it was determined that three RC phases provided the most suitable representation of the cell's behavior. Figure shows the SoC profile applying the current profile of Figure . Figure 3.21c shows the voltage estimated by the ECM compared to the voltage measured by the battery cycler. Finally, Figure 3.21d shows the error obtained in the voltage.

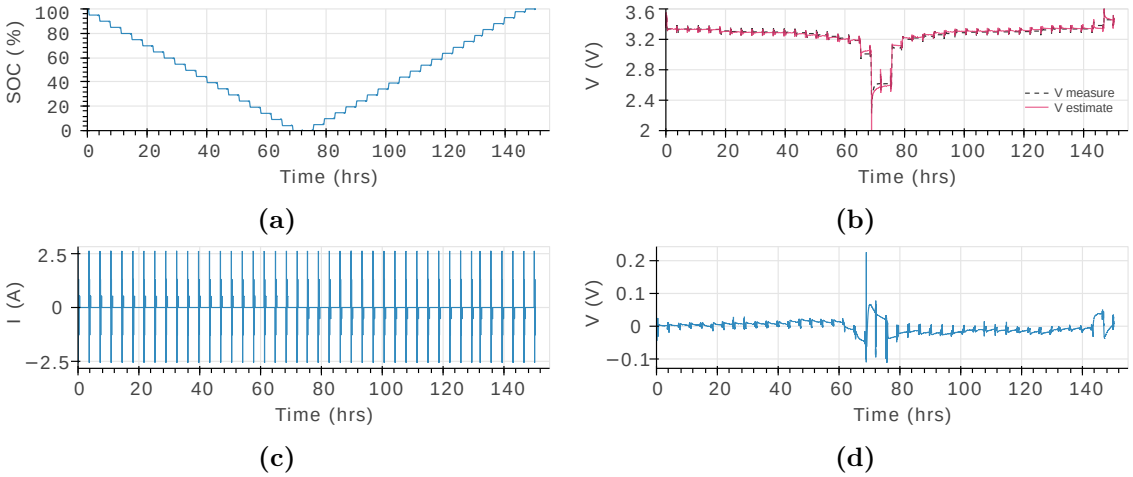

Figure 3.21: HPPT test at 25°C ambient temperature. The plots show a) SoC during the test, b) measured voltage versus ECM estimated voltage, c) applied current profile, and d) ECM error in voltage.

Figure 3.21 shows that the parameters fit well in order to estimate the dynamics in this HPPT test. A higher error is observed when the cell is close to 100% SoC and especially when it is completely discharged (SoC at 0%), with a maximum error of 0.225 V but the average error is 0.002 V.

In addition to the optimized parameters at 25°C, it has also been verified that the parameters at the other two temperatures (10°C and 45°C) have been correctly identified. With this confirmation, the validation of the ECM at the three temperatures will be carried out. That validation of the ECM parameters was repeated at temperatures of 10°C and 45°C. Figures 3.22, and 3.23 show the results obtained in the quasi-OCV and HPPT tests at 10°C ambient temperature.

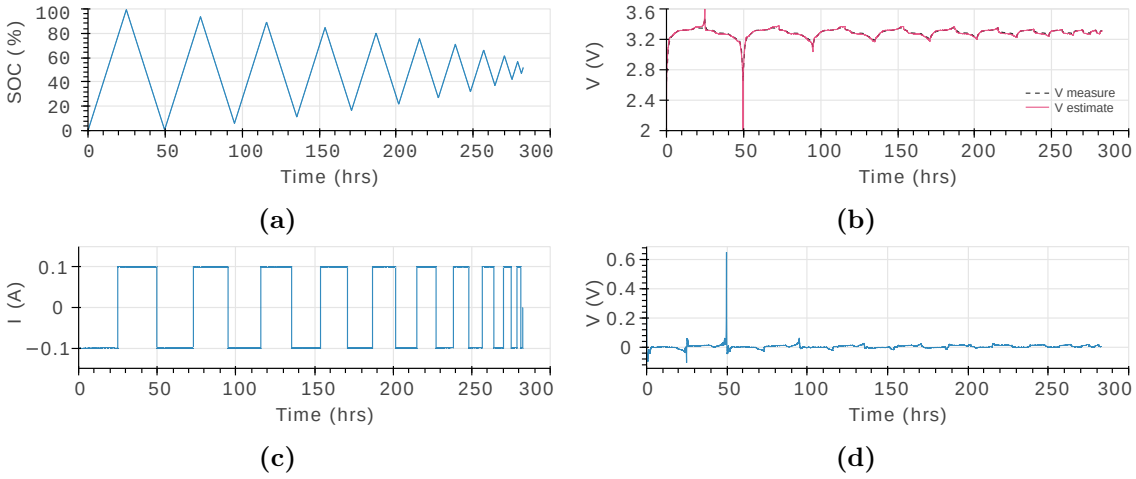

Figure 3.22: Hysteresis test at 10°C ambient temperature. The plots show a) SoC during the test, b) measured voltage versus ECM estimated voltage, c) applied current profile, and d) ECM error in voltage.

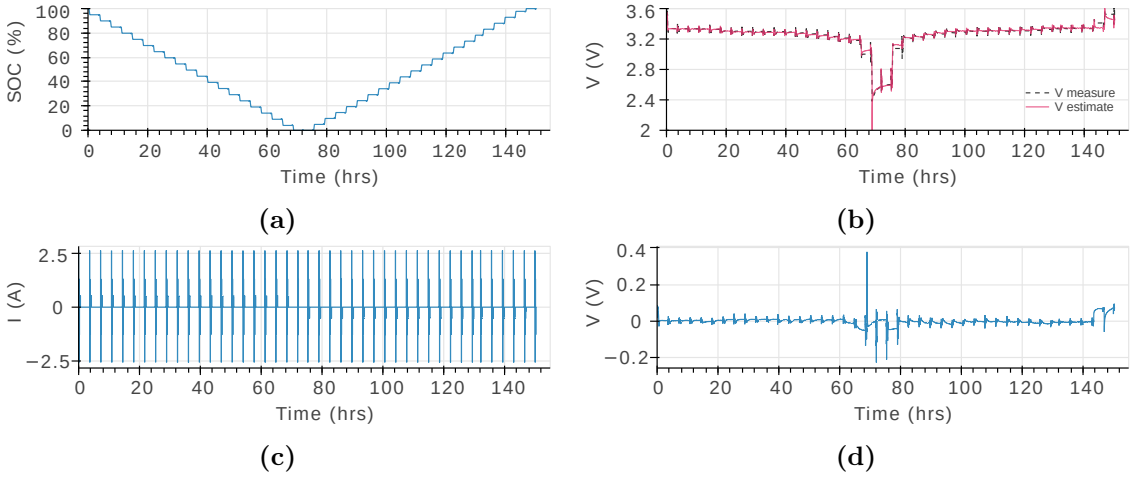

Figure 3.23: HPPT test at 10°C ambient temperature. The plots show a) SoC during the test, b) measured voltage versus ECM estimated voltage, c) applied current profile, and d) ECM error in voltage.

The errors obtained in the tests at ambient temperature of 10°C are similar to those obtained in the tests carried out at 25°C, with 0.003 V and 0.002 V errors on average in the tests. The maximum errors obtained in these tests were 0.65 V and 0.23 V. Once these values were obtained, the validated °C at 10°C was selected.

Similarly, Figures 3.24 and 3.25 show the results obtained in the quasi-OCV and HPPT tests at 45°C room temperature.

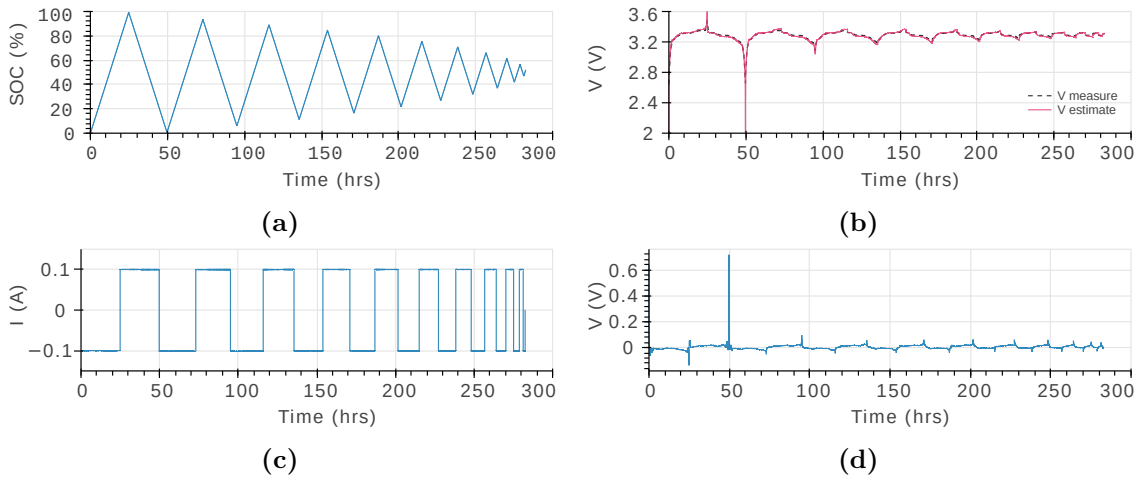

Figure 3.24: Hysteresis test at 45°C ambient temperature. The plots show a) SoC during the test, b) measured voltage versus ECM estimated voltage, c) applied current profile, and d) ECM error in voltage.

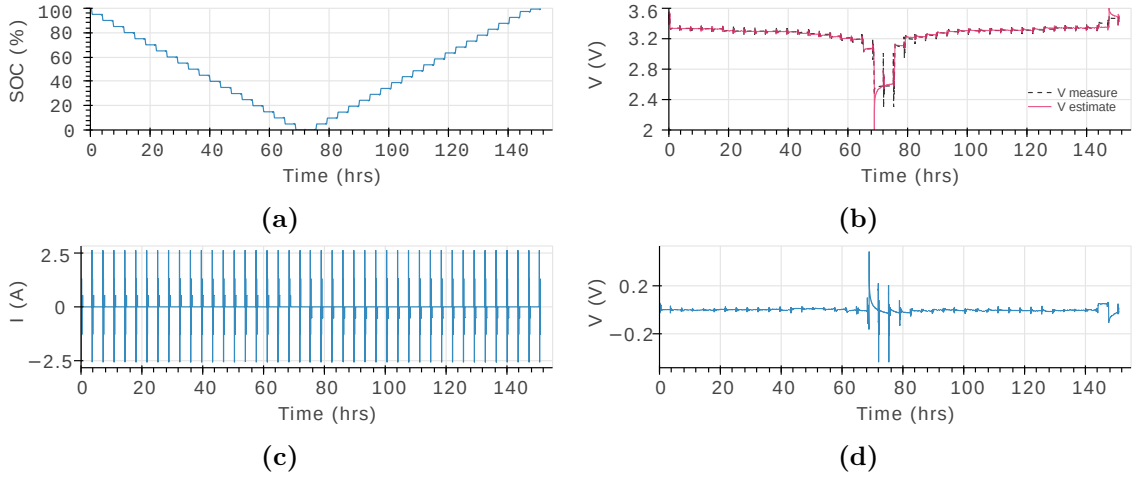

Figure 3.25: HPPT test at 45°C ambient temperature. The plots show a) SoC during the test, b) measured voltage versus ECM estimated voltage, c) applied current profile, and d) ECM error in voltage.

The average error in those test are 0.004 V and 3.11e-05 V and the maximum errors are 0.72 V and 0.49 V. This shows that the model is able to correctly estimate the cell voltage at 45°C ambient temperature.

Once the electrical model was able to correctly estimate both slow dynamics (quasi-OCV) and faster dynamics (pulse test), the validation of the SPKF SoC estimator was performed. The proposed model was integrated into the SPKF, as explained in section 3.5, to achieve a robust SoC estimation. The experimental results used to validate the algorithm are presented below. Several tests were performed to demonstrate the correct performance of the SoC estimator, being able to accurately represent a wide range of different dynamics.

The current profiles used for the validation of the open-loop model were also employed to assess the performance of the SPKF estimator. Specifically, the HPPT test profile was utilised, along with the introduction of a dynamic profile to evaluate the estimator under variable dynamics. The SoC reference used to calculate the error was determined by an accurate Coulomb Counting estimate obtained under laboratory conditions, using the current measured in the cell tester. Although this method has some limitations, it can be considered a good short-term reference and quite reliable when the current measurement is accurate.

First, the HPPT test was repeated. In this case, apart from executing the ECM, the state estimator was used to correct the SoC estimation of the cell. The battery was cycled through the entire SoC range, starting with the cell fully charged and ending when the minimum operating voltage was reached, and then fully charged again, demonstrating that an accurate estimate was maintained throughout the test. Figure 3.26 shows the results of the pulse test over the entire SoC range at 25°C. The actual cell voltage is shown along with the estimated voltage. The reference SoC and the estimated SoC with the SPKF integrating the proposed model are also plotted. Finally, the absolute SoC error of the developed method is shown.

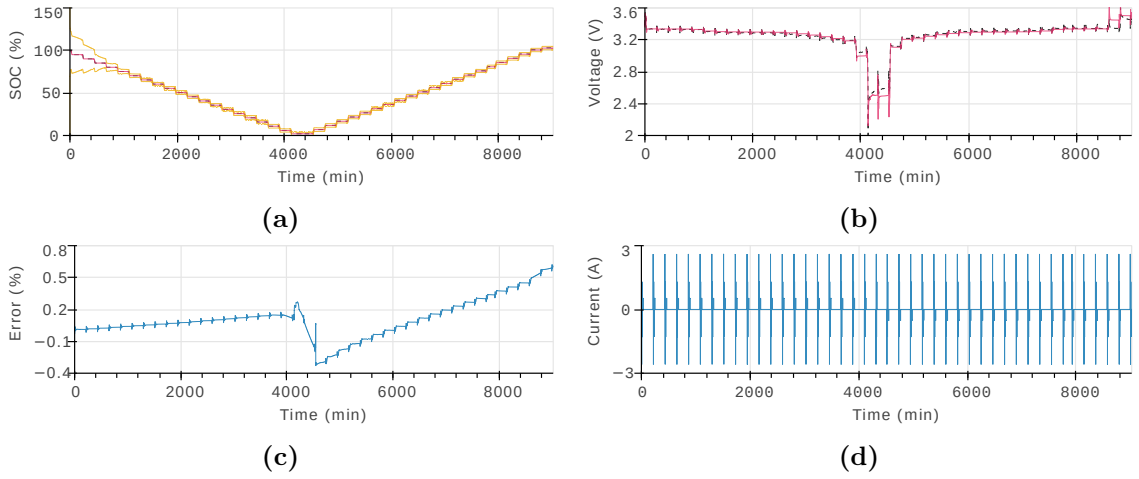

Figure 3.26: HPPT test at 25°C ambient temperature. The plots show a) SoC during the test, b) measured voltage versus ECM estimated voltage, c) SoC error during the test, and d) test currrent profile.

The maximum error of the estimator is less than 1% of SoC in the test shown. In this test, where the cell was subjected to charge and discharge pulses of different C-rates over the entire SoC range, the SoC RMS error is 0.39 %. Furthermore, when using the SPKF, the SoC prediction remained within the upper and lower limits at all times, ensuring a realistic estimation of the state of charge.

The electrical model and the SoC estimator also demonstrated their ability to correctly estimate faster dynamics. This profile represents more demanding cell dynamics. In this case, the model was found to be able to accurately estimate the output voltage and SoC of the cell. Figure 3.27 shows the results obtained with the dynamic test performed in the climatic chamber at 25°C. Figures 3.27b and 3.27c show the current and voltage measured in the test, together with the voltage estimated by the model. Figure 3.27a represents the SoC estimate at 25°C calculated by the proposed SPKF, compared to the reference SoC. The SoC error achieved is also shown in Figure 3.27d.

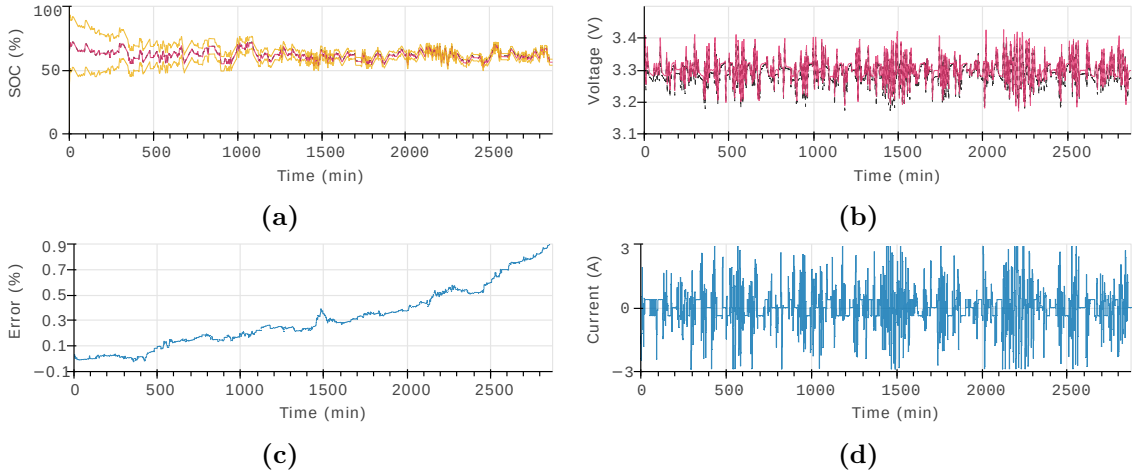

Figure 3.27: Dynamic test at 25°C ambient temperature. The plots show a) SoC during the test, b) measured voltage versus ECM estimated voltage, c) SoC error during the test, and d) test currrent profile.

The SPKF with the ECM model achieves good results in SoC and voltage estimation. The RMS SoC error in the dynamic profile test is 0.48%.The maximum error of the proposed algorithm is typically less than 5%, which confirm the accurate determination of SoC in different scenarios and its ability to represent the dynamics under a more demanding profile excitation.

Both tests were repeated at ambient temperatures of 10°C and 45°C, maintaining the same characteristics as at 25°C. Figure 3.28 shows the results obtained in the HPPT test at 10°C, while Figure 3.29 shows the results obtained by the SPKF in the dynamic test at 10°C.

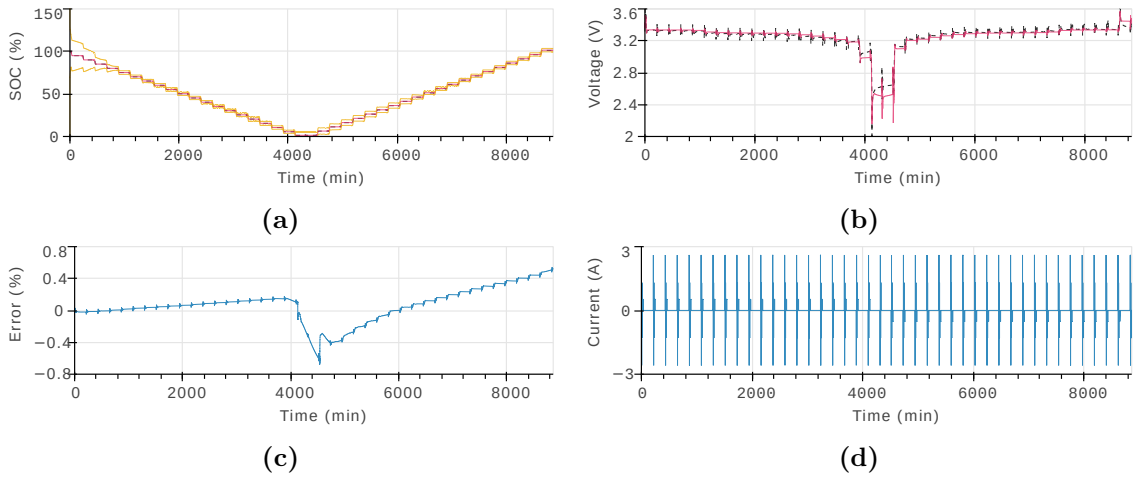

Figure 3.28: HPPT test at 10°C ambient temperature. The plots show a) SoC during the test, b) measured voltage versus ECM estimated voltage, c) SoC error during the test, and d) test currrent profile.

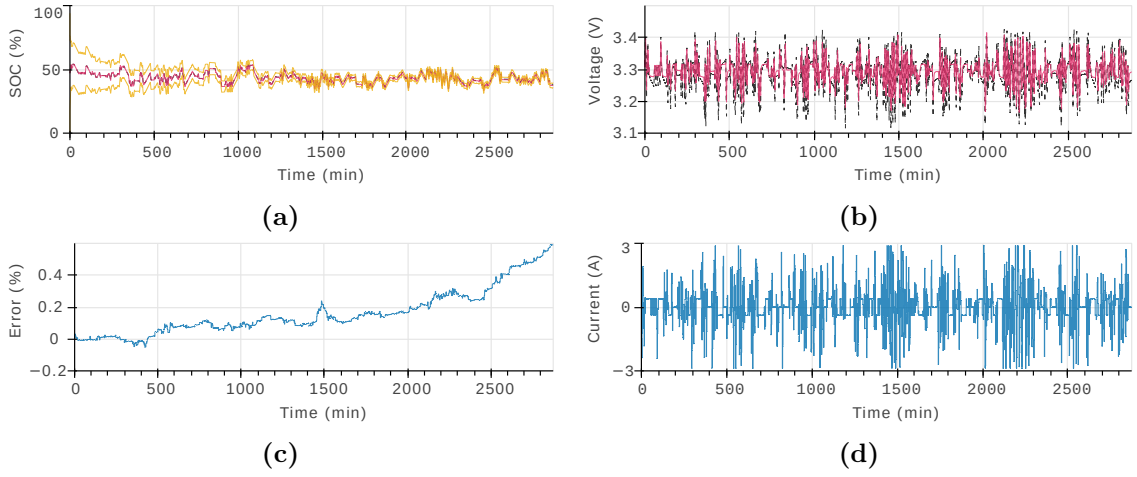

Figure 3.29: Dynamic test at 10°C ambient temperature. The plots show a) SoC during the test, b) measured voltage versus ECM estimated voltage, c) SoC error during the test, and d) test currrent profile.

The RMS error of the SoC estimation obtained in the HPPT test is 0.23%. Regarding the dynamic profile test, the RMS SoC error obtained is 0.22%. In both tests, the SoC estimate and the actual reference SoC remained within the established limits. In this case, the SPKF estimator demonstrated its ability to operate in low temperature conditions (10°C).

Figure 3.30 shows the results obtained in the HPPT test, and Figure 3.31 shows the results obtained by the SPKF in the dynamic test, both at 45ºC ambient temperature.

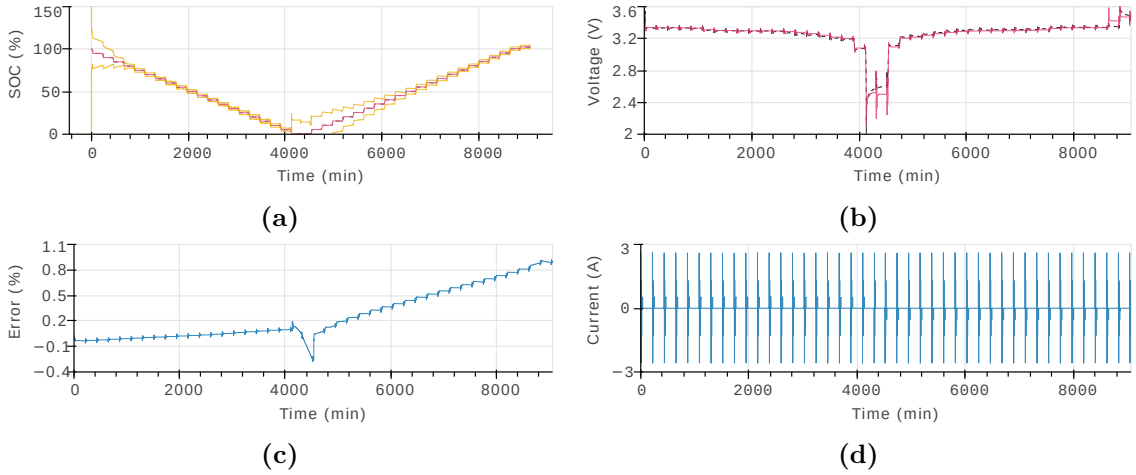

Figure 3.30: Capacity test at 45°C ambient temperature. The plots show a) SoC during the test, b) measured voltage versus ECM estimated voltage, c) SoC error during the test, and d) test currrent profile.

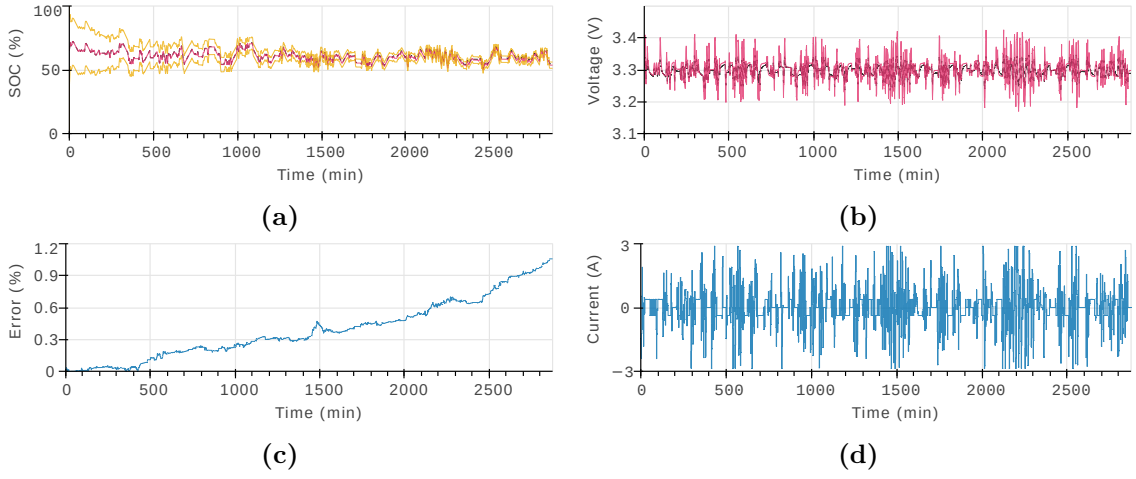

Figure 3.31: Dynamic test at 45°C ambient temperature. The plots show a) SoC during the test, b) measured voltage versus ECM estimated voltage, c) SoC error during the test, and d) test currrent profile.

Figures 3.30d and 3.31d show that the RMS error of the SoC estimation was 0.51% in the HPPT test and 0.47% in the dynamic profile test. In both cases, the SoC estimation curve remained within the established limits. Therefore, the SPKF estimator also demonstrated its ability to operate correctly in 45°C temperature conditions.

3.8 Discussion & Conclusions of the Chapter

During this Chapter, the cell to be used throughout the project has first been introduced (Section 3.2). This is a 2.5 Ah cylindrical cell from the manufacturer LW, with a voltage range of 2 to 3.6 V.

In the following Section, the thermal model of this cell has been detailed. The objective of this model is to estimate the temperature at seven different points in the cell, including the top and bottom, four points on the radial surface and the temperature at the centre. A simplified thermal model (LTM) is used which considers heat generation, heat accumulation and heat transfer by conduction, convection and radiation. The necessary parameters for this model have been obtained through specific tests, as described in the Subsection 3.6.2. Subsequently, in the Subsection 3.7.1, this thermal model has been validated and the correct acquisition of the parameters related to temperature have been verified.

In Section 3.4, the electrical model of the cell has been presented. The output equation of the selected Electrical ECM has been detailed. This ECM model uses an equivalent circuit with three RC branches to adequately capture the electrical characteristics of the cell. Rc branches have been gradually added until an appropriate voltage response has been obtained. In addition, an impedance has been added to represent the non-linear hysteresis of the LFP cell and its impact on the electrical behaviour. The necessary parameters for this model have been determined by specific tests, as explained in the Subsection 3.6.1. Then, in Subsection 3.7.2, the ECM model has been validated and the proper electrical parameters identification has been verified.

On the other hand, in the Section 3.5, the SoC estimator selected to work together with the ECM model of the cell has been detailed. This estimator uses the voltage estimate obtained from the ECM output equation, together with the actual cell voltage measurement, to correct the SoC estimate. In addition to validating the ECM model, this estimation algorithm has been also validated in the Subsection 3.7.2.

Characterisation and validation tests were performed in temperature-controlled environments (CTS and Prebatem climatic chambers, in Appendix A) and using the Digatron multiple tester with BTS-600 data acquisition software (Appendix A).

In this chapter, the focus has been on the cell-level development carried out in this study, which involved defining the cell and its characteristics. In addition to the manufacturer-provided specifications, laboratory tests were conducted to obtain additional cell parame-

ters required for developing the cell models. The chapter aimed to define and explain the fundamentals of these calculations, including the purpose of each model, the estimations they provide, and their interactions with one another.

The thermal model is the starting point, which involves a LTM at the cell level that estimated six temperatures and the core temperature. The thermal model parameters were obtained and validated against laboratory tests, encompassing both slow and faster dynamic profiles.

Subsequently, the electrical ECM of the cell has been introduced, providing the foundation for defining the state space of the SoC estimator and updating the SoC estimation. The state space model was based on an output equation that calculated the cell's terminal voltage, and each electrical effect contributing to this equation was explained and the SoC estimation update in each time step. The model parameters and their acquisition through specific tests were also discussed.

As mentioned, the electrical model worked in conjunction with the SoC estimator of the cell. By introducing the SoC as an additional state variable in the state space, the nonlinear cell system was fully captured. The calculations performed with the SPKF were explained, including the output equation.

Each model was then discussed and evaluated for its validity, assessing the adequacy of the obtained parameters. It was concluded that the models effectively captured both the thermal and electrical dynamics of the cell. All models were validated, providing a solid foundation for the subsequent extrapolation to the module level, which will be discussed in the next chapter.

4

Module-level Models

Summary

This chapter presents the module-level models developed in this thesis, covering electrical and thermal aspects. Firstly, the construction process of the prototype module is described, followed by the extrapolation of the cell-level models to the module level. A LTM is proposed at module level while the ECM together with the SPKF SoC estimator is proposed at cell level for each cell. Additionally, the simulations conducted to determine the parameters for the prototype module are presented. Finally, the models and the estimator are validated against laboratory tests.

4.1 Introduction

Chapter 4 of this thesis covers Stages 2 and 3 of the methodology proposed in Chapter 2. In the previous Chapter, the selected cell for the thesis development and the tests conducted to characterize its electrical and thermal parameters were presented. The models used to estimate temperature, voltage, and SoC of the cells were also discussed and validated at the cell-level through laboratory tests.

In this Chapter, the focus is on proposing extrapolated module-level models and validating them against laboratory tests. The specific models used and how the extrapolation was carried out are detailed.

The Chapter is structured as follows: Section 4.2 presents the experimental prototype used to validate the proposed methodology and its connection to the Cloud platform. Section 4.3 describes the module-level thermal model, while Section 4.4 discusses the module-level electrical model. Section 4.6 describes the simulations conducted to obtain the necessary parameters for developing the thermal model of the module. Section 4.7 presents the validation of the models through static and dynamic tests conducted in the laboratory. Finally, Section 4.8 provides a summary of the results and draws the main conclusions of the Chapter.

4.2 Construction of a Battery Module Prototype

In order to verify the overall efficiency of the platform, a prototype has been built using the selected cells (Section 3.2). The configuration of the connections and module geometry was carefully chosen to align with the objectives of the hypothesis testing. The module-level models were then developed, taking into account the interactions between the cells and ensuring their representation is accurate for this specific prototype.

For the construction of the prototype, the battery module structure previously employed by [209] et al. using A123 cells has been adopted. However, the updated commercial version of the A123 cells has been chosen for this study, ANR26650m1B Cell introduced in 3.2. While the new cells maintain the same general characteristics as the previous ones, they come from the manufacturer LW, representing an updated iteration of the original cells. Unlike the setup in [209], which employed an air-based TMS, no cooling system will be used in this thesis. Instead, the module will rely on natural convection for cooling.

The prototype consists of twelve cylindrical cells connected in a 12S1P electrical configuration, resulting in a module with a capacity of 2.5 Ah and a voltage range of 24 to 39.6 V illustrated in Figure 4.1. The main characteristics of the module have been summarized in Table 4.1.

Table 4.1: Module main Characteristics.

Battery Module Prototype	
Chemistry	LFP
Voltage	12 to 39.6 V
Capacity	2.5 Ah
Cell Configuration	12S1P
Number of Cells	12

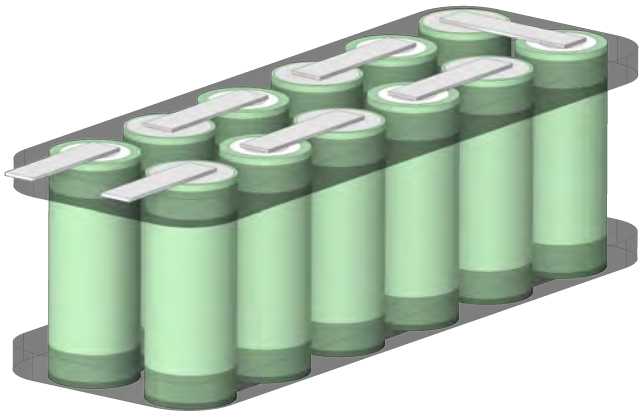

Figure 4.1: Prototype of a twelve cylindrical LFP cell module assembled with a 12S1P configuration.

The main parameters of the module will be obtained from Section 3.6. However, with twelve cells in the module, the thermal interaction involves more factors compared to when only a single cell is considered. To understand the thermal behavior of the battery module and account for the interaction between the twelve cells, a CFD simulation will be conducted (Section 4.6). This simulation will provide detailed information on the temperature distribution in the module and analyze the airflow that occurs naturally for cooling.

The selection of sensor locations for measuring the cells has been an important consideration, as this choice significantly impacts the accuracy and fidelity of the subsequently estimated states using the estimators. To collect module data, a BMS-slave, developed by Ikerlan S.COOP in [210], has been employed. The BMS device is configured to take twelve voltage measurements of the cells, located at the negative terminal of the module and at all the positive terminals of each cell. Additionally, it allows the acquisition of eight temperature measurements using NTC sensors. The arrangement of the temperature sensors in the prototype is illustrated in Figure 4.2.

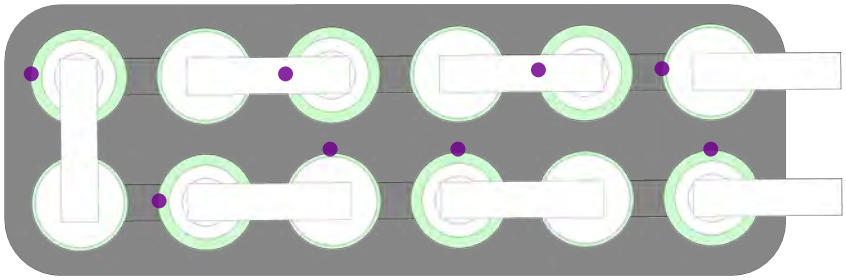

Figure 4.2: Location of the eight NTCs in the LIB prototype. Each purple dot represents a NTC sensor positioned at the midpoint of the cell's height.

The BMS-slave is connected to a BMS-master system, which consists of Serial Peripheral Interface (SPI) converter board, an Arduino Due and a Personal Computer (PC). The overall hardware configuration is depicted in Figure 4.3. The Arduino Due controls the slave and retrieves the measurements taken by the slave. This connection is facilitated by an SPI converter board. Additionally, a current sensor is connected to the negative terminal of the module, and it sends the measurements to the Arduino Due. The Arduino Due is connected to a PC, which serves as an edge device in the system. The Universal Serial Bus (USB) is responsible for wireless communication with the Cloud using the MQTT communications protocol, facilitating the transmission of battery data. In this setup, the PC acts as a gateway, emulating an edge device and enabling data transfer from the local system to the Cloud. The software code for the system is implemented in Python, allowing seamless integration and efficient data transmission. The communication with the Cloud and the integration of the battery models are described in detail in Chapter 5.

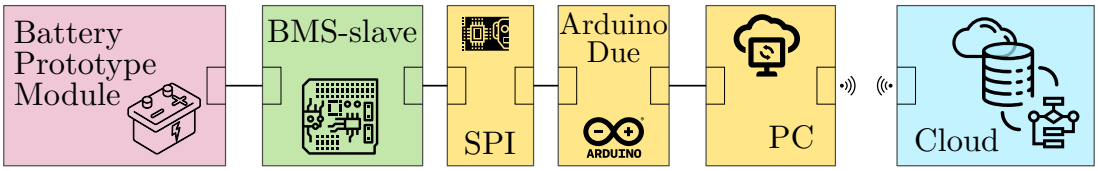

Figure 4.3: General Scheme of the Prototype Hardware.

This system has been integrated with a battery cycler, which applies specific load profiles to the module for the purpose of validating the system.

4.3 Module-level Thermal Model: Lumped Thermal Model

This Section covers a crucial part of Stage 3 in the proposed methodology outlined in Chapter 2. Specifically, this stage focuses on the development and validation of module-level models. In the previous section (Section 4.2), the construction of the prototype module was discussed, and from this prototype, the thermal model for the module will be defined.

In Chapter 1, two types of thermal models for temperature estimation in cells or modules were identified: CFD based models and LTM. CFD based models are computationally intensive and not suitable for real-time applications, while LTM models provide simpler yet effective temperature estimations. However, CFD based models are a very powerful tool to obtain the characteristics related to the thermal behaviour, so this model will be used later in Section 4.6 to obtain the parameters of the model detailed in this Section.

The cell-level thermal model performs energy balance calculations and estimates the thermal gradient within each individual cell. On the other hand, the module-level thermal model not only takes into account the internal calculations of each cell but also considers the heat transfer between the different cells within the module. This enables a more accurate representation of the temperature distribution throughout the module.

The proposed methodology involves adapting the cell's thermal model to the module's characteristics using a meshed circuit. A circuit is designed to represent all the cells and the module's geometry. The module-level model is based on the cell model, which incorporates instantaneous current, battery SoC, and cell temperatures. Each cell is individually considered in the heat generation model, and thermal interactions between adjacent cells are accounted for in the energy balance equations. The parameters obtained in Section 3.6 are reused, while new module-specific parameters (presented in Section 4.6) are incorporated.

The module-level thermal model is based on the module geometry, which requires the definition of cell-to-cell interactions in the main equations. For this purpose, a LTM circuit is placed at the location of each cell, based on the single-cell LTM model as seen in Figure 4.4a and taking into account the position of the cell within the module geometry. Figure 4.4b illustrates how two single-cell models are connected in a meshed circuit. This process is repeated at each location with adjacent cells.

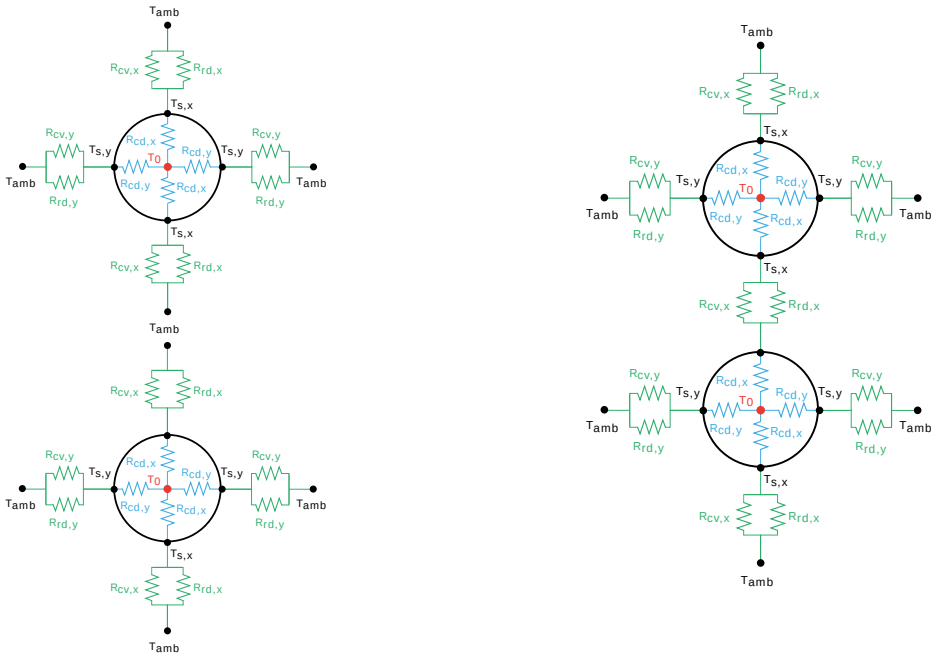

Figure 4.4: Positioning of each single cell LTM according to the geometry of the assembled prototype module a) without connection between them and b) with connection between them.

The single-cell model focuses on the interaction between the cell and its immediate environment, primarily the surrounding air. For this reason, each cell model includes the ambient temperature at its endpoints. However, in the presence of adjacent cells, the ambient temperature points are connected. In Figure 4.5, only six out of the twelve cells are depicted for simplicity, representing a simplified version of the module. All cells can exchange heat with both the ambient environment and neighboring cells. Therefore, when adjacent cells are present, the ambient temperature points on both surfaces are joined to form a closed-mesh circuit. Since the cells are separated by a distance, heat transfer between them is assumed to happen through radiation and convection, while there is no heat transfer by conduction.

As the number of cells in the module increases, the complexity of the model also increases due to the corresponding increase in the number of resistors. This is because the energy balance calculations are multiplied by the number of cells. However, this increased complexity does not pose a significant problem since the computational power provided by the Cloud platform will be utilized. The cloud platform offers ample computing resources that can handle the higher computational demands of the expanded model. Therefore, it becomes feasible to redefine the function matrix and its Jacobian (equations 3.12 and 3.13) to accommodate the larger number of cells. In this model, each cell is treated as an

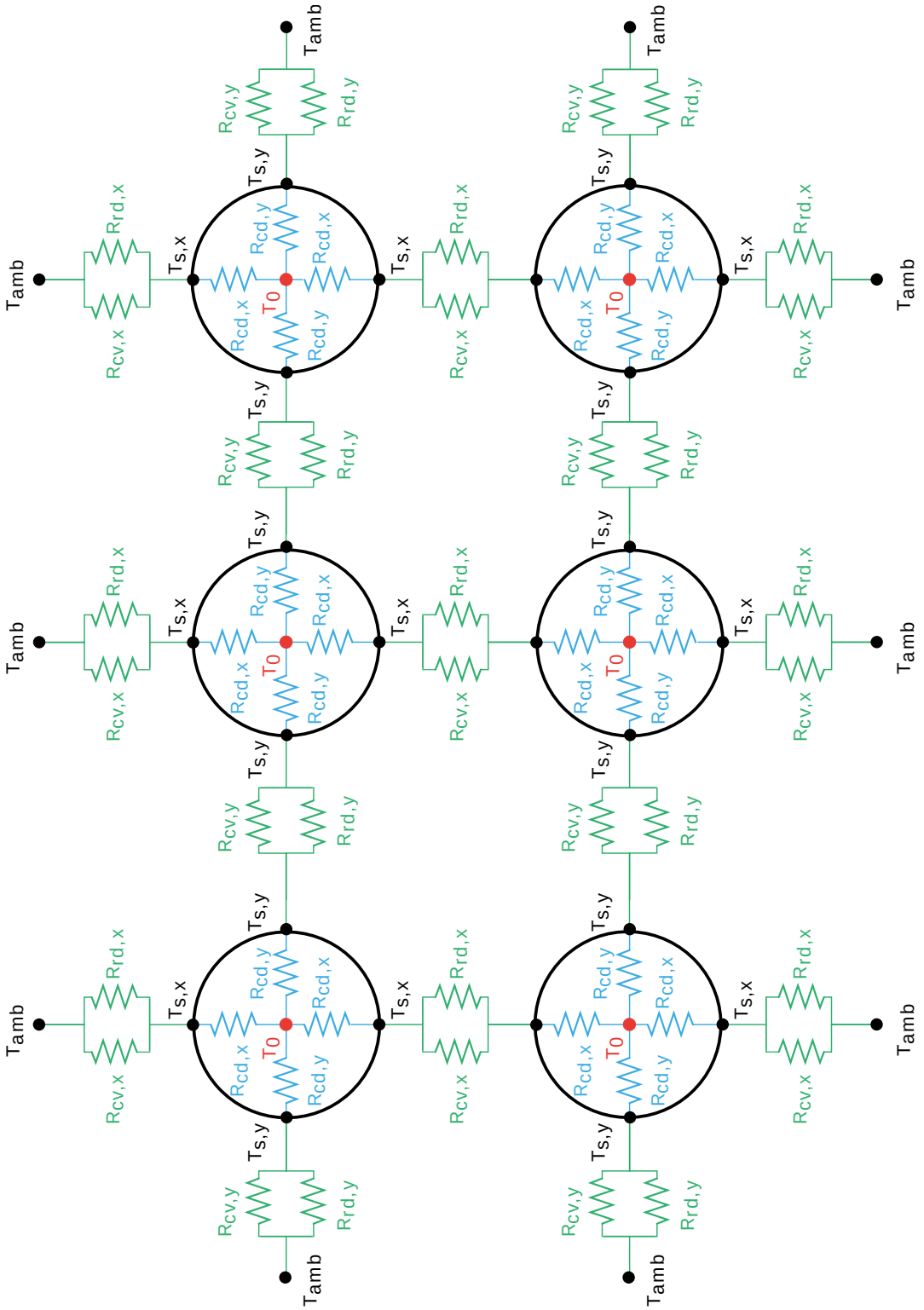

Figure 4.5: Module-level Lumped Thermal Model.

individual unit, and the parameters are determined based on the state of each cell, such as the SoC, at any given time.

The process of calculating the energy balance can be summarized as follows:

1. Perform an initial approximation of the roots (z^0) of all the cells. In this case, a matrix of dimensions 12x7 is obtained.

2. Calculate the values of the function matrix (f_{z^0}) with the initial approximations. To do this, equations 3.1 and 3.2 are applied to each surface. This gives a function matrix of dimension 84x1.

3. Obtain the Jacobian of the function matrix ($J_{f(z_0)}$), resulting in a matrix of 84x84 functions.

4. Apply Gaussian elimination to obtain a new approximation by applying equation 3.14.

5. Repeat steps 2-4 until the determined error tolerance is reached.

Note: Due to the large dimensions of these matrices, an example of their extrapolation applied to two contiguous cells is presented in the Appendix B.

When the module is not in operation, it is assumed that the thermal dispersion between cells within the same module is negligible, resulting in all cells being at the same temperature in the zero state. However, this situation changes when the module starts operating, and thermal gradients appear between cells over time. This is because not all cells operate identically due to variations in internal processes and factors such as internal resistances and self-discharge rates. Additionally, it is crucial to consider the influence of neighboring cells on each other, as there is heat transfer occurring between them continuously. In the case of cells connected in series, the temperature variations can be influenced by the overall thermal behavior of the module and the distribution of heat dissipation.

Figure 4.7 illustrates the temperature estimations obtained by running the module-level thermal model. Each data point represents a temperature estimation for a specific cell within the module. Since there are a total of 7 temperature estimations per cell, the module-level model will generate a corresponding number of data points, resulting in 84 total temperature estimations for the module.

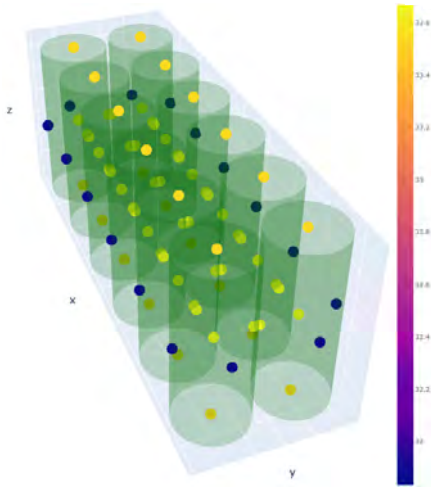

Figure 4.6

Figure 4.7: The thermal distribution within the module in a steady state is depicted, showcasing the temperature estimations provided by the thermal model at various points.

4.4 Module-level Electric Model: Equivalent Circuit Model & Sigma Point Kalman Filter

This Section introduces the proposal for extending the electrical model of the LIB to the module level. Similar to Section 4.3, this Section is part of Step 3 of the methodology outlined in Chapter 2. Its objective is to establish the electrical model at the module level and suggest an extrapolation method.

Sections 3.4 and 3.5 focused on presenting the key aspects of the electrical model for LIB cells and the SPKF, which were successfully implemented and validated for a single cell in Section 3.7. The cell-level electrical model aims to provide real-time estimates of various electrical characteristics for each cell in the module, including voltage and SoC. Instead of estimating a single SoC value for the entire module, individual SoC values are estimated for each cell, enabling more precise simulation and control.

To extend the SoC and SPKF estimator to the module level, the validated parameters from the single cell model will be used. In contrast to the module-level thermal model that treats all cells as a single entity, the electrical model considers each cell as an individual unit. The consideration of each cell as an individual unit in the electrical model is justified by the fact that the electrical behavior of each cell can be analyzed independently, as the interaction between cells in a series configuration is primarily influenced by the shared current. This allows for separate electrical modeling of each cell, enabling a more accurate representation of the overall module behavior. Therefore, a separate electrical model will be applied to each cell, as depicted in Figure 4.8 which describes six of the twelve cells in the module for a simpler illustration. The representation of six cells in the figure serves as

a simplification of the module, illustrating the parallel execution of these processes. The model will utilize the average temperature estimated for each cell, which is derived from the thermal model. This information about the cell temperature will serve as input for the electrical model, enabling the selection of appropriate parameters.

As explained above, for module-level electrical modeling, a cell-by-cell implementation of the model is proposed. This means that all 12 models will be simulated together, running concurrently in separate processes. Consequently, the cells will not interact electrically with each other, but they will share current as input. Each cell considers its own SoC and temperature when selecting the appropriate parameters during each model run for estimations. This is achieved by implementing a parallel model for each cell, where the parameters and states of each model are influenced by the respective states of the corresponding cell. This approach allows for a comprehensive analysis of the electrical behavior of the module, ensuring accurate and individualized estimations for each cell.

The proposed approach involves utilizing an ECM electrical model with an SPKF filter to enhance SoC estimation for individual cells and facilitate cosimulation. The electrical model incorporates an SoC estimation filter, which relies on the accuracy of the ECM model and its initial parameter definition. By discretizing the non-linear system, the model enables estimation of the non-linear states of the LIBs.

While ECMs are commonly used in commercial BMSs due to their simplicity, computing multiple cells simultaneously can pose a significant computational challenge. This is particularly true when attempting to parallelize tasks or instances to execute all the models concurrently. To address this, leveraging cloud-based technologies becomes crucial as they offer enhanced computational capacity and enable efficient multiprocessing. This approach enables the estimation of SoC states for each cell, and the results and validation of this model are presented in Section 4.7.

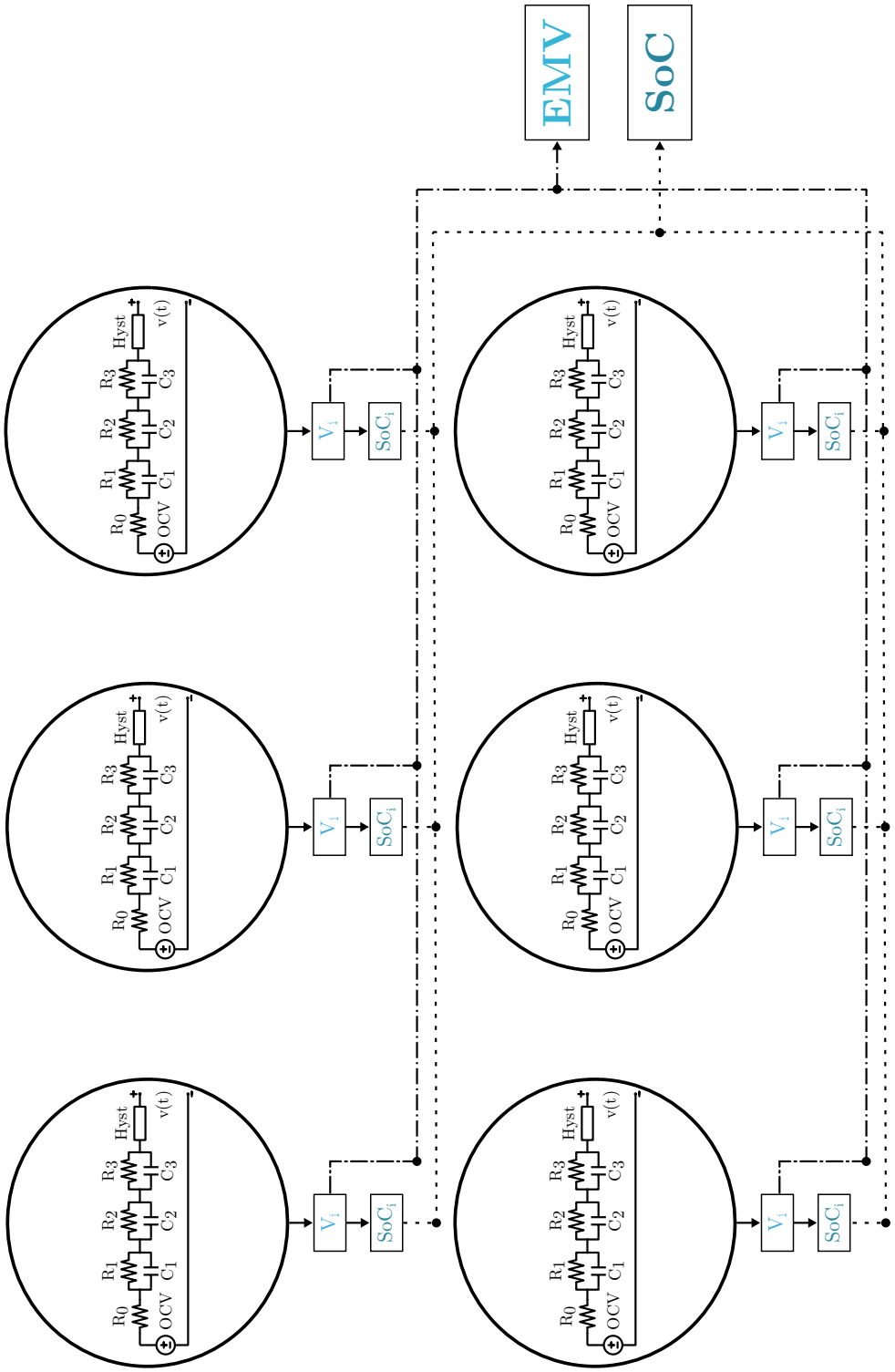

Figure 4.8: Module-level Electric Model.

4.5 Module-level Model Integration

After validating the electrical and thermal models at the module-level, this Section focuses on introducing a integration of both models into a single simulation platform where they can communicate and provide updated feedback of the state one to each other. This integration completes Stage 3 of the proposed methodology. In this section, the ECM electrical model together with the SPKF estimator will be considered in its entirety as the complete electrical model of the module.

The DTSP encompasses a set of models and estimators that describe the instantaneous state of the battery. This Section explores the possibility of integrating these models by examining their input and output data, as well as the parameters required for state estimation. The shared characteristics of input, output, and parameters shared by each model to determine their common features and how the behavior of one model influences the other is going to be analysed. For instance, the influence of temperature on the electrical behavior will be investigated.

The electrical model used in this study is an ECM that incorporates three RC phases and takes into account the battery hysteresis. This model relies on a current profile as input to calculate the battery terminal voltage (model output). Accurate voltage calculation is ensured by including various electrical parameters that represent the electrical phenomena in the battery. At each time step, the model selects appropriate values for these parameters, including an open-circuit voltage (OCV) source, internal resistance (R_0), three RC phases (R_1, C_1, R_2, C_2, R_3 and C_3), and hysteresis characteristics (G, M and M_0) that depend on both the SoC and battery temperature. Therefore, the temperature and SoC from the previous step also serve as inputs to the model.

The thermal model employed in this research is a LTM specifically designed to simulate the thermal characteristics of the battery at the module level. This model requires a current profile as input and incorporates temperature values estimated in the previous execution. Its output provides temperature calculations at different points within the battery. The model parameters include the internal resistance (R_0) and the entropic heat capacity (EHC) of the battery. While R_0 depends on the SoC and temperature, similar to the electrical model, the EHC only depends on the battery's SoC. Hence, the temperature and SoC from the previous step also serve as inputs to the thermal model.

As observed, both models require a current profile as input. Additionally, both the electrical and thermal models rely on the temperature and SoC from the previous step. In terms of parameters, the only parameter shared by both models is the internal resistance of the battery. The internal resistance of the battery consists of two main components: the resistance R_0 and the three phase resistors RC. The three phase resistors (R_1, R_2, R_3) in the electrical model are key components that define the dynamics of the battery module. In the electrical model, these resistors are employed separately to calculate each state of the SPKF state vector. Meanwhile, in the thermal model, the cumulative effect

of all four resistors is considered to simulate the thermal behavior of the battery. This thesis proposes the development of a DT for a LIB and suggests a simulation platform for comprehensive monitoring of the battery's electrical and thermal characteristics. This simulation platform consists of two models. Figure 4.9 illustrates the general framework of the augmented model.

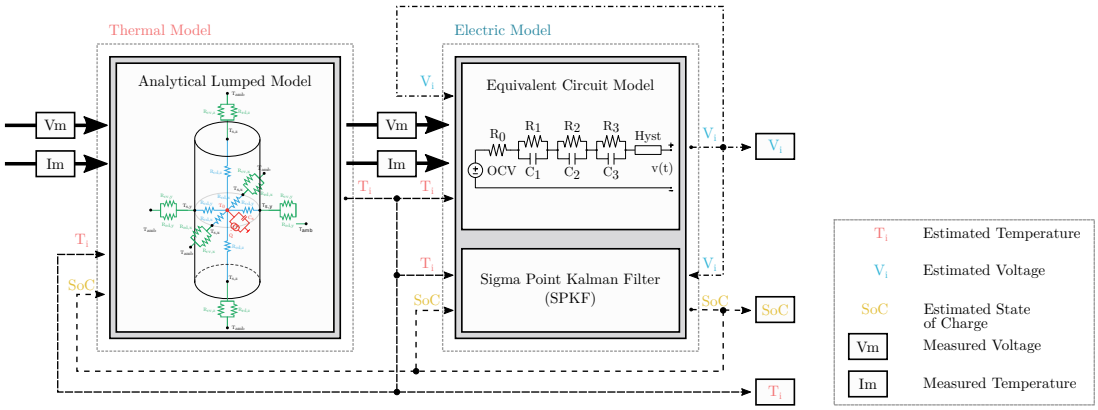

Figure 4.9: DTSP Electric and Thermal Model Integration.

The estimated states of the models will rely on the calculated battery SoC, which is determined by the voltage computed using the electrical model. This SoC value will be utilized by both the thermal and electrical models for feedback. Similarly, the thermal model computes the battery temperature, which serves as input for both models. Furthermore, as can be seen in the figure, there is a reciprocal feedback loop between the models to increase the accuracy of the estimates.

It is worth noting that the dynamics of the models differ: the electrical model exhibits faster dynamics compared to the thermal model. The different dynamics of the models require unequal sampling intervals to update the state estimates. The activation time denotes when each model is activated and executed to fulfill its function (Figure 4.10). The goal is to determine which model should be activated at each time step. Thus, the electrical model will be updated every second, while the thermal model will be updated every few seconds.

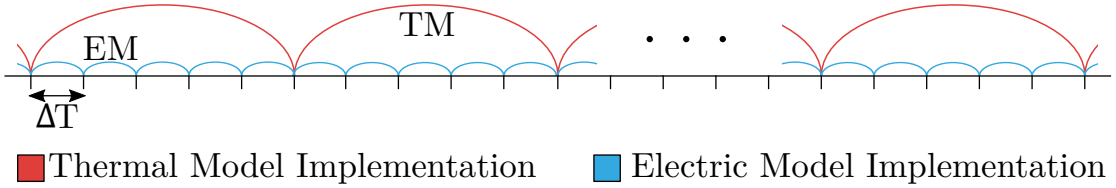

Figure 4.10: DTSP Electric and Thermal Model Activation Frequency.

The data collection rate may impose additional constraints when determining the shortest step time. The sampling rate of the BMS is 100 milliseconds, however, it is not necessary to use all measurements to predict accurately the state of the battery. Executing the electrical model every second provides a sufficient estimate of the battery state, as extracting additional meaningful information from more frequent estimations would be impractical and computationally inefficient. Therefore, it has been decided that a one-second interval is an optimal solution in terms of accuracy and computational efficiency for the electrical model.

In contrast, although temperature measurements are obtained simultaneously with current and voltage measurements, the thermal dynamics are slower than electrical dynamics. Hence, the thermal model aims to achieve accuracy by using a longer time interval. Considering heat dynamics and maintaining accuracy, it has been determined that running the thermal model every 30 seconds is appropriate.

The proposed DTSP incorporates a module-level thermal model that is capable of estimating the temperature at various points within the module, including cells without temperature sensors. These temperature estimates serve as the equivalent temperatures for each cell in the subsequent implementation of the electrical model. This approach allows for estimating the electrical response of cells that potentially experience non-uniform load demands, such as cell balancing or temperature gradients. By knowing the state of each cell, the overall response of the module can be estimated.

To this end, the BMS controls the basic safety of the module. It is responsible for obtaining voltage and temperature measurements, as well as cutting off charges and discharges when the module is out of safe operating range. The charging is cut off when the highest voltage cell reaches the maximum voltage of the module, 3.6V in this case. Discharge, on the other hand, cuts off when the module is at voltages lower than 2V. In addition, the BMS also obtains measurements of the voltage of the entire module. For the estimation of SoC and module temperature, the averages of the values obtained from the individual cells will be used.

Consequently, the DTSP is integrated into a simulation platform where the voltage, SoC, and temperatures of all cells are estimated. The communication between the models enables better parameter selection at each time step, leading to more realistic state estimation. This allows the DTSP to identify and estimate anomalies in the module's operation.

4.6 Experimental Characterisation for Cell-level Models Parameter Identification

In order to construct the prototype module, a total of 16 cells were characterized to identify cells with similar capacity and internal resistance characteristics. These selected

cells were then used for the assembly of the prototype module. These conditioning tests entail subjecting the cells to three full capacity charge and discharge cycles, as well as pulses at 20%, 50%, and 80% SOC levels. Out of the 16 conditioned cells, 12 cells were chosen based on their comparable capacitance and internal resistance values. The selected cells are listed in Table 4.2.

Table 4.2: Conditioning and Selection of Similar Cells.

Conditioning of cells					
	Q $[Ah]$	**R** $[\Omega]$		**Q** $[Ah]$	**R** $[\Omega]$
Cell 1	2.486	0.0208	**Cell 9**	2.469	0.0207
Cell 2	2.492	0.0210	**Cell 10**	2.458	0.0209
Cell 3	2.457	0.0208	**Cell 11**	2.506	0.0209
Cell 4	2.473	0.0207	**Cell 12**	2.462	0.0208
Cell 5	2.462	0.0205	**Cell 13**	2.485	0.0210
Cell 6	2.474	0.0211	**Cell 14**	2.482	0.0217
Cell 7	2.462	0.0208	**Cell 15**	2.502	0.0210
Cell 8	2.472	0.0208	**Cell 16**	2.501	0.0210

The electrical and thermal parameters obtained in Section 3.6 provide an understanding of the behavior of a single cell. In the process of selecting cells for the prototype module, it is important to consider the inherent variations in cell characteristics due to manufacturing tolerances. These variations can affect the parameters used at the module level and may result in changes in the overall performance of the module.

Indeed, when transitioning from a single-cell characterization to the module level, there are changes in the environment and operating conditions that need to be taken into account. These changes can affect the thermal behavior of the cells within the module. Factors such as heat dissipation, thermal conduction between cells, and temperature distribution across the module can all differ from the single-cell scenario. Therefore, it is necessary to re-evaluate and identify certain parameters specifically for the module configuration in order to accurately model the thermal behavior at this level. In this regard, CFD models utilizing the *Ansys-Fluent* software have been employed. CFD is a widely-used technique that predicts fluid flow phenomena by applying principles of mass, momentum, and energy conservation. These mathematical models consider various physical parameters such as velocity, pressure, temperature, density, and viscosity to accurately simulate fluid flow-related events.

The model applies conservation laws to each infinitesimal volume within the physical geometry, discretizing the corresponding partial differential equations. This approach enables the study of air flow around the prototype due to natural convection, facilitating an analysis of its thermal behavior.

For this project, *Ansys-Fluent 2022R1* software was used to implement a thermal model and analyze the prototype. Although the starting point was the model presented in [209], modifications were made to align it with the operating characteristics of the specific prototype module. The original model proposed by Leire et al. was designed for a TMS based on forced air cooling. However, in this project, natural convection was chosen as the cooling method, needing the removal of the cooling system and corresponding adjustments to the model.

Incorporating heat generation into the numerical models is crucial. To simplify the calculations, simulations were performed with a constant heat generation rate, assuming a steady-state operation. A constant heat power was applied until the model achieved convergence and thermal stability. Simulations were conducted for various operating scenarios, gradually incorporating different phenomena occurring in the fluid surrounding the module, until the scenario shown in Figure 4.11 was finalised. This methodology allowed for the step-by-step inclusion of the diverse fluid-related phenomena.

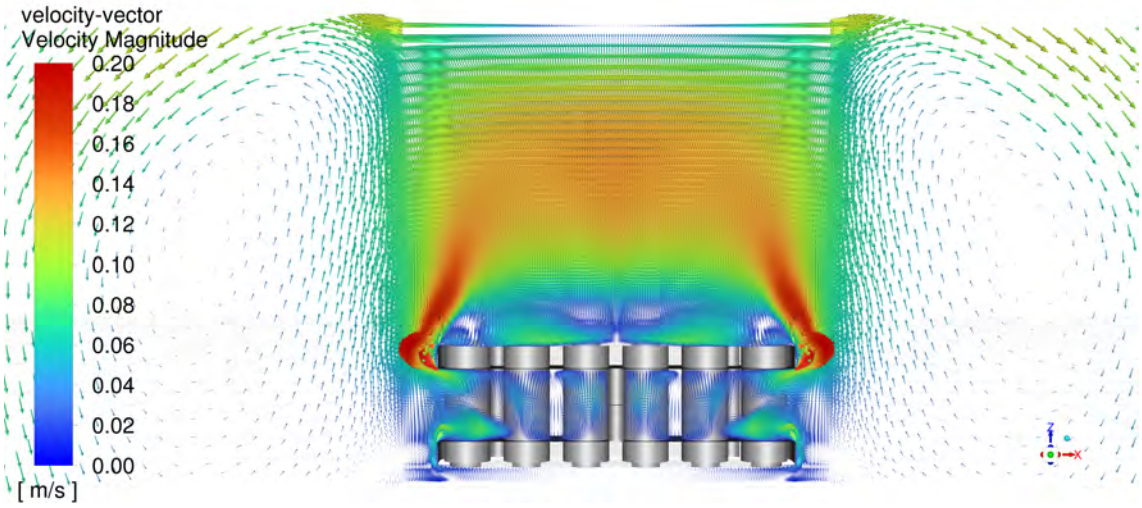

Figure 4.11: Simulations of the prototype module with CFD models incorporating turbulent airflow coupled with the heat transfer by radiation model.

Initially, the airflow was simulated without considering radiation heat transfer and with a laminar flow. Once thermal stability was achieved for both the module and the surrounding air, the turbulent flow was activated and allowed to reach a new thermal stability. The simulation took into account the Reynolds number and Rayleigh number for natural convection. Finally, the radiative heat transfer model was activated, and the simulation was repeated. This sequential process helped to expedite the convergence of parameters and incorporate additional effects that influence the behaviour of the module.

Through these simulations, the values of the convection parameter h were determined for different temperature differentials, along with the View-Factor (VF) provided by *Ansys-Fluent* itself, which are calculated as a function of the module geometry.

As for the electrical parameters of the cells, they remain unchanged (or negligibly affected) even when connected in series with other cells. Hence, no electrical characterization tests were repeated, except for capacity tests. As the twelve cells are connected in series, ideally the capacity of the module should be equal to the capacity of the cell. However, it has been found that each cell has its own capacity. Due to imbalances among the cells, there will always be a limiting cell in terms of charging and another limiting cell in terms of discharging when all cells are in the same SoH. Consequently, the module's capacity will be slightly reduced.

The BMS of the prototype module controls and cuts off charging and discharging when the first cell reaches the upper and lower voltage limits within the operating range of the cells. Due to small imbalances within the module, not all cells are charged or discharged within the full SoC range. To calculate the SoC of each cell, each cell capacity data is considered. This allows for calculating the SoC of each cell relative to the total capacity of the module, providing an accurate estimation of the individual cell's state of charge.

4.7 Results & Discussion of Module-level Models

This section of Chapter 4 aims to present the module-level simulations conducted in this thesis. The ultimate goal is to verify the proper functioning of the proposed module-level models defined in Sections 4.3 and 4.4.

Upon completing this validation, the Objective 2 (*O2*) we will achieved as stated in the introduction of this thesis, which involves developing and validating module-level models to understand and predict the behavior of the overall system and the interactions among multiple cells within the module. Furthermore, this section will partially address the first hypothesis (**H1**) presented in the thesis. The hypothesis states the following: "Models of modules that consider individual cells provide relevant additional information to that obtained by module sensors."

4.7.1 Results & Discussion: Module-level LTM Validation

This subsection presents the results obtained using the module-level thermal model proposed in section 4.3. The objective is to verify the accuracy of the temperature estimation at different points of the module. For this purpose, as shown in section 4.2, eight NTCs have been placed at strategic points to capture the temperature gradient inside the module during its operation (Figure 4.2).

These points are considered strategic, as they are supposed to adequately describe all key points of the module. Points in the coldest areas of the module have been selected as T5 and T6 for temperature measurement. On the other hand, T2 and T3 are expected to be the hottest points of the module, as these are located in the centre of the module and therefore have less cell surface to exchange heat with the surrounding air, which makes

them more sensitive to the heat generated by the neighbouring cells. The thermocouple positions have been illustrated in the Section 4.2 where the prototype module has been defined. All recorded temperatures have been obtained using the BMS connected to the prototype module.

All experimental tests were carried out at the Energy Storage Laboratories of Ikerlan S.COOP, located at its headquarters in Galarreta (Hernani). The prototype module was connected to a battery module tester (details of the cycler are provided in Appendix A). Two types of tests were performed: i) a capacity test in which the module was fully charged and discharged over the entire SoC range, and ii) a dynamic test in which the module was subjected to an electric vehicle driving profile. These two tests were repeated at three temperatures: 10°C, 25°C and 45°C.

First, the results obtained at 25°C in both tests are presented, which will serve to evaluate the model's ability to represent the temperature gradient when the module is operated at this ambient temperature. Figure 4.12 shows the capacity test, where the prototype module is fully charged and discharged for 2 cycles. Figure 4.12a shows the reference SoC of the module, calculated using a Coulomb counting method. Subsequently, Figure 4.12b shows the temperatures measured by the NTCs and Figure 4.12c depicts their respective estimates. In addition, Figure 4.12d shows the errors obtained in the estimations.

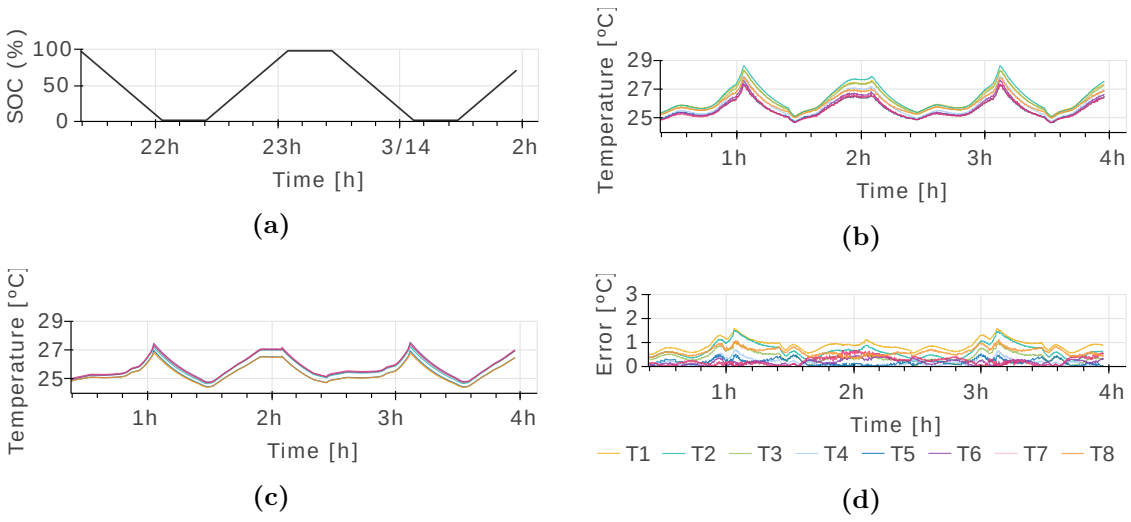

Figure 4.12: Module-level. Capacitance test at 25°C ambient temperature. The graphs show a) the SoC during the test, b) the temperatures measured by the LTM, c) the temperatures estimated by the LTM and d) the error of the LTM in °C.

The estimates in Figure 4.12 are plotted separately in Figure 4.13 for more detail. In Figures 4.13a-4.13g, the discontinuous black curves represent the actual measurements. Meanwhile, the coloured plots represent the LTM estimation of the module at that point of the module.

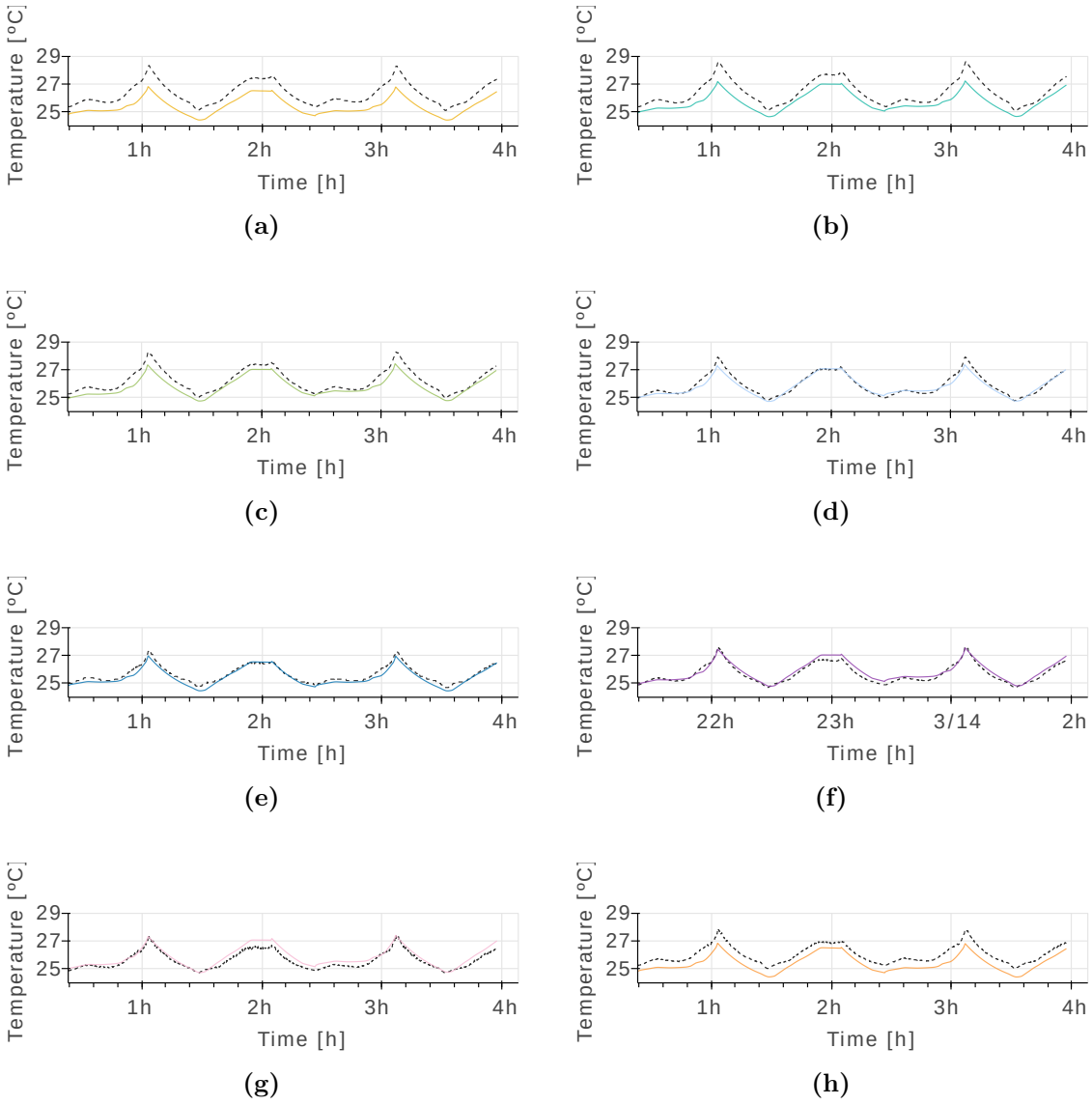

Figure 4.13: Module-level. Capacity test at 25°C ambient temperature. The graphs show the measured temperature by a NTC versus the estimated temperature in a) T1, b) T2, c) T3, d) T4, e) T5, f) T6, g) T7, and h) T8.

The results obtained by the model provide a detailed representation of the temperature in the module. As anticipated, the measurements reveal that the T2 and T3 points have the highest temperature. This is caused due to the thermocouples location in the central area of the module, where the surrounding air has a lower capacity to move and cool these locations (Figure 4.14). In addition, as these cells are located in the centre, they have a

larger heat exchange surface with the adjacent cells. Regarding the LTM of the module, it succeeds in correctly estimating these hottest points, with an average error of 0.4°C and a maximum error of 1.03°C. On the other hand, points T5 and T6 have been identified as the coldest points of the module. This is because these thermocouples are located outside the module, where the surrounding air is present. Similarly, in this case, the model has been able to properly identify these coldest points, with an average error of 0.19°C and a maximum error of 0.53°C.

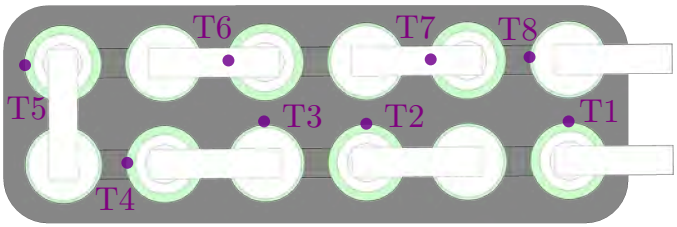

Figure 4.14: Location of the NTCs through the module.

The efficiency of the model has been further tested by performing another dynamic test at an ambient temperature of 25°C, using dynamic profiles, as mentioned earlier. On this test, the module has been subjected to intermittent discharges and charges with more demanding profiles involving higher currents. The profile used resembles an electric car travelling to and from the workplace. In addition, these journeys have been repeated to ensure that the module operates over the full SoC range, from 100% SoC to 0%.

For a clearer visualization, from this point onwards, the estimates of these key points in the module will be shown. However, the error of all the estimated points, obtained by comparing the model's estimation with the actual measurements from the prototype module, will also be provided. These points correspond to locations where an NTC sensor is connected and accurate comparisons can be made.

Figures 4.15 and 4.16 show the results obtained in the dynamic test. Figure 4.15a presents the SoC profile in which the module has been operating during the test, while Figure 4.15b shows the temperatures measured by the thermocouples. Next, Figure 4.16a shows the estimate made at point T3, and Figure 4.16b shows the estimate at the coldest point, T5. Finally, Figure 4.16c shows all the errors obtained in this test.

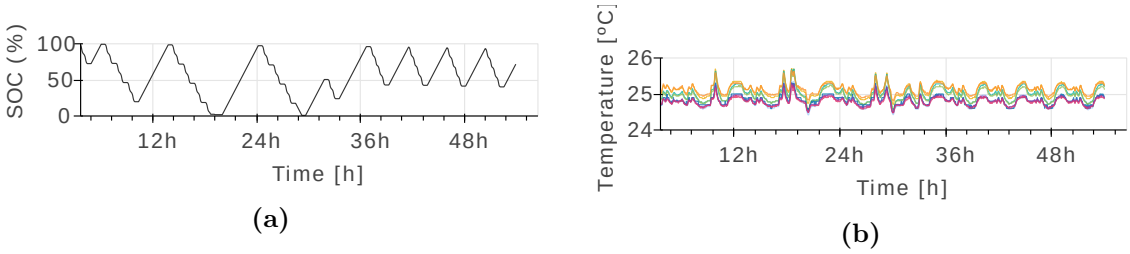

(a) (b)

Figure 4.15: Module-level. Dynamic test at 25 °C ambient temperature. The graphs show a) the SoC during the test and b) the temperatures measured by the NTCs

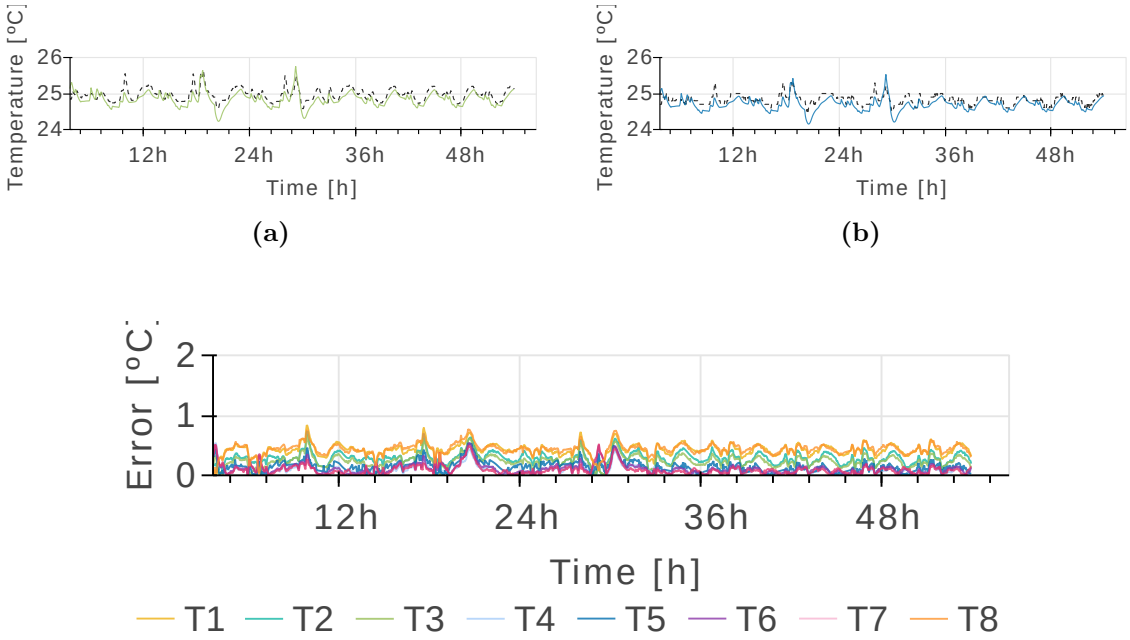

(a) (b)

(c)

Figure 4.16: Module-level. Dynamic test at 25°C ambient temperature. The graphs show the measured temperature by a NTC versus the estimated temperature in a) T3, b) T5, and c) the error in all the estimations of the LTM in °C.

Based on the dynamic test, it can be observed that the model is able to represent the thermal gradient of the module accurately, obtaining a maximum error of 0.66°C. The internal resistance of the cells is higher when the cells operate at low SoC, which causes a higher Joule loss (irreversible heat generation) in the cells. This is evident in the test shown, where the module temperature increases by almost one degree at these points. Nevertheless, Figures 4.16a and 4.16b confirm that the LTM adequately estimates these temperature variations when the ambient temperature is 25°C.

In the following, the results obtained at an ambient temperature of 45°C will be shown. In this case, the estimations at the key points of the module and the errors obtained by comparing the measured temperatures (Figure 4.17b) with those estimated by the LTM (Figures 4.18a and 4.18b) will also be presented.

On the other hand, the same information as in the capacity test is shown in the corresponding dynamic test performed at 45°C ambient temperature in Figures 4.17 and 4.18.

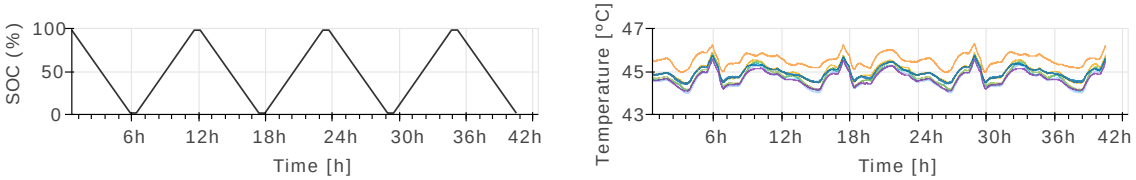

(a) **(b)**

Figure 4.17: Module-level. Capacity test at 45°C ambient temperature. The graphs show a) the SoC during the test and b) the temperatures measured by the NTCs

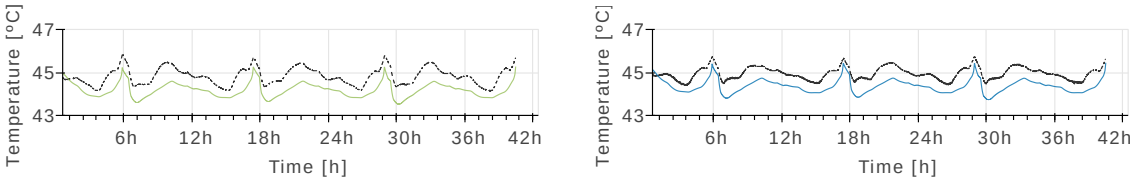

(a) **(b)**

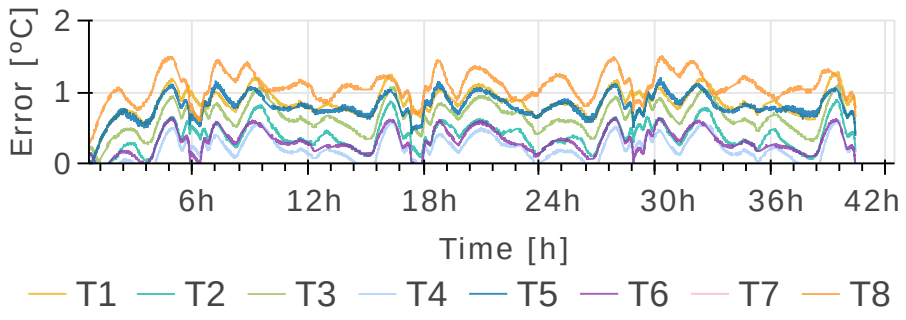

(c)

Figure 4.18: Module-level. Capacity test at 45°C ambient temperature. The graphs show the measured temperature by a NTC versus the estimated temperature in a) T3, b) T5, and c) the error in all the estimations of the LTM in °C.

Furthermore, Figures 4.19 and 4.20 depict the dynamic profile test applied to the module at 45°C.

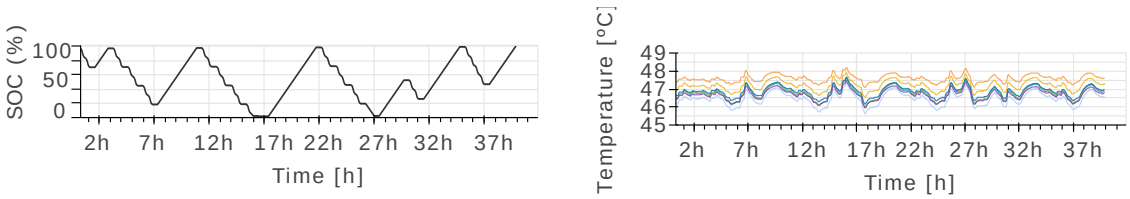

(a) **(b)**

Figure 4.19: Module-level. Dynamic test at 45°C ambient temperature. The graphs show a) the SoC during the test and b) the temperatures measured by the NTCs

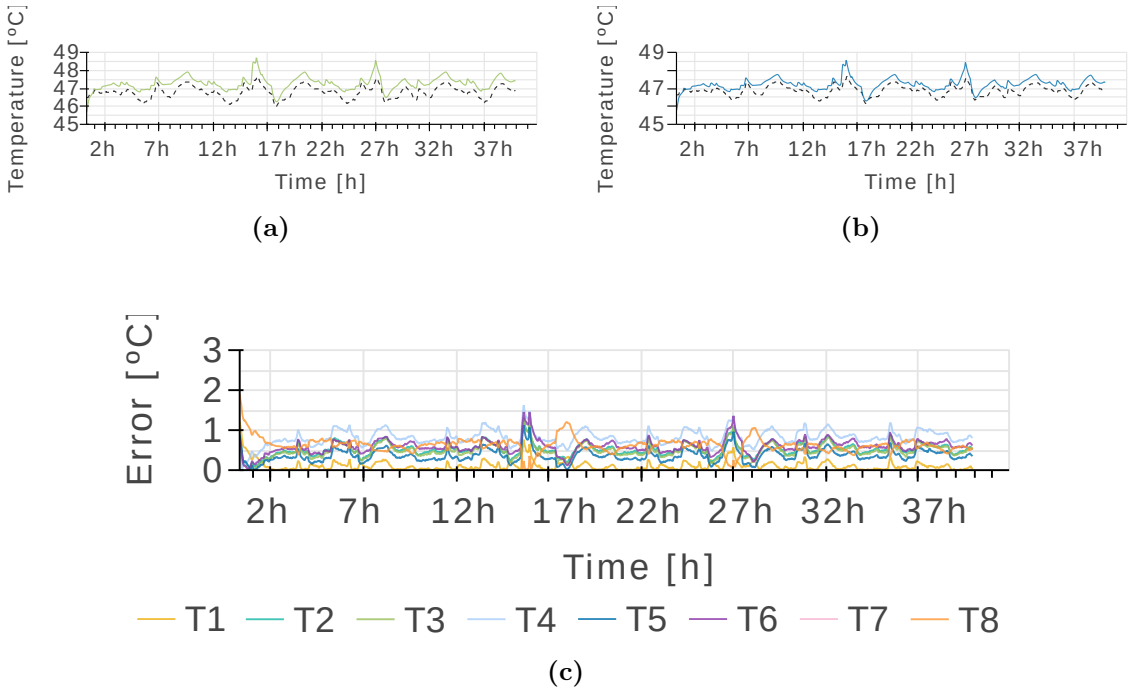

(a) **(b)**

(c)

Figure 4.20: Module-level. Dynamic test at 45°C ambient temperature. The graphs show the measured temperature by a NTC versus the estimated temperature in a) T3, b) T5, and c) the error in all the estimations of the LTM in °C.

In both cases, the error is around 1°C, with the dynamic test exhibiting a lower error that mostly stays within one degree. In the capacity test the model has been shown to be able to track the temperature of the T5 and T3 points adequately with an average error of 0.65°C and 0.8°C and a maximum error of 1.11°C and 1.12°C. This verifies that the model is capable of estimating the temperature gradient in the module at 45°C. Finally, both tests were also repeated at a temperature of 10°C. The results obtained are shown in Figures 4.21 and 4.22. Furthermore, Figures 4.23 and 4.24 depict the dynamic profile test applied to the module at 10°C.

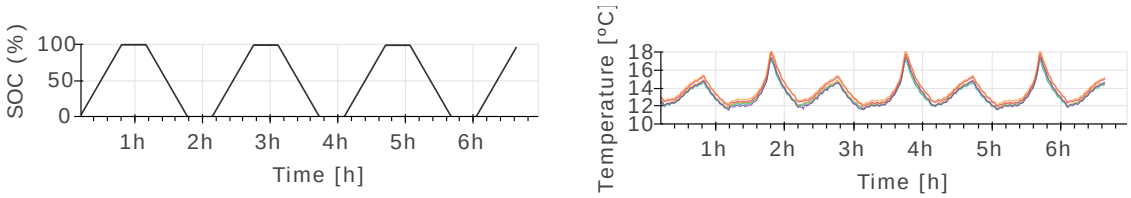

(a) **(b)**

Figure 4.21: Module-level. Capacity test at 10°C ambient temperature. The graphs show a) the SoC during the test and b) the temperatures measured by the NTCs

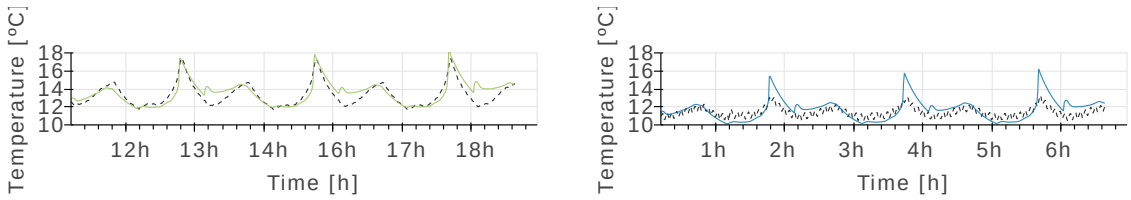

(a) **(b)**

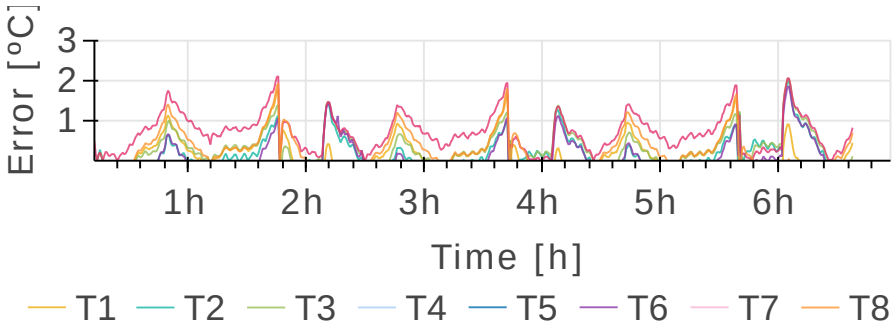

(c)

Figure 4.22: Module-level. Capacity test at 10°C ambient temperature. The graphs show the measured temperature by a NTC versus the estimated temperature in a) T3, b) T5, and c) the error in all the estimations of the LTM in °C.

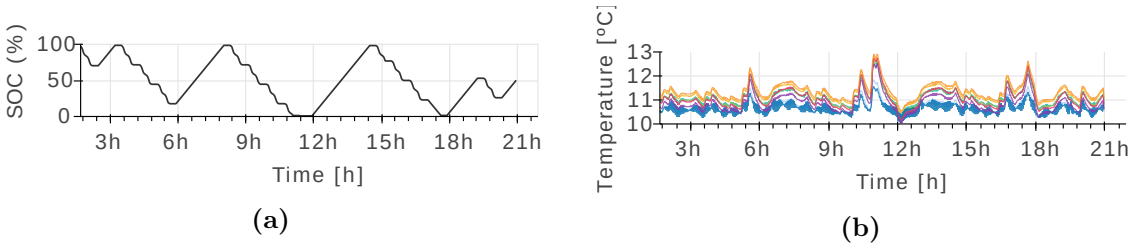

(a) (b)

Figure 4.23: Module-level. Dynamic test at 10°C ambient temperature. The graphs show a) the SoC during the test and b) the temperatures measured by the NTCs

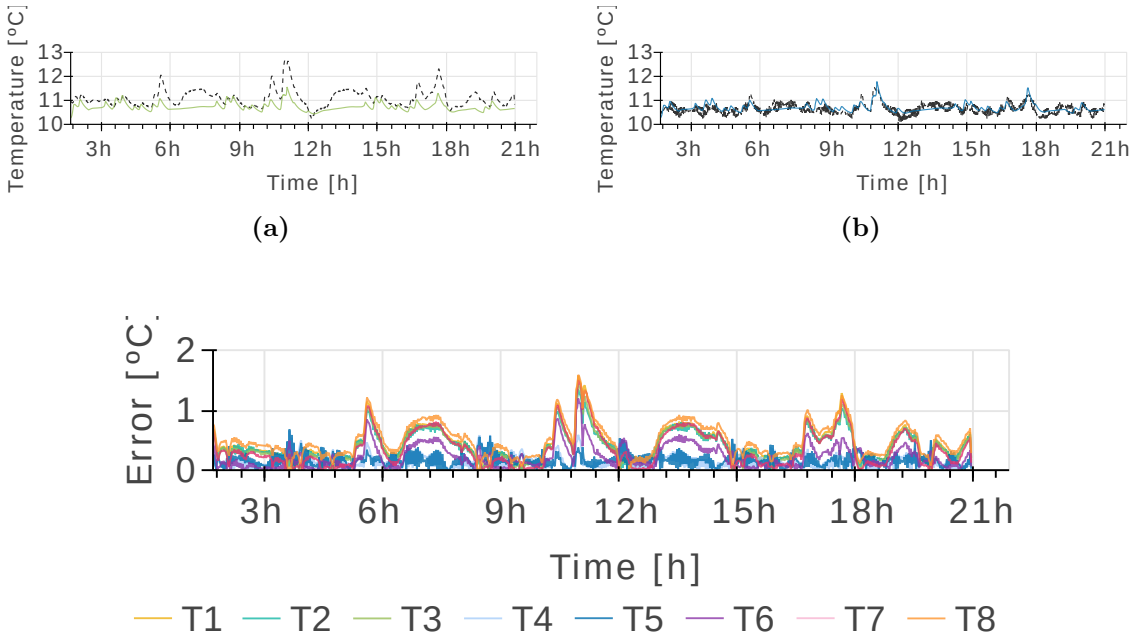

(a) (b)

(c)

Figure 4.24: Module-level. Dynamic test at 10°C ambient temperature. The graphs show the measured temperature by a NTC versus the estimated temperature in a) T3, b) T5, and c) the error in all the estimations of the LTM in °C.

The presented tests have also demonstrated the model's ability to track the temperature of the module. In these tests, average errors of 0.59 and 0.48 °C were obtained, with maximum errors of 1.69 and 1.43 °C.

4.7.2 Results & Discussion: Module-level ECM and SPKF Validation

This final subsection of the chapter aims to present the results obtained with the ECM at the module level and demonstrate its effectiveness in tracking the voltage of each cell in the module, as well as its robustness in estimating the SoC of each cell. To achieve this, all the tests used for the validation of the LTM at the module level in Section 4.7.1 will be utilized.

The voltage measurements of each cell obtained by the BMS connected to the prototype module have been used for this purpose. As explained in Section 4.4 when presenting the proposal for adapting the cell model to the module model, an ECM together with an SPKF will be executed for each cell. Therefore, the electrical model does not require additional parameter identification for its extrapolation to the module level. The parameters already used in the cell models will continue to be utilized.

The measurement of SoC in LIBs is a complex task, and selecting an appropriate reference for this parameter is of utmost importance. One commonly used method is Coulomb counting, which involves tracking the amount of charge entering or leaving the battery over a specific time period. However, this method is subject to cumulative errors over time. In the present study, it is assumed that the duration of the conducted tests is sufficiently short to minimize the impact of cumulative errors in the current integration.

Starting with the analysis of the capacity test at 25°C, first, all the measurements and estimations made by the electrical model will be presented. Figure 4.25 shows these results along with the SoC profile of the test. The measurements obtained by the BMS (Figure 4.25b) are displayed, as well as all the estimations made by the ECM (Figure 4.25d). Subsequently, Figure 4.25 presents the SoC estimation for each cell, along with the comparison of the estimated and measured voltages.

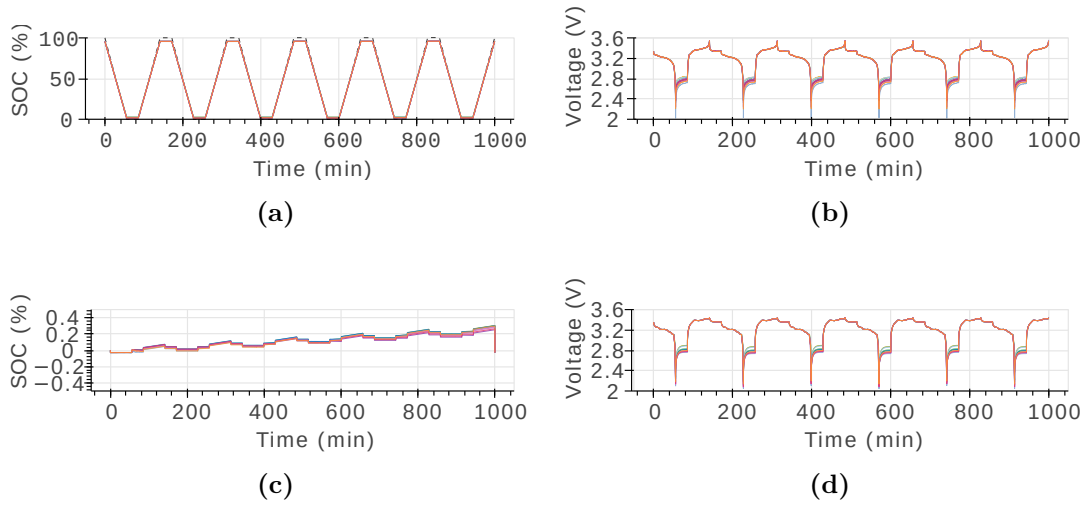

Figure 4.25: Module-level. Capacity test at 25°C ambient temperature. The graphs show a) the SoC during the test, b) the cell voltages measured by the BMS, and c) the cell voltages estimated by the ECM.

Analyzing the results, it has been found that Cell 5 is the most limiting cell at low SoCs, which makes it reach the minimum voltage threshold earlier. This cell is not the cell with the lowest capacity (as shown in Table 4.2), which indicates that it is more discharged than the others. Therefore, moving forward, Cell 5 will be considered the lower limiting cell. On the other hand, the upper limiting cell will be defined as the cell that reaches the upper voltage limit first. In this case, Cell 9 serves as the upper limiting cell. Examining the graph of SoCs errors (Figure 4.25c) obtained by the SPKF, it is evident that the maximum error is 0.15%.

To facilitate visualization and understanding of the results, subsequent sections will focus solely on these two cells. Thus, Figures 4.26 and 4.27 present the results obtained of the Cell 5 and Cell 9 from the capacity test conducted at 25°C. On the other hand, Figures 4.28 and 4.29 show the results obtained in the dynamic test.

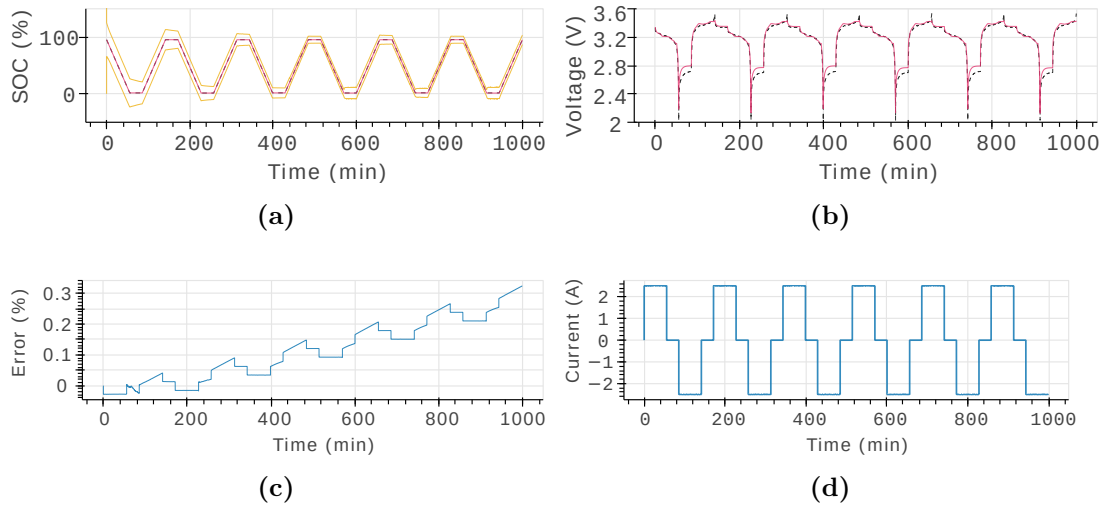

Figure 4.26: Module-level. Cell 5. Capacity test at 25°C ambient temperature. The graphs show a) the SoC during the test, b) the cell voltage measured by the BMS versus estimated by ECM, and c) error of soc obtained, and d) test current.

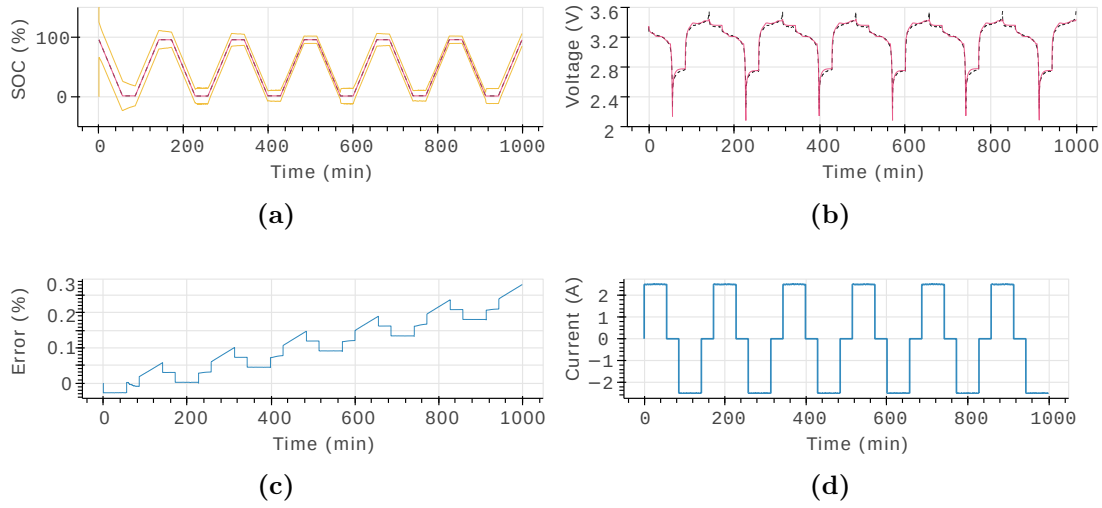

Figure 4.27: Module-level. Cell 9. Capacity test at 25°C ambient temperature. The graphs show a) the SoC during the test, b) the cell voltage measured by the BMS versus estimated by ECM, and c) error of soc obtained, and d) test current.

The RMS error of the SoC estimation obtained in the capacity test is 0.15% and 0.13% in Cell5 and Cell9, respectively. In both figures it can be seen that with the obtained SoC estimation, the voltage in the model output equation correctly represents the voltage measured by the BMS in both cells.

The following are the results obtained for both cells in the dynamic test of the prototype module at 25°C ambient temperature. Figure 4.28 shows the results obtained of Cell 5, and Figure 4.29 shows the results obtained from Cell 9.

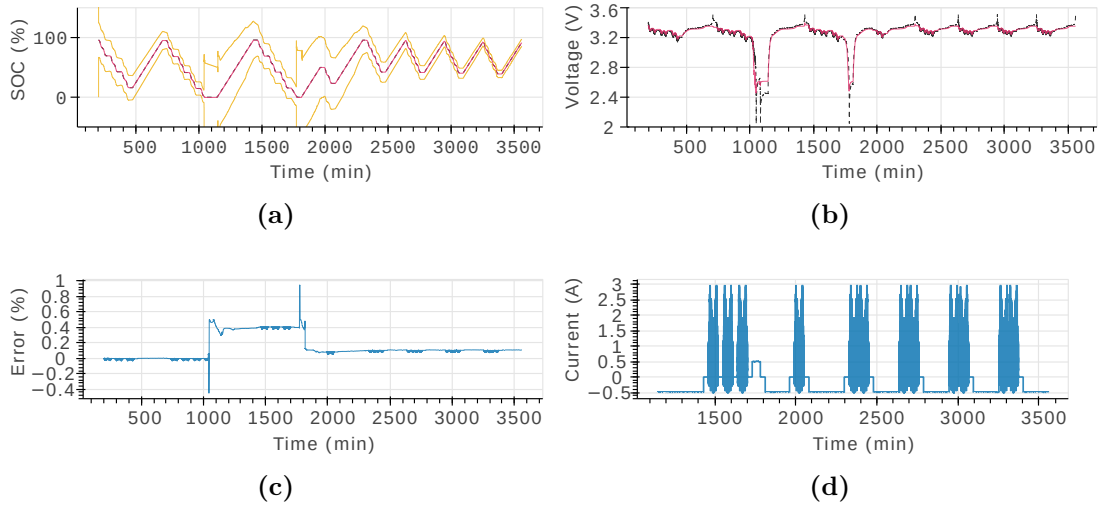

Figure 4.28: Module-level. Cell 5. Dynamic test at 25°C ambient temperature. The graphs show a) the SoC during the test, b) the cell voltage measured by the BMS versus estimated by ECM, and c) error of soc obtained, and d) test current.

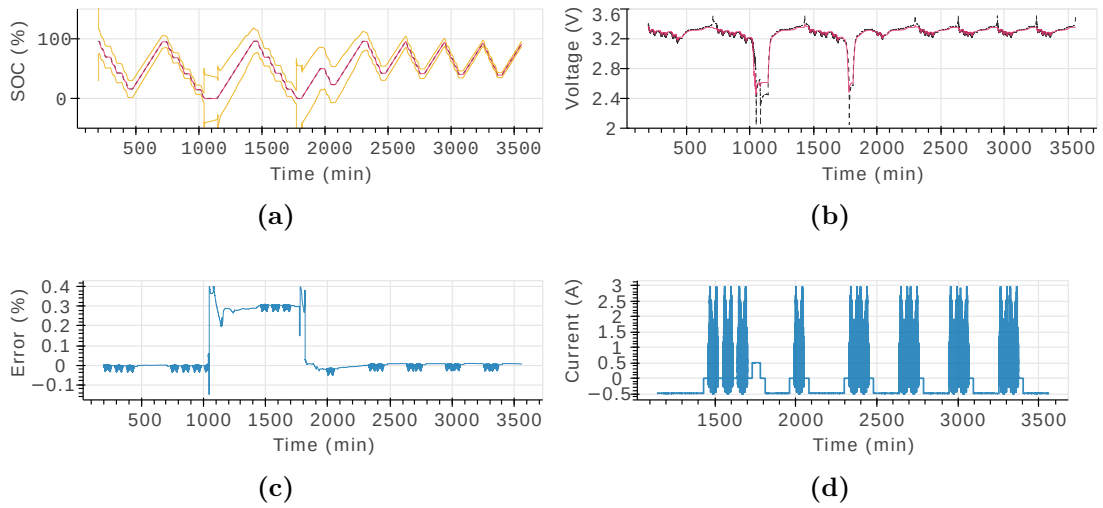

Figure 4.29: Module-level. Cell 9. Dynamic test at 25°C ambient temperature. The graphs show a) the SoC during the test, b) the cell voltage measured by the BMS versus estimated by ECM, and c) error of soc obtained, and d) test current.

The errors obtained in this dynamic test for Cells 5 and 9 in the estimation of SoC are 0.24% and 0.19% respectively. This test has faster dynamics and covers the entire range of module SoC. In both SoC estimations, it can be observed that the SPKF opens its boundaries when the module is at low SoC. This increase in uncertainty in the SoC estimation is due to a greater difference between the measured voltage and the estimated voltage at low SoCs. However, as the test progresses, these boundaries gradually close, demonstrating that the filter is accurately estimating the SoC.

Similar to the cell-level models and the module-level LTM, the module-level electrical model has also been analysed at ambient temperatures of 10°C and 45°C. Below are the results obtained in the capacity test at 10°C, including the results obtained from cells 5 and 9, as shown in Figure 4.30 and Figure 4.31.

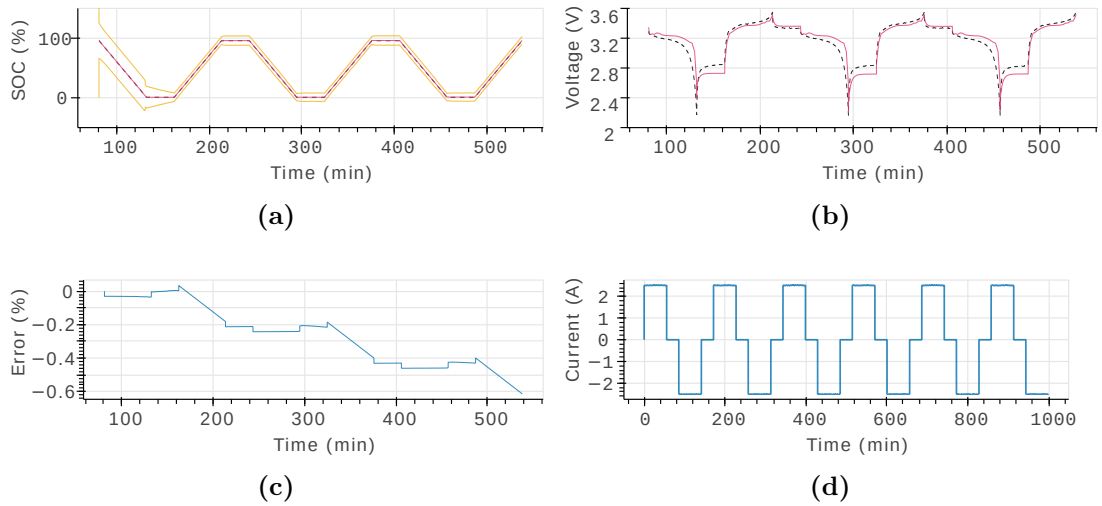

Figure 4.30: Module-level. Cell 5. Capacity test at 10°C ambient temperature. The graphs show a) the SoC during the test, b) the cell voltage measured by the BMS versus estimated by ECM, and c) error of soc obtained, and d) test current.

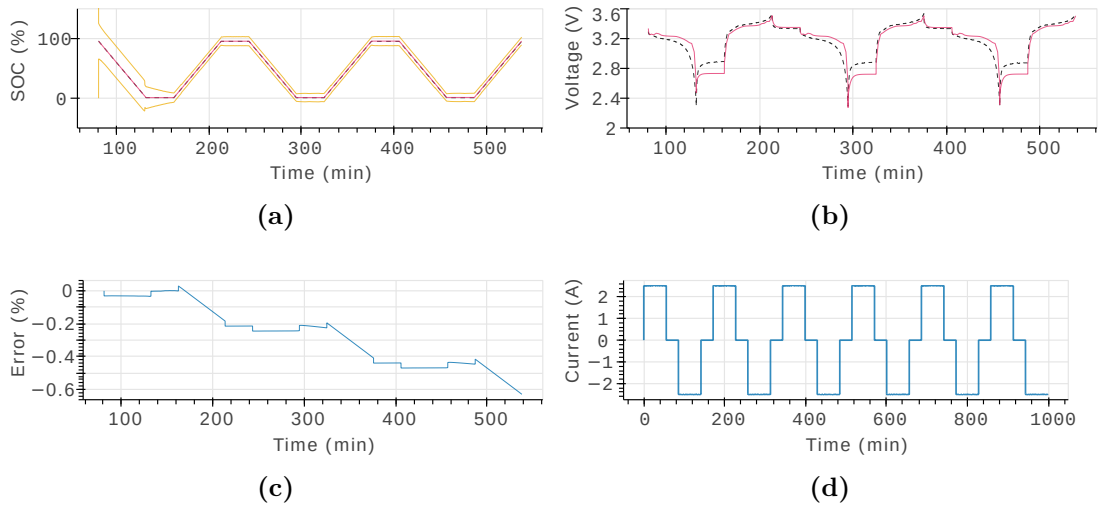

Figure 4.31: Module-level. Cell 9. Capacity test at 10°C ambient temperature. The graphs show a) the SoC during the test, b) the cell voltage measured by the BMS versus estimated by ECM, and c) error of soc obtained, and d) test current.

The obtained RMS errors in SoC for Cells 5 and 9 of the module at 10°C ambient temperature are 0.31% and 0.32%, respectively. These errors are within an acceptable range, indicating that the model is capable of accurately capturing the slower dynamics at 10°C. To further assess the model's performance, a dynamic test was conducted. Figure 4.32 presents the results of the dynamic test for Cell 5, while Figure 4.33 displays the results obtained for Cell 9.

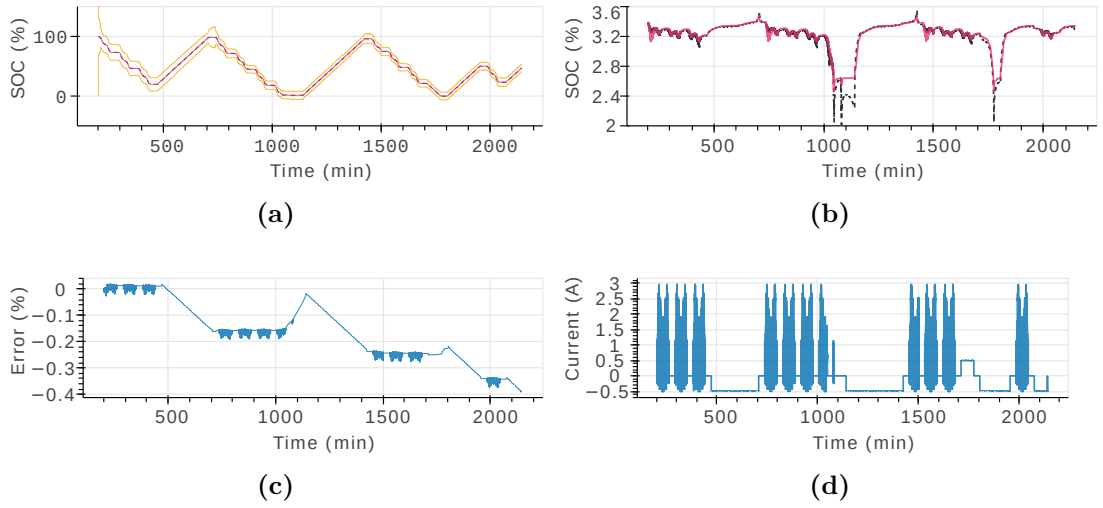

Figure 4.32: Module-level. Cell 5. Dynamic test at 10°C ambient temperature. The graphs show a) the SoC during the test, b) the cell voltage measured by the BMS versus estimated by ECM, and c) error of soc obtained, and d) test current.

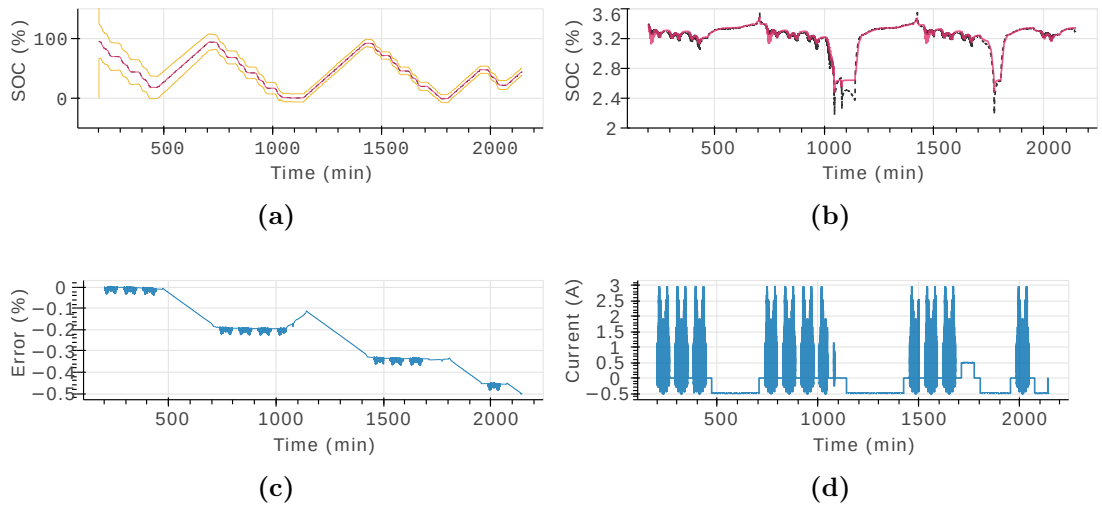

Figure 4.33: Module-level. Cell 9. Dynamic test at 10°C ambient temperature. The graphs show a) the SoC during the test, b) the cell voltage measured by the BMS versus estimated by ECM, and c) error of soc obtained, and d) test current.

In this dynamic test at 10°C, the RMS errors obtained for SoC estimation in Cell 5 are 0.27%. Similarly, errors of 0.25% were obtained for Cell 9. Throughout this test, the SPKF boundaries remained closed for most of the time, indicating that the estimator made estimations with a high degree of confidence. Thus, it can be concluded that the model performs well at low temperatures such as 10°C.

Next, the model's behavior at high temperatures will be analyzed. Figure 4.34 illustrates the capacity test conducted at an ambient temperature of 45°C in the climatic chamber where the module was cycled. Additionally, Figure 4.35 depicts the dynamic profile applied to the module.

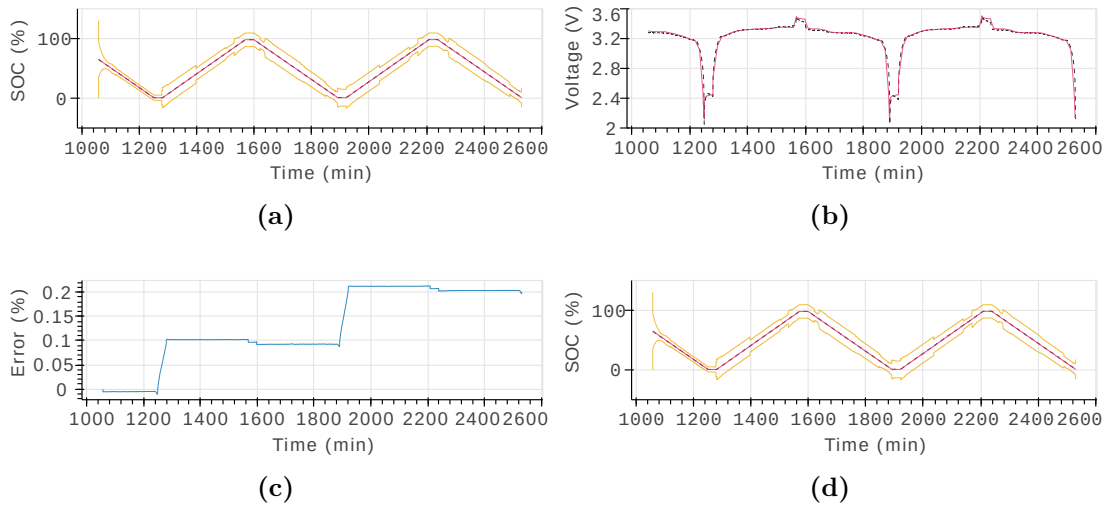

Figure 4.34: Module-level. Cell 5. Capacity test at 45°C ambient temperature. The graphs show a) the SoC during the test, b) the cell voltage measured by the BMS versus estimated by ECM, and c) error of soc obtained, and d) test current.

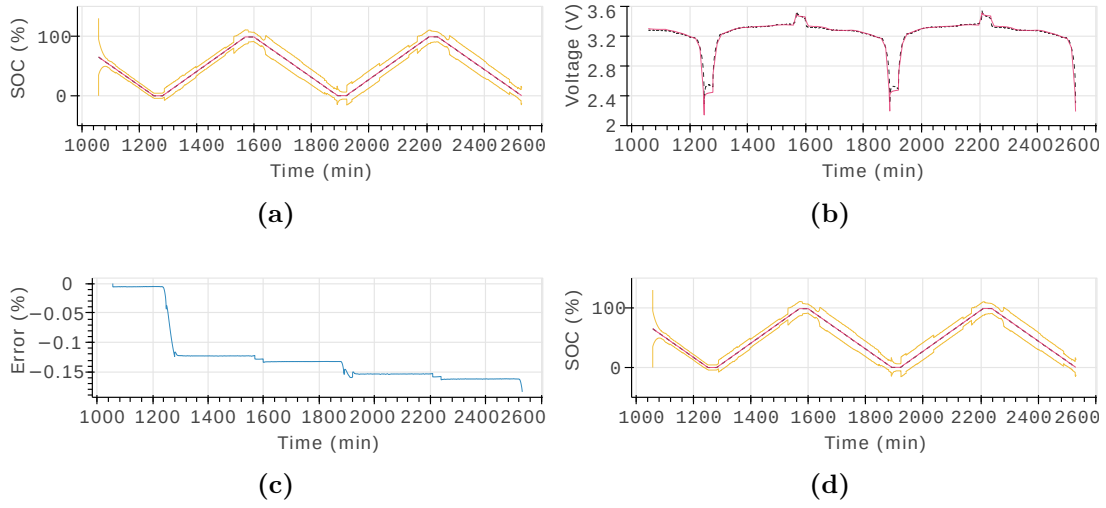

Figure 4.35: Module-level. Cell 9. Capacity test at 45°C ambient temperature. The graphs show a) the SoC during the test, b) the cell voltage measured by the BMS versus estimated by ECM, and c) error of soc obtained, and d) test current.

During the capacity test conducted on the module at 45°C, an RMS error of 0.15% was obtained for the SoC estimation of Cell 5, while Cell 9 exhibited an error of 0.13%. These errors are within an acceptable range, indicating the reliability of the model. Subsequently, the model's performance was evaluated under more demanding and rapidly changing conditions. The dynamic test results at 45°C ambient temperature are presented in Figures 4.36 and 4.37 for Cells 5 and 9, respectively.

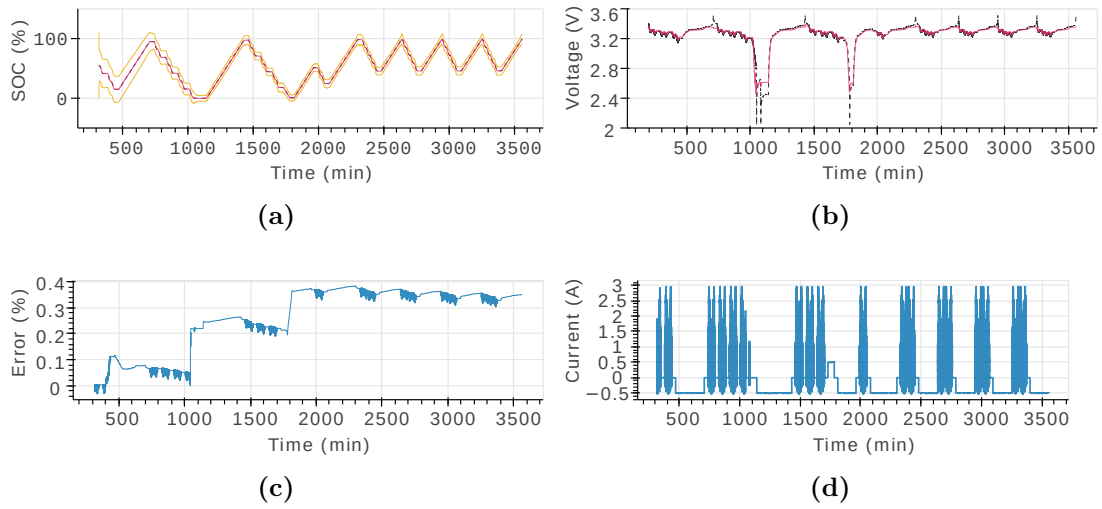

Figure 4.36: Module-level. Cell 5. Dynamic test at 45°C ambient temperature. The graphs show a) the SoC during the test, b) the cell voltage measured by the BMS versus estimated by ECM, and c) error of soc obtained, and d) test current.

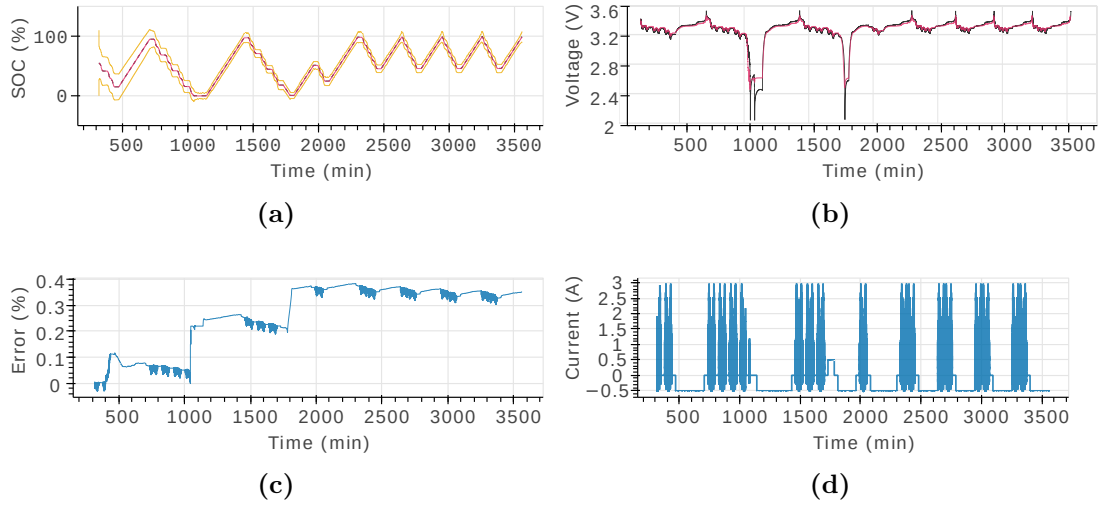

Figure 4.37: Module-level. Cell 9. Dynamic test at 45°C ambient temperature. The graphs show a) the SoC during the test, b) the cell voltage measured by the BMS versus estimated by ECM, and c) error of soc obtained, and d) test current.

In the dynamic test at an ambient temperature of 45°C, the RMS errors obtained in the experiment were 0.37% for Cell 5 and 0.33% for Cell 9. In this case, the SPKF initially exhibited higher uncertainty, but it gradually decreased throughout the test, resulting in accurate SoC estimations.

In this section, the electrical model at the module level, along with the proposed SPKF estimator at the module level discussed in Section 4.4, has been analyzed. After evaluating the model's behavior under various dynamics (including slow capacity tests and higher-speed dynamic tests) and over a wide range of operating temperatures (ranging from 10°C to 45°C), it was observed that the proposed model closely aligns with the electrical behavior of the cycled module.

4.8 Discussion & Conclusions of the Chapter

This chapter covers the work related to the development of module-level models, including the proposal and implementation. The validated models from the previous chapter were used as the foundation, considering the electrical and geometric characteristics of the prototype module constructed specifically for this thesis.

Before proceeding with the model development, a prototype module was built. This module consisted of 12 LW cells and served as a physical validation platform for the technical developments of the thesis. The module was tested in the laboratory for cycles and configured with the BMS developed by Ikerlan, which was connected and configured for cloud connectivity. The module was subjected to low and high dynamic profiles during testing. All cell voltages were measured and compared with the estimated module voltages. The SOC estimation by the Kalman filter and the thermal model's ability to capture temperature dispersion within the module were also evaluated. The results were satisfactory, indicating that the module exhibited accurate estimations and calculations. This was further validated by conducting a test that compared the SOC estimation of each cell with the overall module SOC estimation.

The LTM is a practical alternative for estimating the temperature distribution in battery modules compared to the computationally intensive CFD models. While the LTM may not provide the same level of detailed thermal analysis, it offers a high level of accuracy to determine the module's temperature. One advantage of the LTM is its simplicity, as it requires fewer computational resources and is easier to implement in real-time applications. It allows for temperature estimation at various points within the module, considering the interactions between cells. However, it is important to note that the LTM requires careful parameter definition to ensure accurate results (Section 4.6).

As the number of cells in the module increases, the computational complexity of the LTM also increases. This may cause challenges for commercial BMS that are not specifically designed to handle such large-scale models in their processing units. To address these challenges and enable the widespread use of the LTM in conjunction with commercial BMS, the adoption of cloud-based technologies is proposed. Leveraging cloud resources can provide the necessary computational power and memory capacity to effectively implement and execute the LTM for real-time thermal analysis of battery modules.

In summary, the module-level LTM presents a practical and efficient solution for estimating the temperature distribution in battery modules. By considering the state and positioning of each cell, it accounts for thermal interactions within the module, enabling optimized design and operation of thermal systems in real-time scenarios. The results and validation of the LTM model, as presented in Section 4.7, play a vital role in advancing the development of battery modules and enhancing their thermal management capabilities.

On the other hand, the electrical module-level ECM, coupled with the SPKF estimator, provides accurate SoC information for each cell. Unlike module-level electrical models that consider the module itself as the smallest entity, considering the cell as the smallest unit for estimation yields deeper insights into the module's state.

To estimate the SoC of each cell, the implementation of the ECM model together with the previously developed and validated SPKF estimator in Chapter 3 has been proposed. However, in order to accelerate computations and enable real-time estimations, performing these calculations through co-simulation using the power of cloud computing is suggested, which will be discussed in detail in Chapter 5.

In summary, the module-level ECM and SPKF estimator offer a precise and suitable solution for estimating the SoC of individual cells within a battery module. Considering the state of each cell enables the design of energy management strategies and facilitates cell balancing techniques. Moreover, having knowledge of each cell's state can help identify operational anomalies within the module. The results and validation of the ECM model, as presented in Section 4.7, play a vital role in advancing the development of battery modules and enhancing overall performance and efficiency.

In conclusion, the module demonstrated reliable estimations and calculations. The testing and evaluation process provided valuable insights and highlighted the importance of considering individual cell SOC variations rather than assuming uniformity, as it had a significant impact on the thermal behavior of the module.

5

Digital Twin Simulation Platform

Summary

This Chapter introduces the simulation platform developed in the Cloud environment. First, the services used from AWS for this development are described, providing a brief definition of each of them. Next, two case studies are presented that aim to validate the DTSP developed in this thesis. The first case study focuses on the simulation of anomalies, while the second case study focuses on the disconnection of the Cloud environment. Finally, a critical discussion on the use of DT tools in the context of LIBs is carried out.

5.1 Introduction

This Chapter presents the developed DTSP within the scope of this doctoral thesis. It concludes the research conducted in the previous stages, specifically addressing the second part of Stage 4 as outlined in Chapter 2. The main objective is to define the key characteristics of the cloud-based architecture and provide justification for selecting the employed services. Additionally, two case studies are presented to validate the DTSP: one involving thermal anomalies in the operation of the tested prototype module, and another simulating voltage anomaly en the module.

The analysis of various cloud service providers conducted in Chapter 1 has led to the selection of AWS as the most suitable option for this work. This Chapter focuses on presenting the specific AWS services chosen for this study, building upon the earlier examination of the available services within the AWS ecosystem.

The Chapter is structured as follows: Section 5.2 presents the developed Cloud architecture for deploying the module-level models validated in Chapter 4. It outlines the architecture used to host the DTSP and provides an overview of the deployment process. Next, two case studies are presented to validate the DTSP. In Section 5.3.1, the first case study focuses on introducing an anomaly in the operation of the prototype module and analyzing its impact. Subsequently, in Section 5.3.2, the second case study explores the disconnection of the prototype module from the Cloud platform where the DTSP is hosted. Both case studies provide insights into the behavior of the system and its response to abnormal conditions. In Section 5.4, a critical discussion is conducted regarding the application of DT tools in LIB batteries. This Section examines the advantages, limitations, and potential challenges associated with using DT techniques in the context of LIB batteries, providing a balanced analysis of their suitability and effectiveness summarizing the key findings and drawing the main conclusions of this Chapter.

5.2 Cloud Architecture for the Digital Twin Simulation Platform

For the deployment of the module models, the cloud services platform provided by Amazon, known as AWS, will be utilized. AWS offers a wide range of cloud-hosted services and solutions, such as storage, data processing, databases, and developer tools. The platform is known for its reliability and the variety of available services. AWS provides users with flexibility, enabling them to choose and utilize resources that best suit their specific needs. However, new users may face a initial learning curve due to the complexity of the offered services. One advantage is that users only pay for the resources they use, making it cost-effective, particularly for companies. Additionally, AWS ensures high availability and offers geographical regions of use, guaranteeing high fault tolerance.

The proposed Cloud environment combines public and private cloud resources. It utilizes a combination of public services for algorithms, data, communications with IoT, and visualization, while incorporating an Amazon Virtual Private Cloud (VPC) to add control and isolation to the resources used. This hybrid architecture provides flexibility and customization.

5.2.1 Implemented Architecture for the DTSP

Among the various services offered by AWS, those that meet the requirements of this study have been selected. These services relate to computation, data storage, visualization, and data communication with the module's BMS. It is important to note that while this Cloud architecture may not be the optimal choice for implementing LIBs, it provides a suitable simulation environment to meet the requirements of this thesis. The architecture offers flexibility, reliability, and cost-effectiveness, allowing users to select and utilize resources that best suit their specific needs. The characteristics of the services chosen for the development of the DTSP are detailed below.

Data Transfer.

The prototype module has been cycled in the laboratory, connected to a BMS with a connection to the Cloud. The BMS master was responsible for sending the measured data to AWS, including the current, voltage of each cell and the module, as well as the temperatures of the NTCs.

Two main communication protocols for sending data were analysed: Message Queuing Telemetry Transport MQTT protocol [211] and Hypertext Transfer Protocol (HTTP) protocol [212]. However, MQTT was chosen over HTTP because MQTT is mainly used for efficient communication between IoT devices, with an emphasis on real-time data transfer. HTTP, on the other hand, is used for the transfer of resources on the web, with a focus on information retrieval.

AWS IoT Core

Figure 5.1: Amazon IoT Core. The selected data transfer service between BMS-master of the prototype module and AWS.

The data transfer was performed using the MQTT communication protocol and the IoT services offered by AWS. Figure 5.1 shows the used IoT Core service. MQTT is a lightweight messaging protocol designed for communication between devices on networks with limited bandwidth or unstable connections. It offers flexibility in communication

through message subscription and publication, and scalability to handle multiple connected devices simultaneously. MQTT is particularly suitable for the IoT due to its low power consumption, small size and efficiency in low-speed networks. These characteristics make MQTT a suitable choice for sending data from the BMS to the simulation platform.

The MQTT protocol consists of three elements: the input device, the broker and the output device. The input device is the data sender (*publish*), in this case the master BMS. The broker is an element located between the sender and the receiver and has two main purposes: to store the records of the input and output devices, and to facilitate the routing of messages to their intended recipients. Finally, the output device receives (*subscribe*) the data from the intermediary, in this case, AWS (Figure 5.2).

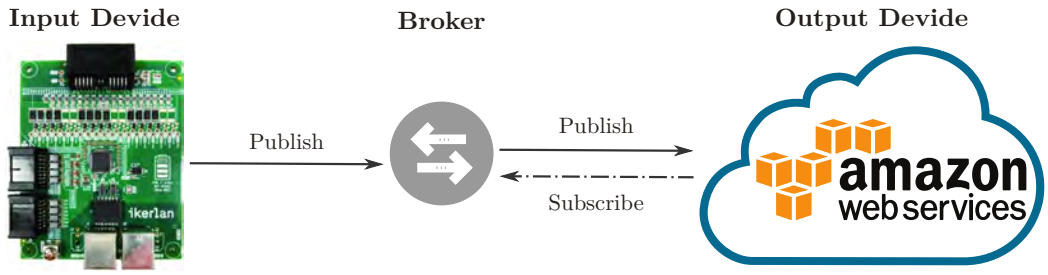

Figure 5.2: MQTT publish/subscribe communication protocol between the BMS of the prototype module and AWS.

This publish/subscribe approach allows bidirectional communication, which is useful for updating the master BMS with the estimates made and performing control actions on the battery.

Computation.

AWS offers a variety of computing services, the most widely used being Amazon Elastic Compute Cloud (EC2) [213] and AWS Lambda [214]. Amazon EC2 is a virtual machine managed by Amazon that allows running the models developed in this thesis. By selecting the appropriate parameters, such as instance, processor, memory and operating system, the computing power and memory of the virtual machine is adjusted. On the other hand, AWS Lambda is a serverless service that runs code automatically, without the need to manage the infrastructure. The Lambda infrastructure is automatically updated according to the characteristics of the code to be executed.

In this case, it has been chosen to execute the models in EC2 because of its greater control and flexibility over the execution environment of the applications. EC2 allows to have a complete virtual server to customise the operating system and manage the network configuration. Figure 5.3 shows the used EC2 service.

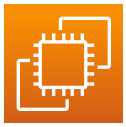

Amazon EC2

Figure 5.3: Elastic Compute Cloud. The selected computation service for module-level models deployment in AWS.

EC2 is a cloud computing service designed specifically for computational tasks. It offers specialised instances, such as those of the "c7g" family [215], optimised for this particular compute purpose. When launching an EC2 instance, the processor, memory and operating system, among other things, can be configured according to the specific needs. In addition, EC2 facilitates a connection to databases. It also offers a variety of instance types with different Central Processing Units (CPUs), allowing the processing capacity to be adapted according to project requirements. For instance, in this thesis, it was required to run 12 electrical cell-level models. Initially, these models were executed in a serialized manner, one after another. However, it was observed that there was no significant change in the execution time of the estimates. To improve efficiency and accelerate the process, the decision was made to parallelize these models or processes. This involved running multiple models simultaneously using parallel computing resources. By parallelizing the models, a noticeable difference in performance was observed as it allowed for better utilization of available resources and faster and more efficient computations.

Database.

Two different data storage systems have been analysed in this Section: object storage systems and databases. Regarding object storage systems, the Simple Storage Service (S3) service offered by AWS has been evaluated. For databases, a comparison was made between relational databases and non-relational databases.

Amazon S3. Amazon Simple Storage Service (S3) is an AWS object storage service offers unlimited capacity and high durability. It allows to store objects generated by AWS applications and services, protecting them by automatically creating backups on different systems. Objects are stored in "buckets", which are directories within S3. Access permissions can be configured using AWS identity and access management. The cost of the service is calculated based on the type of storage, the number of objects and the requests made.

Relational databases: Relational databases are data storage systems that use tables to organise and relate information. They usually use SQL language to perform queries and data manipulation. They are suitable for hierarchical models and eliminate duplicate data by relating tables. Capacity is automatically updated as the number of data increases.

Non-relational databases: These data storage systems have evolved beyond traditional tabular structures and relationships commonly found in databases. They emerged to handle more complex applications and programmes such as Big data analytics or Mobile and gaming applications. There are different models, such as key-value storage, document storage and columnar storage. They are more flexible and support both structured and unstructured data. Each database has its own search language and there are no replication restrictions.

The data received from the BMS will be structured and stored in separate tables, ensuring consistent data structure for both input data and output estimates of the DTSP. This ensures that the data is organized and follows a predefined format, allowing for efficient storage, retrieval, and analysis of the information. By maintaining the same data structure, it becomes easier to perform operations, queries, and comparisons on the data, enabling effective data processing within the DTSP framework.

To meet the requirements for the DTSP database, an Relational Database Service (RDS) has been employed. Specifically, the data structure is based on a data flow structure in the Amazon RDS PostgreSQL. The data flow describes how data is collected, transformed, processed, and distributed throughout a system or process. PostgreSQL was chosen for its efficiency and flexibility in storing and manipulating structured data. Unlike AWS S3, which is designed for storing objects and files, PostgreSQL offers fast performance and the ability to handle large data sets with low memory usage. Figure 5.4 shows the chosen RDS service for the DTSP.

Amazon Relational
Database Service

Figure 5.4: Amazon Relational Database. Selected database service to storage module prototype data in AWS.

To establish and manage the database from EC2, an specific algorithm is used. This allow EC2 to make automatic calls to the database, once it has been scheduled properly. In addition, in order to secure the connection and authentication, Private Keys are used. These keys provide the necessary security to ensure that only authorised users can access and perform operations on the database providing the necessary security to protect the integrity of the connection and the data stored in the database.

Visualisation.

The QuickSight service is used for data visualisation. Amazon QuickSight is an AWS service that focuses on collecting, storing and analysing data. It aims to improve the

analysis of data stored in other AWS services, such as Amazon S3, RDS or DynamoDB, and to provide real-time monitoring. It has been decided to use Amazon QuickSight as a visualisation service on AWS because of its native integration with other AWS services. This is a data visualisation tool provided by AWS that allows an automatic connection to databases. Figure 5.5 illustrates the utilization of the RDS service for the DTSP.

Amazon QuickSight

Figure 5.5: Amazon QuickSight. Selected data visualisation service to of stored data in AWS.

Within the service, QuickSight offers an intuitive and easy-to-use interface, allowing users to program and visualise essential information in an easy way. For this purpose, a dashboard was designed to display the values measured in the battery BMS and the DTSP estimates.

Pricing for the service is based on four factors: the number of authors, the number of readers, the use of irregularity detection tools and alerts, and memory consumption. In addition, QuickSight offers tools to detect errors or irregularities in the data. Finally, The cost of these services is directly proportional to their usage.

Final Architecture.

After reviewing each of the selected services individually, the overall architecture of the DTSP is presented in Figure 5.6. This diagram illustrates the connections established between the services and the sequence in which they are executed. It provides a clear visual representation of how the different components of the DTSP interact with each other.

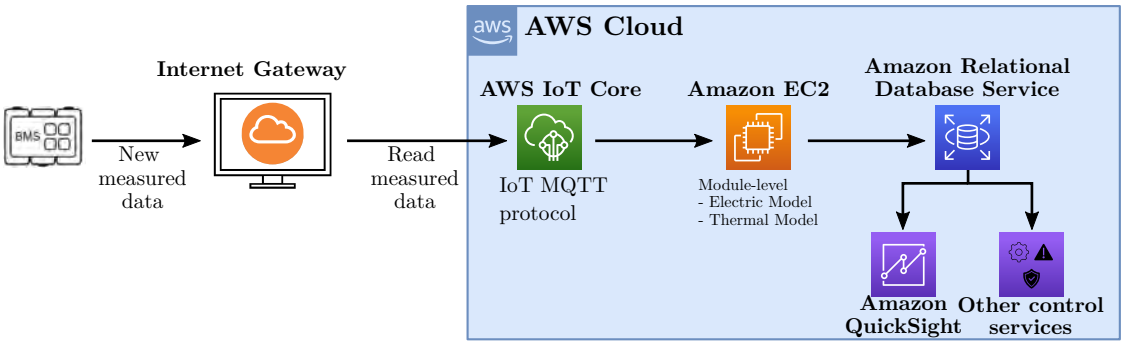

Figure 5.6: Complete Cloud Architecture of the DTSP in AWS.

5.2.2 BMS and DTSP State Machines

The DTSP operates two state machines: i) in the onboard BMS of the prototype module and ii) in the simulation platform located in the Cloud. These state machines are key elements for the operation and coordination of the system. The state machine in the onboard BMS controls the behaviour and operation of the prototype module, while the state machine in the simulation platform in the Cloud supervises and manages the simulations and estimates performed by the implemented models. Both state machines (Figure 5.7) collaborate to ensure the correct data flow and execution of the essential procedures required for the successful operation of the DTSP system.

- The BMS state machine is located in the BMS master, defines the rules and the control flow that governs the behaviour of the LIB according to its current state and the events that occur. Thus, this will be responsible for controlling the basic safety functions of the module by cutting the charge or discharge when the LIB reaches the established voltage or temperature limits. On the other hand, it will send the measured information from the prototype to the Cloud using the MQTT protocol and guarantees at each time step that there is a connection to the Cloud. The BMS will make continuous attempts to connect to the Cloud, and in case there is no connection to the DTSP, it will activate the SoC estimation function of the BMS using a simple Coulomb Counting method. This estimated data is stored until the connection is re-established, at which point all accumulated information will be sent to the Cloud.

- The Cloud state machine is located in the Cloud which will define the rules and control the flow of the data coming to the Cloud from the BMS. This state machine is constantly trying to receive the data sent by the BMS through the MQTT protocol. Once the data is received, the state machine decides according to the elapsed time to activate the execution of the electrical model or the thermal model. The electrical model will be run every second while the thermal model will be run every 10 seconds. After completing the calculations and estimations, the state machine establishes periodic connections to the database for storing the corresponding measurements and estimates. It is also responsible for displaying the information stored in the database in case a user requests to activate the visualisation functionality. Finally, the state machine sends back to the BMS the current SoC of the LIB, ensuring that there is an established connection to the Cloud via the Internet.

Next, the two case studies will be conducted in order to investigate and validate the complete DTSP system as part of this thesis.

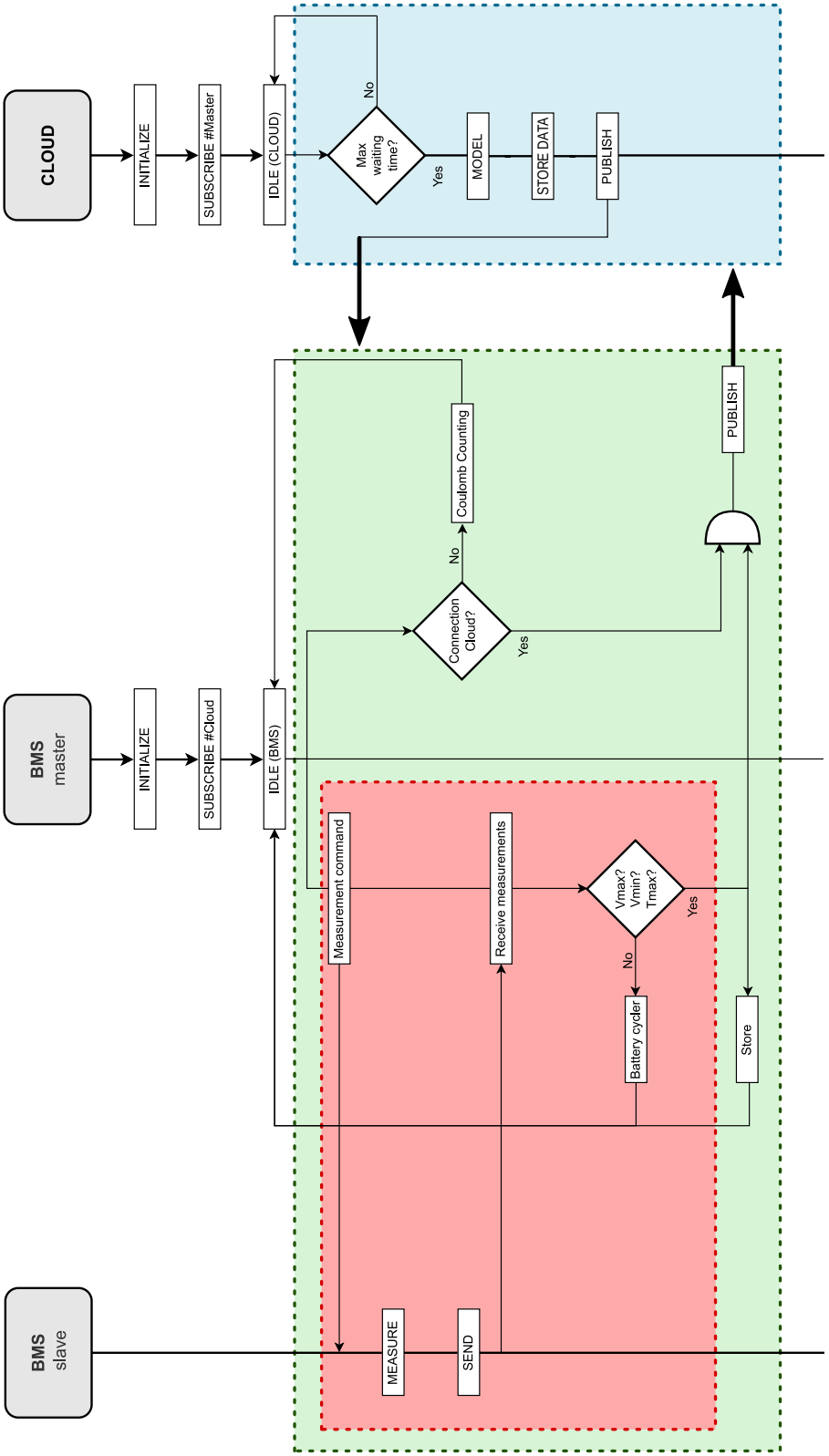

Figure 5.7: Complete Cloud Architecture of the DTSP in AWS.

5.3 Digital Twin Simulation Platform Validation

In this section, two case studies are presented to further illustrate the findings and implications of the research. These case studies serve as practical examples to validate the effectiveness of the proposed models and estimator. Through these real-world scenarios, the ability to detect anomalies in SoC and voltage within the battery module is demonstrated. The insights gained from these case studies contribute to the overall understanding of battery behavior and highlight the importance of considering individual cell characteristics in module-level analysis.

5.3.1 Case Study 1: Anomalies in the Operating Battery Condition: Unbalances in Voltage

This section presents the first case study conducted in this thesis. The purpose of this test was to observe the simulation platform's capability to detect anomalies in the module voltage and verify its ability to accurately estimate the module temperature.

To achieve this, a capacity test will be conducted on the module. An anomaly will be introduced by discharging one cell more than the others, resulting in an unbalance of a cell voltages and consequently the module voltage. This capacity test will be performed at the same C-rate as the capacity test at 25°C ambient temperature.

Firstly, one cell will be discharged with the help of an externally connected resistor. At the end of the discharge, this cell will be at approximately 8% lower SoC than the other cells.

Discharging one of the cells means that it will reach the minimum voltage threshold much earlier than the others. As a result, the total capacity of the module will decrease since the charge and discharge processes are terminated when the first cell among the 12 reaches the voltage limits. This cell, reaching lower SoC limit earlier, will experience a significant increase in its internal resistance at that moment, as observed in the parameter acquisition of the cells in Chapter 3, where it was found that internal resistance is higher at low SoC levels. Consequently, this will lead to higher heat generation as a greater portion of the heat will be irreversible due to the influence of the internal resistance. At this point, the thermal model is expected to estimate a higher temperature at the location of the discharged cell within the module. Additionally, the difference between estimating the SoC of each individual cell for temperature gradient estimation proposed to using the module's SoC value for all cells will also be observed.

Figure 5.8 shows the BMS reading that was taken in the case study test.

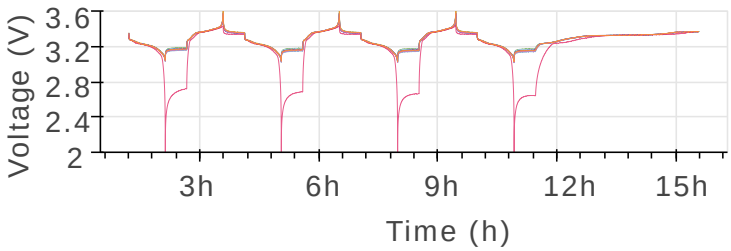

Figure 5.8: Measured voltages on the module in the first case study test. In the picture it can be seen how one of the cells is unbalanced in terms of voltage.

Figure 5.8 shows how the imbalanced cell reaches the minimum voltage with a significant difference compared to the others. In this case, the influence on the temperature will be observed. Figure 5.9 displays the measurements of all NTC temperatures.

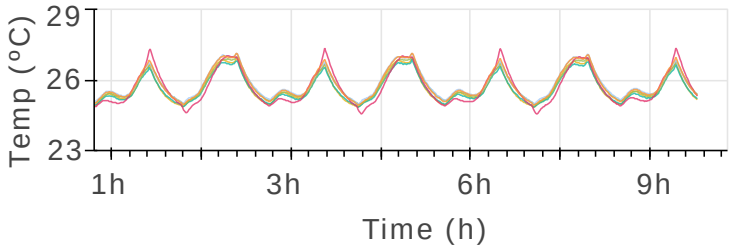

Figure 5.9: Measured temperatures on the module by the NTCs in the first case study test.

In Figure 5.9, it is confirmed that the X temperature measured in the most discharged cell is the highest among all cells when they are at low SoCs.In this case, the thermal model's ability to accurately estimate these temperatures, and the results are shown in Figure 5.10.

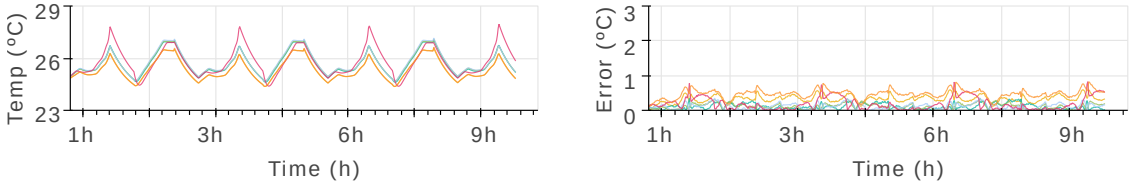

(a) **(b)**

Figure 5.10: Estimated temperatures on the module in the first case study test considering each cell SoC.

It can be observed that the model is able to accurately estimate this temperature rise in the specific cell. Thus, this test demonstrates that the module-level thermal model that considers the interactions between cells provides more information than what can be obtained from sensors alone. Furthermore, the same simulation was performed, but this

time considering the SoC of the entire module, to confirm that the estimations considering the individual cell SoCs are more precise. The results of this simulation are shown in Figure 5.11.

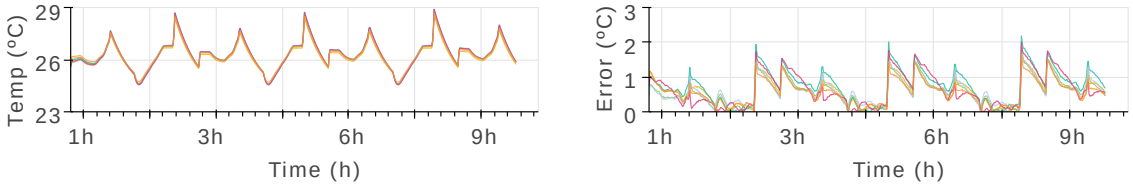

(a) **(b)**

Figure 5.11: Estimated temperatures on the module in the first case study test considering module´s SoC.

In this case, it can be observed that when the module's SoC is higher than that of the cell, the thermal model is unable to estimate the temperature rise accurately, resulting in a loss of precision in the overall module information. In summary, the individual cell-level simulations have successfully detected unbalances in voltage within the battery module. This approach has provided valuable insights that would not have been attainable if the module was treated as a single unit, thus validating the third hypothesis of this thesis.

H3: The implementation of the advanced algorithms in the Cloud could allow to detect anomalies and battery failures more efficiently and faster, which will lead to the mitigation of the computational load of the onboard BMS and improve system performance.

5.3.2 Case Study 2: Anomalies in the Operating Battery Condition: Unbalances in Temperature

This section presents the second case study carried out in this thesis. The objective of this test is to verify that the simulation platform is able to detect anomalies of temperature in the operation of the module.

The test proposed to observe the behaviour of the model is a capacity test in which the prototype module is fully charged and discharged for 5 cycles. This capacity test has been performed at the same C-rate as the capacity test at 25°C ambient temperature.

In this case, an external anomaly has been introduced in the prototype module. The anomaly consists of an increase in temperature in one of the prototype cells. This has been achieved by enveloping the cell with a electric heater. The thermal blanket was only rolled around cell 6, which is located in a corner of the prototype. While the rest of the module was operating at temperatures around 25°C, the temperature of this single cell was raised to 40°C.

Increasing the temperature of a cell implies that this cell operates differently from neighbouring cells. As discussed in section 3.6, as the temperature of the cell increases, more energy can be obtained from the cell. Therefore, it is anticipated that a difference in voltage measurements will be observed. This is due to the fact that as the temperature increases, the capacity of the cell also increases, resulting in a lower discharge rate. As a result, it is expected that the cell will have a higher voltage compared to the other cells in the module. Although the cell is and LFP chemistry model, characterised by its voltage plateau during most of the SoC, the voltage of this cell with the introduced anomaly is expected to be different from the rest of the cells in the module.

Figure 5.12 shows the voltages measured by the BMS in the capacity test without the thermal blanket (Figure 5.12a) and with the thermal blanket (Figure 5.12b).

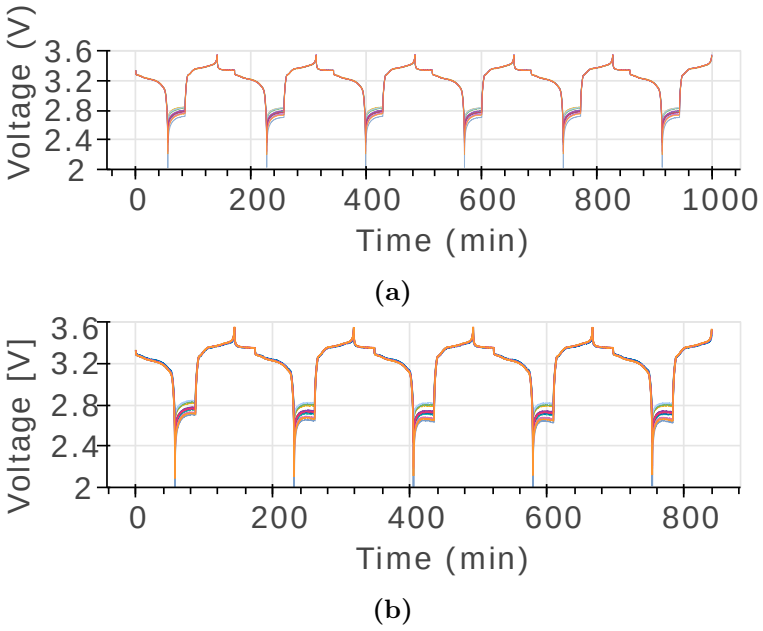

Figure 5.12: Applied profiles in the module. a) Capacity test without a thermal blanket, and b) Capacity test with a thermal blanket.

On the image, the expectation is confirmed, as a delay in the voltage of cell 6 can be observed in Figure 5.12b. This delay causes the cell to discharge less due to the incremental of capacity of the heated cell when the module reaches 0% SoC.

The test was simulated with the anomaly in the DTSP and the results are depicted in Figure 5.13. This figure shows the SoC during the test (Figure 5.13a), the comparison between the measured voltage of cell 6 (represented by the black discontinuous line) and the voltage estimated by the electrical model (represented by the pink line) in Figure 5.13b and the SoC estimated of the cell 6 in Figure 5.13c. In addition, the error in SoC estimate obtained by the SPKF is shown in Figure 5.13d.

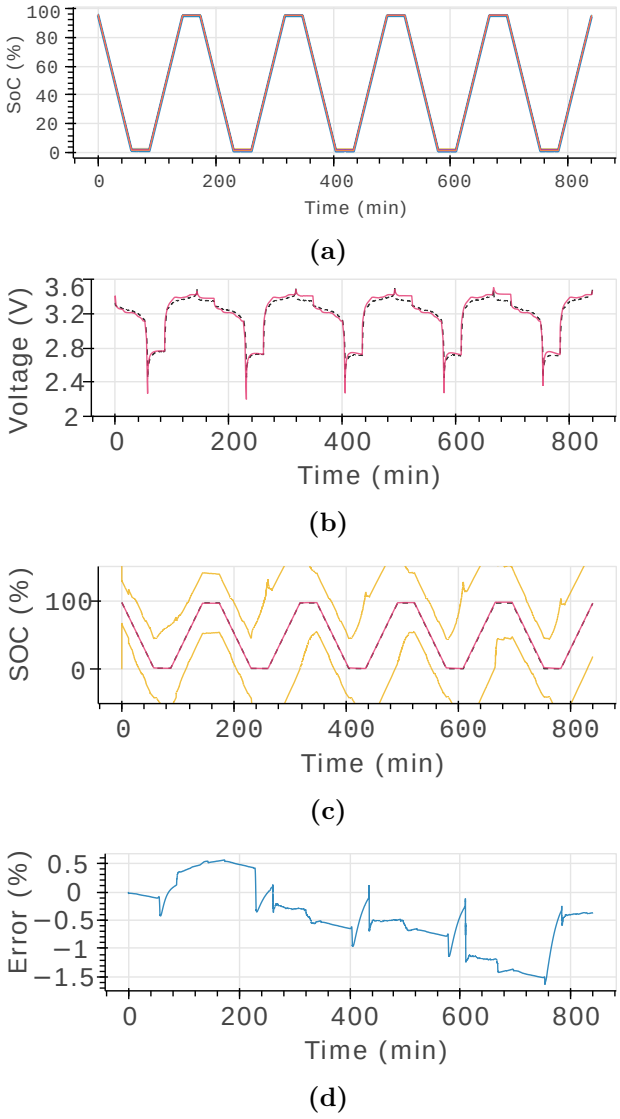

Figure 5.13: Case study 1. The graphs show: a) the estimated SoC of all cells, b) the estimated voltage of all cells, c) the estimated SoC of cell 6 and d) the measured voltage versus the estimated voltage of cell 6.

In Figure 5.13, it can be noted that the SPKF estimates the SoC of this cell similarly to the rest of the cells. That is, the SoC estimator does not estimate a higher SoC for the anomalous cell, but corrects the voltage difference and assumes that all cells are operating homogeneously. This is due to the plateau mentioned above, where the voltage difference observed in this test is 10 mV.

The aforementioned voltage correction is done by means of SPKF gain updates. This gain has allowed to identify the correction in cell 6. Figure 5.14 shows the gain related to the SoC in the test without the thermal blanket (Figure 5.14a) and with the thermal blanket (Figure 5.14b).

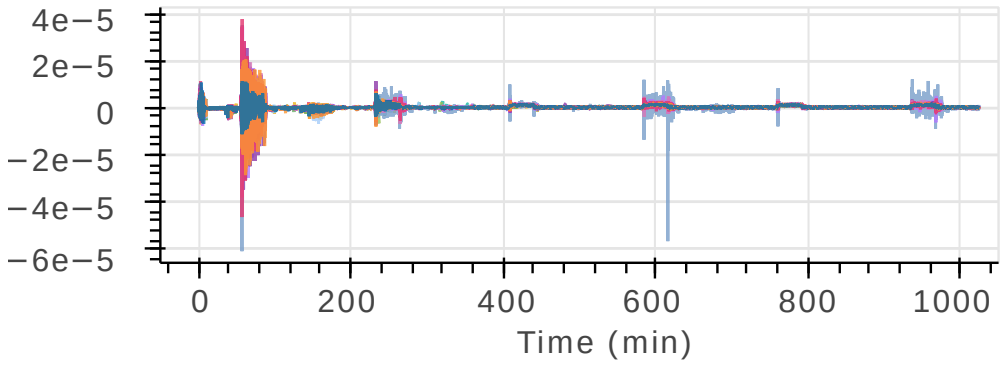

(a)

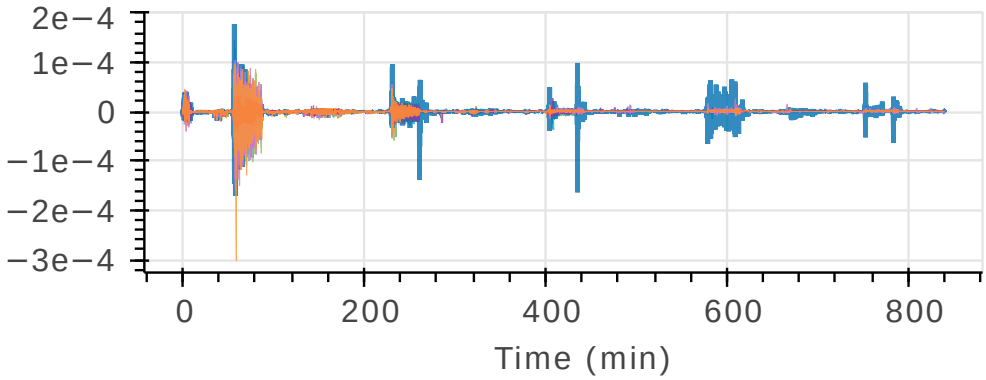

(b)

Figure 5.14: SoC related Kalman Gain in a) Capacity test without a thermal blanket, and b) Capacity test with a thermal blanket.

The gain of the cell operating at higher temperature is shown in blue colour in the figure. Observing the capacity test performed without the electric heater, at the beginning of the test the SPKF corrects the SoC of the cells but as the test progresses all the cells converge. Concerning the test with the electric heater, it can be observed that in the first cycle of the test, the SPKF has been correcting the SoC of different cells, such as Cell 2 illustrated in colour orange or Cell 5 in colour pink. However, these cells converge and from cycle 2 onwards, the SoC correction decreases and becomes constant. This is not the case for cell 6. The SoC correction of cell 6 is similar to the others at the beginning of the test. However, the gain peaks, which occur mainly when the module is at low SoCs, become larger each time and drift away from convergence.

In conclusion, the individual cell-level simulations have successfully identified the specific cell presenting an anomaly. This demonstrates the advantage of considering each cell individually, as the classical approach of treating the entire module as a unit would not have allowed for the detection of such anomalies. It is important to note that the thermal model does not accurately predict the temperature rise caused by the capacity increase

due to temperature. While the voltage difference introduced by temperature may not be significant, the ability to detect the anomaly is still possible through the individual estimation of SoC. This supports the third hypothesis of the thesis, highlighting the effectiveness of estimating SoC individually in anomaly detection, even when the thermal model does not precisely predict temperature variations.

H3: The implementation of the advanced algorithms in the Cloud could allow to detect anomalies and battery failures more efficiently and faster, which will lead to the mitigation of the computational load of the onboard BMS and improve system performance.

5.4 Discussion & Conclusions of the Chapter

In this final technical chapter, the development that has been presented in the previous chapters of this document has been summarized. The main objective of this chapter, which addresses Stage 4 of the methodology proposed in Chapter 2, was to select the necessary services and develop the Digital Twin Simulation Platform in which the module-level models developed in Chapter 4 were deployed. Furthermore, this simulation platform has been validated through two case studies in which the prototype module was tested in the laboratory with imbalances in both voltage and temperature.

Section 5.2 has been divided into two subsections. The first one has presented the potential services offered by AWS for contracting and setting up the desired cloud platform. In this context, various data transfer, computing, database, and visualization services have been analyzed. For each of them, the service that best suited the framework of this thesis was chosen. Thus, AWS IoT Core was selected as the data transfer service between the BMS and the Cloud, applying the MQTT communication protocol due to its flexibility and efficiency in sending real-time data compared to the HTTP protocol used for web data transmission. On the other hand, concerning the computing services offered by AWS, the Lambda service was discarded, and the decision was made to use the Amazon EC2 service, as it is faster than Lambda, allows for a constantly running instance, and offers the ability to configure the characteristics of the virtual machine, such as RAM, the number of processors, and the operating system. It is within this virtual machine that the module-level models will be deployed.

All the data measured by the BMS and sent to the Cloud, including the estimates generated by the models, are stored in a database. For the selection of this database, services such as Amazon S3, Relational Databases, and Non-Relational Databases were analyzed. Among these options, Amazon Relational Database Service was chosen, as the data to be handled by the DTSP always maintains the same structure. This type of database allows for searches across related data tables using identification parameters. Additionally, it provides the ability to apply security measures with passwords. Lastly, the QuickSight visualizer was chosen for its ease of integration with other AWS services, including the database. It has proven to be a user-friendly and efficient visualization tool.

In subsection 5.2.2, the two state machines have been presented. The first one, located in the BMS-master, is responsible for performing all the measurements and sending data related to current, voltage, and temperature to the Cloud. The second state machine resides in the Cloud, specifically within the EC2 service. Its functionality is to continuously execute the battery DT and run both the electrical and thermal models at the specified frequencies.

The second case study aimed to verify the DTSP's ability to detect a temperature imbalance within the module. For this purpose, one cell in the module was heated using an external heat source. In this case, the electrical model demonstrated sufficient accuracy in the anomalous cell, with an RMS error of 0.134% of SoC. This is because the cell, being at a higher temperature, experienced less discharge compared to the other cells due to the increased capacity associated with the temperature rise. As the cells were LFP, the voltage difference during charging and discharging was approximately 10mV. This voltage difference was not sufficient for the SPKF to consider it as a significant factor, and it was observed that the SPKF corrected it by following the SoC estimation of the other cells. Since all cells operated at the same SoC, the thermal model was unable to estimate this temperature increase and assumed an operating temperature of 25 °C. However, as mentioned earlier, the SPKF was correcting the voltage difference, and this was reflected in the gain of the filter in terms of SoC. Thus, it has been verified that the model is capable of detecting an anomaly in one of the cells (as it exhibited the largest gain), and this was made possible by simulating the cells individually.

Critical Discussion on the Use of Digital Twin Tools in the Battery Framework

In Chapter 1, during the SoA review, several key points have been highlighted regarding the benefits of using a DT in the battery domain.

- *Performance optimization*: A DT allows for real-time monitoring and simulation of battery performance. This has been demonstrated in both this and the previous chapter, where the module-level models provided additional information beyond what is typically obtained from traditional sensors found in battery modules.

- *Fault diagnosis*: With a DT, it is possible to detect and diagnose battery faults more quickly and accurately. This has been demonstrated in both case studies where the models were capable of detecting anomalies. This is particularly useful for predictive maintenance, as it enables the early detection of cells that deviate from normal operation, even before they pose a dangerous or catastrophic failure.

- *Improved energy efficiency*: DTs can contribute to enhancing the energy efficiency of LIBs by providing continuous monitoring of performance, optimizing battery management algorithms, and simulating different usage and charging scenarios.

These advantages of utilizing a DT in the battery framework have been discussed and validated throughout this thesis, demonstrating the potential for enhancing battery performance, enabling fault detection, and improving energy efficiency. However, not everything is positive as cloud-based DTs are directly dependent on the internet connectivity available at any given time. This means that when the module becomes disconnected from the network, the DT may become inaccessible in some cases. Additionally, utilizing cloud-based technologies introduces implementation and maintenance costs for these platforms. Lastly, aspects such as data security and privacy must also be considered.

In conclusion, the evaluation of the complete simulation platform demonstrated its effectiveness in capturing and analyzing various scenarios. The case studies provided valuable insights into the importance of monitoring individual cell states, detecting anomalies, and optimizing system performance. The successful validation of the platform showcased its potential for predictive maintenance, anomaly detection, and optimization of battery systems using DT technology. The findings contribute to the growing body of knowledge on DT applications in the field of battery technology and open avenues for further research and development in this domain. The module provided reliable estimates and calculations, highlighting the significance of considering SoC variations in each cell for accurate thermal behavior. The testing and evaluation process yielded valuable insights for future improvements.

6

General conclusions, discussion & future trends

Summary

In this final chapter, the conclusions, main findings, and key contributions of this Ph.D. thesis are reviewed. Furthermore, the future research directions to expand upon the topics explored in this work are identified.

6.1 Summary & General Conclusions

The use of LIBs has seen significant growth due to their versatility and energy storage capabilities. However, analyzing and optimizing large-scale LIB installations present challenges, particularly regarding module-level performance. Imbalances, heterogeneities, and variations in cell states within the LIB module can negatively affect performance and pose risks. Monitoring individual cells is essential to address these issues effectively. Accurate and real-time models are needed to estimate SoC and analyze battery behavior. However, estimating SoC and SoH non-invasively during normal operation is challenging. Existing works often oversimplify module-level studies, ignoring complex cell interactions. Model-based analysis at the module level is crucial for optimizing LIB performance and ensuring system safety. To overcome these challenges, **a Cloud-based Digital Twin-based Simulation Platform is proposed including thermal and electric models that consider individual cell characteristics**. Cloud-based technologies facilitate the deployment of computationally intensive models. This approach enables plant or fleet management strategies, improved communication, real-time monitoring, and extended LIB lifetimes.

To achieve this, the main objective of this thesis was to **Develop, Validate, and Deploy Module Level Models within a Cloud-based Digital Twin Simulation Platform for Lithium-Ion Battery that incorporate the SoX variations of individual cells**. In addition to the main objective, the secondary objectives proposed have also been achieved.

The first was to **develop and validate cell-level models** to understand the behavior and interactions of basic system characteristics, in order to use them as a basis for extrapolation to more advanced module-level models. This objective was fulfilled in Chapter 3, where a LTM, an ECM, and a SPKF were validated at the module level under different operating conditions. The errors obtained in these models and estimator are 0.52 ºC, 0.0023V and 0.38% respectively. Based on these models at the cell level, the second objective was to **develop and validate module-level models** to understand and predict the behavior of the overall system and the interactions of multiple cells in the module, using the models developed in the previous objective as a basis. This objective was accomplished in Chapter 4, where the proposed extrapolated models were validated. In this extrapolation, the average error obtained from the electrical model was 0.24 % in the SoC estimation and an error of 0.49 ºC was the error obtained in the LTM at the module level.

In terms of the objectives related to Cloud architecture, the first was to **develop a secure and scalable cloud architecture** that enables efficient deployment and execution of models, ensuring proper integration with all the services and resources comprising the system. The cloud architecture was defined and implemented during Chapter 5 of this document, thus achieving this objective. On the other hand, another objective was related to **select the most appropriate compute and memory resources** on the

Cloud platform to improve system performance and efficiency, ensuring optimal resource utilization. This objective was addressed in the Section 5.2.1 of this thesis. After evaluating the various computing services provided by AWS, the decision was made to utilize the EC2 service. This service offers the flexibility to select the desired computing configuration. In this particular case, the chosen configuration consists of 4 vCPUs and 8 GiB of RAM. In addition to **develop an alarm system for early detection and notification of potential problems** in the BMS, anticipating system failures, improving system efficiency and security, minimizing interruptions or issues during operation, and empowering users to take corrective action.

Finally, the last objective related to **develop and assemble a functional prototype**, establish and optimize necessary connections and communication channels, and configure the Cloud platform to enable seamless transmission and reception of real-time data from the prototype. This objective was achieved in the Section 4.2, where the necessary communications for establishing connections with the Cloud were defined and implemented.

By achieving these objectives, this research has made significant contributions to the field, contributing to the development of module-level models integrated within a Cloud-based Digital Twin Simulation Platform for Lithium-Ion Batteries. The successful validation and deployment of these models provide a foundation for optimizing battery system performance, enabling predictive maintenance, and improving overall system efficiency. These achievements demonstrate the effectiveness and practicality of the proposed methodologies and solutions, highlighting the potential for further advancements in the field of lithium-ion battery systems. Once the objectives set in the introductory part of this document (Chapter) have been achieved, the hypotheses formulated in the same section have been addressed. Each hypothesis is named and discussed below:

- **H1**: Models of modules that consider individual cells provide relevant additional information compared to that obtained from module sensors.

  This hypothesis has been validated in Chapter 4. The proposed module-level models, based on the cell-level models validated in Chapter 3, offer valuable information at the module level. By considering each individual cell and estimating their state individually, these models provide additional insights beyond the voltage information provided by the BMS. They can estimate the SoC and temperature of each cell, thus mapping the SoX of the module's cells. SoC is a key state for optimizing the available energy of the module, making this information useful for designing management strategies for the EMS. Moreover, modules typically have only a few temperature sensors placed at key points. With the module's thermal model, the temperature gradient across the module can be obtained, even in areas without a temperature sensor.

- **H2**: Cloud Computing technologies may offer the computational power and memory required for deploying module-level models, enabling additional services compared to local environments.

  This hypothesis is addressed in Chapter 5, where the chosen Cloud architecture for deploying the module's models and estimator in the DTSP is presented. The calculations required by these models, considering individual cells, are computationally intensive and complex. Additionally, for the proposed electrical model, parallel processing for co-simulation is suggested. Commercial BMSs, as seen in the SoA review in Chapter 1, are generally not designed for these functionalities, thus requiring external computing power. In this thesis, performing these calculations in a Cloud environment is proposed, as this technology offers the necessary computing power and ample memory.

- **H3**: The implementation of advanced algorithms in the Cloud could efficiently and rapidly detect anomalies and battery failures, reducing the computational load of the onboard BMS and improving system performance.

  This hypothesis is verified through two case studies conducted in Chapter 5. Different voltage and temperature anomalies were introduced to examine whether the models capture these anomalies during operation. In the first case study, the module operated under voltage imbalance conditions, and it was observed that the thermal model is more effective when estimating the temperature considering the SoC of each cell instead of the module's SoC. In the second case study, a thermal blanket heated one of the cells, increasing its capacity and causing its voltage to behave differently. Although the thermal model did not detect the anomaly in this case, the electrical model detected it, and the SoC estimator SPKF, while continuously correcting it, showed the anomaly in the filter's gain. Therefore, satisfactory results were achieved in both the first and second case studies.

In conclusion, the hypotheses formulated at the beginning of this thesis have been validated, demonstrating the significance and effectiveness of the proposed methodologies and solutions.

6.2 Thesis Contributions

These are the main contributions of the research activities performed throughout the development of this Thesis:

- A comprehensive review of the SoA related to the modeling of LIBs at both the cell and module levels was presented. Additionally, the utilization of DT and Cloud computing technologies in the context of LIBs was analyzed.

- Thermal and electrical models were developed, along with a SoC estimator, for LIBs at both the cell and module levels. The module-level models consider the SoX variations of individual cells, providing more information than traditional sensor-based approaches.

- A Cloud platform was established where the module-level models were deployed and validated. This Cloud platform consists of computing services, a database, and a visualization service for monitoring the measurements and estimations performed by the DTSP.

- A methodology was developed for extrapolating cell-level models to the module level, detailing the process of obtaining parameters and adapting well-known cell-level models to the module level. This methodology allows for the integration of individual cell models into a comprehensive module-level representation.

6.3 Future Works

After completing the Ph.D. Thesis, several potential avenues for future research have emerged. These areas were not explored within the scope of this thesis but have the potential to advance the current state of the art.

- *Integration of temperature measurements* into the thermal model estimates: A potential future research direction is to enhance the thermal model of the battery module by incorporating direct temperature measurements as inputs to the model. This would enable the use of temperature measurements as a corrective factor to improve the accuracy of temperature gradient estimates. Techniques such as Kalman filters or adaptive filters could be employed to achieve more precise and robust temperature estimations.

- *Anomaly detection in temperature variations*: Building upon the case study analyzed in this thesis, a potential future research avenue is to enhance the model to detect and respond to abnormal temperature variations in real-time. This would involve developing algorithms or techniques that can identify anomalies and trigger appropriate actions to ensure the reliability and safety of battery systems.

- Exploring *future functionalities of the Cloud*: It is important to investigate the potential applications and functionalities that can be derived from the data collected through measurements and estimations made by the model. Storing this data in a centralized database for multiple deployed batteries could enable the detection of patterns and anomalies, as well as serve as valuable input for developing battery degradation models. It is important to note that the findings of this study reinforce the future line mentioned above, which is already a well-established trend in scientific research.

- *Extrapolation of the Digital Twin Simulation Platform to battery pack level*: Extending the Digital Twin Simulation Platform to simulate multiple modules working together in a battery pack represents an intriguing research direction. This would provide valuable insights into the overall energy storage system's state, enabling the development of comprehensive management strategies for complete installations or battery fleets.

Appendices

A

Laboratory Equipment

As the proposed methodology relies heavily on experimental activities for the parameter identification and cell and module-level modelling, the use of appropriate laboratory equipment is essential to minimise experimental errors and obtain reliable results. The main resources used for testing are described in this Appendix.

A.1 Battery Tester

Specialised equipment is used to analyse the parameters of the reference cells during this thesis. In this thesis, due to the testing of realistic operating profiles, the use of battery cyclers with dynamic capabilities is necessary. The description of the main characteristics of the Digatron battery cyclers used can be found in Tables A.1 and A.1. For the configuration of the battery test equipment, the BTS-600 software is used. In the tests at cell level (MCT cycler) the test equipment detailed in Table A.1 is used, while in the tests at module level the equipment described in Table A.2 is used.

MCT technical data	
PC Software	BTS-600
Accuracy	± 0.1% full-scale
Resolution	± 15 Bit
Data Acquisition Rate	10 ms
Control Rate	2 ms
Voltage	0 - 6 V
Current	0.1 - 100 A

Table A.1: Battery cell tester

BNT technical data	
PC Software	BTS-600
Accuracy	± 0.1% full-scale
Resolution	± 15 Bit
Data Acquisition Rate	20 ms
Control Rate	2 ms
Voltage	5 - 100 V
Current	0.05 - 50 A

Table A.2: Battery modle tester.

A.2 Climate Chambers

As temperature stands as a critical factor that greatly influences battery performance and parameters, it was imperative to exercise meticulous control over the ambient and/or cell temperature throughout the testing process. This was crucial in order to conduct an unbiased and comprehensive analysis of battery performance. To this end, specialized climatic chambers were employed, providing a controlled environment for the experiments.

For the battery tests and characterization tests, the CTS/C-40/200/Li and Prebatem Selecta climatic chambers were utilized. These chambers were selected based on their specific features and specifications, which are outlined in Tables A.3 and A.4.

CTS/C-40/200/Li technical data	
Internal capacity	200 L
Internal Dimensions	750 x 650 x 400 mm
External Dimensions	1800 x 920 x 1345 mm
Temperature range	-40 to 180 °C
Heating/Cooling speed	4°/min
Temperature fluctuation	± 0.3°C
Relatice Humidity Range	10 - 95%

Table A.3: CTS climate chamber

Prebatem Selecta	
Internal capacity	80 or 150 L
Internal Dimensions	500 x 400 x 400 mm - 80 L 500 x 600 x 500 mm - 150 L
External Dimensions	700 x 750 x 590 mm - 80L 700 x 950 x 680 mm - 150L
Temperature range	5 to 50 °C
Temperature fluctuation	± 0.3°C
Homogeneity	± 0.5°C
Setpoint error	± 0.25°C

Table A.4: Prebatem Selecta climate oven

A.3 Temperature measurements

For increased accuracy, cell voltage and temperature are measured using a data acquisition system (DAQ) *Agilent 34970A*, along with T-type thermocouples. The DAQ has an accuracy of ±0.0035 % reading and 0.0005 % of range for voltage. Additionally, DAQ's temperature precision is ±0.5 ºC of range and 0.2 % of reading, while type-T thermocouples have a ±1.0 ºC accuracy.

B

Extrapolation of the Lumped Thermal Model

Appendix B presents an example of the extrapolation of the single-cell LTM model to a module of two contiguous cells.

The NR follows the following steps:

1. An initial approximation of the roots (z_0) is made, in this case temperatures.

$$z^0 = \begin{bmatrix} \mathrm{T}_{00}, & \mathrm{T}_{01}, & \mathrm{T}_{02}, & \mathrm{T}_{03}, & \mathrm{T}_{04}, & \mathrm{T}_{05}, & \mathrm{T}_{06} \\ \mathrm{T}_{10}, & \mathrm{T}_{11}, & \mathrm{T}_{12}, & \mathrm{T}_{13}, & \mathrm{T}_{14}, & \mathrm{T}_{15}, & \mathrm{T}_{16} \end{bmatrix} \tag{B.1}$$

2. Calculate the values of the function matrix (f_z) with the initial approximations, in this case, equation 3.1 and equation 3.2 is applied on each surface of the cell in B.2.

$$f_{z^0} = \begin{bmatrix} f_{00} = I^2 \cdot R_{0\_0} + I \cdot EHC_0 \cdot \mathrm{T}_{00} - m \cdot c_p \cdot \dfrac{\mathrm{T}_{00} - T_{00}(k-1)}{\Delta t} \\ \qquad - \dfrac{k_{ra} \cdot A_{ra}}{L_{ra}} \cdot (4 \cdot \mathrm{T}_{00} - \mathrm{T}_{01} - \mathrm{T}_{02} - \mathrm{T}_{03} - \mathrm{T}_{04}) \\ \qquad - \dfrac{k_{ax} \cdot A_{ax}}{L_{ax}} \cdot (2 \cdot \mathrm{T}_{00} - \mathrm{T}_{05} - \mathrm{T}_{06}) \\ f_{01} = \frac{k_{ra} \cdot A_{ra}}{L_{ra}} \cdot (\mathrm{T}_{00} - \mathrm{T}_{01}) - h_{ra} \cdot A_{ra} \cdot (\mathrm{T}_{01} - \mathrm{T}_{amb}) - \varepsilon_{ra} \cdot \theta \cdot A_{ra} \cdot ({\mathrm{T}_{01}}^4 - {\mathrm{T}_{amb}}^4) \\ f_{02} = \frac{k_{ra} \cdot A_{ra}}{L_{ra}} \cdot (\mathrm{T}_{00} - \mathrm{T}_{02}) - h_{ra} \cdot A_{ra} \cdot (\mathrm{T}_{02} - \mathrm{T}_{amb}) - \varepsilon_{ra} \cdot \theta \cdot A_{ra} \cdot ({\mathrm{T}_{02}}^4 - {\mathrm{T}_{amb}}^4) \\ f_{03} = \frac{k_{ra} \cdot A_{ra}}{L_{ra}} \cdot (\mathrm{T}_{00} - \mathrm{T}_{03}) - h_{ra} \cdot A_{ra} \cdot (\mathrm{T}_{03} - \mathrm{T}_{14}) - \varepsilon_{ra} \cdot \theta \cdot A_{ra} \cdot ({\mathrm{T}_{03}}^4 - {\mathrm{T}_{14}}^4) \\ f_{04} = \frac{k_{ra} \cdot A_{ra}}{L_{ra}} \cdot (\mathrm{T}_{00} - \mathrm{T}_{04}) - h_{ra} \cdot A_{ra} \cdot (\mathrm{T}_{04} - \mathrm{T}_{amb}) - \varepsilon_{ra} \cdot \theta \cdot A_{ra} \cdot ({\mathrm{T}_{04}}^4 - {\mathrm{T}_{amb}}^4) \\ f_{05} = \frac{k_{ax} \cdot A_{ax}}{L_{ax}} \cdot (\mathrm{T}_{00} - \mathrm{T}_{05}) - h_{ax} \cdot A_{ax} \cdot (\mathrm{T}_{05} - \mathrm{T}_{amb}) - \varepsilon_{ax} \cdot \theta \cdot A_{ax} \cdot ({\mathrm{T}_{05}}^4 - {\mathrm{T}_{amb}}^4) \\ f_{06} = \frac{k_{ax} \cdot A_{ax}}{L_{ax}} \cdot (\mathrm{T}_{00} - \mathrm{T}_{06}) - h_{ax} \cdot A_{ax} \cdot (\mathrm{T}_{06} - \mathrm{T}_{amb}) - \varepsilon_{ax} \cdot \theta \cdot A_{ax} \cdot ({\mathrm{T}_{06}}^4 - {\mathrm{T}_{amb}}^4) \\ f_{10} = I^2 \cdot R_{0\_1} + I \cdot EHC_1 \cdot \mathrm{T}_{10} - m \cdot c_p \cdot \dfrac{\mathrm{T}_{10} - T_{10}(k-1)}{\Delta t} \\ \qquad - \dfrac{k_{ra} \cdot A_{ra}}{L_{ra}} \cdot (4 \cdot \mathrm{T}_{10} - \mathrm{T}_{11} - \mathrm{T}_{12} - \mathrm{T}_{13} - \mathrm{T}_{14}) \\ \qquad - \dfrac{k_{ax} \cdot A_{ax}}{L_{ax}} \cdot (2 \cdot \mathrm{T}_{10} - \mathrm{T}_{15} - \mathrm{T}_{16}) \\ f_{11} = \frac{k_{ra} \cdot A_{ra}}{L_{ra}} \cdot (\mathrm{T}_{10} - \mathrm{T}_{11}) - h_{ra} \cdot A_{ra} \cdot (\mathrm{T}_{11} - \mathrm{T}_{amb}) - \varepsilon_{ra} \cdot \theta \cdot A_{ra} \cdot ({\mathrm{T}_{11}}^4 - {\mathrm{T}_{amb}}^4) \\ f_{12} = \frac{k_{ra} \cdot A_{ra}}{L_{ra}} \cdot (\mathrm{T}_{10} - \mathrm{T}_{12}) - h_{ra} \cdot A_{ra} \cdot (\mathrm{T}_{12} - \mathrm{T}_{amb}) - \varepsilon_{ra} \cdot \theta \cdot A_{ra} \cdot ({\mathrm{T}_{12}}^4 - {\mathrm{T}_{amb}}^4) \\ f_{13} = \frac{k_{ra} \cdot A_{ra}}{L_{ra}} \cdot (\mathrm{T}_{10} - \mathrm{T}_{13}) - h_{ra} \cdot A_{ra} \cdot (\mathrm{T}_{13} - \mathrm{T}_{amb}) - \varepsilon_{ra} \cdot \theta \cdot A_{ra} \cdot ({\mathrm{T}_{13}}^4 - {\mathrm{T}_{amb}}^4) \\ f_{14} = \frac{k_{ra} \cdot A_{ra}}{L_{ra}} \cdot (\mathrm{T}_{10} - \mathrm{T}_{14}) - h_{ra} \cdot A_{ra} \cdot (\mathrm{T}_{14} - \mathrm{T}_{03}) - \varepsilon_{ra} \cdot \theta \cdot A_{ra} \cdot ({\mathrm{T}_{14}}^4 - {\mathrm{T}_{03}}^4) \\ f_{15} = \frac{k_{ax} \cdot A_{ax}}{L_{ax}} \cdot (\mathrm{T}_{10} - \mathrm{T}_{15}) - h_{ax} \cdot A_{ax} \cdot (\mathrm{T}_{15} - \mathrm{T}_{amb}) - \varepsilon_{ax} \cdot \theta \cdot A_{ax} \cdot ({\mathrm{T}_{15}}^4 - {\mathrm{T}_{amb}}^4) \\ f_{16} = \frac{k_{ax} \cdot A_{ax}}{L_{ax}} \cdot (\mathrm{T}_{10} - \mathrm{T}_{16}) - h_{ax} \cdot A_{ax} \cdot (\mathrm{T}_{16} - \mathrm{T}_{amb}) - \varepsilon_{ax} \cdot \theta \cdot A_{ax} \cdot ({\mathrm{T}_{16}}^4 - {\mathrm{T}_{amb}}^4) \end{bmatrix} \tag{B.2}$$

3. Obtain the Jacobian matrix of the f_z matrix.

4. Apply Gaussian elimination to obtain a new approximation by (B.1).

$$z^1 = z^0 + \Delta x^0 = J_f(z_0)^{-1} \cdot f_{z^0} \tag{B.3}$$

5. Repeat steps 2-4 until the determined error tolerance is reached.

Bibliography

[1] Iea - International Energy Agency. *Global EV Outlook 2023: Catching up with climate ambitions*. Tech. rep. 2023. URL: https://www.iea.org/reports/global-ev-outlook-2023/trends-in-batteries.

[2] BloombergNEF. *Electric Vehicle Outlook 2022*. Tech. rep. 2022. URL: https://about.newenergyfinance.com/electric-vehicle-outlook/.

[3] Veronika Henze. *Lithium-ion Battery Pack Prices Rise for First Time to an Average of $151/kWh*. Tech. rep. BloombergNEF, Dec. 2022. URL: https://about.bnef.com/blog/lithium-ion-battery-pack-prices-rise-for-first-time-to-an-average-of-151-kwh/.

[4] Mahammad A. Hannan et al. "State-of-the-Art and Energy Management System of Lithium-Ion Batteries in Electric Vehicle Applications: Issues and Recommendations". In: *IEEE Access* 6 (Mar. 2018), pp. 19362–19378. ISSN: 2169-3536. DOI: 10.1109/ACCESS.2018.2817655. URL: https://ieeexplore.ieee.org/document/8320763/.

[5] Andreas Dinger et al. *Batteries for Electric Cars. Challenges, Opportunities, and the Outlook to 2020.* The Boston Colsulting Group, 2010. URL: www.bcg.com..

[6] Lip Huat Saw, Yonghuang Ye, and Andrew A.O. Tay. "Integration issues of lithium-ion battery into electric vehicles battery pack". In: *Journal of Cleaner Production* 113 (Feb. 2016), pp. 1032–1045. ISSN: 09596526. DOI: 10.1016/j.jclepro.2015.11.011. URL: https://linkinghub.elsevier.com/retrieve/pii/S0959652615016406.

[7] Billy Wu et al. "Battery digital twins: Perspectives on the fusion of models, data and artificial intelligence for smart battery management systems". In: *Energy and AI* 1 (Aug. 2020), p. 100016. ISSN: 26665468. DOI: 10.1016/j.egyai.2020.100016. URL: https://linkinghub.elsevier.com/retrieve/pii/S2666546820300161.

[8] Wenwen Wang et al. *Application of Digital Twin in Smart Battery Management Systems*. Dec. 2021. DOI: 10.1186/s10033-021-00577-0. URL: https://cjme.springeropen.com/articles/10.1186/s10033-021-00577-0.

[9] Jialin Liang et al. "Multilayer electrochemical-thermal coupled modeling of unbalanced discharging in a serially connected lithium-ion battery module". In: *Energy* 209 (Oct. 2020), p. 118429. ISSN: 03605442. DOI: 10.1016/j.energy.2020.118429. URL: https://linkinghub.elsevier.com/retrieve/pii/S0360544220315371.

[10] Tanvir R. Tanim et al. "Advanced diagnostics to evaluate heterogeneity in lithium-ion battery modules". In: *eTransportation* 3 (Feb. 2020), p. 100045. ISSN: 25901168. DOI: 10.1016/j.etran.2020.100045. URL: https://linkinghub.elsevier.com/retrieve/pii/S2590116820300023.

[11] Bing Wang et al. "Study of non-uniform temperature and discharging distribution for lithium-ion battery modules in series and parallel connection". In: *Applied Thermal Engineering* 168 (Mar. 2020), p. 114831. ISSN: 13594311. DOI: 10.1016/j.applthermaleng.2019.114831. URL: https://linkinghub.elsevier.com/retrieve/pii/S135943111933412X.

[12] Shahid A. Hasib et al. "A Comprehensive Review of Available Battery Datasets, RUL Prediction Approaches, and Advanced Battery Management". In: *IEEE Access* 9 (2021), pp. 86166–86193. ISSN: 2169-3536. DOI: 10.1109/ACCESS.2021.3089032. URL: https://ieeexplore.ieee.org/document/9454160/.

[13] Abbas Fotouhi et al. "A review on electric vehicle battery modelling: From Lithium-ion toward Lithium–Sulphur". In: *Renewable and Sustainable Energy Reviews* 56 (Apr. 2016), pp. 1008–1021. ISSN: 13640321. DOI: 10.1016/j.rser.2015.12.009. URL: https://linkinghub.elsevier.com/retrieve/pii/S1364032115013921.

[14] S. Abada et al. "Safety focused modeling of lithium-ion batteries: A review". In: *Journal of Power Sources* 306 (Feb. 2016), pp. 178–192. ISSN: 03787753. DOI: 10.1016/j.jpowsour.2015.11.100. URL: https://linkinghub.elsevier.com/retrieve/pii/S037877531530598X.

[15] Xiaosong Hu et al. "Battery Lifetime Prognostics". In: *Joule* 4 (2 Feb. 2020), pp. 310–346. ISSN: 25424351. DOI: 10.1016/j.joule.2019.11.018. URL: https://linkinghub.elsevier.com/retrieve/pii/S2542435119305859.

[16] Venkatasailanathan Ramadesigan et al. "Modeling and Simulation of Lithium-Ion Batteries from a Systems Engineering Perspective". In: *Journal of The Electrochemical Society* 159 (3 Jan. 2012), R31–R45. ISSN: 0013-4651. DOI: 10.1149/2.018203jes. URL: https://iopscience.iop.org/article/10.1149/2.018203jes.

[17] Mohammed B. Effat, Chili Wu, and Francesco Ciucci. "Modeling efforts in the key areas of thermal management and safety of lithium ion battery cells: a mini review". In: *Asia-Pacific Journal of Chemical Engineering* 11 (3 May 2016), pp. 399–406. ISSN: 19322135. DOI: 10.1002/apj.1999. URL: https://onlinelibrary.wiley.com/doi/10.1002/apj.1999.

[18] Bo Lu et al. "Review on electrode-level fracture in lithium-ion batteries*". In: *Chinese Physics B* 29 (2 Feb. 2020), p. 026201. ISSN: 1674-1056. DOI: 10.1088/1674-1056/ab6841. URL: https://iopscience.iop.org/article/10.1088/1674-1056/ab6841.

[19] Mina Naguib, Phillip Kollmeyer, and Ali Emadi. "Lithium-Ion Battery Pack Robust State of Charge Estimation, Cell Inconsistency, and Balancing: Review". In: *IEEE Access* 9 (2021), pp. 50570–50582. ISSN: 2169-3536. DOI: 10.1109/ACCESS.2021.3068776. URL: https://ieeexplore.ieee.org/document/9386065/.

[20] Christoph Jan Bartodziej. *The Concept Industry 4.0: An Empirical Analysis of Technologies and Applications in Production Logistics*. Springer Fachmedien Wiesbaden, 2017. ISBN: 978-3-658-16501-7. DOI: 10.1007/978-3-658-16502-4. URL: http://link.springer.com/10.1007/978-3-658-16502-4.

[21] David S. Landes. *The unbound Prometheus: technological change and industrial development in Western Europe from 1750 to the present*. Cambridge U.P, 1969. ISBN: 052107200X.

[22] Phyllis Deane. *The First Industrial Revolution*. Pbk Cam. 363. University Press, 1965. ISBN: 9787470000457.

[23] Marco Liserre, Thilo Sauter, and John Hung. "Future Energy Systems: Integrating Renewable Energy Sources into the Smart Power Grid Through Industrial Electronics". In: *IEEE Industrial Electronics Magazine* 4 (1 Mar. 2010), pp. 18–37. ISSN: 1932-4529. DOI: 10.1109/MIE.2010.935861. URL: http://ieeexplore.ieee.org/document/5439057/.

[24] Fei Tao et al. "Digital twin-driven product design, manufacturing and service with big data". In: *The International Journal of Advanced Manufacturing Technology* 94 (9-12 Feb. 2018), pp. 3563–3576. ISSN: 0268-3768. DOI: 10.1007/s00170-017-0233-1. URL: http://link.springer.com/10.1007/s00170-017-0233-1.

[25] Michael Rüßmann et al. *Industry 4.0: The Future of Productivity and Growth in Manufacturing Industries*. 1. 2015, pp. 54–89.

[26] Petre Prisecaru. "Challenges of the fourth industrial revolution". In: *Knowledge Horizons. Economics* 8.1 (2016), p. 57.

[27] Roland Rosen et al. "About The Importance of Autonomy and Digital Twins for the Future of Manufacturing". In: *IFAC-PapersOnLine* 48 (3 May 2015), pp. 567–572. ISSN: 24058963. DOI: 10.1016/j.ifacol.2015.06.141. URL: https://linkinghub.elsevier.com/retrieve/pii/S2405896315003808.

[28] Mehmet Baygin et al. "An effect analysis of industry 4.0 to higher education". In: IEEE, Sept. 2016, pp. 1–4. ISBN: 978-1-5090-0778-3. DOI: 10.1109/ITHET.2016.7760744. URL: http://ieeexplore.ieee.org/document/7760744/.

[29] Ulrich Dahmen and Juergen Rossmann. "What is a Digital Twin – A Mediation Approach". In: vol. 2021-May. IEEE, May 2021, pp. 165–172. ISBN: 978-1-6654-1846-1. DOI: 10.1109/EIT51626.2021.9491883. URL: https://ieeexplore.ieee.org/document/9491883/.

[30] Werner Kritzinger et al. "Digital Twin in manufacturing: A categorical literature review and classification". In: *IFAC-PapersOnLine* 51 (11 Jan. 2018), pp. 1016–1022. ISSN: 24058963. DOI: 10.1016/j.ifacol.2018.08.474. URL: https://linkinghub.elsevier.com/retrieve/pii/S2405896318316021.

[31] Michael Grieves. *Digital Twin: Manufacturing Excellence through Virtual Factory Replication*. Tech. rep. Florida Institute of Technology, 2014.

[32] Mike Shafto et al. *DRAFT Modeling, Simulation, information Technology & Processing Roadmap—Technology Area 11*. 2010.

[33] Eric J. Tuegel et al. "Reengineering Aircraft Structural Life Prediction Using a Digital Twin". In: *International Journal of Aerospace Engineering* 2011 (2011), pp. 1–14. ISSN: 1687-5966. DOI: 10.1155/2011/154798. URL: http://www.hindawi.com/journals/ijae/2011/154798/.

[34] Pierpaolo Caricato and Antonio Grieco. "An Application of Industry 4.0 to the Production of Packaging Films". In: *Procedia Manufacturing* 11 (2017), pp. 949–956. ISSN: 23519789. DOI: 10.1016/j.promfg.2017.07.199. URL: https://linkinghub.elsevier.com/retrieve/pii/S2351978917304079.

[35] Thomas H.-J. Uhlemann, Christian Lehmann, and Rolf Steinhilper. "The Digital Twin: Realizing the Cyber-Physical Production System for Industry 4.0". In: *Procedia CIRP* 61 (2017), pp. 335–340. ISSN: 22128271. DOI: 10.1016/j.procir.2016.11.152. URL: https://linkinghub.elsevier.com/retrieve/pii/S2212827116313129.

[36] Chiara Cimino, Elisa Negri, and Luca Fumagalli. "Review of digital twin applications in manufacturing". In: *Computers in Industry* 113 (Dec. 2019), p. 103130. ISSN: 01663615. DOI: 10.1016/j.compind.2019.103130. URL: https://linkinghub.elsevier.com/retrieve/pii/S0166361519304385.

[37] Edward Glaessgen and David Stargel. "The digital twin paradigm for future NASA and US Air Force vehicles". In: Apr. 2012, p. 1818. ISBN: 978-1-60086-937-2. DOI: 10.2514/6.2012-1818.

[38] Kasey Panetta. *Gartners Top 10 Technology Trends 2017*. Gartner. 2016-10-18. URL: https://www.gartner.com/smarterwithgartner/gartners-top-10-technology-trends-2017 (visited on 05/28/2023).

[39] Kasey Panetta. *Gartner Top 10 Strategic Technology Trends for 2018*. Gartner. 2017-10-03. URL: https://www.gartner.com/smarterwithgartner/gartner-top-10-strategic-technology-trends-for-2018 (visited on 05/28/2023).

[40] Kasey Panetta. *Gartner Top 10 Strategic Technology Trends for 2019*. Gartner. 2018-10-15. URL: https://www.gartner.com/smarterwithgartner/gartner-top-10-strategic-technology-trends-for-2019 (visited on 05/28/2023).

[41] Kasey Panetta. *Gartner Top 10 Strategic Technology Trends For 2020*. Gartner. 2019-10-21. URL: https://www.gartner.com/smarterwithgartner/gartner-top-10-strategic-technology-trends-for-2020 (visited on 05/28/2023).

[42] Fei Tao, Meng Zhang, and A.Y.C. Nee. "Five-Dimension Digital Twin Modeling and Its Key Technologies". In: *Digital Twin Driven Smart Manufacturing*. Ed. by Fei Tao, Meng Zhang, and A.Y.C. Nee. Academic Press, 2019. Chap. 3, pp. 63–81. ISBN: 978-0-12-817630-6. DOI: 10.1016/B978-0-12-817630-6.00003-5. URL: https://www.sciencedirect.com/science/article/pii/B9780128176306000035.

[43] Qinglin Qi et al. "Enabling technologies and tools for digital twin". In: *Journal of Manufacturing Systems* 58 (Jan. 2021), pp. 3–21. ISSN: 02786125. DOI: 10.1016/j.jmsy.2019.10.001. URL: https://linkinghub.elsevier.com/retrieve/pii/S027861251930086X.

[44] Itxaro Errandonea, Sergio Beltrán, and Saioa Arrizabalaga. "Digital Twin for maintenance: A literature review". In: *Computers in Industry* 123 (Dec. 2020), p. 103316. ISSN: 01663615. DOI: 10.1016/j.compind.2020.103316. URL: https://linkinghub.elsevier.com/retrieve/pii/S0166361520305509.

[45] Fei Tao et al. "Digital twin modeling". In: *Journal of Manufacturing Systems* 64 (July 2022), pp. 372–389. ISSN: 02786125. DOI: 10.1016/j.jmsy.2022.06.015. URL: https://linkinghub.elsevier.com/retrieve/pii/S0278612522001108.

[46] Maulshree Singh et al. "Applications of Digital Twin across Industries: A Review". In: *Applied Sciences* 12 (11 June 2022), p. 5727. ISSN: 2076-3417. DOI: 10.3390/app12115727. URL: https://www.mdpi.com/2076-3417/12/11/5727.

[47] Wei Yu et al. "Energy digital twin technology for industrial energy management: Classification, challenges and future". In: *Renewable and Sustainable Energy Reviews* 161 (June 2022), p. 112407. ISSN: 13640321. DOI: 10.1016/j.rser.2022.112407. URL: https://linkinghub.elsevier.com/retrieve/pii/S136403212200315X.

[48] Sin Yong Teng et al. "Recent advances on industrial data-driven energy savings: Digital twins and infrastructures". In: *Renewable and Sustainable Energy Reviews* 135 (Jan. 2021), p. 110208. ISSN: 13640321. DOI: 10.1016/j.rser.2020.110208. URL: https://linkinghub.elsevier.com/retrieve/pii/S1364032120304974.

[49] Weihan Li et al. "Digital twin for battery systems: Cloud battery management system with online state-of-charge and state-of-health estimation". In: *Journal of Energy Storage* 30 (Aug. 2020), p. 101557. ISSN: 2352152X. DOI: 10.1016/j.est.2020.101557. URL: https://linkinghub.elsevier.com/retrieve/pii/S2352152X20308495.

[50] Naga Durga Krishna Mohan Eaty and Priyanka Bagade. "Digital twin for electric vehicle battery management with incremental learning". In: *Expert Systems with Applications* 229 (Nov. 2023), p. 120444. ISSN: 09574174. DOI: 10.1016/j.eswa.2023.120444. URL: https://linkinghub.elsevier.com/retrieve/pii/S0957417423009466.

[51] Concetta Semeraro et al. "Digital twin in battery energy storage systems: Trends and gaps detection through association rule mining". In: *Energy* 273 (June 2023), p. 127086. ISSN: 03605442. DOI: 10.1016/j.energy.2023.127086. URL: https://linkinghub.elsevier.com/retrieve/pii/S0360544223004802.

[52] F. Naseri et al. “Digital twin of electric vehicle battery systems: Comprehensive review of the use cases, requirements, and platforms”. In: *Renewable and Sustainable Energy Reviews* 179 (June 2023), p. 113280. ISSN: 13640321. DOI: 10.1016/j.rser.2023.113280. URL: https://linkinghub.elsevier.com/retrieve/pii/S1364032123001363.

[53] Martin Robert Enders and Nadja Hoßbach. “Dimensions of digital twin applications-a literature review”. In: 2019.

[54] Reinhardt Klein et al. “Electrochemical Model Based Observer Design for a Lithium-Ion Battery”. In: *IEEE Transactions on Control Systems Technology* 21 (2 Mar. 2013), pp. 289–301. ISSN: 1063-6536. DOI: 10.1109/TCST.2011.2178604. URL: http://ieeexplore.ieee.org/document/6121920/.

[55] Nicolas Watrin, Benjamin Blunier, and Abdellatif Miraoui. “Review of adaptive systems for lithium batteries State-of-Charge and State-of-Health estimation”. In: IEEE, June 2012, pp. 1–6. ISBN: 978-1-4673-1408-4. DOI: 10.1109/ITEC.2012.6243437. URL: https://ieeexplore.ieee.org/document/6243437.

[56] S. Al Hallaj et al. “Thermal modeling and design considerations of lithium-ion batteries”. In: *Journal of Power Sources* 83 (1-2 Oct. 1999), pp. 1–8. ISSN: 03787753. DOI: 10.1016/S0378-7753(99)00178-0. URL: https://linkinghub.elsevier.com/retrieve/pii/S0378775399001780.

[57] Shuiguang Deng et al. “Edge Intelligence: The Confluence of Edge Computing and Artificial Intelligence”. In: *IEEE Internet of Things Journal* 7 (8 Aug. 2020), pp. 7457–7469. ISSN: 2327-4662. DOI: 10.1109/JIOT.2020.2984887. URL: https://ieeexplore.ieee.org/document/9052677/.

[58] Yucong Duan et al. “Everything as a Service (XaaS) on the Cloud: Origins, Current and Future Trends”. In: IEEE, June 2015, pp. 621–628. ISBN: 978-1-4673-7287-9. DOI: 10.1109/CLOUD.2015.88. URL: http://ieeexplore.ieee.org/document/7214098/.

[59] Fei Tao and Meng Zhang. “Digital Twin Shop-Floor: A New Shop-Floor Paradigm Towards Smart Manufacturing”. In: *IEEE Access* 5 (Sept. 2017), pp. 20418–20427. ISSN: 2169-3536. DOI: 10.1109/ACCESS.2017.2756069. URL: http://ieeexplore.ieee.org/document/8049520/.

[60] Gholam-Abbas Nazri and Gianfranco Pistoia. *Lithium Batteries*. Ed. by Gholam-Abbas Nazri and Gianfranco Pistoia. 1st ed. Springer US, Jan. 2009. ISBN: 978-0-387-92674-2. DOI: 10.1007/978-0-387-92675-9. URL: http://link.springer.com/10.1007/978-0-387-92675-9.

[61] Ghanishtha Bhatti, Harshit Mohan, and R. Raja Singh. “Towards the future of smart electric vehicles: Digital twin technology”. In: *Renewable and Sustainable Energy Reviews* 141 (May 2021), p. 110801. ISSN: 13640321. DOI: 10.1016/j.rser.2021.110801. URL: https://linkinghub.elsevier.com/retrieve/pii/S1364032121000964.

[62] Alessandro Birolini. *Reliability Engineering*. Springer Berlin Heidelberg, 2010, pp. 1–610. ISBN: 978-3-642-14951-1. DOI: 10.1007/978-3-642-14952-8. URL: https://link.springer.com/10.1007/978-3-642-14952-8.

[63] Yujie Wang et al. "Digital twin and cloud-side-end collaboration for intelligent battery management system". In: *Journal of Manufacturing Systems* 62 (Jan. 2022), pp. 124–134. ISSN: 02786125. DOI: 10.1016/j.jmsy.2021.11.006.

[64] Davide Andrea. *Battery management systems for large lithium-ion battery packs*. EBL-Schweitzer. Artech house, 2010, pp. 51–105. ISBN: 9781608071050.

[65] Andrea Vezzini. *Lithium-Ion Battery Management*. Elsevier, 2014, pp. 345–360. ISBN: 9780444595133. DOI: 10.1016/B978-0-444-59513-3.00015-7. URL: https://linkinghub.elsevier.com/retrieve/pii/B9780444595133000157.

[66] A. Jossen et al. "Reliable battery operation — a challenge for the battery management system". In: *Journal of Power Sources* 84 (2 Dec. 1999), pp. 283–286. ISSN: 03787753. DOI: 10.1016/S0378-7753(99)00329-8. URL: https://linkinghub.elsevier.com/retrieve/pii/S0378775399003298.

[67] Phillip. Weicker. *A systems approach to lithium-ion battery management*. Artech house, 2014, pp. 71–94. ISBN: 9781608076598.

[68] Muhammad Uzair, Ghulam Abbas, and Saleh Hosain. "Characteristics of Battery Management Systems of Electric Vehicles with Consideration of the Active and Passive Cell Balancing Process". In: *World Electric Vehicle Journal* 12 (3 Aug. 2021), p. 120. ISSN: 2032-6653. DOI: 10.3390/wevj12030120. URL: https://www.mdpi.com/2032-6653/12/3/120.

[69] Weixiong Wu et al. "A critical review of battery thermal performance and liquid based battery thermal management". In: *Energy Conversion and Management* 182 (Feb. 2019), pp. 262–281. ISSN: 01968904. DOI: 10.1016/j.enconman.2018.12.051. URL: https://linkinghub.elsevier.com/retrieve/pii/S0196890418313876.

[70] Alexander Popp et al. "Battery Management Systems Topologies: Applications : Implications of different voltage levels". In: *2021 IEEE 4th International Conference on Power and Energy Applications, ICPEA 2021* (2021), pp. 43–50. DOI: 10.1109/ICPEA52760.2021.9639285.

[71] Markus Lelie et al. "Battery Management System Hardware Concepts: An Overview". In: *Applied Sciences* 8 (4 Mar. 2018), p. 534. ISSN: 2076-3417. DOI: 10.3390/app8040534. URL: http://www.mdpi.com/2076-3417/8/4/534.

[72] Shichun Yang et al. "Implementation for a cloud battery management system based on the CHAIN framework". In: *Energy and AI* 5 (Sept. 2021). ISSN: 26665468. DOI: 10.1016/j.egyai.2021.100088.

[73] Francisco José Gimeno-Sales et al. "Pv monitoring system for a water pumping scheme with a lithium-ion battery using free open-source software and iot technologies". In: *Sustainability (Switzerland)* 12 (24 Dec. 2020), pp. 1–28. ISSN: 20711050. DOI: 10.3390/su122410651.

[74] M.S. Hossain Lipu et al. "A review of state of health and remaining useful life estimation methods for lithium-ion battery in electric vehicles: Challenges and recommendations". In: *Journal of Cleaner Production* 205 (Dec. 2018), pp. 115–133. ISSN: 09596526. DOI: 10.1016/j.jclepro.2018.09.065. URL: https://linkinghub.elsevier.com/retrieve/pii/S0959652618327793.

[75] C Su and H J Chen. "A review on prognostics approaches for remaining useful life of lithium-ion battery". In: *IOP Conference Series: Earth and Environmental Science* 93 (1 Nov. 2017), p. 012040. ISSN: 1755-1307. DOI: 10.1088/1755-1315/93/1/012040. URL: https://iopscience.iop.org/article/10.1088/1755-1315/93/1/012040.

[76] Lifeng Wu, Xiaohui Fu, and Yong Guan. "Review of the Remaining Useful Life Prognostics of Vehicle Lithium-Ion Batteries Using Data-Driven Methodologies". In: *Applied Sciences* 6 (6 May 2016), p. 166. ISSN: 2076-3417. DOI: 10.3390/app6060166. URL: http://www.mdpi.com/2076-3417/6/6/166.

[77] Yi Li et al. "Data-driven health estimation and lifetime prediction of lithium-ion batteries: A review". In: *Renewable and Sustainable Energy Reviews* 113 (Oct. 2019), p. 109254. ISSN: 13640321. DOI: 10.1016/j.rser.2019.109254. URL: https://linkinghub.elsevier.com/retrieve/pii/S136403211930454X.

[78] Samuel Pelletier et al. "Battery degradation and behaviour for electric vehicles: Review and numerical analyses of several models". In: *Transportation Research Part B: Methodological* 103 (Sept. 2017), pp. 158–187. ISSN: 01912615. DOI: 10.1016/j.trb.2017.01.020. URL: https://linkinghub.elsevier.com/retrieve/pii/S0191261516303794.

[79] Shuai Ma et al. "Temperature effect and thermal impact in lithium-ion batteries: A review". In: *Progress in Natural Science: Materials International* 28 (6 Dec. 2018), pp. 653–666. ISSN: 10020071. DOI: 10.1016/j.pnsc.2018.11.002. URL: https://linkinghub.elsevier.com/retrieve/pii/S1002007118307536.

[80] Ahmad Pesaran, Shriram Santhanagopalan, and Gi-Heon Kim. "Addressing the Impact of Temperature Extremes on Large Format Li-Ion Batteries for Vehicle Applications". In: May 2013. URL: https://www.osti.gov/biblio/1082548.

[81] Shovon Goutam et al. "Comparative Study of Surface Temperature Behavior of Commercial Li-Ion Pouch Cells of Different Chemistries and Capacities by Infrared Thermography". In: *Energies* 8 (8 Aug. 2015), pp. 8175–8192. ISSN: 1996-1073. DOI: 10.3390/en8088175. URL: http://www.mdpi.com/1996-1073/8/8/8175.

[82] S.S. Zhang, K. Xu, and T.R. Jow. "The low temperature performance of Li-ion batteries". In: *Journal of Power Sources* 115 (1 Mar. 2003), pp. 137–140. ISSN: 03787753. DOI: 10.1016/S0378-7753(02)00618-3. URL: https://linkinghub.elsevier.com/retrieve/pii/S0378775302006183.

[83] Xiao-Guang Yang et al. "Asymmetric Temperature Modulation for Extreme Fast Charging of Lithium-Ion Batteries". In: *Joule* 3 (12 Dec. 2019), pp. 3002–3019. ISSN: 25424351. DOI: 10.1016/j.joule.2019.09.021. URL: https://linkinghub.elsevier.com/retrieve/pii/S2542435119304817.

[84] G. Nagasubramanian. "Electrical characteristics of 18650 Li-ion cells at low temperatures". In: *Journal of Applied Electrochemistry* 31 (1 2001), pp. 99–104. ISSN: 0021891X. DOI: 10.1023/A:1004113825283.

[85] Simon Tippmann et al. "Low-temperature charging of lithium-ion cells part I: Electrochemical modeling and experimental investigation of degradation behavior". In: *Journal of Power Sources* 252 (Apr. 2014), pp. 305–316. ISSN: 03787753. DOI: 10.1016/j.jpowsour.2013.12.022. URL: https://linkinghub.elsevier.com/retrieve/pii/S0378775313019897.

[86] Zhongfeng Tang et al. "Facilitating Lithium-Ion Diffusion in Layered Cathode Materials by Introducing Li ⁺ /Ni ²⁺ Antisite Defects for High-Rate Li-Ion Batteries". In: *Research* 2019 (Jan. 2019). ISSN: 2639-5274. DOI: 10.34133/2019/2198906. URL: https://spj.science.org/doi/10.34133/2019/2198906.

[87] Hua Zhang et al. "On-line Measurement of Internal Resistance of Lithium Ion Battery for EV and Its Application Research". In: *International Journal of u- and e-Service, Science and Technology* 7 (4 Aug. 2014), pp. 301–310. ISSN: 20054246. DOI: 10.14257/ijunesst.2014.7.4.27. URL: http://article.nadiapub.com/IJUNESST/vol7_no4/27.pdf.

[88] Michel Rosso et al. "Dendrite short-circuit and fuse effect on Li/polymer/Li cells". In: *Electrochimica Acta* 51 (25 July 2006), pp. 5334–5340. ISSN: 00134686. DOI: 10.1016/j.electacta.2006.02.004. URL: https://linkinghub.elsevier.com/retrieve/pii/S0013468606001265.

[89] Todd M. Bandhauer, Srinivas Garimella, and Thomas F. Fuller. "A Critical Review of Thermal Issues in Lithium-Ion Batteries". In: *Journal of The Electrochemical Society* 158 (3 2011), R1. ISSN: 00134651. DOI: 10.1149/1.3515880. URL: https://iopscience.iop.org/article/10.1149/1.3515880.

[90] D. Bernardi, E. Pawlikowski, and J. Newman. "A General Energy Balance for Battery Systems". In: *Journal of The Electrochemical Society* 132 (1 Jan. 1985), pp. 5–12. ISSN: 0013-4651. DOI: 10.1149/1.2113792. URL: https://iopscience.iop.org/article/10.1149/1.2113792.

[91] Akram Eddahech, Olivier Briat, and Jean-Michel Vinassa. "Thermal characterization of a high-power lithium-ion battery: Potentiometric and calorimetric measurement of entropy changes". In: *Energy* 61 (Nov. 2013), pp. 432–439. ISSN: 03605442. DOI: 10.1016/j.energy.2013.09.028. URL: https://linkinghub.elsevier.com/retrieve/pii/S0360544213007792.

[92] Xiongping Lin et al. "State of Charge and Lithium Manganate Batteries Internal Resistance Estimation at Low Charge/discharge rates". In: *International Journal of Electrochemical Science* 16 (1 Jan. 2021), p. 151024. ISSN: 14523981. DOI: 10.20964/2021.01.48. URL: http://www.electrochemsci.org/abstracts/vol16/16010151024.pdf.

[93] Divya Chalise et al. “Heat of Mixing During Fast Charge/Discharge of a Li-Ion Cell: A Study on NMC523 Cathode”. In: *Journal of The Electrochemical Society* 167 (9 Jan. 2020), p. 090560. ISSN: 0013-4651. DOI: 10.1149/1945-7111/abaf71. URL: https://iopscience.iop.org/article/10.1149/1945-7111/abaf71.

[94] Yunpeng Zhuang et al. “Effect of cation mixing of Li ⁺ /Ni ²⁺ on heat generation of NCM811 cathode during long-term cycling at elevated temperature”. In: *Applied Physics Letters* 121 (8 Aug. 2022), p. 083902. ISSN: 0003-6951. DOI: 10.1063/5.0100557. URL: https://pubs.aip.org/aip/apl/article/2834177.

[95] Xuning Feng et al. “Mechanisms for the evolution of cell variations within a LiNixCoyMnzO2/graphite lithium-ion battery pack caused by temperature non-uniformity”. In: *Journal of Cleaner Production* 205 (Dec. 2018), pp. 447–462. ISSN: 09596526. DOI: 10.1016/j.jclepro.2018.09.003. URL: https://linkinghub.elsevier.com/retrieve/pii/S095965261832715X.

[96] Noreffendy Tamaldin et al. “Design Optimization of Thermal Management System for Electric VehicleUtilizing CFD Analysis, DFMEA and CES”. In: *Procedia Engineering* 68 (2013), pp. 305–312. ISSN: 18777058. DOI: 10.1016/j.proeng.2013.12.184. URL: https://linkinghub.elsevier.com/retrieve/pii/S1877705813020389.

[97] Yuqi Huang et al. “Study on the thermal interaction and heat dissipation of cylindrical Lithium-Ion Battery cells”. In: *Energy Procedia* 142 (Dec. 2017), pp. 4029–4036. ISSN: 18766102. DOI: 10.1016/j.egypro.2017.12.321. URL: https://linkinghub.elsevier.com/retrieve/pii/S1876610217360630.

[98] Ximing Cheng et al. “Influences of Structure Components on Thermal Distribution of a Cylindrical Lithium-ion Battery”. In: *Energy Procedia* 158 (Feb. 2019), pp. 4959–4966. ISSN: 18766102. DOI: 10.1016/j.egypro.2019.01.692. URL: https://linkinghub.elsevier.com/retrieve/pii/S1876610219307295.

[99] Paul T. Coman et al. “A Reduced-Order Lumped Model for Li-Ion Battery Packs during Operation”. In: *Journal of The Electrochemical Society* 168 (10 Oct. 2021), p. 100525. ISSN: 0013-4651. DOI: 10.1149/1945-7111/ac2dcb. URL: https://iopscience.iop.org/article/10.1149/1945-7111/ac2dcb.

[100] Li Sun, Wen Sun, and Fengqi You. “Core temperature modelling and monitoring of lithium-ion battery in the presence of sensor bias”. In: *Applied Energy* 271 (Aug. 2020), p. 115243. ISSN: 03062619. DOI: 10.1016/j.apenergy.2020.115243. URL: https://linkinghub.elsevier.com/retrieve/pii/S0306261920307558.

[101] Manuel Antonio Perez Estevez et al. “An electro-thermal model and its electrical parameters estimation procedure in a lithium-ion battery cell”. In: *Energy* 234 (Nov. 2021), p. 121296. ISSN: 03605442. DOI: 10.1016/j.energy.2021.121296. URL: https://linkinghub.elsevier.com/retrieve/pii/S0360544221015449.

[102] Mohsen Akbarzadeh et al. “Thermal modeling of a high-energy prismatic lithium-ion battery cell and module based on a new thermal characterization methodology”. In: *Journal of Energy Storage* 32 (Dec. 2020), p. 101707. ISSN: 2352152X. DOI:

10.1016/j.est.2020.101707. URL: https://linkinghub.elsevier.com/retrieve/pii/S2352152X20315449.

[103] Edwin Paccha-Herrera et al. "Thermal Modeling Approaches for a LiCoO2 Lithium-ion Battery—A Comparative Study with Experimental Validation". In: *Batteries* 6 (3 Aug. 2020), p. 40. ISSN: 2313-0105. DOI: 10.3390/batteries6030040. URL: https://www.mdpi.com/2313-0105/6/3/40.

[104] Gregory L. Plett. *Battery Management Systems, Volume II: Equivalent-Circuit Methods*. Artech House, 2015, p. 336. ISBN: 1630810282.

[105] Alexandros Nikolian et al. "Classification of Electric modelling and Characterization methods of Lithium-ion Batteries for Vehicle Applications". In: Dec. 2014.

[106] Gaizka Saldaña et al. "Analysis of the Current Electric Battery Models for Electric Vehicle Simulation". In: *Energies* 12 (14 July 2019). OSO INTERESGARRIA!

Modelo elektrikoei buruzko laburpen at egiten du eta modelo bakoitzaren ventaja eta desventajak izendatu.

** Estacionarioako EIS neurketak direla onenak komentatzen du., p. 2750. ISSN: 1996-1073. DOI: 10.3390/en12142750. URL: https://www.mdpi.com/1996-1073/12/14/2750.

[107] Maheshwari Adaikkappan and Nageswari Sathiyamoorthy. "Modeling, state of charge estimation, and charging of lithium-ion battery in electric vehicle: A review". In: *International Journal of Energy Research* 46 (3 Mar. 2022), pp. 2141–2165. ISSN: 0363-907X. DOI: 10.1002/er.7339. URL: https://onlinelibrary.wiley.com/doi/10.1002/er.7339.

[108] Gang Ning and Branko N. Popov. "Cycle Life Modeling of Lithium-Ion Batteries". In: *Journal of The Electrochemical Society* 151 (10 2004), A1584. ISSN: 00134651. DOI: 10.1149/1.1787631. URL: https://iopscience.iop.org/article/10.1149/1.1787631.

[109] Christopher Wett et al. "Method of Lines for flexible coupling of the Single Particle Model for Lithium-Ion Batteries demonstrated by thermal modelling". In: *Journal of Energy Storage* 68 (Sept. 2023), p. 107459. ISSN: 2352152X. DOI: 10.1016/j.est.2023.107459. URL: https://linkinghub.elsevier.com/retrieve/pii/S2352152X23008563.

[110] Ferran Brosa Planella and W. Dhammika Widanage. "A Single Particle model with electrolyte and side reactions for degradation of lithium-ion batteries". In: *Applied Mathematical Modelling* 121 (Sept. 2023), pp. 586–610. ISSN: 0307904X. DOI: 10.1016/j.apm.2022.12.009. URL: https://linkinghub.elsevier.com/retrieve/pii/S0307904X22005959.

[111] Toshan Wickramanayake, Mehrnaz Javadipour, and Kamyar Mehran. "A Novel Root-Finding Algorithm to Solve the Pseudo-2D Model of a Lithium-ion Battery". In: IEEE, Mar. 2023, pp. 1–6. ISBN: 979-8-3503-4689-3. DOI: 10.1109/ESARS-ITEC57127.2023.10114840. URL: https://ieeexplore.ieee.org/document/10114840/.

[112] Weilong Ai et al. "Electrochemical Thermal-Mechanical Modelling of Stress Inhomogeneity in Lithium-Ion Pouch Cells". In: *Journal of The Electrochemical Society* 167 (1 Oct. 2020), p. 013512. ISSN: 0013-4651. DOI: 10.1149/2.0122001JES. URL: https://iopscience.iop.org/article/10.1149/2.0122001JES.

[113] A.M. Bizeray et al. "Lithium-ion battery thermal-electrochemical model-based state estimation using orthogonal collocation and a modified extended Kalman filter". In: *Journal of Power Sources* 296 (Nov. 2015), pp. 400–412. ISSN: 03787753. DOI: 10.1016/j.jpowsour.2015.07.019. URL: https://linkinghub.elsevier.com/retrieve/pii/S0378775315300677.

[114] John Newman et al. "Modeling of lithium-ion batteries". In: *Journal of Power Sources* 119-121 (June 2003), pp. 838–843. ISSN: 03787753. DOI: 10.1016/S0378-7753(03)00282-9. URL: https://linkinghub.elsevier.com/retrieve/pii/S0378775303002829.

[115] Wei-Jen Lin and Kuo-Ching Chen. "Evolution of parameters in the Doyle-Fuller-Newman model of cycling lithium ion batteries by multi-objective optimization". In: *Applied Energy* 314 (May 2022), p. 118925. ISSN: 03062619. DOI: 10.1016/j.apenergy.2022.118925. URL: https://linkinghub.elsevier.com/retrieve/pii/S0306261922003476.

[116] Z. Khalik et al. "Parameter estimation of the Doyle–Fuller–Newman model for Lithium-ion batteries by parameter normalization, grouping, and sensitivity analysis". In: *Journal of Power Sources* 499 (July 2021), p. 229901. ISSN: 03787753. DOI: 10.1016/j.jpowsour.2021.229901. URL: https://linkinghub.elsevier.com/retrieve/pii/S0378775321004341.

[117] Gregory Plett. *Battery Management Systems, Volume I: Battery Modeling*. Artech House, Sept. 2015. ISBN: 9781630810238.

[118] Md Ashiqur Rahman, Sohel Anwar, and Afshin Izadian. "Electrochemical model parameter identification of a lithium-ion battery using particle swarm optimization method". In: *Journal of Power Sources* 307 (Mar. 2016), pp. 86–97. ISSN: 03787753. DOI: 10.1016/j.jpowsour.2015.12.083. URL: https://linkinghub.elsevier.com/retrieve/pii/S0378775315306959.

[119] Wenlu Zhou et al. "Review on the Battery Model and SOC Estimation Method". In: *Processes* 9 (9 Sept. 2021), p. 1685. ISSN: 2227-9717. DOI: 10.3390/pr9091685. URL: https://www.mdpi.com/2227-9717/9/9/1685.

[120] Younes Boujoudar, Hassan Elmoussaoui, and Tijani Lamhamdi. "Lithium-Ion batteries modeling and state of charge estimation using Artificial Neural Network". In: *International Journal of Electrical and Computer Engineering (IJECE)* 9 (5 Oct. 2019), p. 3415. ISSN: 2722-2578. DOI: 10.11591/ijece.v9i5.pp3415-3422. URL: http://ijece.iaescore.com/index.php/IJECE/article/view/15552.

[121] Renato G. Nascimento et al. "Hybrid physics-informed neural networks for lithium-ion battery modeling and prognosis". In: *Journal of Power Sources* 513 (Nov. 2021), p. 230526. ISSN: 03787753. DOI: 10.1016/j.jpowsour.2021.230526. URL: https://linkinghub.elsevier.com/retrieve/pii/S0378775321010259.

[122] Christian Fleischer et al. “On-line self-learning time forward voltage prognosis for lithium-ion batteries using adaptive neuro-fuzzy inference system”. In: *Journal of Power Sources* 243 (Dec. 2013), pp. 728–749. ISSN: 03787753. DOI: 10.1016/j.jpowsour.2013.05.114. URL: https://linkinghub.elsevier.com/retrieve/pii/S037877531300904X.

[123] Verena Klass, Mårten Behm, and Göran Lindbergh. “Capturing lithium-ion battery dynamics with support vector machine-based battery model”. In: *Journal of Power Sources* 298 (Dec. 2015), pp. 92–101. ISSN: 03787753. DOI: 10.1016/j.jpowsour.2015.08.036. URL: https://linkinghub.elsevier.com/retrieve/pii/S0378775315301919.

[124] S. Gold. “A PSPICE macromodel for lithium-ion batteries”. In: IEEE, pp. 215–222. ISBN: 0-7803-3631-3. DOI: 10.1109/BCAA.1997.574106. URL: http://ieeexplore.ieee.org/document/574106/.

[125] Simone Barcellona and Luigi Piegari. “Lithium Ion Battery Models and Parameter Identification Techniques”. In: *Energies* 10 (12 Dec. 2017), p. 2007. ISSN: 1996-1073. DOI: 10.3390/en10122007. URL: http://www.mdpi.com/1996-1073/10/12/2007.

[126] Alberto Berrueta et al. “Lithium-ion battery model and experimental validation”. In: IEEE, Sept. 2015, pp. 1–8. ISBN: 978-9-0758-1522-1. DOI: 10.1109/EPE.2015.7309337. URL: http://ieeexplore.ieee.org/document/7309337/.

[127] J.P. Cun et al. “The experience of a UPS company in advanced battery monitoring”. In: IEEE, 1996, pp. 646–653. ISBN: 0-7803-3507-4. DOI: 10.1109/INTLEC.1996.573404. URL: http://ieeexplore.ieee.org/document/573404/.

[128] J. Marcos et al. “An approach to real behaviour modeling for traction lead-acid batteries”. In: vol. 2. IEEE, 2001, pp. 620–624. ISBN: 0-7803-7067-8. DOI: 10.1109/PESC.2001.954185. URL: http://ieeexplore.ieee.org/document/954185/.

[129] J. Alvarez et al. “A fully digital smart and fast lead-acid battery charge system”. In: vol. 2. IEEE, pp. 913–917. ISBN: 0-7803-7754-0. DOI: 10.1109/PESC.2003.1218177. URL: http://ieeexplore.ieee.org/document/1218177/.

[130] Zhai Haizhou. “Modeling of Lithium-ion Battery for Charging/Discharging Characteristics Based on Circuit Model”. In: *International Journal of Online Engineering (iJOE)* 13 (06 June 2017), p. 86. ISSN: 1861-2121. DOI: 10.3991/ijoe.v13i06.6799. URL: http://online-journals.org/index.php/i-joe/article/view/6799.

[131] Dan Liu et al. “SOC Estimation of Lithium Battery Based on N-2RC Model in Electric Vehicle”. In: IEEE, June 2019, pp. 2916–2921. ISBN: 978-1-7281-0106-4. DOI: 10.1109/CCDC.2019.8833008. URL: https://ieeexplore.ieee.org/document/8833008/.

[132] Tedjani Mesbahi et al. “Dynamic Model of Li-Ion Batteries Incorporating Electrothermal and Ageing Aspects for Electric Vehicle Applications”. In: *IEEE Transactions on Industrial Electronics* 65 (2 Feb. 2018), pp. 1298–1305. ISSN: 0278-0046. DOI: 10.1109/TIE.2017.2714118. URL: http://ieeexplore.ieee.org/document/7945538/.

[133] Paul Nelson et al. “Design modeling of lithium-ion battery performance”. In: *Journal of Power Sources* 110 (2 Aug. 2002), pp. 437–444. ISSN: 03787753. DOI: 10.1016/S0378-7753(02)00209-4. URL: https://linkinghub.elsevier.com/retrieve/pii/S0378775302002094.

[134] Xiangyong Liu, Wanli Li, and Aiguo Zhou. “PNGV Equivalent Circuit Model and SOC Estimation Algorithm for Lithium Battery Pack Adopted in AGV Vehicle”. In: *IEEE Access* 6 (Mar. 2018), pp. 23639–23647. ISSN: 2169-3536. DOI: 10.1109/ACCESS.2018.2812421. URL: https://ieeexplore.ieee.org/document/8308729/.

[135] Hongwen He, Rui Xiong, and Jinxin Fan. “Evaluation of Lithium-Ion Battery Equivalent Circuit Models for State of Charge Estimation by an Experimental Approach”. In: *Energies* 4 (4 Mar. 2011), pp. 582–598. ISSN: 1996-1073. DOI: 10.3390/en4040582. URL: http://www.mdpi.com/1996-1073/4/4/582.

[136] Noshin Omar et al. “Rechargeable Energy Storage Systems for Plug-in Hybrid Electric Vehicles—Assessment of Electrical Characteristics”. In: *Energies* 5 (8 Aug. 2012), pp. 2952–2988. ISSN: 1996-1073. DOI: 10.3390/en5082952. URL: http://www.mdpi.com/1996-1073/5/8/2952.

[137] Noshin Omar et al. “Optimization of an advanced battery model parameter minimization tool and development of a novel electrical model for lithium-ion batteries”. In: *International Transactions on Electrical Energy Systems* 24 (12 Dec. 2014), pp. 1747–1767. ISSN: 20507038. DOI: 10.1002/etep.1815. URL: https://onlinelibrary.wiley.com/doi/10.1002/etep.1815.

[138] Zhong Ren and Changqing Du. “A review of machine learning state-of-charge and state-of-health estimation algorithms for lithium-ion batteries”. In: *Energy Reports* 9 (Dec. 2023), pp. 2993–3021. ISSN: 23524847. DOI: 10.1016/j.egyr.2023.01.108. URL: https://linkinghub.elsevier.com/retrieve/pii/S235248472300118X.

[139] Masood Ul Hassan et al. “A comprehensive review of battery state of charge estimation techniques”. In: *Sustainable Energy Technologies and Assessments* 54 (Dec. 2022), p. 102801. ISSN: 22131388. DOI: 10.1016/j.seta.2022.102801. URL: https://linkinghub.elsevier.com/retrieve/pii/S2213138822008499.

[140] Dickson N. T. How et al. “State of Charge Estimation for Lithium-Ion Batteries Using Model-Based and Data-Driven Methods: A Review”. In: *IEEE Access* 7 (2019). Bateria abten modeliñaren eskema polita egiten du (kuadernoan eginda).
**Key issues and challenges sekzioan kontuan hartu behar diren caracterizazio garrantzitsuak azaltzen dira (tesi honetatik kanpo geratzen direnak, Future lines?), pp. 136116–136136. ISSN: 2169-3536. DOI: 10.1109/ACCESS.2019.2942213. URL: https://ieeexplore.ieee.org/document/8843918/.

[141] M.A. Hannan et al. “A review of lithium-ion battery state of charge estimation and management system in electric vehicle applications: Challenges and recommendations”. In: *Renewable and Sustainable Energy Reviews* 78 (August 2016 Oct. 2017). ESTATE STIMATION:
Kalman filterrari buruzko erreferentziak eta banaka nahiko ondo esplikatuta ematen duenez, pp. 834–854. ISSN: 13640321. DOI:

10.1016/j.rser.2017.05.001. URL: https://linkinghub.elsevier.com/retrieve/pii/S1364032117306275.

[142] Muhammad Umair Ali et al. "Towards a Smarter Battery Management System for Electric Vehicle Applications: A Critical Review of Lithium-Ion Battery State of Charge Estimation". In: *Energies* 12 (3 Jan. 2019). Oso interesgarria, 6orrian eginda daukan eskema., p. 446. ISSN: 1996-1073. DOI: 10.3390/en12030446. URL: http://www.mdpi.com/1996-1073/12/3/446.

[143] Woosung Choi et al. "Modeling and applications of electrochemical impedance spectroscopy (Eis) for lithium-ion batteries". In: *Journal of Electrochemical Science and Technology* 11 (1 2020), pp. 1–13. ISSN: 22889221. DOI: 10.33961/jecst.2019.00528.

[144] Li Zhao, Muyi Lin, and Yong Chen. "Least-squares based coulomb counting method and its application for state-of-charge (SOC) estimation in electric vehicles". In: *International Journal of Energy Research* 40 (10 Aug. 2016), pp. 1389–1399. ISSN: 0363907X. DOI: 10.1002/er.3530. URL: https://onlinelibrary.wiley.com/doi/10.1002/er.3530.

[145] Gregory L. Plett. "Extended Kalman filtering for battery management systems of LiPB-based HEV battery packs". In: *Journal of Power Sources* 134 (2 Aug. 2004), pp. 252–261. ISSN: 03787753. DOI: 10.1016/j.jpowsour.2004.02.031. URL: https://linkinghub.elsevier.com/retrieve/pii/S0378775304003593.

[146] Gregory L. Plett. "Extended Kalman filtering for battery management systems of LiPB-based HEV battery packs". In: *Journal of Power Sources* 134 (2 Aug. 2004), pp. 262–276. ISSN: 03787753. DOI: 10.1016/j.jpowsour.2004.02.032. URL: https://linkinghub.elsevier.com/retrieve/pii/S037877530400360X.

[147] Gregory L. Plett. "Extended Kalman filtering for battery management systems of LiPB-based HEV battery packs". In: *Journal of Power Sources* 134 (2 Aug. 2004), pp. 277–292. ISSN: 03787753. DOI: 10.1016/j.jpowsour.2004.02.033. URL: https://linkinghub.elsevier.com/retrieve/pii/S0378775304003611.

[148] Andrei Romanenko and José A.A.M. Castro. "The unscented filter as an alternative to the EKF for nonlinear state estimation: a simulation case study". In: *Computers & Chemical Engineering* 28 (3 Mar. 2004), pp. 347–355. ISSN: 00981354. DOI: 10.1016/S0098-1354(03)00193-5. URL: https://linkinghub.elsevier.com/retrieve/pii/S0098135403001935.

[149] Gregory L. Plett. "Sigma-point Kalman filtering for battery management systems of LiPB-based HEV battery packs. Part 1: Introduction and state estimation". In: *Journal of Power Sources* 161 (2 Oct. 2006), pp. 1356–1368. ISSN: 03787753. DOI: 10.1016/j.jpowsour.2006.06.003. URL: %7Bhttps://linkinghub.elsevier.com/retrieve/pii/S0378775306011414%7D.

[150] Gregory L. Plett. "Sigma-point Kalman filtering for battery management systems of LiPB-based HEV battery packs. Part 2: Simultaneous state and parameter estimation". In: *Journal of Power Sources* 161 (2 Oct. 2006), pp. 1369–1384. ISSN:

03787753. DOI: 10.1016/j.jpowsour.2006.06.004. URL: %7Bhttps://linkinghub.elsevier.com/retrieve/pii/S0378775306011438%7D.

[151] Kailong Liu et al. "An advanced Lithium-ion battery optimal charging strategy based on a coupled thermoelectric model". In: *Electrochimica Acta* 225 (Jan. 2017), pp. 330–344. ISSN: 00134686. DOI: 10.1016/j.electacta.2016.12.129. URL: https://linkinghub.elsevier.com/retrieve/pii/S0013468616326883.

[152] Changfu Zou et al. "Electrothermal dynamics-conscious lithium-ion battery cell-level charging management via state-monitored predictive control". In: *Energy* 141 (Dec. 2017), pp. 250–259. ISSN: 03605442. DOI: 10.1016/j.energy.2017.09.048. URL: https://linkinghub.elsevier.com/retrieve/pii/S0360544217315712.

[153] Zhuo Yang, Devendra Patil, and Babak Fahimi. "Electrothermal Modeling of Lithium-Ion Batteries for Electric Vehicles". In: *IEEE Transactions on Vehicular Technology* 68 (1 Jan. 2019), pp. 170–179. ISSN: 0018-9545. DOI: 10.1109/TVT.2018.2880138. URL: https://ieeexplore.ieee.org/document/8526315/.

[154] Xiaosong Hu et al. "Optimal Multistage Charging of NCA/Graphite Lithium-Ion Batteries Based on Electrothermal-Aging Dynamics". In: *IEEE Transactions on Transportation Electrification* 6 (2 June 2020), pp. 427–438. ISSN: 2332-7782. DOI: 10.1109/TTE.2020.2977092. URL: https://ieeexplore.ieee.org/document/9018113/.

[155] Jianguo Wang et al. "Effect analysis on thermal behavior enhancement of lithium–ion battery pack with different cooling structures". In: *Journal of Energy Storage* 32 (Dec. 2020), p. 101800. ISSN: 2352152X. DOI: 10.1016/j.est.2020.101800. URL: https://linkinghub.elsevier.com/retrieve/pii/S2352152X20316376.

[156] Tao Wang, K.J. Tseng, and Jiyun Zhao. "Development of efficient air-cooling strategies for lithium-ion battery module based on empirical heat source model". In: *Applied Thermal Engineering* 90 (Nov. 2015), pp. 521–529. ISSN: 13594311. DOI: 10.1016/j.applthermaleng.2015.07.033. URL: https://linkinghub.elsevier.com/retrieve/pii/S1359431115007176.

[157] Wen Yang et al. "Thermal performance of axial air cooling system with bionic surface structure for cylindrical lithium-ion battery module". In: *International Journal of Heat and Mass Transfer* 161 (Nov. 2020), p. 120307. ISSN: 00179310. DOI: 10.1016/j.ijheatmasstransfer.2020.120307. URL: https://linkinghub.elsevier.com/retrieve/pii/S0017931020332439.

[158] Joshua Smith et al. "Simulative method for determining the optimal operating conditions for a cooling plate for lithium-ion battery cell modules". In: *Journal of Power Sources* 267 (Dec. 2014), pp. 784–792. ISSN: 03787753. DOI: 10.1016/j.jpowsour.2014.06.001. URL: https://linkinghub.elsevier.com/retrieve/pii/S0378775314008490.

[159] Mohsen Akbarzadeh et al. "A comparative study between air cooling and liquid cooling thermal management systems for a high-energy lithium-ion battery module". In: *Applied Thermal Engineering* 198 (Nov. 2021), p. 117503. ISSN: 13594311.

DOI: 10.1016/j.applthermaleng.2021.117503. URL: https://linkinghub.elsevier.com/retrieve/pii/S1359431121009352.

[160] Weichao Zhuang et al. "An intelligent thermal management system for optimized lithium-ion battery pack". In: *Applied Thermal Engineering* 189 (May 2021), p. 116767. ISSN: 13594311. DOI: 10.1016/j.applthermaleng.2021.116767. URL: https://linkinghub.elsevier.com/retrieve/pii/S1359431121002222.

[161] Fan He, Haoting Wang, and Lin Ma. "Experimental demonstration of active thermal control of a battery module consisting of multiple Li-ion cells". In: *International Journal of Heat and Mass Transfer* 91 (Dec. 2015), pp. 630–639. ISSN: 00179310. DOI: 10.1016/j.ijheatmasstransfer.2015.07.069. URL: https://linkinghub.elsevier.com/retrieve/pii/S0017931015007899.

[162] Xuning Feng et al. "A 3D thermal runaway propagation model for a large format lithium ion battery module". In: *Energy* 115 (Nov. 2016), pp. 194–208. ISSN: 03605442. DOI: 10.1016/j.energy.2016.08.094. URL: https://linkinghub.elsevier.com/retrieve/pii/S0360544216312075.

[163] Yunhua Gan et al. "Development of thermal equivalent circuit model of heat pipe-based thermal management system for a battery module with cylindrical cells". In: *Applied Thermal Engineering* 164 (Jan. 2020), p. 114523. ISSN: 13594311. DOI: 10.1016/j.applthermaleng.2019.114523. URL: https://linkinghub.elsevier.com/retrieve/pii/S1359431118365104.

[164] Hongguang Sun et al. "Three-dimensional thermal modeling of a lithium-ion battery pack". In: *Journal of Power Sources* 206 (May 2012), pp. 349–356. ISSN: 03787753. DOI: 10.1016/j.jpowsour.2012.01.081. URL: https://linkinghub.elsevier.com/retrieve/pii/S0378775312001802.

[165] Jiacheng He et al. "A lumped electro-thermal model for a battery module with a novel hybrid cooling system". In: *Applied Thermal Engineering* 221 (Feb. 2023), p. 119874. ISSN: 13594311. DOI: 10.1016/j.applthermaleng.2022.119874. URL: https://linkinghub.elsevier.com/retrieve/pii/S135943112201804X.

[166] B.E. Lebrouhi et al. "Low-cost numerical lumped modelling of lithium-ion battery pack with phase change material and liquid cooling thermal management system". In: *Journal of Energy Storage* 54 (Oct. 2022), p. 105293. ISSN: 2352152X. DOI: 10.1016/j.est.2022.105293. URL: https://linkinghub.elsevier.com/retrieve/pii/S2352152X22012919.

[167] Anup Barai et al. "Scale-up of lithium-ion battery model parameters from cell level to module level – identification of current issues". In: *Energy Procedia* 138 (Oct. 2017), pp. 223–228. ISSN: 18766102. DOI: 10.1016/j.egypro.2017.10.154. URL: https://linkinghub.elsevier.com/retrieve/pii/S187661021735097X.

[168] Jianwei Li et al. "Bandwidth based electrical-analogue battery modeling for battery modules". In: *Journal of Power Sources* 218 (Nov. 2012), pp. 331–340. ISSN: 03787753. DOI: 10.1016/j.jpowsour.2012.07.006. URL: https://linkinghub.elsevier.com/retrieve/pii/S0378775312011202.

[169] Chitradeep Sen and Narayan C Kar. "Battery pack modeling for the analysis of battery management system of a hybrid electric vehicle". In: *2009 IEEE vehicle power and propulsion conference*. IEEE. 2009, pp. 207–212.

[170] Anandh Ramesh Babu et al. "System-Level Modeling and Thermal Simulations of Large Battery Packs for Electric Trucks". In: *Energies* 14 (16 Aug. 2021), p. 4796. ISSN: 1996-1073. DOI: 10.3390/en14164796. URL: https://www.mdpi.com/1996-1073/14/16/4796.

[171] Leo Wildfeuer et al. "Experimental Characterization of Li-Ion Battery Resistance at the Cell, Module and Pack Level". In: IEEE, May 2019, pp. 1–12. ISBN: 978-1-7281-3703-2. DOI: 10.1109/EVER.2019.8813578. URL: https://ieeexplore.ieee.org/document/8813578/.

[172] Lisa Calearo et al. "A methodology to model and validate electro-thermal-aging dynamics of electric vehicle battery packs". In: *Journal of Energy Storage* 55 (Nov. 2022), p. 105538. ISSN: 2352152X. DOI: 10.1016/j.est.2022.105538. URL: https://linkinghub.elsevier.com/retrieve/pii/S2352152X22015298.

[173] Majid Astaneh et al. "Multiphysics simulation optimization framework for lithium-ion battery pack design for electric vehicle applications". In: *Energy* 239 (Jan. 2022), p. 122092. ISSN: 03605442. DOI: 10.1016/j.energy.2021.122092. URL: https://linkinghub.elsevier.com/retrieve/pii/S0360544221023409.

[174] Matthieu Dubarry, Nicolas Vuillaume, and Bor Yann Liaw. "From single cell model to battery pack simulation for Li-ion batteries". In: *Journal of Power Sources* 186 (2 Jan. 2009), pp. 500–507. ISSN: 03787753. DOI: 10.1016/j.jpowsour.2008.10.051. URL: https://linkinghub.elsevier.com/retrieve/pii/S0378775308019411.

[175] Xiaosong Hu, Shengbo Li, and Huei Peng. "A comparative study of equivalent circuit models for Li-ion batteries". In: *Journal of Power Sources* 198 (Jan. 2012), pp. 359–367. ISSN: 03787753. DOI: 10.1016/j.jpowsour.2011.10.013. URL: https://linkinghub.elsevier.com/retrieve/pii/S0378775311019628.

[176] Patrick C Vratny et al. "Battery pack modeling methods for universally-electric aircraft". In: *4th CEAS Air & Space Conference*. Linköping University Electronic Press Linköping, Sweden. 2013, pp. 525–535.

[177] Saeed Sepasi, Reza Ghorbani, and Bor Yann Liaw. "Improved extended Kalman filter for state of charge estimation of battery pack". In: *Journal of Power Sources* 255 (June 2014), pp. 368–376. ISSN: 03787753. DOI: 10.1016/j.jpowsour.2013.12.093. URL: https://linkinghub.elsevier.com/retrieve/pii/S037877531302082X.

[178] Xinyuan Fan et al. "Simplified Battery Pack Modeling Considering Inconsistency and Evolution of Current Distribution". In: *IEEE Transactions on Intelligent Transportation Systems* 22 (1 Jan. 2021), pp. 630–639. ISSN: 1524-9050. DOI: 10.1109/TITS.2020.3010567. URL: https://ieeexplore.ieee.org/document/9153803/.

[179] Lokendra Ramotar et al. "Experimental verification of a thermal equivalent circuit dynamic model on an extended range electric vehicle battery pack". In: *Journal of Power Sources* 343 (Mar. 2017), pp. 383–394. ISSN: 03787753. DOI: 10.1016/j.jpowsour.2017.01.040. URL: https://linkinghub.elsevier.com/retrieve/pii/S037877531730040X.

[180] Selvaraj Vedhanayaki and Vairavasundaram Indragandhi. "Certain investigation and implementation of Coulomb counting based unscented Kalman filter for state of charge estimation of lithium-ion batteries used in electric vehicle application". In: *International Journal of Thermofluids* 18 (May 2023), p. 100335. ISSN: 26662027. DOI: 10.1016/j.ijft.2023.100335. URL: https://linkinghub.elsevier.com/retrieve/pii/S266620272300054X.

[181] Hafiz Farhaj Khan et al. "A Lagrange multiplier and sigma point Kalman filter based fused methodology for online state of charge estimation of lithium-ion batteries". In: *Journal of Energy Storage* 41 (Sept. 2021), p. 102843. ISSN: 2352152X. DOI: 10.1016/j.est.2021.102843. URL: https://linkinghub.elsevier.com/retrieve/pii/S2352152X21005673.

[182] Joaquín Klee Barillas et al. "A comparative study and validation of state estimation algorithms for Li-ion batteries in battery management systems". In: *Applied Energy* 155 (Oct. 2015), pp. 455–462. ISSN: 03062619. DOI: 10.1016/j.apenergy.2015.05.102. URL: https://linkinghub.elsevier.com/retrieve/pii/S0306261915007357.

[183] Michael Armbrust et al. "A view of cloud computing". In: *Communications of the ACM* 53.4 (2010), pp. 50–58.

[184] Antonio Regalado. *Who Coined 'Cloud Computing'?* Gartner. 2011-10-31. URL: https://www.technologyreview.com/2011/10/31/257406/who-coined-cloud-computing/ (visited on 06/13/2023).

[185] Tharam Dillon, Chen Wu, and Elizabeth Chang. "Cloud Computing: Issues and Challenges". In: IEEE, 2010, pp. 27–33. ISBN: 978-1-4244-6695-5. DOI: 10.1109/AINA.2010.187. URL: http://ieeexplore.ieee.org/document/5474674/.

[186] Mohammad Ilyas Malik. "CLOUD COMPUTING-TECHNOLOGIES". In: *International Journal of Advanced Research in Computer Science* 9 (2 Apr. 2018), pp. 379–384. ISSN: 09765697. DOI: 10.26483/ijarcs.v9i2.5760. URL: http://www.ijarcs.info/index.php/Ijarcs/article/view/5760/4747.

[187] Borko Furht and Armando Escalante. *Handbook of Cloud Computing*. Ed. by Borko Furht and Armando Escalante. Springer US, 2010. ISBN: 978-1-4419-6523-3. DOI: 10.1007/978-1-4419-6524-0. URL: http://link.springer.com/10.1007/978-1-4419-6524-0.

[188] Vanitha Kumar. *CLOUD COMPUTING COMPONENTS, SERVICES, TOOLS AND ITS ROADMAP TO ORGANIZATION*. 2020. URL: https://www.researchgate.net/publication/338965765.

[189] Amazon Web Services. *What is AWS?* Amazon. URL: https://aws.amazon.com/what-is-aws/?nc1=h_ls (visited on 06/13/2023).

[190] Amazon Web Services. *Regions and Availability Zones*. Amazon. URL: https://aws.amazon.com/about-aws/global-infrastructure/regions_az/?nc1=h_ls (visited on 06/13/2023).

[191] Microsoft Azure. *What is Azure?* Microsoft Azure. URL: https://azure.microsoft.com/en-us/resources/cloud-computing-dictionary/what-is-azure/ (visited on 06/13/2023).

[192] Microsoft Azure. *Azure Availability Zones: An In-Depth Look*. Microsoft Azure. URL: https://bluexp.netapp.com/blog/azure-availability-zones-an-in-depth-look (visited on 06/13/2023).

[193] Google Cloud. *What is Google Cloud Platform?* Google. URL: https://cloud.google.com/ (visited on 06/13/2023).

[194] Google Cloud. *Cloud locations*. Google. URL: https://cloud.google.com/about/locations (visited on 06/13/2023).

[195] Hao Zhang et al. "A Digital Twin-Based Approach for Designing and Multi-Objective Optimization of Hollow Glass Production Line". In: *IEEE Access* 5 (Oct. 2017), pp. 26901–26911. ISSN: 2169-3536. DOI: 10.1109/ACCESS.2017.2766453. URL: http://ieeexplore.ieee.org/document/8082476/.

[196] Yuxin Wen et al. "Recent advances and trends of predictive maintenance from data-driven machine prognostics perspective". In: *Measurement* 187 (Jan. 2022), p. 110276. ISSN: 02632241. DOI: 10.1016/j.measurement.2021.110276. URL: https://linkinghub.elsevier.com/retrieve/pii/S0263224121011805.

[197] Qisong Zhang et al. "A deep learning method for lithium-ion battery remaining useful life prediction based on sparse segment data via cloud computing system". In: *Energy* 241 (Feb. 2022), p. 122716. ISSN: 03605442. DOI: 10.1016/j.energy.2021.122716. URL: https://linkinghub.elsevier.com/retrieve/pii/S0360544221029650.

[198] Muhammad Sameer Sheikh, Jun Liang, and Wensong Wang. "Security and Privacy in Vehicular Ad Hoc Network and Vehicle Cloud Computing: A Survey". In: *Wireless Communications and Mobile Computing* 2020 (Jan. 2020), pp. 1–25. ISSN: 1530-8669. DOI: 10.1155/2020/5129620. URL: https://www.hindawi.com/journals/wcmc/2020/5129620/.

[199] *Lithium-ion 26650 Cells | Nanophosphate Batteries | Lithium Werks*. URL: https://lithiumwerks.com/products/lithium-ion-26650-cells/.

[200] D Bernardi, E Pawlikowski, and J Newman. *A General Energy Balance for Battery Systems*. Apr. 1984. URL: %7Bhttps://escholarship.org/uc/item/9fx5f0h8%7D.

[201] Nerea Nieto et al. "Thermal Modeling of Large Format Lithium-Ion Cells". In: *Journal of The Electrochemical Society* 160 (2 Nov. 2013), A212–A217. ISSN: 0013-4651. DOI: 10.1149/2.042302jes. URL: %7Bhttps://iopscience.iop.org/article/10.1149/2.042302jes%7D.

[202] Christophe Forgez et al. “Thermal modeling of a cylindrical LiFePO4/graphite lithium-ion battery”. In: *Journal of Power Sources* 195 (9 May 2010), pp. 2961–2968. ISSN: 03787753. DOI: 10.1016/j.jpowsour.2009.10.105. URL: %7Bhttps://linkinghub.elsevier.com/retrieve/pii/S037877530901982X%7D.

[203] Zhenpo Wang, Wentao Fan, and Peng Liu. “Simulation of Temperature Field of Lithium Battery Pack Based on Computational Fluid Dynamics”. In: *Energy Procedia* 105 (May 2017), pp. 3339–3344. ISSN: 18766102. DOI: 10.1016/j.egypro.2017.03.764. URL: %7Bhttps://linkinghub.elsevier.com/retrieve/pii/S1876610217308275%7D.

[204] Fei Gao and Zhiyuan Tang. “Kinetic behavior of LiFePO4/C cathode material for lithium-ion batteries”. In: *Electrochimica Acta* 53 (15 June 2008), pp. 5071–5075. ISSN: 00134686. DOI: 10.1016/j.electacta.2007.10.069. URL: %7Bhttps://linkinghub.elsevier.com/retrieve/pii/S0013468607013576%7D.

[205] Pallavi Verma, Pascal Maire, and Petr Novák. “A review of the features and analyses of the solid electrolyte interphase in Li-ion batteries”. In: *Electrochimica Acta* 55 (22 Sept. 2010), pp. 6332–6341. ISSN: 00134686. DOI: 10.1016/j.electacta.2010.05.072. URL: %7Bhttps://linkinghub.elsevier.com/retrieve/pii/S0013468610007747%7D.

[206] Yongling He et al. “Modeling of Dynamic Hysteresis Characters for the Lithium-Ion Battery”. In: *Journal of The Electrochemical Society* 167 (9 Jan. 2020), p. 090532. ISSN: 0013-4651. DOI: 10.1149/1945-7111/ab8b96. URL: %7Bhttps://iopscience.iop.org/article/10.1149/1945-7111/ab8b96%7D.

[207] R. E. Kalman. “A New Approach to Linear Filtering and Prediction Problems”. In: *Journal of Basic Engineering* 82 (1 Mar. 1960), pp. 35–45. ISSN: 0021-9223. DOI: 10.1115/1.3662552. URL: %7Bhttps://asmedigitalcollection.asme.org/fluidsengineering/article/82/1/35/397706/A-New-Approach-to-Linear-Filtering-and-Prediction%7D.

[208] Jaemoon Lee, Oanyong Nam, and B.H. Cho. “Li-ion battery SOC estimation method based on the reduced order extended Kalman filtering”. In: *Journal of Power Sources* 174 (1 Nov. 2007), pp. 9–15. ISSN: 03787753. DOI: 10.1016/j.jpowsour.2007.03.072. URL: %7Bhttps://linkinghub.elsevier.com/retrieve/pii/S0378775307007112%7D.

[209] Leire Martín-Martín et al. “Modeling based on design of thermal management systems for vertical elevation applications powered by lithium-ion batteries”. In: *Applied Thermal Engineering* 102 (June 2016), pp. 1081–1094. ISSN: 13594311. DOI: 10.1016/j.applthermaleng.2016.02.127. URL: https://linkinghub.elsevier.com/retrieve/pii/S1359431116302708.

[210] David Marcos et al. “Functional Safety BMS Design Methodology for Automotive Lithium-Based Batteries”. In: *Energies* 14 (21 Oct. 2021), p. 6942. ISSN: 1996-1073. DOI: 10.3390/en14216942. URL: https://www.mdpi.com/1996-1073/14/21/6942.

[211] *AWS IoT MQTT Protocol*. https://docs.aws.amazon.com/iot/latest/developerguide/mqtt.html. Accessed: July 10, 2023.

[212] *AWS API Gateway HTTP API*. https://docs.aws.amazon.com/apigateway/latest/developerguide/http-api.html. Accessed: July 5, 2023.

[213] *Amazon EC2 Documentation*. https://aws.amazon.com/ec2/?nc1=h_ls. Accessed: July 5, 2023.

[214] *AWS Lambda*. https://aws.amazon.com/lambda/.

[215] *Amazon EC2 Instance Types - C7g Instances*. https://aws.amazon.com/ec2/instance-types/c7g/.